SCIENCE & ENGINEERING

SERS

RESEARCH SEMESTER

Lawrence Livermore National Laboratory

Fall 1994

ABSTRACTS FOR STUDENT SYMPOSIUM

December 9, 1994

Sponsored by:

The U.S. Department of Energy
Office of Energy Research

DISTRIBUTION OF THIS DOCUMENT IS UNLIMITED

Conf-941

DISCLAIMER

SCIENCE & ENGINEERING
SERS
RESEARCH SEMESTER

Fall 1994 Student Symposium Abstracts

Table of Contents

Electrochemical Cells in the Reduction of Hexavalent Chromium

Shipra Bansal
University of California, Berkeley
Engineering Research Division

ABSTRACT

Electrochemical reduction of hexavalent chromium (Cr^{+6}) to its trivalent state (Cr^{+3}) is showing promising results in treating ground water at Lawrence Livermore National Laboratory's (LLNL) Main Site. An electrolytic cell using stainless-steel and brass electrodes has been found to offer the most efficient reduction while yielding the least amount of precipitate. Trials have successfully lowered concentrations of Cr^{+6} to below the 11 parts per billion state standard.

Currently, several trials are being run to determine optimal voltage in running the cell; each trial consists of running a voltage between 6V and 48V for ten minutes through samples obtained at Treatment Facility C (TFC). No conclusive data has been obtained and hence, the methodology is being reevaluated.

An Automated System for Studying the Power Distribution of Electron Beams

Christina A. Filarowski
Suffolk University
Computer Applications Science & Engir. Division

ABSTRACT

Precise welds with an electron beam welder are difficult to reproduce because the factors effecting the electron beam current density distribution are not easily controlled. One method for measuring the power density distribution in EB welds uses computer tomography to reconstruct an image of the current density distribution[1,2]. This technique uses many separate pieces of hardware and software packages to obtain the data and then reconstruct it consequently, transferring this technology between different machines and operators is difficult. Consolidating all of the hardware and software into one machine to execute the same tasks will allow for real-time measurement of the EB power density distribution and will provide a facilitated means for transferring various welding procedure between different machines and operators, thereby enhancing reproducibility of electron beam welds.

The Mapping of Novel Genes to Human Chromosome 19.

Joel Buenaventura
Sarah Lawrence College, New York
Department of Biology and Biotechnology

ABSTRACT

The principle goal of our laboratory is the discovery of new genes from human chromosome 19. One of the strategies to achieve this goal is the use of cDNA clones known as "expressed sequence tags" (ESTs). ESTs, short segments of a cDNA clone that correspond to the mRNA, occur as unique regions in the genome and, therefore, can be used as markers to identify new genes. In collaboration with researchers from Genethon in France, fifteen cDNA clones from a normalized human infant brain cDNA library were tested and determined to map to chromosome 19. A verification procedure is then followed to confirm assignment to chromosome 19. First, primers for each cDNA clone are developed and then amplified by polymerase chain reaction from genomic DNA. Next, a ^{32}P-radiolabeled probe is made by polymerase chain reaction for each clone and then hybridized against filters containing an LLNL chromosome 19-specific cosmid library to find putative locations on the chromosome. The location is then verified by running a polymerase chain reaction against the positive cosmids. With the Browser database at LLNL, additional information about the positive cosmids can be found. Through use of the BLAST database at the National Library of Medicine, homologous sequences to the clones can be found.

Among the fifteen cDNA clones received from Genethon, all have been amplified by polymerase chain reaction. Three have turned out as repetitive elements in the genome. Two have been mapped to specific locations on chromosome 19. Putative locations have been found for the remaining ten clones and verification is in progress.

Bolometer Analysis Comparisons

Jennifer M. Daniel
Athens State College
Magnetic Fusion Engineering Division

ABSTRACT

This paper describes the work done to develop a bolometer post processor that converts volumetric radiated power values taken from a UEDGE solution to a line integrated radiated power along chords of the bolometers in the DIII-D tokamak. The UEDGE code calculates plasma physics quantities, such as plasma density, radiated power, or electron temperature, and compares them to actual diagnostic measurements taken from the scrape off layer (SOL) and divertor regions of the DIII-D tokamak. Bolometers are devices measuring radiated power within the tokamak. The bolometer interceptors are made up of two complete arrays, an upper array with a vertical view and a lower array with a horizontal view, so that a two dimensional profile of the radiated power may be obtained. The bolometer post processor stores line integrated values take from UEDGE solutions into a file in tabular format. Experimental data is then put into tabular form and placed in another file. Comparisons can be made between the UEDGE solutions and actual bolometer data. Analysis has been done to determine the accuracy of the plasma physics involved in producing UEDGE simulations.

Design and Implementation of the LLNL Gigabit Testbed

Daniel Garcia
East Stroadsburg University
Computations Department

ABSTRACT

This paper will discuss the design philosophy and implementation of the LLNL Gigabit Testbed (LGTB). The LGTB will be used to test the interoprobability of high speed networking technologies from numerous vendors. This paper will look at how the LGTB intends to test these technologies, as well as take a look at the current implementation of the Testbed Control System.

In Vitro Synthesis and Purification of PhIP-Deoxyguanosine and PhIP-DNA Covalent Complexes

Jenatta Freeman
Alabama A & M
Division

ABSTRACT

2-amino-1-methyl-6-phenylimidazo[4,5-*b*]pyridine (PhIP) is a heterocyclic amine compound formed when meats are cooked at high temperatures. PhIP damages DNA by forming covalent complexes with DNA guanine bases and is moderately mutagenic. Thus, PhIP is a suspected human carcinogen. In an effort to understand how the binding of PhIP to DNA may cause cancer, it is important to characterize the structures of PhIP-damaged DNA molecules. The initial step in this process is synthesizing PhIP-damaged DNA molecules and purifying them for structural analysis. To make PhIP-damaged DNA, *N*-hydroxy PhIP was reacted with acetic acid and acetic anhydride to produce *N*-acetoxy-PhIP, the ultimate carcinogen that binds DNA *in vivo*. This step was followed by the adduction reaction in which the *N*-acetoxy-PhIP was covalently bound to an eleven base oligodeoxynucleotide [5'd(CCTACGCATCC)3'] or to 2'-deoxyguanosine (dG) in separate reactions, producing the adduct at the guanine. The level of adduction was quantified by absorbance spectroscopy using the Beer-Lambert equation. Phenyl and polystyrene reversed-phase columns were selected to separate and purify the adducts of dG and oligodeoxynucleotides, respectively, by high performance liquid chromatography (HPLC). The HPLC data and fluorescence spectroscopy indicated the presence of several species of oligodeoxynucleotide- or dG-PhIP adducts. The reaction of PhIP with dG resulted in a reddish precipitate that was likely the *N*-(deoxyguanosin-8-yl)-PhIP (dG-C8-PhIP) adduct, with a more polar adduct fraction remaining in the supernatant. Reversed-phase HPLC analysis of the adducts in the supernatant revealed the existence of species of much shorter retention times than the dG-C8-PhIP adduct, confirming that these species are more polar than dG-C8-PhIP. These more polar PhIP adducts were fraction-collected and their structures will be solved by nuclear magnetic resonance.

Pre-thymic Somatic Mutation leads to High Mutant FrequencyHypoxanthine-guanine Phosphoribosyl Transferase Gene

Jamie Jett
University of Arkansas
Biology and Biotechnology Research Department

ABSTRACT

While characterizing the background mutation spectrum of the Hypoxathine-guanine phosphoribosyl transferase (HPRT) gene in a normal population, an outlier with a high mutant frequency of thioguanine resistant lymphocytes was found. When studied at the age of 46, this individual had been smoking 60 cigarettes per day for 38 years. His mutant frequency was calculated at 3.6 and 4.2×10^{-4} for two sampling periods eight months apart. Sequencing analysis of the HPRT gene in his mutant thioguanine resistant T lymphocytes was done to find whether the cells had a high rate of mutation or if the mutation was due to a single occurrence of mutation and ,if so, when in the T lymphocyte development the mutation occurred.

By T-cell receptor analysis it was found that out of 40 thioguanine resistant clones there was no dominant gamma T cell receptor gene rearrangement. By DNA sequencing analysis thirty nine of those clones were found to have the same base substitution of G -> T at cDNA position 617. Due to the consistent mutant frequency from both sampling periods and the varying T cell receptors, the high mutant frequency cannot be due to recent proliferation of a mutant T lymphocyte.

From the TCR and DNA sequence analysis we conclude that the G -> T mutation must have occurred in a T lymphocyte precursor before thymic differentiation so that the thioguanine resistant clones would share the same base substitution but not the same gamma T cell receptor gene.
20

Characterization of Thin Film Multi-layers with Magnetization Curves and Modeling of Low Angle X-Ray Diffraction Data

Michael W. Lane
Emory & Henry College
Chemistry and Materials Science Division

ABSTRACT

A series of FM/SP multi-layer systems with FM=Fe, Co, and NiFe and SP-Si, Ge, FeSi2, and CoSi2 were studied using magnetization curves and modeling of low angle x-ray diffraction data. The magnetization of the multi-layers was compared for different deposition conditions and layer thicknesses. The magnetic characteristics were compared to structural information derived from the modeling of the x-ray data. Of the three FMs used we find the magnetization of Fe/SP MLs is closest to the predicted value for a perfect ML. Modeling shows that the interfaces of the multi-layer are anisotropic, with the metal-on-SP interfaced being wider than the Sp-on-metal interfaces, similar to previous results of Mo/Si x-ray mirrors. Annealing experiments were performed to study the thermal stability of the MLs and gain an understanding of the change in film morphology as the samples are heated.

Total Least Squares

Daniel Leo Lau
Purdue University
Electronics Engineering Department

ABSTRACT

Least Squares (LS) is a method of curve fitting used with the assumption that errors exist in the observation vector. The method of Total Least Squares (TLS) is more useful in cases where there is error in the data matrix as well as the observation vector. This paper describes work done in comparing the LS and TLS results for parameter estimation of a motor trajectory based on a time series of angular observations. To improve the results, several derivations of the LS and TLS methods were investigated, and early findings show slight improvements from the TLS over the LS method.

Determining the Water Content of The Geysers Graywacke of Northern California

Alice Marsh
University of Montana
Earth Sciences Division

ABSTRACT

The water content, porosity and permeability measurements of The Geysers geothermal reservoir rocks are used to predict the lifetime of the resource. The Geysers reservoir rock, drilled from defunct well SB-15-D, is a highly fractured and veined, weakly metamorphosed Franciscan graywacke. Upon removal from the well, the cores were sealed in aluminum tubes to prevent water loss.

Archimedes principle, humidity detection, ultrasonics and x-ray scanning are viable methods to measure the in-situ water content of the graywacke. Archimedes principle will be used to determine the density of the core before and after drying. Humidity measurements were taken of the air around a one and a half foot encased core, recovered from a depth of 918.9 feet. Over a seven day period, the humidity reached almost 100% indicating that the air around the core was saturated in water vapor. The sealing method is effective, preserving the in-situ water content. Ultrasonic measurements will be taken of the core upon removal from aluminum tube to determine the change of p-wave velocity with change in water content. Water in the pores increases the effective compressibility of the rock therefore increasing the p-velocity. The measured p-wave velocities can then be used in the field to determine in-situ water content. Three dimensional x-ray images will be used to determine the deviations from average density within individual cores. Since the density depends on water content as well as mineralogy, images can show the location of pore fluid and drilling mud.

A General Approach to Sharing Data Between Scientific Representations

Joe McCormick
California State University, Chico
Computations Department

ABSTRACT

Climate modeling is a computationally intensive process. Until recently computers were not powerful enough to perform the complex calculations required for an earth climate simulation. As a result standalone programs were created that represent the major components of the earth's climate (e.g., Atmospheric Circulation Model). Recent advances in computing, including massively parallel computing, make it possible to couple the major components forming a complete earth climate simulation.

The ability to couple different climate model components will significantly improve the reliability and accuracy on climate prediction. Historically each major component of the coupled earth simulation is a stand along program designed independently with different coordinate systems and data representations. In order for two component models to be coupled, the data of one model must be mapped to the coordinate system of the second model. The focus of this project is to provide a general tool to facilitate the mapping of data between simulation components, with an emphasis on using object-oriented programming techniques to develop polynomial interpolation, line and area weighting, and aggregation algorithms.

Nanomechanical Properties of SiC Thin Films Grown From C_{60} Precursors

Kathryn Morse
Colorado School of Mines
Material Fabrication Division, M.E.

ABSTRACT

C_{60} was deposited on a silicon substrate in vacuum at about 1250 K. The C_{60} reacts with the surface to form a think film of SiC. The Auger spectra suggests that the structure is stoichiometric. Hardness and friction were measured under atmospheric conditions using an atomic force microscope with diamond and silicon nitride tips respectively. The hardness is found to be between 25 and 50 GPa depending on the morphology of the film. The friction is about one third that of the silicon nitride sliding on a silicon substrate. In order to better understand the atomic scale mechanisms that determine the hardness and friction of SiC, molecular dynamics simulations of a diamond indenting and sliding against a crystalline SiC substrate were performed.

Advanced Information Technology, A Tool Set for Building Clean Database Applications

David Price
East Stroudsburg University
Computations Department

ABSTRACT

This paper discussed the attributes of the Advanced Information Technology (AIT) tool set, a database application builder designed at the Lawrence Livermore National Laboratory. AIT consists of a C library and several utilities that provide referential integrity across a database, interactive menu and field level help, and a code generator for building tightly controlled data entry support. AIT also provides for dynamic menu trees, report generation support to consolidate and format data into human readable form, and creation of user groups to control access to both menu tree nodes and database tables. Composition of the library and utilities is discussed, along with relative strengths and weaknesses. In addition, an instantiation of the AIT tool set is presented using a specific application. Conclusions about the future and value of the tool set are then drawn based on the use of the tool set with that specific application.

The Design of an Automated Electrolytic Enrichment Procedure for Tritium

Jeffrey L. Myers
University of Washington
Radiation Analytical Sciences Section of the
Environmental Protection Department

Abstract

The present thrust in our laboratories today is toward automation and microprocessor control of many of the laboratory operations, including data collection, analysis, archiving, and reporting.

One of our standard operations is the analysis of low-level tritium concentrations in various natural water samples. Tritium, a radioactive isotope of hydrogen, is pre-concentrated using electrolytic enrichment apparatus and then analyzed by liquid scintillation counting. The apparatus, including the purification process by vacuum distillation is currently undertaken manually, hence being highly labor-intensive. The whole process takes about 2 to 3 weeks to complete per sample, with a dedicated personnel operating the process.

Our intention is to automate the entire process, specifically having its operation to be PC-LabVIEW controlled with real-time monitoring capability. I have been involved in the design and fabrication of an automated prototypical electrolytic enrichment cell and vacuum distillation apparatus. Work has been done for optimizing the electrolytic process by assessing the different parameters of the electrolysis process. Hardware and software development have been an integral component of this project.

Fluvial Terrace Dating Using In-Situ Cosmogenic ^{21}Ne

Edward Sexton
University of Illinois
Nuclear Chemistry Division

ABSTRACT

Through the analysis of cosmic-ray produced radio-genic and stable nuclide concentrations, specifically ^{21}Ne, we hope to date certain geomorphic features located along the tributaries of the Colorado River in the Eastern Grand Canyon. During the Quaternary, the Colorado River system has been fed by glacial melting and run-off of the Wind River and Colorado Mountain Ranges. Past periods of aggradation allowed the emplacement of terrace features from debris flow activity. By dating these features we can further constrain the timing of key events such as river downcutting and terrace formation and exposure age. By knowing the age and elevation of each terrace we can determine an average rate of downcutting of this river system. This, in turn, will perhaps offer information regarding alpine glaciation which is a sensitive indicator to global climate change. In turn, studying the relative concentrations of these species in surface rocks can be useful in studying gladiologic periodicity and the long term relation ship between solar activity and climate.

Computer-Aided Mapping of Stream Channels Beneath the Lawrence Livermore National Laboratory, Livermore, CA

Mike Sick
Guilford College, N.C.
Environmental Protection Department

ABSTRACT

Stream channels beneath the Lawrence Livermore National Laboratory (LLNL) were mapped using the SLICE software package developed at LLNL. Once detailed mapping of the channels is complete, the 2D correlations from map view will be connected to form a 3D model of the channel system. This model will be used to optimize the placement of ground water extraction wells as part of the pump and treat remediation of the plume.

The SLICE program constructs both vertical (cross section) and map view geologic images of the subsurface for geologic interpretation. The study area is located in the southwest corner of the LLNL site where ground water is contaminated by a plume of volatile organic compounds (VOCs). The plume covers an area of approximately 1.4 square miles and is moving off site to the west. The area is underlain by 300-400 feet of heterogeneous alluvial sediments that represent a braided stream environment. The braided stream channels are filled with course grained gravels and sands whose higher permeability controls the migration of ground water.

X-ray Spectroscopic Technique for Energetic Electron Transport Studies in Short-Pulse Laser/Plasma Interactions

Teresa E. Tutt
Rensseloer Polytechnic
Y Division, NOVA

ABSTRACT

When a solid target is irradiated by a laser beam, the material is locally heated to a very high temperature and a plasma forms. The interaction of the laser with plasma can produce energetic electrons. By observing the behavior of these "hot" electrons, we hope to obtain a better understanding of Laser/Plasma Interactions.

In our work we employ a layered fluorescer technique to study the transport, and therefore the energetics, of the electrons. The plasma is formed on a thin foil of metallic Palladium (Pd) which is bonded to thin layer of metallic Tin (Sn). Electrons formed from the plasma penetrate first the Pd and then the Sn. In both layers the electrons remove inner (K) shell electrons which lead to the emission of characteristics K x-rays (photons of energies 21 keV for Pd, and 25 keV for Sn). In our experiments an x-ray CCD camera is employed, which records the individual photo strikes. The brightness of an event is proportional to the photon energy that created it. By plotting the energy distribution and number of energetic electrons it is possible to obtain a spectrum of the emitted x-rays. From this x-ray spectrum emitted by the two foils, the penetration power (i.e., energy) of the electrons and their numbers can be estimated.

An understanding of Laser/Plasma interactions is relevant to "fast ignitor" fusion experiments. These experiments use a short-pulse high-intensity laser beam to couple energy into the plasma in order to achieve a self-sustaining fusion reaction. This is the ultimate goal of the National Ignition Facility (NIF).

Electrochemical Reduction of Hexavalent Chromium in Ground Water

Shipra Bansal
Environmental Restoration Department
Lawrence Livermore National Laboratory
December 15, 1994

Abstract

Electrochemical reduction of hexavalent chromium (Cr^{+6}) to its trivalent state (Cr^{+3}) is showing promising results in treating ground water at Lawrence Livermore National Laboratory's (LLNL's) Main Site. An electrolytic cell using stainless-steel and brass electrodes has been found to offer the most efficient reduction while yielding the least amount of precipitate. Trials have successfully lowered concentrations of Cr^{+6} to below 11 parts per billion (micrograms/liter), the California state standard.

We ran several trials to determine optimal voltage for running the cell; each trial consisted of applying a voltage between 6V and 48V for ten minutes through samples obtained at Treatment Facility C (TFC). No conclusive data has been obtained yet.

Introduction

In nature, chromium generally exists in two oxidation states, hexavalent (Cr^{+6}), and trivalent (Cr^{+3}). While Cr^{+6} is a known carcinogen, Cr^{+3} hasn't shown to have such effects. Cr^{+6} is especially difficult to contain as it doesn't adsorb to soil or other inorganic surfaces. Cr^{+3} on the other hand, is very ready to precipitate out; it is therefore much easier to handle and control. National Pollution Discharge Elimination System (NPDES) regulations mandate that ground water concentrations of Cr^{+6} not surpass 11 parts per billion (ppb) if being discharged into an arroyo or navigable water way. At the Lawrence Livermore National Laboratory Main Site, however, the Cr^{+6} concentration ranges from 10 to 150 ppb. Naturally occurring deposits of manganese dioxide (MnO_2) are believed to oxidize Cr^{+3} to Cr^{+6} (figure 1) (Ridley, 1994). Also, plating operations on the site are possible contributors to some of the Cr^{+6} present.

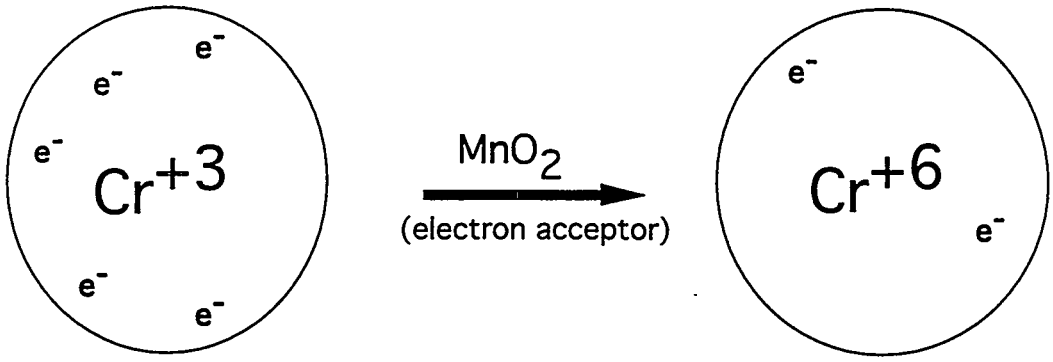

Figure 1: Common Phases of Chromium

Electrochemical reduction (ER) of Cr^{+6} is showing promising results as a means of reducing concentrations of Cr^{+6} in LLNL's ground water. An electrochemical cell causes an unspontaneous reaction to occur by the use of a power supply. To differentiate, a battery produces electricity using a spontaneous reaction while an electrochemical cell uses electricity to cause an unspontaneous reaction to occur. The cell consists of two electrodes, partially submerged in a solution, that are hooked up to a power source (figure 2). Electrons travel from the power source to the cathode which becomes negatively charged. Positively charged ions in solution are attracted to the cathode where they accept electrons (reduction). Likewise, negatively charged electrons are attracted to the positively anode where they donate electrons (oxidation). Electrons are forced back up to the power source, thus completing the circuit.

Research to date has shown that using electrodes of carbon-steel and brass provides the best results in terms of producing minimal precipitate while most effectively reducing Cr^{+6}. The cathode (carbon-steel) donates electrons which are then taken up by Cr^{+6}, reducing it to Cr^{+3}. Precipitate formation during the reaction has yet to be characterized though it is hypothesized to contain $Cr(OH)_3$ and copper ions. Brass (the anode) is an alloy mainly consisting of copper and zinc. Copper

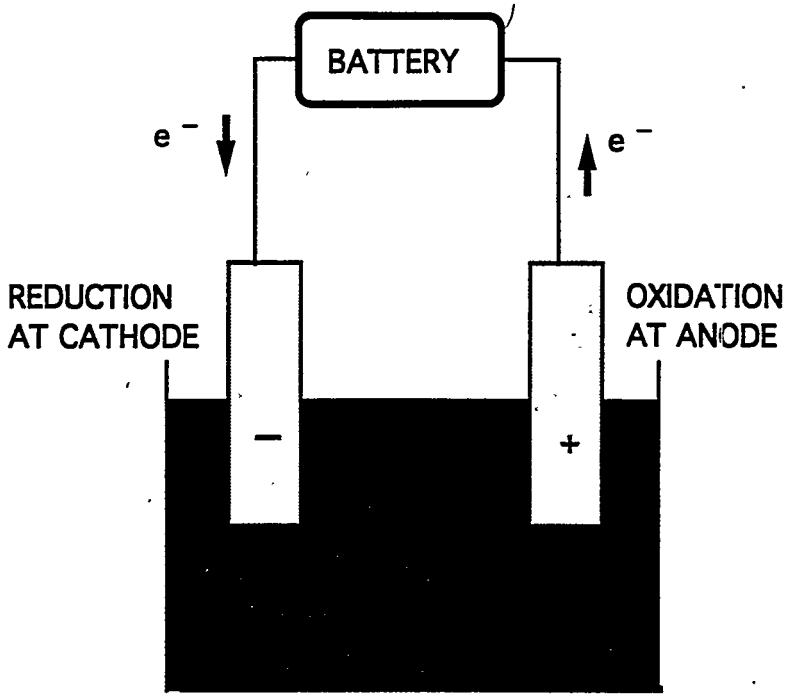

Figure 2: A Basic Electrochemical Cell

metal is oxidized to Cu^{+2} and then precipitated out. At the cathode, H^+ ions are being reduced to H_2 gas and expelled out into the air. The reactions thought to be taking place are as follows:

1. $Cu \text{----} > Cu^{+2} + 2e^-$
2. $3H_2O + Cr^{+6} + 3e^- \text{-----} > Cr(OH)_3 + 3H^+$
3. $2H^+ + 2e^- \text{-----} > H_2$

There are several problems with electrochemical reduction that have yet to be dealt with before the technology can be practically viable. As of now, there are a large number of electrodes necessary to run the cell. Though relatively cheap, the metals can be difficult to dispose of and clean. Second, the excessive generation of precipitation is likely to clog up machinery and require continual filter replacements. Third, varying conditions present in different water channels require that the cell be tailored to each

situation. Different background chemistry, contaminants, and soil characteristics will require extensive testing to best accommodate diverse conditions (Trombly, 1994, as in Lin, 1994). While one type of electrode at a certain voltage may be suitable for hypothetical area A, a different metal and voltage may work better for area B.

Other treatments of hexavalent chromium have associated problems. Ion exchange, which uses resins to bind Cr^{+6} and remove it from the water, is presently being used at two treatment facilities at LLNL, In addition to being expensive, it is not sufficiently ion specific. Electrochemical reduction of Cr^{+6} to Cr^{+3} may offer a viable solution.

Methodology

Methodology was derived from Tina's Lin's experiments during the summer of 1994 at LLNL. An electrochemical cell was set up as shown in the schematic (figure 3). Voltages ranging from 6 to 48 were applied in increments of 6 volts and current was monitored with a multimeter.

We obtained a set of 24 for each, carbon-steel and brass electrodes. The dimensions of the electrodes were 6" X 1/4" X 1" in height, depth, and width respectively; only the bottom 1" was dipped into the electrochemical cell which contained 250 ml of well water from treatment facility C (TFC). The electrodes were measured before and after each run. Suspended with clamps, the electrodes were adjusted to the appropriate height above a 400 ml beaker. The approximate distance between the electrodes was 1.5 inches and did not vary over the course of the runs. Each trial ran for exactly 10 minutes.

After each run, the precipitate was collected on filter paper with a 22 micrometer mesh. The filtrate was saved under beakers to dry and be weighed the next day. The filtered solution was analyzed for Cr^{+6} content through the use of a colorimetric method. In the hexavalent chromium analysis, a color indicator (diphenylcarbazide) is used that turns red-violet when it comes in contact with Cr^{+6} in acid solution. The

sample is then placed in an ultraviolet spectra photometer which passes a beam of light through the sample and measures the absorbance of the light by the sample. At a wavelength of 540 nm, the absorbance of the red-violet shade is highly sensitive. The more Cr^{+6} present, the greater the absorption and the darker the shade of the solution. The measure of absorbance can finally be converted into a concentration of Cr^{+6} (in ppb) present in solution.

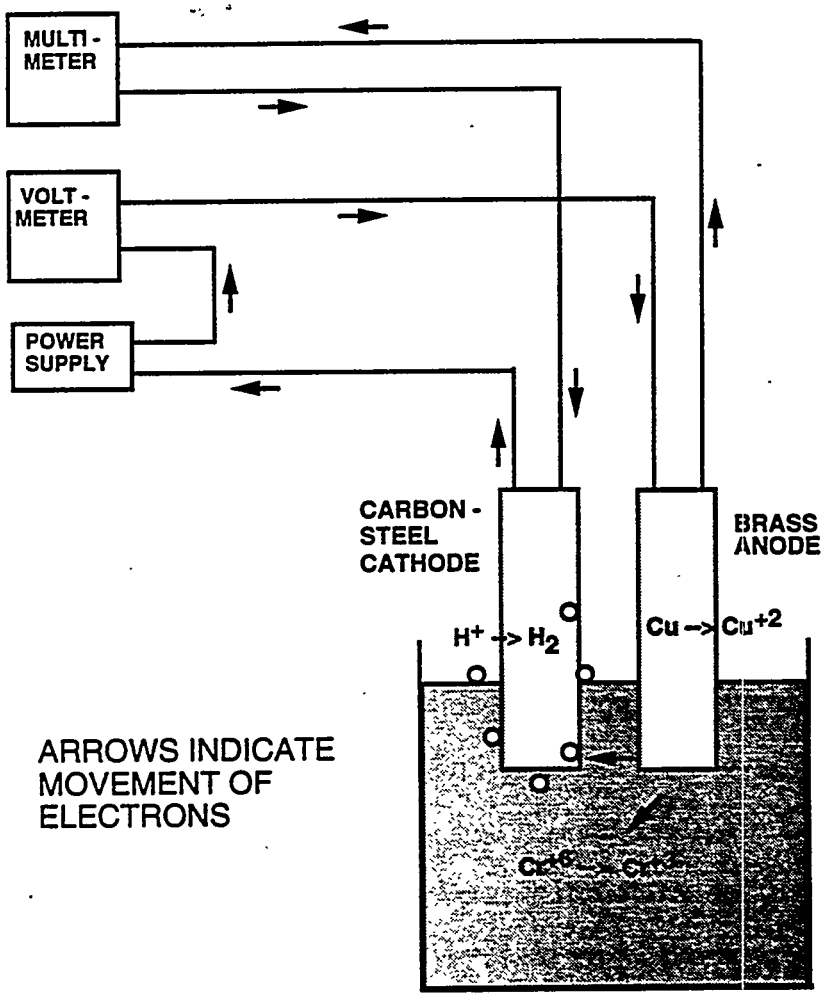

Figure 3: Schematic of Electrochemical Cell

My methodology deviated from previous work as far as cleaning of the electrodes is concerned. Tina had been using a steel-wool scrubber to rub off all the coating taking place during the runs and rinsed with deionized water. Twice, she dipped the electrodes in a solution of 10% nitric acid. This corroded the electrodes, causing them to have an uneven surface and changed the surface area exposed. I first tried to use a wire wheel[1] and bead blaster[2] to remove any coating present. While the coating was probably removed adequately, there is also a good chance that trace amounts of other metals were imbedded onto the electrodes. The bead blaster required using the wire wheel afterwards to remove any sand residue. Finally, a special mix of acids (hydrosulfuric + hydrochloric + nitric) was used for the last two trials. It seems the acid will better clean the electrodes without corroding the surface significantly.

Results

Several criteria were monitored. Table one summarizes the trends found.

Criteria	Trend
electrode weight	electrodes were weighed before and after each run. While the weight of the carbon-steel electrode remained relatively consistent, the weight of the brass electrode consistently decreased with both, cleaning at the wire-wheel and reacting during trials.
voltage and current	while voltage remained consistent, the current decreased over the 10 minutes. Possibly this is due to a reduction in the number of ions in the solution as they precipitate out.
precipitate	the amount of precipitate increased steadily with an increase in voltage applied
pH of samples	With increasing voltage, the pH of the sample also increased. It is thought that H^+ ions are being reduced at the cathode to H_2 thus causing the solution to become more basic.
final Cr^{+6} present	there were several inconsistencies in the data

Table 1: Criteria Measured During Runs

[1] Used to clean metals, a wire wheel consists of bristles of coarse steel wool on a wheel that spins rapidly, thus causing friction between the wheel and metal to remove any coatings.

[2] A bead blaster used very fine particles of sand blasted at high pressure to "scrape" off coatings.

When analyzing six trials at once, there is little consistency (figure 4). Taking four of these, however, we can start to see some trends such as a rise in hexavalent chromium, concentrations near 20V, a sharp decrease at 30 V, a moderate increase around 36V, and finally a decline (figure 5). Trials one and four seem to offer the most consistent data, differing by less than 5 ppb at any time. However, as the standard to be met is only 11 ppb, a more accurate method must be found.

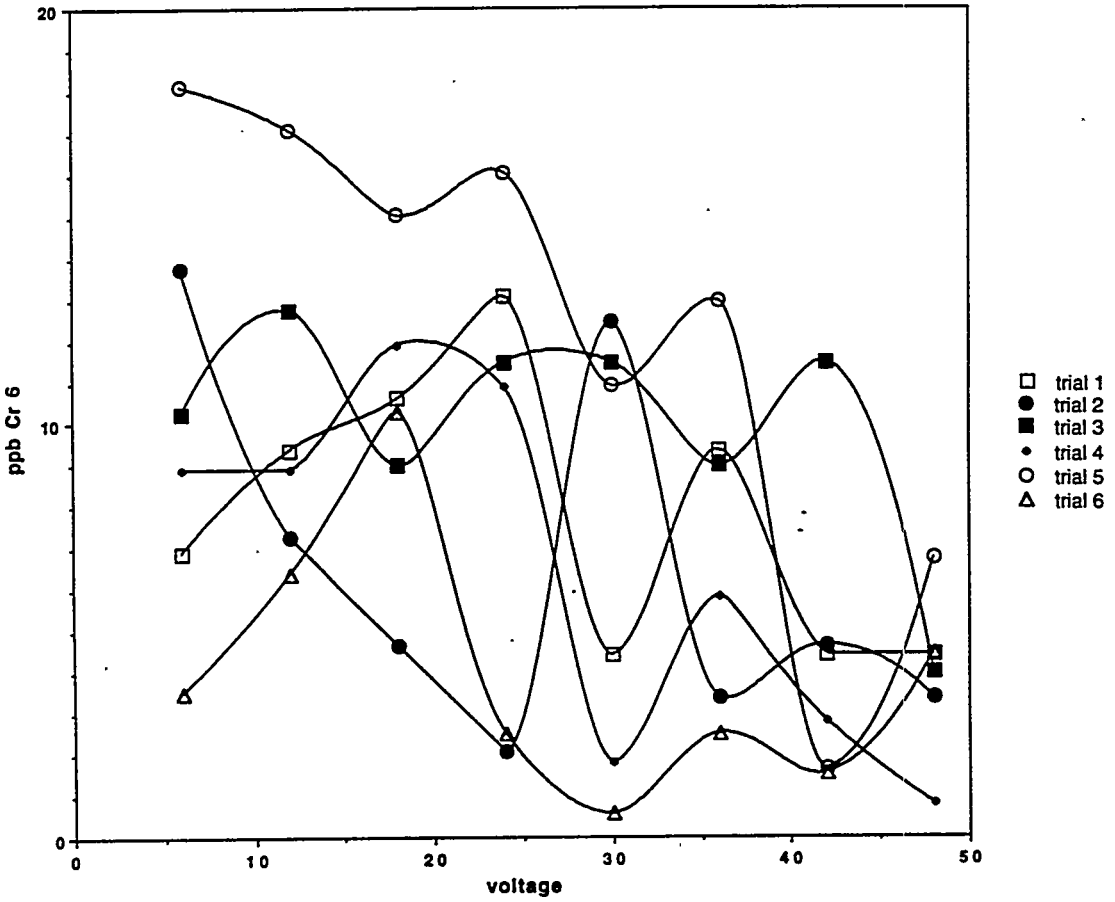

Figure 4: Data From Six Trials

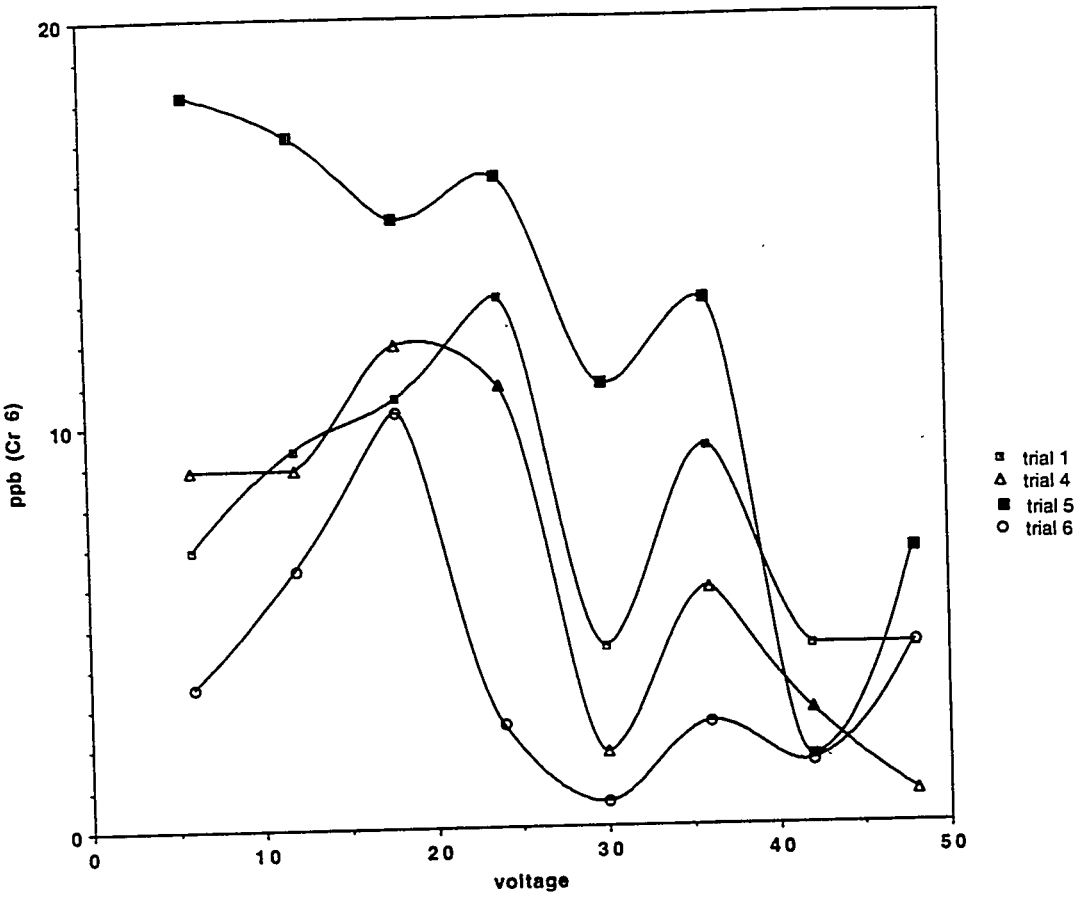

Figure 5: Data From Four Trials

There are a couple sources of inconsistency apparent. First, the cleaning methods discussed above could easily cause metals present from other work done at the wire wheel to embed themselves onto the electrodes deeply enough that wiping with a tissue would fail to remove them. The new acid wash seems to be a better method though more runs have to be made to confirm this. Second, the photo spectrometer lamp was experiencing some difficulty and may have provided inaccurate readings. Finally, wear on the electrodes, especially the brass one, resulted in a change in the surface area being exposed. This is likely to be a small factor in comparison to the others.

Higher precipitate does not mean that more hexavalent chromium is being reduced. Data shows that though the precipitate increases consistently with the voltage applied, the amount of hexavalent chromium in solution fluctuates (table 2).

Voltage	Avg ppb. Cr 6	Avg ppt. (mg)
6	9.361	0.002
12	10.450	0.014
18	11.970	0.017
24	10.649	0.034
30	4.444	0.046
36	7.688	0.052
42	2.620	0.069
48	4.131	0.080

Table 2: Cr^{+6} and Precipitate Patterns

It seems counter intuitive that the level of Cr^{+6} does not decrease steadily with the increase of voltage. There are some hypotheses concerning this lack of consistent decrease in hexavalent chromium. Reduction and then reversal back to hexavalent chromium may occur under certain conditions or after a certain amount of time. Also, at a specific voltage other metals present in solution or in the electrodes can start to react, thus causing more precipitate but not necessarily more chromium reduction (Caufield, 1994).

Conclusion

Though electrochemical reduction is showing promise, there is still much data that needs to be obtained in order to determine its usefulness at LLNL. Several trials need to be run in order to check if the new method of acid washing yields consistent results. After this, voltage, duration, and electrode gap need to be experimented with to find the most efficient conditions. Optimal voltage and duration will use the least

amount of energy while reducing the most chromium. Electrode gap can change the ef[illegible] of the cell by making it harder or easier for ions to travel from one [illegible]ode to the other. It is possible that electrodes placed closely to one another may carry a better current but not allow for complete mixing of the solution and hence adequate removal of hexavalent chromium. Finally, analyzing the contents of the precipitate may help to explain the wave-like patterns in chromium concentration with different voltages applied.

While there is indeed a great deal of work to be done, electrochemical reduction of hexavalent chromium to its trivalent state does seem to offer a promising route and one worth pursuing very seriously.

References

Caufield, Rex, Environmental Scientist, Lawrence Livermore National Laboratory (LLNL), personal communication, 1994.

Lin, Tina, Student Intern, LLNL, *Electrochemical Reduction of Hexavalent Chromium*, August 1994.

Ridley, Maureen, Environmental Scientist, LLNL, personal Communication, 1994.

Trombly, Jeanne, Electrochemical Remediation Takes to the Field, *Environmental Science and Technology*, 1994, vol. 28, No. 6, pp. 289-291.

An Automated System for Studying the Power Distribution of Electron Beams

Prepared by: Christina A. Filarowski

Project Advisors: John W. Elmer
Jeff Parrett
Alan T. Teruya

December 14, 1994

ABSTRACT

Precise welds with an electron beam welder are difficult to reproduce because the factors effecting the electron beam current density distribution are not easily controlled. One method for measuring the power density distribution in EB welds uses computer tomography to reconstruct an image of the current density distribution[1,2]. This technique uses many separate pieces of hardware and software packages to obtain the data and then reconstruct it consequently, transferring this technology between different machines and operators is difficult. Consolidating all of the hardware and software into one machine to execute the same tasks will allow for real-time measurement of the EB power density distribution and will provide a facilitated means for transferring various welding procedure between different machines and operators, thereby enhancing reproducibility of electron beam welds.

Table of Contents

I. INTRODUCTION

Although electron beam welding can have many applications, for the Lawrence Livermore National Laboratory there was one main application of this technology, namely in the area of defense. The laboratory would design and build prototypes of certain weapons and in this process would need to use very precise electron beam welding to weld various weapons components. Because the Livermore Laboratory is not a production facility, but rather a design laboratory, if these weapons were to built on a larger scale, the design specifications for building the weapons and their many individual components would be sent to a manufacturer. These design specifications would have to necessarily include how to reproduce the precise welding that the laboratory had done in the building of the prototype.

Specifying how to reproduce these precise welds, however, was not an easy task. One characteristic of the beam that needed to be specified was it's strength, or the power of the beam. Although the power can be described by specifying the current and voltage, two variables that can easily be quantified, the distribution of that power is not as easily quantified. The power distribution of the beam was important to specify because at different focus setting, at different heights of the beam, the power distribution varied, thereby producing a very different weld. Because no method for quantifying the power distribution of the beam exited, electron beam welding relied heavily on operator experience and precision, where the operator controlled the focus of the beam by observing the visible radiation.

Eventually, a new method was developed[1,2] that measures directly the beam current density, thereby controlling precisely the beam power distribution. This method involves computer controlled data acquisition, where an electron beam is swept across a narrow slit in a tungsten block at different angles. When the electron beam is swept across the slit, some of the electrons are collected in a modified Faraday cup (MFC). A wire connects the MFC to ground through a resistor. As the electrons travel from the Faraday cup through the wire and resistor, the current creates a potential difference across the resistor. This potential difference is measured as the beam is swept across the slit, resulting in a beam profile which is the raw data that is recorded. A series of beam profiles is taken at evenly spaced angles around the beam and eventually becomes reconstructed using computer tomography.

To obtain the tomographic reconstruction of the EB power distribution, several steps need to be taken. First, the data provided by the beam sweeps is saved on a 5 1/4" floppy disk, then brought to a PC (IBM AT), which is able to read the Nicolet disk and transfer the data to the hard drive. An FTP transfer is then done to a Silicon Graphics Indigo Workstation which uses a software package, PV-Wave, to create a two dimensional image consisting of many rows of one dimensional waveforms, called sinograms. Each row of the two dimensional image is a representation of the data produced by one sweep of the beam, at a given angle. This is the first step in the tomographic reconstruction process. PV-Wave is then used to generate the actual tomographic reconstruction of the power density distribution in the form of a contour plot, surface plot, or false color image. This data is then used by the operator and compared to the depth of penetration of the beam to determine how to adjust or refocus the beam.

Although this method produces the desire result, namely quantifying the EB power distribution, no real-time applications are being done presently because of the

constraints of the many pieces of equipment needed to control the beam, acquire the data, analyze it, and finally reconstruct it in a form useful to the operator. Consolidation of all the equipment into one machine that would execute the above mentioned tasks not only would allow for a real-time application but would also provide a facilitated means for transferring various welding procedures between different machines and operators, thereby enhancing reproducibility of electron beam welds. This paper will focus on how this automated and consolidated system for studying the power distribution of electron beams was designed, built, and tested. Some recommendations will also be made for improving certain features of the automated system that although they meet specifications, still could be improved upon.

II. DESIGN SPECIFICATIONS

A. Hardware

The necessary hardware and software needed to complete the project has been determined to include a pentium based system with a digitizing card, a waveform generation card, and a stepper motor control card. The digitizing card will replace the Nicolet digitizing oscilloscope on the existing data acquisition portion of the system, and convert the analog signal reading from across the resistor to a digital signal. The waveform card will generate two triangular pulses to control the x-y sweep of the beam across the slit. Finally, the stepper motor control card will control the drive chassis that turns the Faraday cup to various angles.

Specifications for the pentium PC include:

- 16 MB memory
- 500 MB hard disk
- 1 parallel, 2 serial ports
- 1 hard drive, 2 floppy drive controllers
- 5 1/4" and 3 1/2" floppy drives
- Windows
- DOS
- Mouse
- Keyboard
- 4 4-MB 72 pin SIMMS

Specifications for the digitizing card include:

- digitization at rate of at least 1MHz
- must have LabVIEW drivers
- adjustable gain

Specifications for the waveform generation card include:

- two 16 bit analog output lines
- LabVIEW driver

Specifications for the stepper motor controller card include:

- 3 digital output lines
- LabVIEW driver

B. Software

The software to control both boards and produce the image reconstruction will be written using LabVIEW for Windows 3.0. The requirements for the final piece of equipment include a user interface that will allow the operator to set various input parameters, such as the number of angles to sweep, the number of sweeps per angle, scan speed, and other sweep parameters. The operator should also be able to view the data produced from the sweeps to determine the validity of the data, then instruct the computer to continue with the analysis and reconstruction. The tomographic reconstruction will be done on the same machine and will produce an image of the power density distribution at the output, in a form to be specified by the operator. Refer to the Software Specification document in Appendix B for more details.

III. IMPLEMENTATION

A. Hardware

The hardware necessary for acquiring the raw data, digitizing it, and then reconstructing it, includes a Compaq Deskpro XE 560 and two plug-in boards: a National Instruments AT-MIO-16X Multifunction board and an Industrial Computer Source WIN-30PG Digitizing board. The AT-MIO-16X will generate the required waveform to control the magnetic deflection coils to direct the sweeps of the beam, and also output the necessary signals to a drive chassis to control the rotation of the MFC. The WIN-30PG will sample the analog signal from across the resistor as the beam sweeps across the slit and digitize it.

A pentium was purchased by the Purchasing Dept. of the Lawrence Livermore National Laboratory based on the specifications given by the client. Several steps were taken to determine exactly which boards would be used for this application. Some of the issues that were considered included the following:

1. *Waveform generation.* It was already known, from another application, that the National Instruments board could be used to generate the waveforms necessary for controlling the magnetic deflection coils. It still had to be determined whether a 12 bit or 16 bit output would be required so that the triangle wave would not be stepped. Two boards were tested on a Macintosh and their outputs viewed on an oscilloscope. A National Instruments AT-MIO-16H board with 12 bit resolution produced a stepped waveform at a particular setting of the oscilloscope, whereas a NB-A2100 with 16 bit resolution did not produce a stepped waveform. From this it was determined that a 16 bit board would be purchased from National Instruments, the AT-MIO-16X.

2. *Stepper motor control.* Originally it was thought that another board would be required to control the drive chassis. Many boards were researched, but none were selected when it became clear that the AT-MIO-16X would also be able to generate the necessary signals to control the rotation of the MFC. All that was required were three digital output lines to send signals to the drive chassis. Refer to Appendix I for a complete list of manufacturers that were contacted and the reasons that their products were not considered appropriate for this application.

3. *Digitization.* Five manufacturers were contacted and their products researched. Refer to Appendix J for a complete list of manufacturers and why their products were not selected. The Industrial Computer Source WIN30-PGL was selected because

it had the features listed in the hardware design specifications and because of the cost.

When the PC, the two boards, and the software arrived, the hardware was assembled and the software installed. The National Instruments AT-MIO-16X board was assigned slot number 1 and the Industrial Computer Source WIN30-PGL was assigned slot number 3. A ribbon cable was attached to the AT-MIO-16X with a connector block to facilitate testing the output of the board at a later date.

B. Software

Refer to Appendices C through G for implementation of waveform generation, motor control, digitization, and image reconstruction software.

IV. TESTING AND EVALUATION

A. Waveform generation

When the hardware was configured and the software to produce the waveform generation was written, the signals that would control the x and y deflection coils were view on an oscilloscope. Setup VI was used to generate the triangle wave. A smooth triangle wave was viewed.

B. Stepper motor control

Connections were made between the connector block from the AT-MIO-16X to the stepper motor controller in the following manner:

AT-MIO-16X Board	Stepper Motor Controller
pin #29 (ADIO 0)	full/half step control
pin #27 (ADIO 1)	direction control
pin #25 (ADIO 2)	step clock

Setup VI was used to generate the signals by pressing the CLOCKWISE and COUNTERCLOCKWISE buttons. When the CLOCKWISE button was pressed, the MFC rotated a halfstep in the clockwise direction. When the COUNTERCLOCKWISE button was pressed, the MFC rotated a halfstep in the counterclockwise direction. In the diagram, the binary bit patterns were changed to produce full step rotations. This also showed the system to be functioning as desired.

C. Digitization

Digitization will be tested when the entire system is connected to the electron beam welder and an experiment can be run.

D. Image reconstruction

The image reconstruction software has yet to be written and tested. The testing can however be done before connecting the system to the electron beam welder and running an experiment. There are several files that contain the digitized data from

previous experiments. These can be transferred from tapes onto the system and the image reconstruction software can be tested based on that data.

V. CONCLUSIONS

Based on all the aspects of the project that have been implemented and tested, the automated and consolidated system is functioning properly. There are, however, some features that have yet to be implemented. These include the following:

1. Implementation and testing of the image reconstruction software.
2. Addition of code that will return the motor to the home position after the completion of an experiment. This should be added to the code in Main VI.
3. In the manual data acquisition mode in Main VI, code needs to be added to allow the user to rotate the motor a full step clockwise or counterclockwise.
4. Code needs to be added in Main VI to not allow changes in the values of the parameters being used in the current experiment, such as number of sweeps per angle, number of profiles, etc.
5. The user needs to be prompted when to turn the beam on and off. This code should be added to the manual acquisition mode in Main VI.
6. Code needs to be added to do the display of the data to the front panel of Main VI, so that the profiles are overlaid.
7. The code to do the averaging of the beam profiles needs to be added to Main VI.

These additions will be made in January, 1995, before the system is linked to the electron beam welder and an experiment is run.

VI. RECOMMENDATIONS

There are several features of the automated system, that although they meet specifications outlined above, could still be improved upon. These include:

1. Addition of a mechanism, in the software, that would force the user to select Setup and then Calibrate before any of the other parts of the experiment can proceed. This is important because the parameters selected in both the Setup and Calibrate modes are used in other parts of the experiment.
2. An added feature in Main VI could include a setup file that can be called and loaded, where the parameters are already preselected. This could be implemented when several experiments have been run and the operator is familiar enough with the EB welder to be able to predict which parameters would most often be used.
3. The stepper motor control could be operated in closed loop mode. Although this would require purchasing additional hardware, it could be useful if an additional copper housing is added to the MFC. Presently, the two-second delay between steps in the rotation of the MFC is sufficient. However, if the weight is increased, the motor may overshoot the step when the MFC is rotated. Operating in a closed loop mode would allow for this to be corrected more easily while running the experiment.
4. Another useful addition would be to put the contents of the appendices and user's manual into the software itself. With this information in the help windows of the software, the operator would have easier access to instructions and help while running an experiment.

Time permitting, some of these modifications and improvements could also be made in January, 1995.

VII. POSSIBLE FUTURE APPLICATIONS

Possible future work and research, using this automated system, may include closer examination of the filaments that produce the electron beam. Understanding how the filament evolves over time may lead to an understanding of how the deterioration of the filament impacts the electron beam profile. The final result of this project may also prove to be a useful diagnostic tool for determining the current stage of the filament in its life cycle. The possibility of examining the power distribution of the electron beam as different components of the EB welder are studied could also provide more information on how to improve electron beam welders in general.

REFERENCES

1. Elmer, J.W., Teruya, A.T., and O'Brien, D.W. 1993. Tomographic Imaging of Noncircular and Irregular Electron Beam Current Density Distributions. Welding Research Supplement to the *Welding Journal*: 493-s to 505-s.

2. Teruya, A.T., Elmer, J.W., and O'Brien, D.W. 1991. A System for the Tomographic Determination of the Power Distribution in Electron Beams. *The Laser and the Electron Beam in Welding, Cutting and Surface Treatment State-of-the-Art* 1991, Bakish Materials Corp., pp. 125-140.

Appendix A

Proposal to:

Lawrence Livermore National Laboratory

Electron Beam Welding Project
Consolidation of Data Acquisition and Control Systems

Prepared by: Christina A. Filarowski

Project Advisors: John W. Elmer
Jeff Parrett
Alan T. Teruya

September 30, 1994

ABSTRACT

Precise welds with an electron beam welder are difficult to reproduce because the factors effecting the electron beam current density distribution are not easily controlled. One method for measuring the power density distribution in EB welds uses computer tomography to reconstruct an image of the current density distribution[1,2]. This technique uses many separate pieces of hardware and software packages to obtain the data and then reconstruct it, consequently, transferring this technology between different machines and operators is difficult. Consolidating all of the hardware and software into one machine to execute the same tasks will allow for real-time measurement of the EB power density distribution and will provide a facilitated means for transferring various welding procedures between different machines and operators, thereby enhancing reproducibility of electron beam welds.

Table of Contents

I. INTRODUCTION

A primary concern in electron beam welding is reproducibility of precise welds. There are, however, many factors that determine the reproducibility of electron beam welds, one of which is the current density distribution, which is difficult to accurately control. One of the many variables influencing electron beam current density distribution is filament design. The differences in current density distribution produced by different filaments are discussed by Elmer, Teruya, and O'Brien in "Tomographic Imaging of Noncircular and Irregular Electron Beam Current Density Distributions." Their discussion focuses on two filaments in particular, hairpin and ribbon filaments, and shows that the filament shape will impact the electron beam current density distribution. This suggests that the beam power density distribution may be controlled by using different filaments.

Presently, however, electron beam welding does not make use of this fact, but rather relies heavily on operator experience and precision, where the operator controls the beam by observing the visible radiation. An alternative method proposed also by Teruya, Elmer, and O'Brien in "A System for the Tomographic Determination of the Power Distribution in Electron Beams" introduces a new method that measures directly the beam current density, thereby controlling precisely the beam power distribution.

While this project will focus mainly on consolidating the data acquisition and control systems of the electron beam welder in order to improve reproducibility and portability, future work and research may include closer examination of filaments. Understanding how the filament evolves over time may lead to an understanding of how the deterioration of the filament impacts the electron beam profile. The final result of this project may also prove to be a useful diagnostic tool for determining the current stage of the filament in its life cycle.

II. PROBLEM DEFINITION

Generally, the method currently being used in the welding process involves data acquisition, where an electron beam is swept across a narrow slit at different angles. Computer tomography is then used to reconstruct an image of the beam current density distribution. This provides the necessary information to the electron beam welder operator so that the focus of the beam can be adjusted.

More specifically, when the electron beam is swept across the slit, the electrons are collected in a modified Faraday cup. A wire connects the Faraday cup to a resistor, which is connected to ground. As the electrons travel from the Faraday cup through the wire and resistor, the current creates a potential difference across the resistor. This potential difference is measured by a Nicolet digitizing oscilloscope. The modified Faraday cup is then rotated and the procedure is repeated, sweeping the beam at various angles between zero and 180 degrees.

The data provided by these sweeps is saved on a 5 1/4" floppy disk, then brought to a PC (IBM AT), which is able to read the Nicolet disk and transfer the data to the hard drive. An FTP transfer is then done to a Silicon Graphics Indigo Workstation which uses a software package, PV-Wave, to create a two dimensional image consisting of many rows of one dimensional waveforms, called sinograms. Each row of the two dimensional image is a representation of the data produced by one sweep of the beam, at a given angle. This is the first step in the tomographic reconstruction process. PV-Wave is then used to generate the actual tomographic reconstruction of the power

density distribution in the form of a contour plot, surface plot, or false color image. This data is then used by the operator and compared to the depth of penetration of the beam to determine how to adjust or refocus the beam.

Presently, however, no real-time applications are being done given the constraints of the many pieces of equipment needed to control the beam, acquire the data, analyze it, and finally reconstruct it in a form useful to the operator. Consolidation of all the equipment into one machine that would execute the above mentioned tasks not only would allow for a real-time application but would also provide a facilitated means for transferring various welding procedures between different machines and operators, thereby enhancing reproducibility of electron beam welds. Building this piece of equipment would involve identifying the necessary hardware and software, acquiring it, actually building the machine, writing the necessary software, and finally testing and debugging the system.

The requirements for the final piece of equipment include a user interface that will allow the operator to set various input parameters, such as the number of angles to sweep, the number of sweeps per angle, scan speed, and other sweep parameters. The operator should also be able to view the data produced from the sweeps to determine the validity of the data, then instruct the computer to continue with the analysis and reconstruction. The tomographic reconstruction will be done on the same machine and will produce an image of the power density distribution at the output, in a form to be specified by the operator.

III. STATEMENT OF WORK

The necessary hardware and software needed to complete the project has been determined to include a pentium based system with a digitizing card, a waveform generation card, and a stepper motor control card. The digitizing card will replace the Nicolet digitizing oscilloscope on the existing data acquisition portion of the system, and convert the analog signal reading from across the resistor to a digital signal. The waveform card will generate two triangular pulses to control the x-y sweep of the beam across the slit. Finally, the stepper motor control card will control the drive chassis that turns the Faraday cup to various angles. The software will be implemented using LabVIEW for Windows 3.0.

The work will be carried out in four phases.

Phase 1

The first phase of the project, which has already begun, will involve analysis, specification, and acquisition of all the necessary equipment. During this phase of the project, two waveform generation boards will be tested to determine which produces a better triangular wave and whether the board can also produce the necessary signals to control the stepper motor. If this proves successful, only one board will be purchased that will drive the stepper motor and generate the necessary waveforms.

Phase 2

Once the purchased hardware arrives, Phase 2 of the project will begin with assembling the hardware and then proceed to hardware testing. Assembly will include inserting the boards and configuring the PC. The hardware will then be tested to ensure that the stepper motor is properly controlled, the necessary

waveforms are generated to the x-y deflection coils, and the digitizing card is receiving inputs and properly converting the data.

Phase 3

This phase of the project will involve software design and implementation. The software will include a main program that calls several sub-routines to do both, the control and data acquisition portions of the program. Also during this phase, an attempt will be made to write the software to do the tomographic reconstruction using LabVIEW. A software specification document will be generated detailing all of the elements of the program.

Phase 4

Testing and experimentation of the entire PC-based data acquisition and control system, with the electron beam welder will be the fourth and final phase of the project.

The first three phases of the project are expected to be completed by mid-November, allowing the remaining time to be used to run tests and acquire data with the electron beam welder. A more detailed timeline for the project along with a progress report will be distributed by late October. A user's manual, detailing the functioning of each part and how to run the software, will be presented as a final report on the project, by December 16, 1994.

IV. RESOURCES

A. Facilities and Equipment

Lawrence Livermore National Laboratory will provide all the necessary resources needed to acquire the hardware and software, along with the facilities in which to do the work.

B. Personnel Qualifications

John W. Elmer - John Elmer received his B.S. and M.S. degrees in Metallurgical Engineering from the Colorado School of Mines in 1979 and 1981, and his Sc.D. degree in Metallurgy from the Massachusetts Institute of Technology in 1988. John joined Lawrence Livermore National Laboratory in 1981 and is currently a staff scientist in the Condensed Matter and Analytical Sciences Division of LLNL. He is also the principal investigator on the Electron Beam Welding Project and will be supporting all aspects of the project.

Alan T. Teruya - Alan Teruya studied engineering at Harvey Mudd College, Claremont, CA, where he received both, his B.S. and Master of Engineering degrees in 1983 and 1984. Since that time, Alan has been working at Lawrence Livermore National Laboratory and is presently assigned to the Electronic Engineering Group supporting the Chemistry and Materials Science Department of LLNL. Alan will be acting as technical advisor for the hardware portion of the Electron Beam Welding Project.

Jeff Parrett - Jeff Parrett received his B.S. in Applied Mathematics from the University of California at Berkeley in 1981 and is currently working on a Masters degree in Computer Science at California State University at Chico. Jeff has been

working at Lawrence Livermore National Laboratory since 1987 and his present role is project leader for the Laboratory Information Management System for the Environmental Analytical Science Group. Jeff will be acting as technical advisor for the software portion of the Electron Beam Welding Project.

Christina A. Filarowski - Christina Filarowski is presently enrolled at Suffolk University, in Boston, MA, from where she will receive her B.S. in Computer Engineering in December of 1994. Christina is at Lawrence Livermore National Laboratory participating in the Department of Energy's Science and Engineering Research Semester. She will be responsible for consolidating the equipment presently being used in the control and data acquisition systems of the electron beam welder.

C. Budget

The following is an itemization of estimated expenses:

A. LabView for Windows, Full Development System	$1,995.00
B. Pentium PC 16 MB memory 500 MB hard disk 1 parallel, 2 serial ports 1 hard drive, 2 floppy drive controllers 51/4" and 31/2" floppy drives Windows DOS Mouse Keyboard 4 4-MB 72 pin SIMMS	$3,000.00
C. Win-30PGL, 12-Bit A/D Board	$1,625.00
D. AT-MIO-16X High Resolution Multifunction Card	$1,995.00
TOTAL EXPENSES	$8,615.00

REFERENCES

1. Elmer, J.W., Teruya, A.T., and O'Brien, D.W. 1993. Tomographic Imaging of Noncircular and Irregular Elctron Beam Current Density Distributions. Welding Reasearch Supplement to the *Welding Journal*: 493-s to 505-s.

2. Teruya, A.T., Elmer, J.W., and O'Brien, D.W. 1991. A System for the Tomographic Determination of the Power Distribution in Electron Beams. *The Laser and the Electron Beam in Welding, Cutting and Surface Treatment State-of-the-Art* 1991, Bakish Materials Corp., pp. 125-140.

Appendix B

Software Specification for Automated Control and Data Acquisition Systems of an Electron Beam Welder

Prepared by: Christina A. Filarowski

Project Advisors: John W. Elmer
Jeff Parrett
Alan T. Teruya

November 6, 1994

Table of Contents

1.0 GENERAL

1.1 Purpose

Precise welds with an electron beam welder are difficult to reproduce because the factors effecting the electron beam current density distribution are not easily controlled. One method for measuring the power density distribution in EB welds uses computer tomography to reconstruct an image of the current density distribution[1,2]. This technique uses many separate pieces of hardware and software packages to obtain the data and then reconstruct it consequently, transferring this technology between different machines and operators is difficult. Consolidating all of the hardware and software into one machine to execute the same tasks will allow for real-time measurement of the EB power density distribution and will provide a facilitated means for transferring various welding procedure between different machines and operators, thereby enhancing reproducibility of electron beam welds.

1.2 Brief Functional Description of the System

The method developed[1,2] to study the power distribution of electron beams involves computer controlled data acquisition, where an electron beam is swept across a narrow slit in a tungsten block at different angles. When the electron beam is swept across the slit, some of the electrons are collected in a modified Faraday cup (MFC). A wire connects the MFC to ground through a resistor. As the electrons travel from the Faraday cup through the wire and resistor, the current creates a potential difference across the resistor. This potential difference is measured as the bweam is swept across the slit, resulting in a beam profile which is the raw data that is recorded. A series of beam profiles is taken at evenly spaced angles around the beam and eventually become reconstructed using computer tomography.

The hardware necessary for acquiring this data includes a Compaq Deskpro XE 560 and two plug-in boards: a National Instruments AT-MIO-16X Multifunction board and an Industrial Computer Source WIN-30PG Digitizing board. The AT-MIO-16X will generate the required waveform to control the magnetic deflection coils to direct the sweeps of the beam, and also output the necessary signal to a drive chassis to control the rotation of the MFC. The WIN-30PG will sample the analog signal from across the resistor as the beam sweeps across the slit and digitize it.

The software to control both boards and produce the image reconstruction will be written using LabVIEW for Windows 3.0

1.3 Scope

This specification will focus on software development and define requirements for the control and data acquisition systems for the electron beam welder, and also for reconstructing an image from the acquired data.

1.4 Major Units

1.4.1 CONTROL SYSTEM

The control system will consist of two parts:

1.4.1.1 Software to control the generation of a waveform from the AT-MIO-16X to control the X and Y deflection coils.

1.4.1.2 Software to control the generation of digital pulses from the AT-MIO-16X to control the rotation of the MFC.

1.4.2 DATA ACQUISITION SYSTEM

The data acquisition system will consist of software to control the sampling and digitization of the raw data from across the resistor.

1.4.3 IMAGE RECONSTRUCTION

The image reconstruction software will produce a representation of the beam power density distribution of the electron beam based on the digitized data.

2.0 FUNCTIONAL, OPERATING, AND PERFORMANCE REQUIREMENTS

2.1 Control System

2.1.1 Control of X and Y Deflection Coils to Sweep the Beam

2.1.1.1 The operator will be able to position the beam away from the slit before the start of the experiment. This will be a "home" position.

2.1.1.2 The operator will be able to set the scan frequency of the beam.

2.1.1.3 The operator will have the option to change the amplitude of the beam deflection signal. The default value will be 1 volt.

2.1.1.4 The operator will have the option to change the number of sweeps per angle. The default value will be 10.

2.1.1.5 Once the experiment is begun, the operator will not have the option to change any of the sweep parameters for the duration of the experiment.

2.1.2 Control of MFC Rotation

2.1.2.1 The operator will be able to specify the number of angles at which to profile the beam. The options will be limited to integer factors of 100 due to the limitations imposed by the stepper motor.

2.1.2.2 The MFC will have a "home" position to be set at the beginning of each experiment.

2.1.2.3 After the MFC has been rotated 180 degrees to profile the beam, the MFC will be returned to the "home" position.

2.1.2.4 The MFC will always be rotated counterclockwise during the experiment and returned to the home position in the clockwise direction.

2.1.2.5 The operator will be able to rotate the MFC at half step increments before the start of the experiment to align the slit perpendicularly to the beam path.

2.1.2.6 During the experiment, while in the manual mode, the operator will be able to rotate the MFC at full step increments in either the clockwise or the counterclockwise direction, in the event that the motor misses or overshoots a step.

2.1.2.6 Once the experiment is begun, the operator will not have the option to change the number of angles at which to profile the beam, or the number of sweeps per angle.

2.2 Data Acquisition System

2.2.1 Sampling And Digitization Of Data

2.2.1.1 Data will be acquired and digitized at the maximum sampling capacity of the WIN-30PG digitizing board.

2.2.1.2 The operator will specify in which mode to acquire the data; manually, semi-automatically, or automatically.

2.2.1.3 In the manual data acquisition mode, the operator will be prompted to turn the beam on before acquisition begins, and to turn the beam off after the profiles have been acquired for that angle.

2.2.2 Display Of Acquired Data

2.2.2.1 Manual Mode

2.2.2.1.1 In the manual mode, beam profiles will be acquired at a given angle, the system will display the data from the sweeps at that angle, then pause for operator input.

2.2.2.1.2 The operator will have the option to view the beam profiles one at a time or all overlaid. By default, the system will display the data overlaid.

2.2.2.1.3 The operator will be able to discard some, all or none to the data from any of the beam profiles at that angle.

2.2.2.1.4 If all of the beam profiles are discarded, the operator will have the option of reacquiring the beam profiles for that angle, or proceeding to the next angle.

2.2.2.1.5 If some or none of the beam profiles are discarded, the operator will be prompted to average the sweeps and proceed acquiring data at the next angle.

2.2.2.1.6 When data acquisition begins, the operator will always have the option to stop acquiring beam profiles and quitting the experiment, or proceeding to the image reconstruction.

2.2.2.1.7 When the profiles from all the angles specified at the start of the experiment have been acquired, digitized and averaged, the operator will have the option of viewing the averaged beam profiles at any of the angles

2.2.2.1.8 The operator will have the option of discarding some, all, or none of the averaged beam profiles, then proceeding to the image reconstruction.

2.2.2.1.9 The option to quit the experiment will always be available.

2.2.2.2 Semi-Automatic Mode

2.2.2.2.1 In the semi-automatic mode, the profiles will be acquired and digitized for all of the angles specified at the start of the experiment. The system will then pause for operator input.

2.2.2.2.2 The operator will have the option to continue with the image reconstruction or review the acquired profiles.

2.2.2.2.3 If the operator chooses to review the acquired profiles, the averaged curve of all the sweeps at the specified angle will be shown.

2.2.2.2.4 The operator will have option to discard the profiles from any angle, then continue with the reconstruction with the data from the remaining angles.

2.2.2.3 Automatic Mode

2.2.2.3.1 In the automatic mode, the profiles will be acquired and digitized for all the angles specified at the start of the experiment, and an image of the power density distribution will be reconstructed with no intervention from the operator.

2.3 Image Reconstruction

2.3.1 The operator will be able to specify the type of reconstruction to produce and display; contour plot, surface plot, or false color image.

2.3.2 The capability will exist to display all forms of the reconstruction simultaneously.

2.3.3 The reconstruction(s) will be displayed to the screen.

2.3.4 The operator will have the option to print the reconstruction(s).

3.0 TESTING

The software to control the X and Y deflection coils to sweep the beam, will be tested by viewing the generated waveform on an oscilloscope. The MFC rotation software will be tested by making the appropriate connections between the AT-MIO-16X board and the stepper motor controller and observing the rotations. The sampling, digitization, and reconstruction will be tested by simulating a potential difference across the resistor with a waveform generated from another LabVIEW analog output VI and viewing the results of the data acquisition.

4.0 DELIVERABLES

4.1 LabVIEW VI's

The final product to be delivered to the customer will include the Compaq Deskpro XE 560 with the two plug-in boards, as described in section 1.2 of this document, and the necessary LabVIEW VI's to control the functioning of the control system, the data acquisition system, and the image reconstruction.

4.2 Design Algorithms

All design documentation and algorithms outlining the functioning of the software implemented using LabVIEW for Windows 3.0 will be provided to the customer.

4.3 User's Manual

Upon completion of the project, a User's Manual will be provided detailing the operation of both the hardware and the software components of the system.

REFERENCES

1. Elmer, J.W., Teruya, A.T., and O'Brien, D.W. 1993. Tomographic Imaging of Noncircular and Irregular Elctron Beam Current Density Distributions. Welding Reasearch Supplement to the *Welding Journal*: 493-s to 505-s.

2. Teruya, A.T., Elmer, J.W., and O'Brien, D.W. 1991. A System for the Tomographic Determination of the Power Distribution in Electron Beams. *The Laser and the Electron Beam in Welding, Cutting and Surface Treatment State-of-the-Art* 1991, Bakish Materials Corp., pp. 125-140.

Appendix C

Setup VI Design

Electron Beam Welding Project
Automation of Data Acquisition and Control Systems

Prepared by: Christina A. Filarowski

Project Advisors: John W. Elmer
Jeff Parrett
Alan T. Teruya

November 12, 1994

Table of Contents

I. FRONT PANEL FEATURES AND OPERATION

The purpose of the Setup VI is to allow the EB welder operator to input various parameters to be used during an experiment. These parameters are the amplitude, in volts, and frequency, in Hz, of the triangle waveform to be generated, the number of sweeps of the electron beam at each position of the modified Faraday cup (MFC), and the number of 1.8 degree steps to rotate the MFC at each turn of the motor.

As the operator is selecting the values for the parameters to be used during the experiment, a triangle wave is being continuously output to one of the analog output ports of the AT-MIO-16X board that controls the x-direction deflection coil. The waveform being generated takes its inputs from the front panel and updates the waveform output if the amplitude or frequency is changed. The operator is instructed on the front panel to turn on the beam. As it is sweeping at the specified amplitude and frequency, the operator can rotate the MFC in half step (0.9 degree) increments, either clockwise or counter-clockwise, to position the slit in the MFC perpendicularly to the beam path.

Setup VI also calculates the number of degrees that the MFC will be rotated at each turn of the motor and the number of profiles that will be generated. Both calculations are based on the value that the operator selects for the number of steps to rotate the MFC per increment, and their values are displayed on the front panel. When the operator has finished specifying run-time parameter values and depresses the DONE button, waveform generation stops, the analog output channel is cleared, and the value of the amplitude is set to position the beam away from the slit in the MFC.

II. DIAGRAM FUNCTION

A while-loop is used for continuous execution. The loop ceases when the DONE button is pressed on the front panel or if an error occurs. The while-loop controls several functions:

1. Waveform Generation

The iteration counter of the while loop is used to control a case structure in which the waveform generation is done. The first iteration (i = 0) causes the TRUE case to execute, which outputs the triangle wave using the amplitude and frequency values from the front panel. Subsequent iterations of the while loop cause the FALSE case to execute. Here, the present values for amplitude and frequency are compared with the previous ones. The previous values are passed to the next iteration of the while loop with a shift register. A bundle is used for signal parameters to save space in shift register and comparison code. If either of the values has changed, this will cause the TRUE case of the nested case structure to output an updated triangle wave using the new values for amplitude and frequency. The FALSE case performs no function.

Several sub-VI's are called in order to generate and output the waveform:

A. *Triangle Wave.VI* computes the triangle wave. It takes amplitude and frequency as inputs and outputs the waveform to *AO Write.* Build Array, Transpose 2D Array, and a double to single precision floating-point conversion function are used to convert the data into the proper format for *AO Write.*

B. *AO Config* is used to specify on which device and channel to output the data. It has 1 as the device number (for the AT-MIO-16X) and 0 as the channel. *AO Config* outputs Task ID and Error Out to *AO Write* .

C. *AO Write* takes as inputs Task ID In, Error In and Voltage Data. Voltage Data is in two-dimensional array form. It outputs Task ID Out and Error Out to *AO Start* in the first iteration of the while loop

D. *AO Start* begins the analog output operation and takes as inputs Task ID In and Error In from *AO Write*, and two constant values for Number of Buffer Iterations and Update Rate. Number of Buffer Iterations is set to 0 for continuous generation and Update Rate is set to 100,000 updates/second. *AO Start* passes Task ID and Error Out to *AO Clear.*

E. *AO Clear* stops analog output generation.

2. Motor Control

If either of the *clockwise* or *counterclockwise* buttons on the front panel is pressed, the MFC will be rotated in that direction by 0.9 degrees. Each button on the front panel controls the execution of a case statement in the diagram. If the *clockwise* button is pressed, the TRUE case of the case structure will execute, otherwise the FALSE case will execute. The motor controller requires three binary bits to be set in order to rotate the MFC: half/full step, direction, and step clock. Therefore, the execution of the TRUE case involves writing the appropriate binary bit pattern to a digital output port of the AT-MIO-16X board, which is connected to the motor controller, then waiting 2 seconds for the MFC to stabilize before rotating again. When the false case executes, the same bit pattern is written except for the bit controlling the step clock because the motor controller is edge triggered and reads the high-to-low transition on step clock in order to turn the MFC. The *counterclockwise* rotation code functions in a similar manner, except that the binary bit pattern written to the digital port differs by one bit, namely, the direction bit.

The sub-VI's called by Setup VI to control motor rotation are as follows:

A. *DIO Port Config*, done outside the while loop, establishes which port will be used and in which direction data will flow. Device is set to 1 so that the AT-MIO-16X board will be used. Port number is 0 to specify port A of the board. Port width is the total width of the port in bits and is set to 4 (only 3 are needed, but configuring a 4 bit port as opposed to separately configuring 3 bits on that port requires less code). Line direction map is set to -1 so that all lines of the specified port will be output lines. The outputs of *DIO Port Config* are Task ID Out and Error Out and are wired to *DIO Port Write*.

B. *DIO Port Write* takes Task ID In and Error In from *DIO Port Config*. Line Mask is given a value of -1 so that all lines in the port will set to the states specified in Pattern. The pattern for clockwise rotation (TRUE case) is 1110 and 1100 for counterclockwise rotation, and 1111 and 1101 (FALSE case) for clockwise and counterclockwise rotation, respectively. The first bit written to pin 31 and is not used, the second is written to pin 29 of the AT-MIO-16X board and is the half/full step control, the third bit is written to pin 27 and controls direction of rotation, and the fourth bit is written to pin 25 and controls the step clock.

NOTE: This configuration requires that the AT-MIO-16X and motor controller be connected in the following manner:

AT-MIO-16X Board	Stepper Motor Controller
pin #29 (ADIO 0)	full/half step control
pin #27 (ADIO 1)	direction control
pin #25 (ADIO 2)	step clock

3. Calculations

During execution of Setup VI, the program allows the operator to change several controls, including Steps to Rotate per Increment, then displays the corresponding number of profiles and number of degrees (theta) at which the MFC will be turned at each repositioning of the motor. Other calculations are also made so that those values can be used when Setup VI is called as a sub VI in a larger program.

A. Theta. Steps per Increment is given as an enumeration control on the front panel. It has 5 cases: 1, 2, 4, 5, and 10. These correspond to cases 0 through 4, respectively. To display theta in the indicator on the front panel, each case contains the corresponding number of degrees in a digital display in that case and is then wired to the theta indicator.

B. Profiles. To obtain the number of Profiles, theta is divided into 180 and the result displayed in the Profiles indicator on the front panel.

C. Sweeps per Angle. The operator can choose 2, 4, 6, 8, 10, 12, or 14 sweeps per angle from an enumeration control on the front panel. These values correspond to cases 0 through 6, respectively. In order to get the actual number of sweeps, the case number is multiplied by 2 and then added to 6.

III. Setup VI As A Sub-VI In A Larger Program.

If Setup VI is called as a sub VI in a larger program, the following variables can be accessed as double-precision floating-point data types. All are outputs of Setup VI.

Variable	Description
theta	number of degrees to turn the motor to acquire the next beam profile.
profiles	this will be the number of beam profiles generated based on the number of steps per increment chosen by the operator.
sweeps/angle	the number of times that the beam will traverse the slit in the MFC, at each angle.
amplitude	amplitude, in volts, of the triangle wave.
frequency	frequency, in Hz, of the triangle wave.

Appendix D

Calibrate VI Design

Electron Beam Welding Project
Automation of Data Acquisition and Control Systems

Prepared by: Christina A. Filarowski

Project Advisors: John W. Elmer
Jeff Parrett
Alan T. Teruya

December 12, 1994

Table of Contents

I. FRONT PANEL FEATURES AND OPERATION

Calibrate VI allows the EB welder operator to input values for gain and samples/channel and acquire a profile to check those parameters. Values for amplitude (in volts), frequency (in Hz), theta, and sweeps/angle can also be specifed. When the operator depressed the Acquire button, the profile will be acquired and the data from the specified number of sweeps will be shown, overlaid, on the front panel. The gain and samples/channel, if required, can then be changed, another profile acquired at that same angle, and that data displayed to the front panel. The operator can continue with this process until the appropriate values for gain and samples/channel are found. The Done button can be depressed at any time to stop execution.

II. DIAGRAM FUNCTION

A while-loop is used for continuous execution. The loop ceases when the DONE button is pressed on the front panel. Inside the while-loop is a case statement, whose TRUE case will execute when the Acquire button is pressed. The TRUE case calls one sub-VI: Profile VI. The values for amplitude, frequency, theta, sweeps/angle, and samples/channel are taken from the front panel. Gain is given as an enumeration control on the front panel. It has 4 cases: 1, 10, 100, and 1000. These correspond to cases 0 through 4, respectively. In order to access the actual gain values, the gain value is written in the case statement and then wired to the appropriate terminal in Profile VI. The value for profiles and steps/inc are constant. Profiles is 1 and steps/inc is 0 so that the MFC will not be rotated and subsequent acquisitions will be done at the same angle. The only output is a two-dimensional array diplayed to a graph on the front panel.

The FALSE case inside the main while loop does nothing.

III. Calibrate VI As A Sub-VI In A Larger Program.

If Setup VI is called as a sub VI in a larger program, the following variables can be accessed as double-precision floating-point data types. All are outputs of Setup VI.

Variable (inputs)	Description
theta	number of degrees to turn the motor to acquire the next beam profile.
sweeps/angle	the number of times that the beam will traverse the slit in the MFC, at each angle.
amplitude	amplitude, in volts, of the triangle wave.
frequency	frequency, in Hz, of the triangle wave.

Variable(outputs)	Description
gain	value to be used in the digitization of the analog signal.
samples/channel	number of samples to acquire during digitization for each sweep.
data	two dimensional array containing digitized signal.

Appendix E

Profile VI Design

Electron Beam Welding Project
Automation of Data Acquisition and Control Systems

Prepared by: Christina A. Filarowski

Project Advisors: John W. Elmer
Jeff Parrett
Alan T. Teruya

December 12, 1994

Table of Contents

I. FRONT PANEL FEATURES AND OPERATION

Profile VI, by default, acquires data on the beam at only one angle, digitizes it at the specified gain and samples per channel, and then turns the motor the specified number of steps. The user can set the amplitude (in volts) and frequency (in Hz) of the triangle wave used to control the sweep of the beam, the number of sweeps per angle, the number of profiles, the gain, samples per channel, steps per increment to rotate the modified Faraday cup (MFC), and the corresponding number of degrees that this will be (theta). The only output is a two dimensional array, data, containing the digitized signal.

II. DIAGRAM FUNCTION

The main part of this VI is inside a for loop. The for loop will execute once, by default, but can be called as many times as necessary in a larger program by changing the value of profiles. Inside the for loop is a case statement, where the first case, case 0, controls the waveform generation and digitization of the signal, then writes the maximum value of the amplitude of the waveform to the x and y deflection coils, in order to position the beam away from the slit in the MFC. The second case, case 1, turns the MFC the specified number of full steps in the clockwise direction. The digitization and waveform generation codes are enclosed in case statements so that an artificial data dependency can be imposed, forcing digitization to start, before waveform generation begins, then writing the maximum amplitude values to the x and y deflection coils.

All board configurations are done outside the for loop.

1. Digitization

There are several sub-VI's used to configure the Win30-PGL board and the appropriate channels. These are *Config Board* and *AD Channel Config*.

A. *Config Board* has several inputs and one output. Device Number is arbitrary and is set to 3. This value will be carries through all sub-VI's necessary for digitization using Task ID In and Out. *Config Board* passes this value to *AD Channel Config*.

B. *AD Channel Config* takes several inputs including channel, gain, and mode. Channel can be a list of channels, but for this application only one is used. It is therefore set to 0 and converted into the appropriate format, a two dimensional array for *AD Channel Config* using a String-to-Integer Array Conversion VI. The value for gain is taken from the front panel, task ID is taken from *Config Board*, and mode is set to one, indicating differential mode.

C. *AD Easy Wave* does the actual digitization of the signal. Task ID In is taken from AD Channel Config, samples per channel is taken from the front panel, and sampling rate is set to the maximum capacity of the board, 1MHz. Channel is again set to 0. The only output to the front panel is a two-dimensional array, data. Task ID Out is wired to the nested for loop containing the waveform generation code, to force an artificial data dependency.

2. Waveform Generation

NOTE: Waveform generation in Profile VI is done in a similar manner as described in Setup VI Design. Refer to that document for more details on the functioning of the sub-VI's. Only the unique features of this code will be described here.

Two triangular waveforms are generated in Profile VI, one to the x and one to the y deflection coils.

A. *AO Config* is called twice outside the main for loop in order to configure channel 0 as the output of the x deflection coil signal and channel 1 as the output of the y deflection coil signal. Device number is 1 for both, specifying the AT-MIO-16X board.

B. *Triangle Wave.VI* computes the triangle wave for both the x and the y signals. The amplitude is calculated according to the following formulas:

In x direction: amplitude * cos (theta * i)
In y direction: amplitude * sin (theta * i)

Amplitude is the value specified on the front panel and i is the iteration counter (beginning at 0) in the main for loop.

C. *AO Start* begins the analog output operation and Number of Buffer Iterations is set to 1 so that the buffer is only generated once. Task ID Out from *AO Start* is wired out of the nested for loop and to the case statements containing the code to write the maximum value of the amplitude to the x and y deflection coils. The ensures that the code in these case statements will not execute until the nested for loop ceases executing.

3. Motor Control

NOTE: Rotation of the MFC is done in a similar manner as that described in Setup VI. Refer to that document for more details on the functioning of the sub-VI's. Only the unique features of this code will be described here.

The second case, case 1, in the main for loop, controls the rotation of the MFC. Inside case 1 is a nested for loop that will execute the number of times specified on the front panel in steps per increment. *DIO Port Write* takes as one of its inputs the binary bit pattern. Here, because the MFC is being rotated in full rather than half step increments, the binary bit pattern for the TRUE case will be 1010 and 1011 for the FALSE case.

III. Profile VI As A Sub-VI In A Larger Program.

If Profile VI is called as a sub VI in a larger program, the following variables can be accessed as double-precision floating-point data types.

Variable(inputs)	Description
theta	number of degrees to turn the motor to acquire the next beam profile.

profiles	this will be the number of beam profiles generated based on the number of steps per increment chosen by the operator.
sweeps/angle	the number of times that the beam will traverse the slit in the MFC, at each angle.
amplitude	amplitude, in volts, of the triangle wave.
frequency	frequency, in Hz, of the triangle wave.
steps/inc	number of full steps to rotate the MFC each time it is moved.
gain	value to be used in the digitization of the analog signal.
samples/channel	number of samples to acquire during digitization for each sweep.

Variable(outputs)	**Description**
data	two dimensional array containing digitized signal.

Appendix F

Image VI Design

Electron Beam Welding Project
Automation of Data Acquisition and Control Systems

Prepared by: Christina A. Filarowski

Project Advisors: John W. Elmer
Jeff Parrett
Alan T. Teruya

December 12, 1994

Table of Contents

I. FRONT PANEL FEATURES AND OPERATION

The front panel of Image VI has three digital indicators, one of which contains a two dimensional array. Image VI produces a tomographic reconstruction of the data contained in the two dimensional array and outputs the image to the intensity chart on the front panel.

II. DIAGRAM FUNCTION

This code has yet to be implemented, however, the algorithm for this code is as follows:

1. Beginning with the averaged profile values, take Fourier transform.
2. Multiply times a highpass filter.
3. Take inverse Fourier transform.
4. Build a two dimensional array. For example, if the averaged curve is made up of 100 values in a one dimensional array, build a 100 x 100 array.
5. Then take each 100 x 100 array and rotate it by the angle at which it was acquired.
6. Add all 100 x 100 arrays together.
7. All values less than 0, set to 0.
8. All values greater than a radius of half the original array, set to 0. In this case with an array of 100 values, anything outside a radius of 50 will be set to 0.

III. Image VI As A Sub-VI In A Larger Program.

If Image VI is called as a sub VI in a larger program, the following variables can be accessed as double-precision floating-point data types.

Variable(inputs)	Description
theta	number of degrees to turn the motor to acquire the next beam profile.
profiles	this will be the number of beam profiles generated based on the number of steps per increment chosen by the operator.
data	two dimensional array containing digitized signal.

Variable(outputs)	Description
image	two dimensional array containing reconstructed image of power distribution.

Appendix G

Main VI Design

Electron Beam Welding Project
Automation of Data Acquisition and Control Systems

Prepared by: Christina A. Filarowski

Project Advisors: John W. Elmer
Jeff Parrett
Alan T. Teruya

December 14, 1994

Table of Contents

I. FRONT PANEL FEATURES AND OPERATION

The front panel of Main VI has seven digital indicators, ten Boolean and one enumeration control. The seven indicators display the values for amplitude (in volts), frequency (in Hz), theta, profiles, sweeps/angle, gain, and samples/channel. The values for these parameters determined by other sub-VI's that are called during the execution of Main VI. The enumeration control allows the user to specify in which mode to run the experiment; manual, semi-automatic, or automatic. The Boolean controls allow the operator to enter a setup mode, a calibrate mode, acquire data, stop acquisition, view profiles all or one at a time, average profiles, do the tomographic reconstruction, or quit the experiment. Other Boolean controls allow the operator, when viewing the profiles at a given angle one at a time, to proceed to the next profile, or return to a previous one. These profiles are also displayed to a chart on the front panel.

II. DIAGRAM FUNCTION

A while-loop is used for continuous execution. The loop ceases when the DONE button, a global variable, is pressed on the front panel. The while-loop controls several functions:

1. Setup

A while loop is used for continuous execution and ceases execution when the DONE button is pressed on the front panel. Inside the while loop is a case statement, whose TRUE case executes when the SETUP button is pressed on the front panel. This case calls Setup VI and passes the values that the operator sets for amplitude, frequency, theta, profiles, and sweeps/angle to indicators on the front panel of Main VI. The values for these parameters are bundled and passed outside the Setup while loop to the Calibrate while loop. The FALSE case does nothing except pass the bundled parameters through the case statement using a shift register on the while loop.

2. Calibration

A while loop is used for continuous execution and ceases execution when the DONE button is pressed on the front panel. Inside the while loop is a case statement, whose TRUE case executes when the CALIBRATE button is pressed on the front panel. This case calls Calibrate VI and passes the values that the operator sets for gain and samples/channel to indicators on the front panel of Main VI. The values for these parameters are bundled and passed outside the Calibrate while loop to the Acquire case statement. The FALSE case does nothing except pass the bundled parameters through the case statement using a shift register on the while loop.

3. Acquisition

Acquisition can be done in three modes; manual, semi-automatic, and automatic, depending on which state is chosen from the enumeration control on the front panel.

A. Manual

The manual mode is the first case. It is controlled by a while loop that executes continuously until the DONE button is pressed or when the iteration counter of the while loop equals the number of profiles selected earlier in Setup VI. Inside the while loop, the values for amplitude, frequency, theta, profiles, and sweeps/angle, selected from Setup VI, are unbundled and passed into a case statement. The TRUE case of this case statement executes when the ACQUIRE button is pressed on the front panel. The TRUE case unbundles the values for gain and samples/channel and passes those values along with the values from Setup VI to Profile VI. The value for steps/inc is also calculated using the formula steps/inc = 180/theta, and is passed to Profile VI. Profile VI returns a two dimensional array, data, which contains the digitized signal. The FALSE case of the case statement passes the value of data through the case statement using a shift register on the while loop.

B. Semi-Automatic

Inside the semi-automatic run mode case is a while loop. Inside this while loop is another case statement whose TRUE case executes when the ACQUIRE button is pressed on the front panel. Inside this TRUE case is a while loop, which unbundles the values of the parameters chosen in Setup VI and Calibrate VI, as described in the Manual acquisition case, and calls Profile VI. Profile VI returns a two dimensional array, data, which contains the digitized signal. The FALSE case of the case statement passes the value of data and the condition to cease execution of the while loops, through the case statement using shift registers on the while loop. Both while loops cease executing when the DONE button is pressed on the front panel or when the iteration counter of the while loop equals the number of profiles selected earlier in Setup VI.

C. Automatic

Inside the automatic run mode case is a while loop, inside of which is another case statement. The TRUE case of this case statement executes when the ACQUIRE button is pressed on the front panel. Inside the TRUE case is a sequence structure with three sequences. In the first sequence is a while loop which unbundles the values of the parameters chosen in Setup VI and Calibrate VI, as described in the Manual acquisition case, and calls Profile VI. Profile VI returns a two dimensional array, data, which contains the digitized signal. The while loop will cease executing once all of the profiles have been acquired. The next sequence will then average the profiles. This code has yet to be written, along with the code for the third and final sequence which will call Image VI to do the image reconstruction.

4. Average Profiles

This code has yet to be implemented, however, the algorithm for this code is as follows:

1. Divide each sweep of the beam across the MFC into a separate array.
2. Do a center of mass calculation to find the center of mass of each of the arrays.
3. Overlay the arrays at that point.

4. Add the arrays together and divide by the number of sweeps.

5. Image Reconstruction

This code has yet to be implemented, however, the algorithm for this code is as follows:

1. Beginning with the averaged profile values, take Fourier transform.
2. Multiply times a highpass filter.
3. Take inverse Fourier transform.
4. Build a two dimensional array. For example, if the averaged curve is made up of 100 values in a one dimensional array, build a 100 x 100 array.
5. Then take each 100 x 100 array and rotate it by the angle at which it was acquired.
6. Add all 100 x 100 arrays together.
7. All values less than 0, set to 0.
8. All values greater than a radius of half the original array, set to 0. In this case with an array of 100 values, anything outside a radius of 50 will be set to 0.

Appendix H

User Manual

In order to run an experiment using the automated system, load Main VI and follow the instructions given below.

1. Select SETUP from the front panel of Main VI.

2. Follow the instructions on the front panel of Setup VI. Input the values for the parameters specified. Turn on the beam and adjust the position of the MFC so that the beam path is perpendicular to the slit in the MFC. Then choose QUIT to return to Main VI.

3. Select CALIBRATE from the front panel of MAIN VI.

4. Follow the instructions on the front panel of Calibrate VI. Input values for gain and sample/channel. Acquire a profile and view it on the graph on the front panel. If these values produce the desired response, choose QUIT to return to Main VI. If not, change the values for gain and sample/channel and acquire another profile. Continue changing the values and acquiring profiles until the desired response is achieved.

5. From Main VI, select the mode in which you wish to run the experiment; manual, semi-automatic, or automatic.

6. Turn on the beam.

Automatic

Select ACQUIRE, and the experiment will proceed without any intervention from the user, until the tomographic reconstruction is produced.

Semi-Automatic

Select ACQUIRE. The system will acquire all of the profiles then pause for user input. Now select RECONSTRUCT and the system will produce the tomographic reconstruction of the data based on the acquired profiles.

Manual

Select ACQUIRE. When the acquisition has finished for that angle, turn off the beam. The system will show the profiles all overlaid. If you choose to look at them one at a time, select VIEW PROFILES ONE, then view them using the NEXT and PREVIOUS buttons. When you have finished, select AVERAGE PROFILES to average them and proceed to the next angle. Turn on the beam and repeat this process until the beam has been profiled at all angles. Then select RECONSTRUCT to produce the tomographic reconstruction of the data based on the acquired profiles.

6. When you have finished with the experiment, select QUIT and exit the program.

Appendix I

Stepper Motor Controller Board Research

The following is a list of manufacturers that where contacted, in researching stepper motor control boards, the cost of their products and why they were considered not appropriate for this application.

Company Name	Cost	Reason for rejection
1. Newport Corporation	$2000	Over budget
2. Rogers Labs	-----	No LabVIEW driver, cannot run on pentium, only on 286 machine
3. CTS, Inc.	-----	No LabVIEW driver
4. Microkinetics	$249	No LabVIEW driver
5. Motion Engineering	$1700	No LabVIEW driver, offered to write one
6. Oregon Microsystems	-----	No LabVIEW driver
7. nuLogic	$895	would have purchased this board if the National Instruments AT-MIO-16X was not able to do the motion control required.
8. Technology 80	$695	No LabVIEW driver, offered to write one

Appendix J

Digitizing Board Research

The following is a list of manufacturers that where contacted, in researching digitizing boards, the cost of their products and why they were considered not appropriate for this application.

Company Name	Cost	Reason for rejection
1. National Instruments	$2995	Over budget
2. Data Translation	-----	No LabVIEW driver
3. Strawberry Tree	-----	No LabVIEW driver
4. Gage	$5245	Over budget
5. Industrial Computer Source	$1695	purchased

The Mapping of Novel Genes to Human Chromosome 19*

Joel M. Buenaventura

Sarah Lawrence College
Bronxville, NY 10708

Mentor: Dr. Greg Lennon
Human Genome Center, L-452
Lawrence Livermore National Laboratory
Livermore, CA 94550

December 16, 1994

*Prepared in partial fulfillment of the requirements of the Science and Engineering Research Semester (hereinafter called SERS) program administered by LLNL under **Contract W-7405-Eng-48 with Lawrence Livermore National Laboratory.**

ABSTRACT

The principle goal of our laboratory is the discovery of new genes on human chromosome 19. One of the strategies to achieve this goal is through the use of cDNA clones known as "expressed sequence tags" (ESTs). ESTs, short segments of sequence from a cDNA clone that correspond to the mRNA, occur as unique regions in the genome and, therefore, can be used as markers for specific positions. In collaboration with researchers from Genethon in France, fifteen cDNA clones from a normalized human infant brain cDNA library were tested and determined to map to chromosome 19. A verification procedure is then followed to confirm assignment to chromosome 19. First, primers for each cDNA clone are developed and then amplified by polymerase chain reaction from genomic DNA. Next, a ^{32}P-radiolabeled probe is made by polymerase chain reaction for each clone and then hybridized against filters containing an LLNL chromosome 19-specific cosmid library to find putative locations on the chromosome. The location is then verified by running a polymerase chain reaction from the positive cosmids. With the Browser database at LLNL, additional information about the positive cosmids can be found. Through use of the BLAST database at the National Library of Medicine, homologous sequences to the clones can be found.

Among the fifteen cDNA clones received from Genenthon, all have been amplified by polymerase chain reaction. Three have turned out as repetitive elements in the genome. Ten have been mapped to specific locations on chromosome 19. Putative locations have been found for the remaining two clones and thus verification testing will proceed.

INTRODUCTION

Current estimates place the number of genes in the human genome at 100,000 genes. Identifying coding regions within a complex genome of over 3 billion base pairs is a daunting and time-consuming task. Since only 10% of the genome is considered to code for genes, a quick method to find genes should be utilized.

Complementary DNA ("cDNA") mapping has proven to be a quick method for gene identification (Adams, 1991). One can isolate the mRNA from a specific tissue, synthesize the complementary DNA sequence, and then place it into a vector. This short segment of DNA can be radioactively labeled and used as a probe for specific regions on a chromosome map. Once the probe is hybridized and specific regions found, one can proceed to run a homology search to find similarities to other genes. Also, the cDNA map can suggest a set of candidate genes to test when the approximate location of a disease gene has been mapped by genetic linkage techniques.

This group is working with chromosome 19 sequencing and mapping. Therefore, one interest is finding new genes on chromosome 19. Fifteen cDNA clones were localized by a collaborating laboratory to chromosome 19 through chromosomal hybrid testing. The purpose of these experiments was to map them to specific locations on the high resolution map of chromosome 19.

MATERIALS AND METHODS

cDNA Clones

Fifteen cDNA clones from a normalized human infant brain library were obtained from Genethon. Primers were made according to standard methods.

Polymerase Chain Reaction Optimization

A Perkin Elmer 9600 machine was used in all PCR reactions. For optimization of each clone, a 50µL amplification reaction was performed with 100ng human placental DNA, 40pm of each primer pair, 200µM dNTPs, varying concentrations of MgCl2 (1mM, 2mM, and 3mM), 100mM Tris pH 8.3, 500mM KCl, and 2.5 units Taq polymerase. The reactions were run at the following conditions: 94° 10", 55°-65° 30", 72° 1:30 for 40 cycles. Products were then separated on a 2% agarose gel with 50µg/µl ethidium bromide and visualized with UV fluorescence. The desired gel bands were then excised, placed in a microfuge tube with 40µl distilled H_2O, and heated at 37°C for twenty minutes. Then, the tubes were refrigerated for later use as the template for the radioactive ^{32}P probe.

DNA Probes

A 25µl PCR labeling reaction using the excised band as the template and (alpha-^{32}P) dCTP as the radioactive label was performed. The PCR conditions were the same as the optimization conditions. The PCR products were purified using minispin columns (Worthington) and boiled 5 minutes prior to hybridization to high density cosmid filters.

Hybridization to High Density Cosmid Filters

The radioactively labeled probes were hybridized independently against chromosome 19 filter sets consisting of cosmid clones spanning chromosome 19 as described by Carrano (1988). The filters were prehybridized for two hours at 65°C in a hybridization solution containing 4M NaCl, 0.5M EDTA, 1M Tris (pH 7.4), 5% NA pyrophosphate, 50% dextran sulfate, and 20% SDS. Three agents (500µg salmon sperm, 200µg poly U, and 50 µg Cot-1) were added to block repetitive elements. The probes were added and hybridized at 65°C overnight.

Two fifteen minute washes with a high stringency solution containing 0.1xSSC-0.1% SDS followed. Finally, the filters were exposed to a PhosphorImager (Molecular Dynamics) overnight and analyzed for positive cosmids.

Verification of Positive Cosmids

The positive cosmids were then subjected to verification testing through either two methods: 1) A 50µl PCR reaction using the EST primers and the positive cosmids as template. 2) Southern hybridization according to Maniatis (1989). The DNA from the positive cosmid clone was obtained through overnight culture of the clone in 3ml LB Broth and 90µg/µl of Kanamycin. Then the DNA is isolated through the Wizard Minipreps DNA Purification System (Promega). Next, the DNA was digested overnight in EcoRI, run out on a 1% agarose gel with 50µg/µl ethidium bromide and then blotted to a nylon membrane. A 25µl PCR labelling reaction as above for the respective clone is performed and then hybridized to the Southern blot for verification.

Analysis through Computer Databases.

For each cDNA clone, a sequence homology search is run through the NCBI BLAST program through the blastx database. A probability of $<10^{-3}$ was considered a significant homology.

The location of the positive cosmids was determined through the LLNL Browser program. If the cosmid had been mapped by Fluorescence In Situ Hybridization, the location to the band on chromosome 19 was known.

RESULTS AND DISCUSSION

Of the fifteen cDNA clones, all fifteen were amplified with different concentrations of $MgCl_2$ and a median temperature at 55°C, 60°C, and 65°C. Table 1 shows the $MgCl_2$ concentrations and the median temperature for each

clone. Also, ten clones have been mapped to specific cosmids as shown in Table 1. Of these ten clones, seven have been mapped to specific bands of chromosome 19 as shown in Figure 1.

Three cDNA clones (11a4, 20d1, and 15d5) appeared as repetitive elements and had multiple positives on the filter sets; hence, they could not be mapped to a specific cosmid or region. The BLAST homology search indicated these clones to be members of Alu-like families.

Two clones have yet to be mapped. The two clones (12d7 and 2d9) have putative cosmids and are in the midst of verification.

The BLAST homology search (Table 2) showed five clones (10f9, 12h3, 15a5, 1c12, 20f7)to be similar to previously unassigned, anonymous cDNA clone in the sequence database. Five clones (12d7, 2d9, 3d1, 12g6, 17f3) did not show any sequence homology. Because they did not show homology but are expressed as mRNA, they can be considered segments of new genes in that region.

Two cDNA clones (21h5 and 22e11) had homologies to already characterized genes. Clone 21h5 was homologous to a region of the RSU1 gene which is involved in cell cycle suppression. The primers for this clone have been sent to an investigator to see if this clone could be a member of a larger gene family for RSU1 (M. Cutler, personal communication). The second clone 22e11 is homologous to a Rat glycogen synthase kinase that has been implicated in hormonal control of several regulatory proteins.

All ten mapped cDNA clones on chromosome 19 may be used as candidate genes in the future for genetic diseases linked to those regions of chromosome 19.

SUMMARY AND FUTURE RESEARCH

Of the 15 cDNA clones, three turned out as repetitive elements, ten have been mapped to specific cosmids, and two are awaiting verification. The cDNA map of chromosome 19 has been refined with the locations of ten cDNA clones with two more to follow. Our group hopes to pursue information on the two cDNAs with the already characterized homologies. The remaining clones are available for study to other groups interested in those particular regions of chromosome 19.

Bibliography

Adams, M., et. al. (1991)Science 252, 1651-1656.

Carrano, A.V., de Jong, P.J., Branscomb,E., Slezak, T., and Watkins, B.W. (1989). *Genome* 31 (2): 1059-1065.

Maniatis, T., Sambrook, J., and Fritsch, E.F. (1989) *Molecular Cloning: A Laboratory Manual* (Cold Spring Harbor Laboratory Press, Cold Spring Harbor, NY ed.2).

U.S. Department of Energy. (April 1992) *Human Genome Program: Primer on Molecular Genetics.*

Table 1. This table shows the clone names in the first column. The second column shows the $MgCl_2$ concentration for optimization. The third column shows the median temperature for template annealing. The fourth column shows the cosmid clones identified.

Table 1

Clone Name	MgCl2 Conc (mM)	Tm (°C)	Results of Mapping
10f9	2	65	5843, 5988, 8931, 28562, 29830, 30592, 30831, 32468
11a4	1	55	Long Tandem Repeat
12d7	3	55	putative locations
12h3	3	55	22849
15a5	2	55	25360; 33404
20d1	2	55	ALU-like sequence
21h5	1	60	30914, 31585, 33040
j22e11	2	55	16299, 17092, 25024
1c12	2	55	29820; 29957; 30684; 30777
2d9	1	55	putative locations
3d1	1	55	29502, 30530
12g6	2	55	29654, 33174, 33341, 34120
15d5	2	55	ALU-like sequence
17f3	3	55	32214, 34318
20f7	3	55	29276, 31989, 33571

Figure 1. This figure shows the FISH bands that the 7 cDNA clones mapped in the yellow background. The orange background clones were mapped by another member of the laboratory.

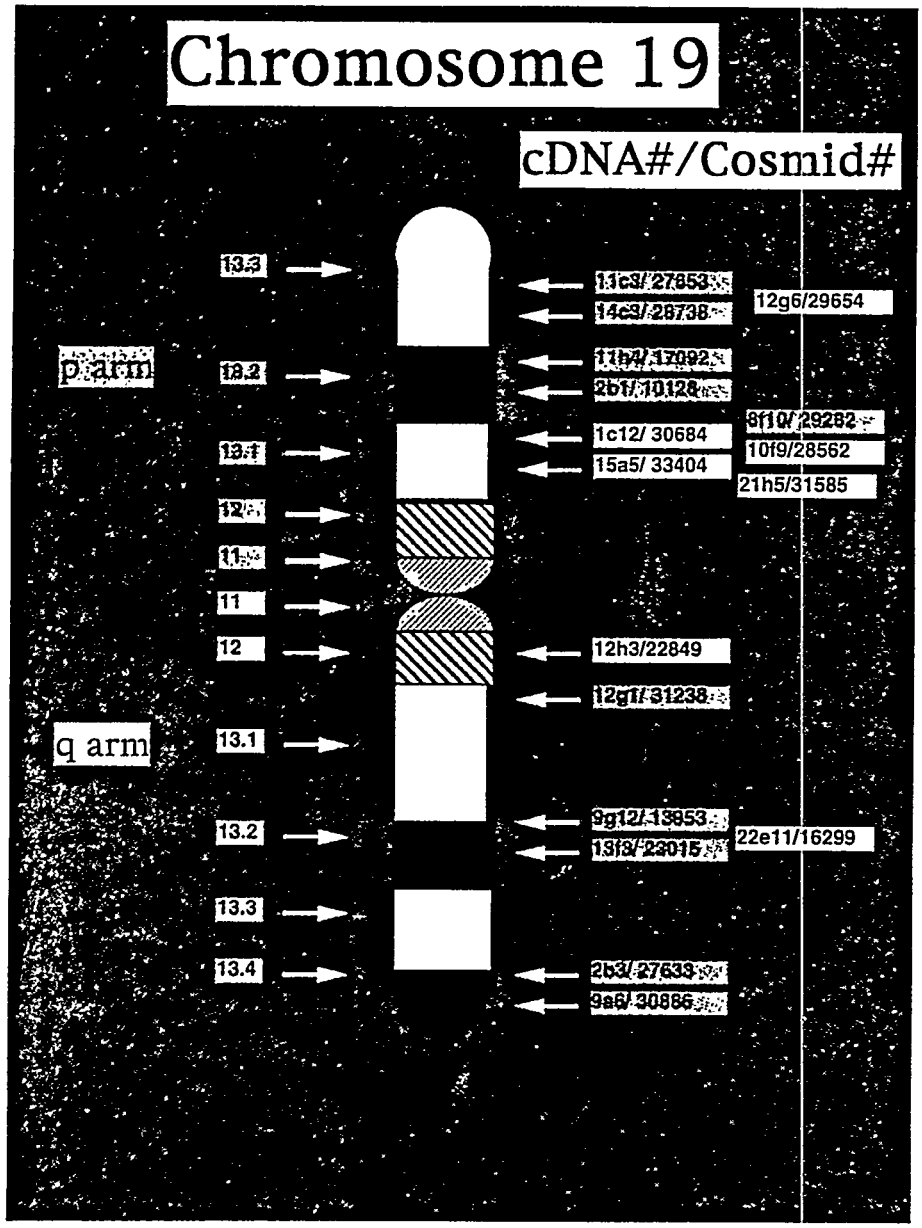

Table 2. This table shows the results of the BLAST homology search. The fourth column shows the probability that the match to the sequence is random.

RESULTS OF BLAST HOMOLOGY SEARCH

cDNA #	BLAST Homology	Mapped	Probability
- 10f9	IB905 cDNA clone	Yes	7.5e-93
- 11a4	Long Tandem Repeat	N/A	5.4e-33
- 12d7	New gene	No	N/A
- 12h3	NIB1945 cDNA clone	Yes	1.5e-74
- 15a5	IB1304 cDNA clone	Yes	4.4e-68
- 20d1	Alu-like repeat	N/A	9.9e-63
- 21h5	Human RSU-1/RSP-1	Yes	5.4e-101
- 22e11	Rat glycogen synthase kinase	Yes	6.4e-59
- 1c12	IB1264 cDNA clone	Yes	7.3e-62
- 2d9	New gene	No	N/A
- 3d1	New gene	Yes	N/A
- 12g6	New gene	Yes	N/A
- 15d5	Alu-like repeat	N/A	3.0e-31
- 17f3	New gene	Yes	N/A
- 20f7	EST0349	Yes	6.5e-98

SCIENCE & ENGINEERING

SERS

RESEARCH SEMESTER

Fall Semester

Final Research Paper

Jennifer M. Daniel
December 14, 1994

Max Fenstermacher
Gary Porter

Lawrence Livermore National Laboratory

GENERAL ATOMICS San Diego, California

UEDGE CODE COMPARISONS WITH DIII-D BOLOMETER DATA*

Jennifer M. Daniel

Athens State College

Lawrence Livermore National Laboratory
Livermore, California 94550

December 14, 1994

Prepared in partial fulfillment of the requirements of the Science and Engineering Research Semester under the direction of Max Fenstermacher and Gary Porter, Research Mentors, in the Lawrence Livermore National Laboratory.

* This research was supported in part by an appointment to the U. S. Department of Energy Science and Engineering Research Semester (hereinafter called SERS) program administered by LLNL under Contract W-7405-Eng-48 with Lawrence Livermore National Laboratory.

UEDGE Code Comparisons With DIII-D Bolometer Data

Jennifer M. Daniel

Athens State College

Magnetic Fusion Energy Division

ABSTRACT

This paper describes the work done to develop a bolometer post processor that converts volumetric radiated power values taken from a UEDGE solution, to a line integrated radiated power along chords of the bolometers in the DIII-D tokamak. The UEDGE code calculates plasma physics quantities, such as plasma density, radiated power, or electron temperature, and compares them to actual diagnostic measurements taken from the scrape off layer (SOL) and divertor regions of the DIII-D tokamak. Bolometers are devices measuring radiated power within the tokamak. The bolometer interceptors are made up of two complete arrays, an upper array with a vertical view and a lower array with a horizontal view, so that a two dimensional profile of the radiated power may be obtained. The bolometer post processor stores line integrated values taken from UEDGE solutions into a file in tabular format. Experimental data is then put into tabular form and placed in another file. Comparisons can be made between the UEDGE solutions and actual bolometer data. Analysis has been done to determine the accuracy of the plasma physics involved in producing UEDGE simulations.

OUTLINE

Thesis: Comparisons of UEDGE generated quantities with DIII-D bolometer data provides a method for bench marking the physics models used in UEDGE plasma simulations.

I. Background Information
   A. Fusion Energy
   B. Tokamaks
   C. Bolometers

II. Bolometer Diagnostic
   A. Sensor Description
   B. Geometry for Viewing
   C. Old versus New arrays

III. UEDGE Code
   A. Purpose of the UEDGE Code
   B. How the UEDGE Code Works
   C. How radiated power along bolometer lines of site is calculated by the UEDGE Code

IV. Bolometer Post Processor
   A. Purpose of the Bolometer Post Processor
   B. How the Bolometer Post Processor Works
   C. How the bolometer Post Processor prepares UEDGE and bolometer data for comparisons

V. Analysis of Shot 82151 and Comparison to UEDGE Simulations
   A. Simulation with no impurity radiation
   B. Simulation with constant impurity concentration
   C. Simulation with impurity transport

VI. Conclusions from Comparisons
   A. Impurity Model Needed
   B. Carbon Impurity Introductions
   C. Physics of Carbon migration

VII. Summary

UEDGE CODE COMPARISONS WITH DIII-D BOLOMETER DATA

Introduction

According to Newton's laws, energy is neither created nor destroyed. However, it is transformed . Power is one form of energy transformation. It is the time rate of change of energy transferred. Some sources for power generation include hydroelectric plants, windmills, solar power, and nuclear power plants. Fusion power, currently being researched and developed, is another source for power generation. The DIII-D experiment at General Atomics in San Diego, California in cooperation with Lawrence Livermore National Laboratory (LLNL), is part of the ongoing research for fusion power. The DIII-D machine uses a toroidal device, called a tokamak, for a magnetic confinement system. This system helps contain a hot ionized gas called plasma, the fourth state of matter. The plasma reaches temperatures of approximately 10 - 50 million degrees Kelvin in the center of the tokamak. There are devices on the tokamak called bolometers which measure the heat or power radiated from the plasma. Lawrence Livermore National Laboratory assists General Atomics in their data analysis for DIII-D. LLNL has a code, UEDGE, that simulates the edge tokamak plasma parameters and generates quantities similar to those measured in actual DIII-D experiments. Current studies are being done to examine the power radiated within DIII-D and compare this to UEDGE simulations at LLNL. Comparisons of UEDGE generated quantities with DIII-D bolometer data provides a method for bench marking the physics models used in UEDGE plasma simulations.

Background

Fusion Energy

Fusion occurs when two light nuclei combine to form a heavier nucleus. In some reactions the mass of the final nucleus is less than the combined rest masses of the original nuclei. Due to a loss of mass in these fusion reactions, there is also an accompanying release of energy (Serway 1395). The goal for fusion research is to capture this released energy from the reactions, and use it for power generation here on earth. One might ask why we need another source of power generation. Although we now have several sources of power generation, studies show, with a future decrease in availability of fuels, other sources of power generation are needed. Currently, nuclear power plants rely on Uranium as a fuel source, which is not very abundant. However, if a fusion reactor is fully developed, the heavy isotope of hydrogen that is required as fuel, can be found in water.

In water there exists a hydrogen isotope called deuterium also known as heavy hydrogen, having twice the mass of ordinary hydrogen. Deuterium is extracted from the water, and then the atoms are fused in reactions such as:

$$ {}_1H^2 + {}_1H^2 \longrightarrow {}_2H^3 + {}_0n^1 $$

The total amount of energy released from each deuterium reaction is around 3.27 MeV (Serway 1396). A similar reaction combining deuterium and tritium, a radioactive hydrogen isotope, produces 17.59 MeV of energy per fusion reaction (Serway 1396). Given the same conditions and temperatures to initiate fusion, the deuterium-deuterium, DD, reaction is less likely to occur, while in the deuterium-tritium, DT, reaction, which releases more energy, and the atoms are more likely to fuse. Although the DT reaction releases more energy, the DD reaction is favored for two reasons: 1) tritium is radioactive, while deuterium is not, and 2) tritium is not naturally occurring in water like deuterium (Wesson 2). The ultimate goal is to use the DD reaction for a fully developed commercial fusion reactor.

In combining two atoms, the repulsive force between two charged nuclei must be overcome. To do this, kinetic energy must be supplied to the nuclei by heating the fuel to high temperatures (approximately 4×10^8 K for the DD reaction and 4.5×10^7 K for the DT reaction) (Serway 1398). At such high temperatures, atoms ionize and a plasma forms.

After the plasma forms the problem is a matter of efficiency and containment. More power must be harnessed from the fusion reaction than is put in to heat the fuel and fuse the atoms together; that is, there must be a net power production. The product of density, temperature and confinement time, $nT\tau$, determines the net power production. According to Lawson's criteria, the product of the density and confinement time for the DD reaction should at least equal 10^{16} s/cm^3 for a net energy output (Serway 1398). High density and confinement allow an increase in the probability of atoms fusing together and releasing energy. With such high temperatures, on the order of one million degrees in the outer region of the plasma, some method other than ordinary materials is needed to confine the plasma to a given volume (Wesson 2).

Tokamaks

Currently, there are two methods being studied to help achieve higher $nT\tau$, magnetic confinement and inertial confinement. The magnetic confinement method uses two different magnetic fields to contain the plasma, toroidal and poloidal fields. Since plasmas are affected by magnetic fields and are good conductors of electricity, magnetic confinement is efficient. Most of these magnetic confinement systems use a toroidal device called a tokamak. There are several tokamak experiments worldwide. For instance, the Tokamak Fusion Test Reactor (TFTR) located at the Princeton Plasma Physics Laboratory was designed largely for studies concerning overall net power production, and recently got a world record for 10 MW (megawatts) of fusion power (Wesson 280). The Joint European Torus (JET) in Abingdon, UK is the world's

largest tokamak. JET studies lie mainly in methods of heating the plasma and energy confinement time, in addition to net power production (Wesson 283). This paper deals with experiments performed on the DIII-D tokamak in San Diego, California. A major part of the DIII-D program is devoted to studying the physics of the edge of the plasma, especially in the divertor regions, and controlling impurities being introduced into the plasma (Mahdavi 1).

DIII-D runs for three weeks at a time with maintenance periods between operations. On a normal operation day, a plasma discharge takes place every fifteen minutes beginning at 9:00 am and ending at 5:00 pm with each discharge lasting for approximately five seconds. It is very important that analysis be done on the shots immediately, so that changes, such as the amount of current in the plasma or an increase or decrease in the pumping out of the neutral gas, can be made, if need be, before the next shot occurs.

Figure 1 shows a schematic of a tokamak. There are two different magnetic fields used in this doughnut shaped device. One is a toroidal field, B_T, produced by coils winding around the tokamak. A second magnetic field is the poloidal field, B_P, produced by coils, circling the tokamak, and current in the plasma (Serway 1399).

Figure 2 gives a vertical view of the DIII-D tokamak at 240°. It defines some important regions and diagnostics discussed in following sections of the paper.

There are several regions and diagnostics labeled in figure 2. The divertor region, which is of primary concern for this paper, consists of everything below the dotted region as shown in figure 2. Underneath the baffle lies the cryopump, which pumps out unwanted neutral gas particles keeping them from drifting back up into the plasma possibly causing disruptions. Due to the forces of the magnetic fields, particles travel in a helical path eventually striking the walls of the tokamak. After the particles strike the floor, a tremendous amount of heat flux and radiated power comes off the floor as there is a transfer of momentum and energy of particles. As a result, some

metallic carbon impurities are knocked off the carbon tiles and introduced into the plasma. Inner and outer strike points (ISP, OSP) are labeled in figure 2. These points are possible areas where neutral particles, plasma ions, and electrons might strike the divertor floor.

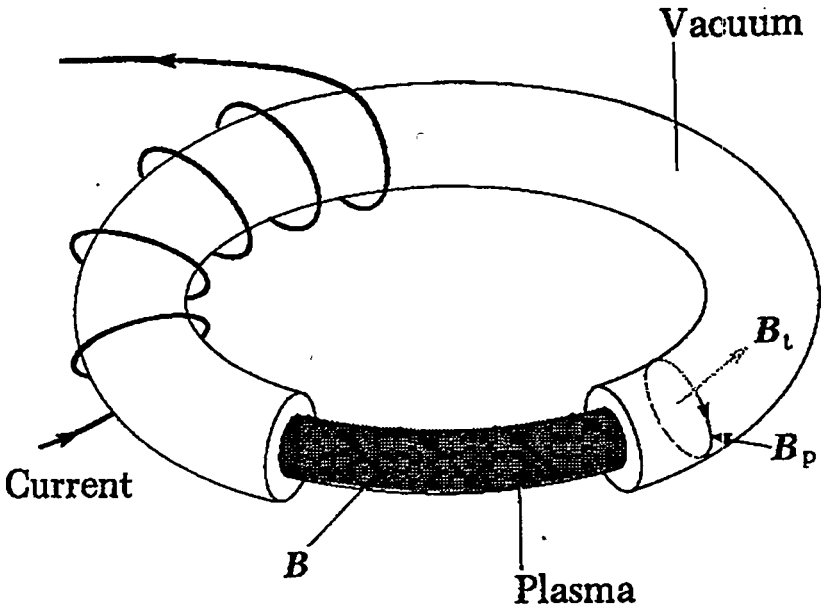

Figure 1: The primary magnetic field is the toroidal field. Current passes through the primary coil; which produces a change in flux through the torus. The change in flux results in a toroidal electric field, which drives a current through the plasma. The resulting magnetic field is helical around the plasma, which helps to confine it within the tokamak walls (Wesson 12).

Bolometers

There are several ports located along the walls of the tokamak as shown in figure 2. These ports contain different diagnostics such as infrared cameras, photo diodes, and bolometers. Bolometers are devices measuring radiated power profiles within DIII-D. The majority of the measured radiated power comes from atoms emitting photons going from one ionization state to another, or emissions from neutral atoms going from excited states to ground states. When particles strike the divertor floor or

walls, energy is transferred in the form of heat to the carbon tiles lining the tokamak. A tiny fraction of the total radiated power measured by the bolometers comes in the form of infrared radiation from the hot carbon tiles. Studies are being done to develop ways of dissipating the heat flux to the divertor floor, possibly by keeping particles from striking the floor. Measurements of the radiated power are necessary to assess applicability of techniques, such as gas puffing, to lessen this heat flux to the floor (Mahdavi).

Bolometer Diagnostic

Sensors

Figure 3 is a diagram of a bolometer interceptor. Each bolometer interceptor has two sensors, a reference sensor and an active sensor, made up of several layers. Mounted beside one another, these two sensors are on an alumina block 0.64 cm wide, 3.02 cm long, and 0.32 cm thick. Under the active sensor, a cut keeps the sensor thermally isolated from the substrate. A cover piece, made of a polymide, Vespal, known for its strength, vacuum capability, and high temperature characteristics, is placed over the sensors to protect them from possible plasma radiation. The sensors have a maximum allowable temperature of 200° C, and cooling is provided for them during a high temperature bake (350° C) of DIII-D. There is an opening in this cover piece over the active sensor exposing it to incoming radiation (Leonard 3). Light radiation strikes platinum foil, the first layer, where it heats the foil. Under the foil is a layer of electrical isolation material called Kapton. A platinum wire connected to gold plated pins lies underneath the Kapton. As the wire heats, it's voltage as well as current changes resulting in a change in resistance, $R = V / I$. The power signal is calculated using the time rate of change of the resistance (Leonard 7).

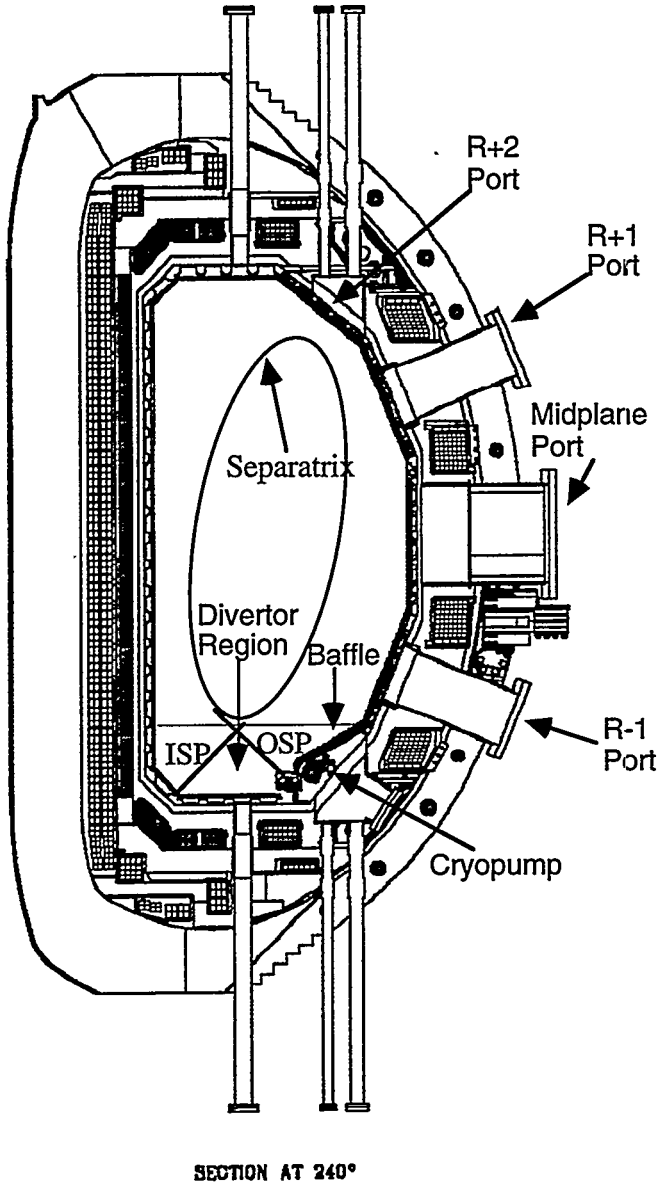

Figure 2: A vertical slice located at 240° for the DIII-D tokamak.

Geometry

There are a total of twenty-four interceptors in each bolometer diagnostic. These interceptors are enclosed in copper housings which have an aperture for viewing the plasma. For one bolometer diagnostic, two housings are needed to

achieve a full view of the plasma. Each housing contains roughly half of the twenty-four interceptors (Leonard 3). There are two bolometer diagnostics in the DIII-D tokamak one located in port R+2 and one in port R-1. Therefore, a total of forty-eight bolometer channels and viewing chords exist. These viewing chords are pictured in figure 4. The diagnostic in port R+2 gives the vertical view of the plasma, and the diagnostic in port R-1 gives the horizontal view. These two views can be combined to get a two dimensional radiated power profile of the plasma.

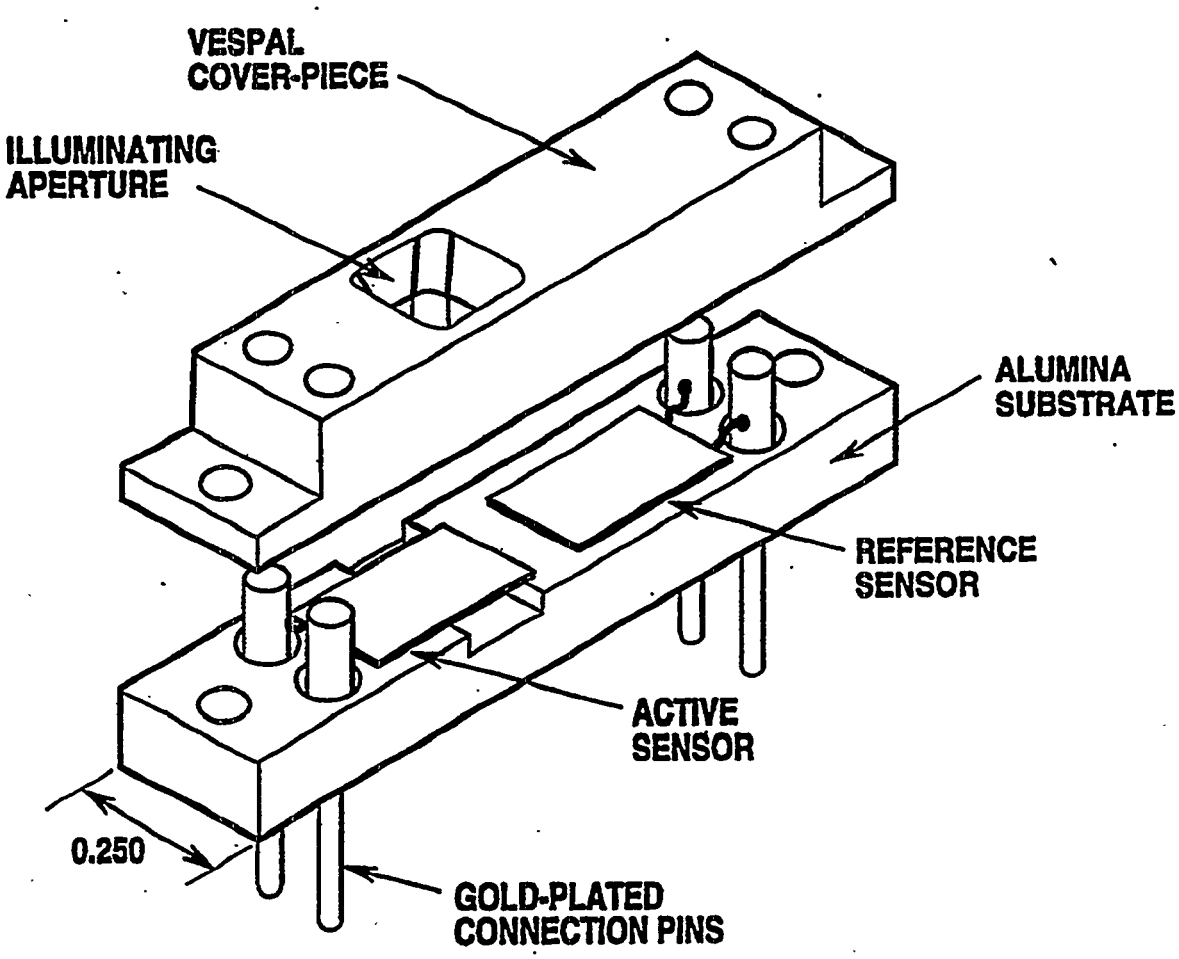

Figure 3: A bolometer interceptor (Leonard 4).

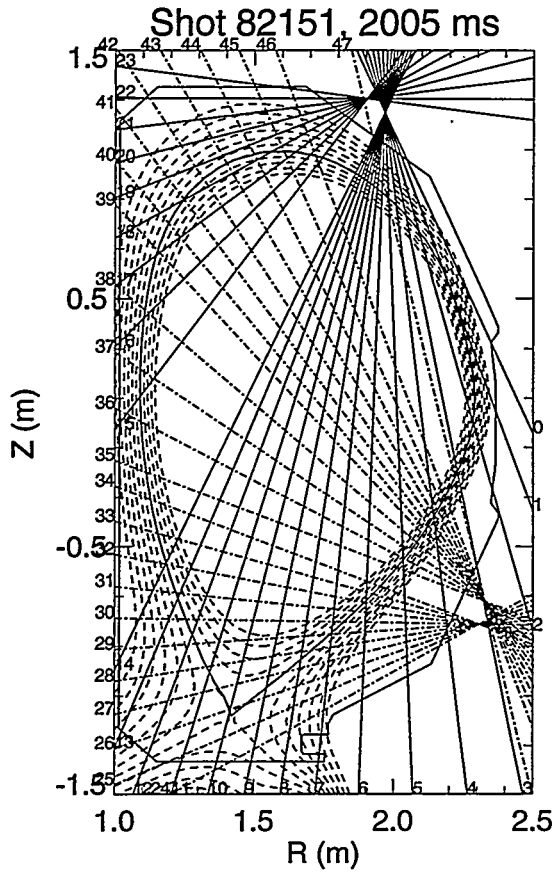

Figure 4: Bolometer viewing chords.

Old versus New Arrays

The two diagnostics located in ports R+2 and R-1 are additions to the DIII-D tokamak. Previously only one bolometer diagnostic located in the midplane port (shown in figure 2) existed. However, it was found that this one diagnostic was not adequate for determining the power radiated in the divertor region. The viewing chords for this region were too large to give a good representation of the divertor region. The mid plane diagnostic also captured power radiated from the core. With only the one diagnostic the geometry for the viewing chords was not accurate, and the power radiated readings were not well understood. The new bolometer diagnostics

provide better spatial resolution in the divertor region and have complete plasma coverage (Leonard 4).

UEDGE Code

Purpose

Since LLNL assists General Atomics with DIII-D data analysis, they also do simulations using a code called UEDGE. The UEDGE code is a Unified Tokamak Edge Physics Modeling Code. Its main interest lies in the edge regions of the plasma formed in a tokamak. Its purpose is to model the plasma physics involved during a fusion reaction simulation. The code calculates quantities such as electron and ion density and temperatures, as well as radiated power (UEDGE Manual).

How UEDGE Works

Using fluid equations and different boundary conditions for the core and outer or inner wall divertor regions, the UEDGE code models the physics of the plasma created within the scrape-off-layer of a tokamak. UEDGE has its own two-dimensional radial and poloidal grid as shown in figure 5 below. This grid consists of an inner region, a separatrix, refer to figure 2, and a scrape off layer (SOL). The UEDGE code can model physics in these regions during ionization , recombination, and impurity radiation. The physics models contained in the UEDGE code must be validated against experimental data before the code is used to aid in the design of future experiments. It is hoped that much will be learned from these UEDGE simulations, and then applied to experimental runs with expectations of getting closer to the goal of developing an efficient commercial fusion reactor.

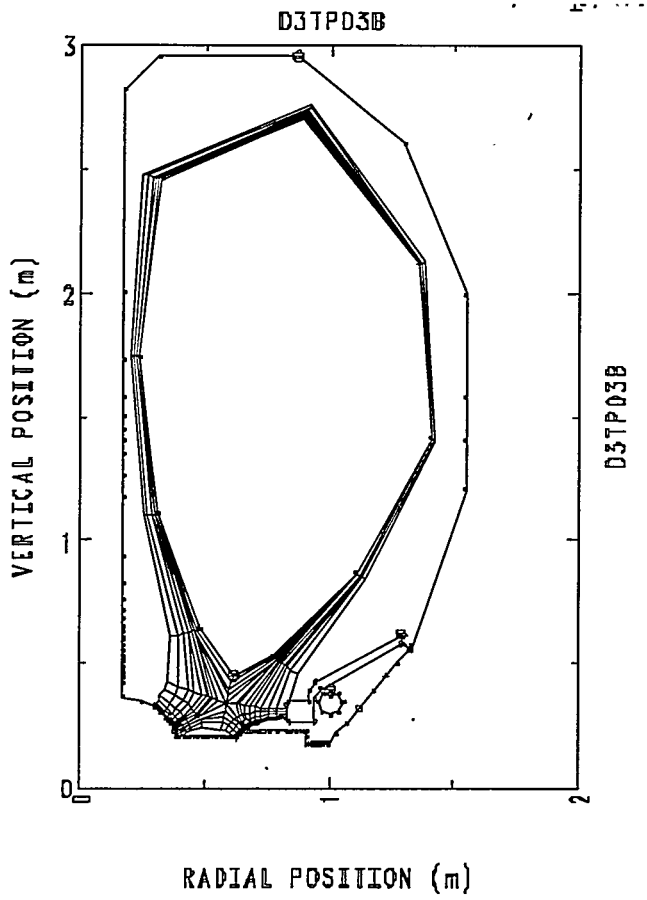

Figure 5: UEDGE grid

Radiated Power Calculations by UEDGE

From the UEDGE grid, the code is able to calculate the radiated power in a toroidally continuous volume represented in the poloidal cut by a UEDGE grid cell.

Bolometer Post Processor

Purpose

A bolometer post processor was developed to obtain volumetric radiated power values as calculated by UEDGE, and convert them into line integrated radiated power along bolometer lines of sight. From these values, a plot is made of the channel number versus radiated power to the distribution of the radiated power. These

calculated values are then compared with actual bolometer experimental data taken from DIII-D in San Diego. These comparisons help to identify which of the UEDGE model assumptions best represent the physics occurring in DIII-D experiments.

How Processor Works

UEDGE is a plasma physics code which runs under the Basis system. UEDGE calculates plasma physics quantities and stores the values in a BASIS database. The post processor accesses these values from the database and within the BASIS system performs calculations with them, eg. line integrals of the radiated power (Dubois 2).

Preparation of UEDGE Data

The bolometer Post Processor, after it has loaded in all the appropriate variables, takes the volumetric UEDGE radiated power values, converts them into an orthogonal RZ grid, and then integrates along the bolometer lines of sight of the bolometer chords to get a calculated line integrated radiated power. This data is then written to a file called "bolo_probname", where probname is the name of the UEDGE problem being run. After this data is obtained, actual bolometer data is received using codes written in the Interactive Data Language, IDL (IDL Reference Guide). Bolometer data is extracted from the DIII-D experimental database and put into tabular form (Preckshot). Both sets of data, UEDGE solutions and actual data, must be in a tabular format before they are read into a spreadsheet program. Once the data is placed in a spreadsheet program, comparison graphs are made and analysis done.

Analysis of Shot 82151 and Comparisons to UEDGE Simulations

Shot 82151 is a DIII-D experimental shot lasting for 5 seconds. The review plot in figure 6 gives a summary of this particular shot. This shot was done to study the effects of injecting gas up into the plasma from the divertor floor in order to decrease

the heat flux to the floor. We were looking for a decrease in the divertor power arising from an increased total radiated power (see last graph in figure 6). The total current used in this shot was 1.62 MA (megaamps) with a magnetic field, B_T, equal to 2.01 T (tesla). An initial deuterium puff began the discharge with another deuterium injection around 2100 ms (milliseconds). Our analysis of this shot takes place at 2005 ms, right before the second deuterium puff.

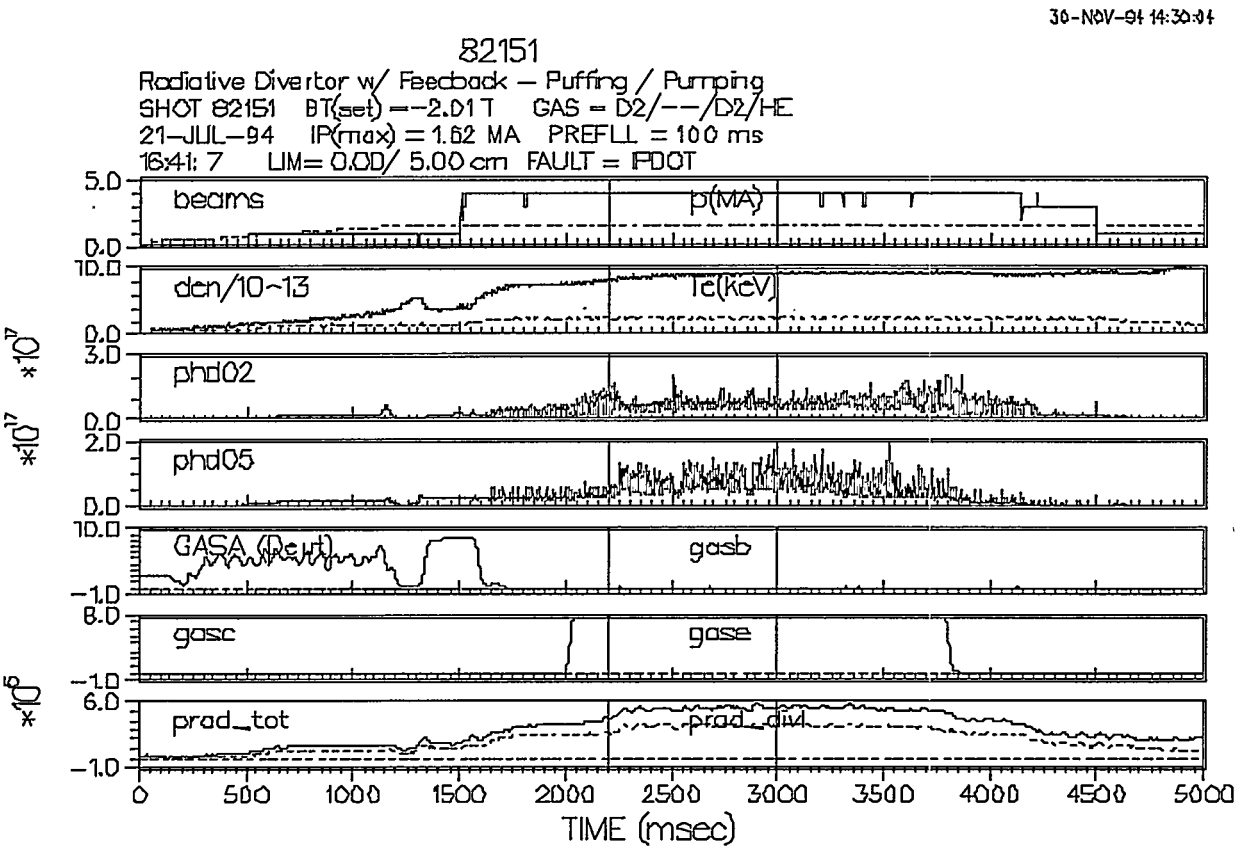

Figure 6: A review plot shows the plasma current, Ip, injected beam power, beams, deuterium gas injection, GAS A and gase, line averaged density, den / 10^13, line integrated H_α emission, phd02 and phd05, electron temperature, Te(keV), total radiated power, prad_tot, and outer divertor power, prad_div.

No Impurity Radiation

The first UEDGE simulation compared to shot 82151, involves only radiation from the hydrogen species. No impurities are included in this simulation. Therefore, this simulation could possibly be leaving a lot out, since we know there are impurities introduced in actual DIII-D shots. Figure 7 shows the plot comparisons. Channel numbers seven and eight from the upper array give a view of the outer strike point radiated power. Channel numbers eleven and twelve from the upper array give the inner strike point power, which is a factor of nearly three greater than the outer strike point power. Channel numbers twenty-four and twenty-five give another view of the inner strike point as seen from the lower bolometer array. At this point the magnitude is less than the actual data. In channel numbers thirty-five and thirty-six we see some power being radiated from the inner wall area. What is important about the results from the UEDGE simulation is not magnitudes of the power, but how well the simulations line up with the actual data as far as the channel numbers. For this no impurity simulation, the curves for the peaks match fairly well.

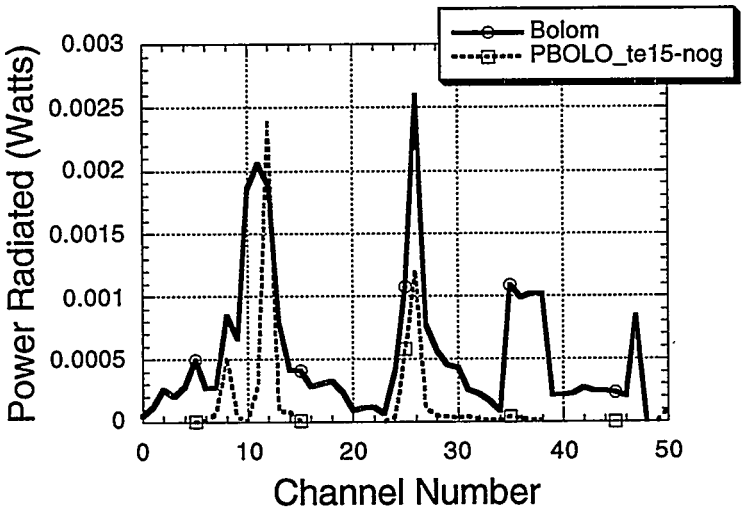

Figure 7: A comparison of Shot 82151 at 2005ms with a UEDGE simulation where hydrogen is the only contributor to the radiated power. No impurity radiation exists in this UEDGE simulation.

Constant Concentration of Impurities

This UEDGE simulation assumes a constant concentration of average Carbon impurities. This simulation ensures constant concentration by specifying the density of Carbon divided by the density of the electrons as the same throughout the UEDGE plasma grid. While there is no reason, a priori, to expect a constant density fraction, this model is a simple way of introducing impurity radiation into the UEDGE simulation. In the cases with constant impurity concentration and with the impurity transport model (see following paragraph), the amount of Carbon impurities introduced is adjusted to match the total calculated radiated power to the measured value. That is, an amount of Carbon impurities is introduced into the simulation until the total radiated power matches that of the DIII-D shot 82151 total radiated power. In the constant concentration model the Carbon impurities are introduced as a fixed fraction of the electron density everywhere, while in the impurity transport model, carbon is introduced uniformly around the SOL of the UEDGE grid. Figure 8 shows this comparison. The simulation, in terms of curve matching, is not a good match to the actual DIII-D data. The peaks for the inner and outer strike points are the only regions in the graph where a good match exists. Similar to the no impurity radiation model, channel numbers eight and nine in figure 8 represent the outer divertor leg peak. Channel number eleven shows the inner divertor leg peak as seen from the upper viewing array. Channel number twenty-five shows a view from the lower array of the inner divertor leg radiated power. No other channel numbers give much, if any, radiated power values.

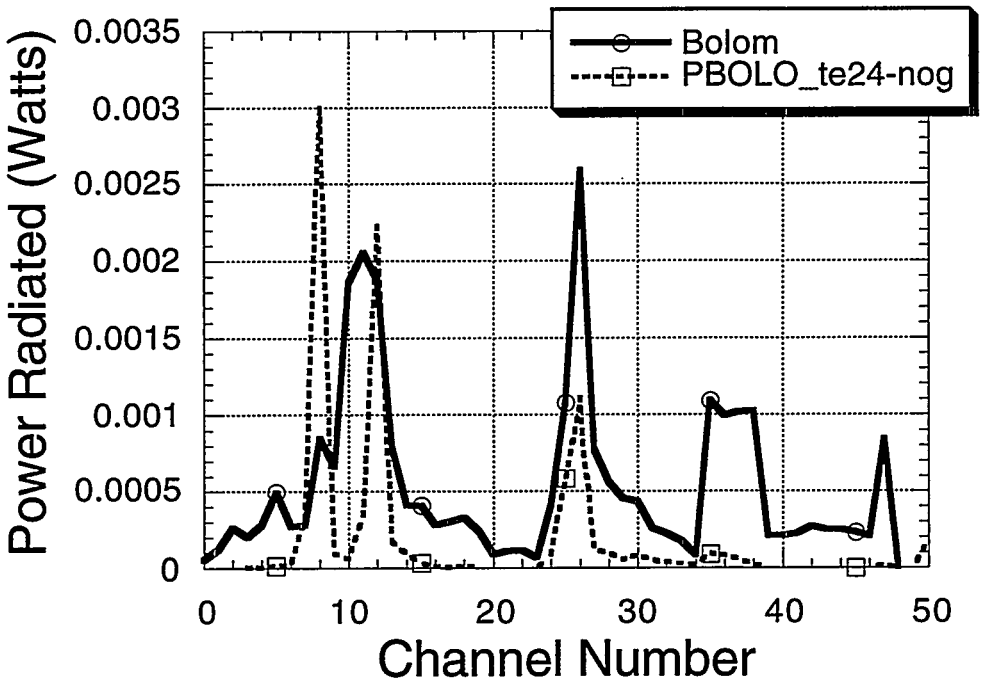

Figure 8: A plot comparison of Shot 82151 at 2005 ms and a UEDGE simulation assuming a constant concentration of impurities.

Impurity Transport

The final impurity model used in UEDGE takes into account all forces, especially plasma flows and temperature gradients, to determine the impurity density. Figure 9 shows a comparison between the data and the simulation. The radiated power peaks at the inner and outer strike points from the upper array in channel numbers eight and nine for the outer divertor leg and channel number eleven for the inner divertor leg. The inner strike point from the lower array shows a peak at channel number twenty-five. Some power is picked up from the inner wall around channel numbers thirty-five and thirty-six. Between the divertor leg peaks, some additional power signals are picked up similar to the actual data. This impurity model gives us the best fit to the actual bolometer data.

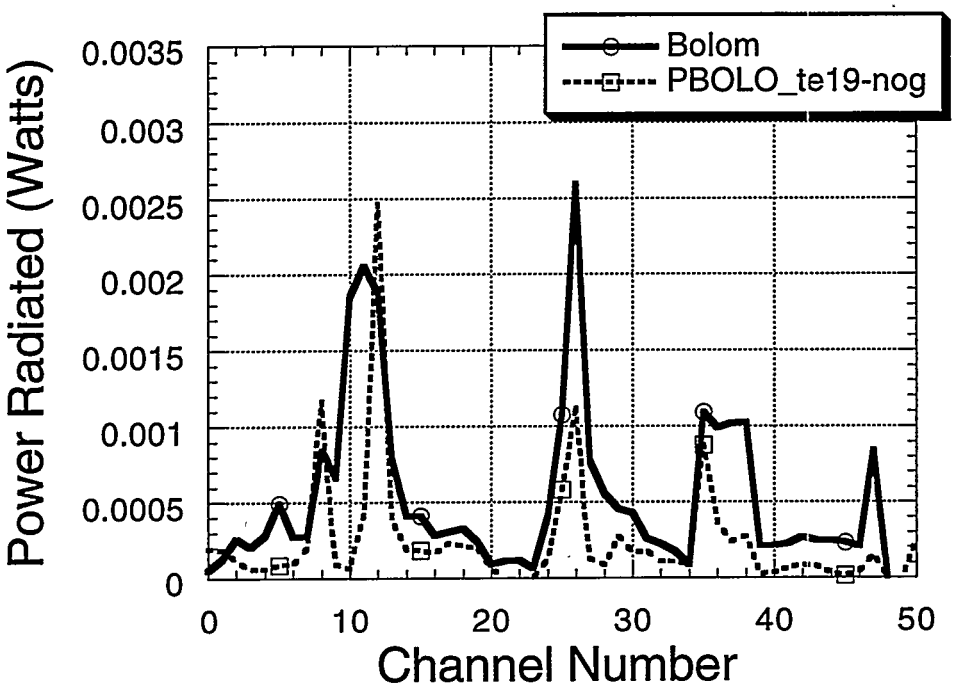

Figure 9: A comparison plot of Shot 82151 at 2005 ms with a UEDGE simulation with a fractional concentration of impurities.

Conclusion From Comparisons

My research has been completed by developing the bolometer post processor. This post processor can now be used as a tool for comparing data from UEDGE simulations against DIII-D bolometer data. Previously, no ways existed to compare the simulations against actual bolometer data. Now corrections can be made to UEDGE plasma simulations to help improve the models used.

Impurity Model Needed

The no impurity model with only hydrogen radiation shows large differences from the actual DIII-D data. The existing peaks come about only from the divertor floor inner and outer strike points. No other similarities in the data exist. This model does

not adequately reproduce the actual data. This comparison justifies that some impurity model is needed for UEDGE plasma simulations.

Carbon Impurity Introductions

In the constant concentration model, the impurities lie in the region of highest density, which is near the plates in the divertor region. As a result, we see in figure 8 the large inner and outer strike point peaks. This constant concentration model appears to be poor because of the way impurities are introduced into the simulation, as a fraction of the electron density.

Physics of Carbon Migration

The introduction of Carbon uniformly around the outer SOL, with the transport model, appears to be a better model, since the physics of Carbon migration pulls the Carbon down to the divertor floor. It is assumed that 90% of the Carbon is then recycled, and a build up of Carbon begins to occur at the divertor floor. The transport model then spreads this Carbon throughout the divertor legs where it radiates. This cools the plasma, reducing the hydrogenic radiation so that the sum near the strike points still matches the measured power for the chords. With a lower density of Carbon at the divertor floor, we get better matches to the bolometer data at the inner and outer strike points than in the constant concentration model.

Before any other conclusions are made, we are increasing the resolution of the grid on which the line integrals of the UEDGE power are calculated, to see if this affects the results. This and further analysis will be reported at a future date.

Summary

My bolometer post processor obtains volumetric radiated power values calculated by UEDGE, and converts them into line integrated radiated power along bolometer lines of sight. From this data, plots are made of the bolometer channel number versus the radiated power along the bolometer lines of sight. These simulated values are compared to actual DIII-D bolometer data. This post processor can now be used for bench marking the physics models used in UEDGE plasma simulations. The first use of the bolometer post processor was to validate the average ion impurity model used in UEDGE. Three power radiation examples were examined to determine the impurity model's accuracy. It is not important, at this stage, that the graphs lie on top of each other, but the curves should at least have the same form. The preliminary conclusion from this comparison is that the impurity transport model gives the best match to the data, and both the no impurity, hydrogenic radiation only, and uniform concentration models give substantially poorer agreement with the data. This bolometer post processor will be used in the future to determine the accuracy of other UEDGE models.

Acknowledgments

This work was performed under the auspices of the U.S. Department of Energy by Lawrence Livermore National Laboratory under contract number W-7405-ENG-48, also by General Atomics under contract number DE-AC03-89ER51114. I would like to thank my two mentors Max Fenstermacher and Gary Porter for all their help and understanding during my research. I wish to thank Bill Meyer and Gary Porter for performing computer calculations with their codes so analysis could be done. I would like to thank Tom Casper, Ray Jong, and Mike Brown for their computer support, Ron Ellis for the graphics pictures, Charlie Lasnier for his help during my stay at General Atomics, Tony Leonard for his help in describing bolometer design and function, and Marv Rensink and Thomas Rognlien for their valuable suggestions.

Reference List

Dubois, P. F., Motteler, Z. C., Willmann, P. A., et al. The Basis System. U.S. Department of Energy: Regents of the University of California, March 26, 1990. 2-15.

IDL Reference Guide. Version 3.5. Research Systems, Inc., Boulder, CO. November 1993.

Leonard, A. W., Meyer, W. H., Geer, B., Behne, D. M., Hill, D. N. 2-D Tomography with Bolometry in DIII-D. General Atomics, July 1994. This is a preprint of a paper to be presented at the Tenth Topical Conference on High Temperature Plasma Diagnostics, May 8-12, 1994. Rochester, New York and to be printed in *Review of Scientific Instruments.*. Work supported by: U.S. Department of Energy under contract Nos. DE-AC03-89ER51114 and W-7405-ENG-48. General Atomics Project 3466.

Mahdavi, M. A., et al. Divertor Heat and Particle Control Experiments on the DIII-D Tokamak. General Atomics, July 1994. This is a preprint of a paper to be presented at the Eleventh International Conference on Plasma Surface Interactions in Controlled Fusion Devices, May 23-27, 1994, Ibaraki-ken, Japan, and to be printed in the *Proceedings.* Work supported by: U.S. Department of Energy under contract Nos. DE-AC03-89ER51114, W-7405-ENG-48, DE-AC05-84OR21400, DE-AC03-76DP00789, and Grant No. DE-FG03-89ER51121. General Atomics Project 3466.

Preckshot, G. G., Butner, D. N., Brown, M. D., Meyer, W. H. Transpaerent Data Access in a Multi-vendor, Distributed Data Acquisition and Data Processing System. 7th Top. Conference High Temperature Plasma Diagnostics, Napa, CA, March 13-17, 1988.

Serway, Raymond A. Modern Physics Supplement to Accompany Physics for Scientists and Engineers. 3rd ed. Philadelphia, Fort Worth, Chicago, San Francisco, Montreal, Toronto, London, Sydney, Tokyo: Saunders Golden Sunburst Series, Saunders College Publishing, 1990. 1394-1400.

UEDGE Manual. The Regents of the University of California, 1994. This work was produced at the University of California, Lawrence Livermore National Laboratory (UC LLNL) under contract no. W-7405-ENG-48 (Contract 48) between the U.S. Department of Energy (DOE) and The Regents of the University of California (University) for the operation of UC LLNL. Copyright is reserved to the University for purposes of controlled dissemination, commercialization through formal licensing, or other disposition under terms of Contract 48; DOE policies, regulations and orders; and U.S. statutes. The rights of the Federal Government are reserved under Contract 48 subject to the restrictions agreed upon by the DOE and University as allowed under DOE Acquisition Letter 88-1.

Wesson, John. Tokamaks. eds. A. Acrivos, F. W. Crawford, L. C. Woods, J. M. Brady, A. L. Cullen, C. P. Wroth. New York: Oxford University Press, 1987.

The Design and Implementation of the LLNL Gigabit Testbed

Daniel Garcia

working under the SERS program
at
Lawrence Livermore National Laboratories

under the direction of

Tim Voss and John Wade

Abstract:

This paper will look at the design and implementation of the LLNL Gigabit testbed (LGTB). The paper will discuss the philosophy behind the design of and the need for the testbed, the tests that are performed in the testbed, and the tools used to implement those tests.

I Introduction

For years now, computers have been networked together via a number of technologies. These technologies were more than enough to provide the services that were asked of them, namely, file sharing, text distribution, be it usenet news or email, and file transfer. Networks were usually small, or, even if they were large, had low enough workloads, that technologies such as ethernet were able to handle the loads.

In recent years, however, new uses for networking have come up that demand much higher performance. Services such as Video on demand, live video teleconfrencing, transfer of large files, and other such, high bandwidth applications, are now becoming more commonplace. With the rise of such demands, new networking technologies are needed to fill in the gaps that older technologies such as ethernet couldn't hope to fill.

In recent years, the new buzzword in networking has been 'gigabaud' networking. Running at rates reaching almost 100-200 times faster than current ethernet networks, these new protocols: ATM, Fibre Channel, HIPPI, and others, promise to supply the necessary bandwidth and performance for both the old uses of networking, as well as the new ones.

These protocols are still developing for the most part. As companies build products to the current specification, and try them out, new ideas are generated, and old ones are thrown out and or reworked. Up till now, for a number of these protocols, notably ATM and Fibre Channel companies have only cooperated on paper, i.e. in the specification, and then have gone off to develop their products.

However, there's another buzzword in modern networking, and that is interoprability, the idea that multiple pieces of equipment from vastly different vendors are able to communicate to per-

form certain types of task, be it email, database processing, etc... So, in order to be able to compete in today's environment, vendors need to be able to show that their products will work with products from other companies.

This is where the LLNL Gigabit testbed comes into play. The LLNL Gigabit testbed is intended to be a neutral testing site, where various high speed networking products, currently Fibre Channel based, can be tested in one, heterogeneous environment. The LGTB will test network adapters, devices, switches, and visualization systems for their functionality, performance, and robustness. It will then put together reports that will be returned to the vendors, and/or made available via the World Wide Web (WWW) for all interested readers.

II The LLNL Gigabit Testbed

The LGTB is a collaborative effort, under a CRADA (Co-operative Research and Development Agreement) between LLNL and a number of Fibre Channel vendors. The CRADA involves gathering together various pieces of equipment from these vendors and running them through tests to determine various aspects of their performance and interoprability.

The LGTB identified four distinct areas that it would be testing. The first are would be network interface cards. These are what give computers their connection to the network. Tests of networking cards would stress normal networking tasks, such as data transfer or interactive session. The second area the testbed will test is somewhat related to network interface cards, network switches. Switches are used in a Fibre Channel network (see appendix A, Fibre Channel) to connect other forms of interfaces, such as network interface cards, i/o devices, other switches. A number of the tests that we would use on networking cards we can move over to help with the testing of switches.

The third area the LGTB will be testing is the realm of devices. One of the features of Fibre Channel is in addition to providing normal network services, it can also act as an I/O bus for devices such as hard disk arrays, or various forms of output devices. The big focus of testing in this area will be the implementation of SCSI over Fibre Channel to control high speed disk arrays.

The fourth, and final area of LGTB testing will be visualization devices. Fibre Channel's bandwidth makes it an excellent choice for carrying high volumes of real-time video data, and there are plans in the works by a number of vendors to build video systems that pull data right off of Fibre Channel.

In each of these areas of testing, the LGTB will be grouping tests under 3 classifications. The first classification of test is the Functionality test. The functionality test does what it sounds like, testing the functionality of the item(s) being tested - basically, does it work in a minimum fashion. The second classification of testing is performance, or how well it performs. Obviously, devices which attain a higher throughput on a test will be 'scored' higher than devices that get low throughput. The final classification of tests is robustness. Under robustness tests, we try to 'break' the devices, by doing things such as sustaining high throughput for long periods of times, rapidly changing connection parameters and seeing how the devices react, etc...

For our first round of testing, we are looking at testing the networking devices. These have been under development for the longest period of time, and a number of vendors have developed Fibre Channel networking products. For these tests, we will be focusing on simple networking tools such as ftp, telnet, rsh, and ping. We decided on these test because they are very common tools used, and it would be easy to write simple test cases around. Plus, these tests will scale well to larger loads, i.e. spamming with pings, ftp of large files, multiple telnets, sending lots of

data with telnet in character mode, etc...

We made a conscious decision to avoid testing of low level protocols (like TCP/IP using something like netperf) for now for a number of reasons. The main reason was because the purpose of the testbed is to show interoprability between vendors, and when that isn't there, assist the vendors in tracking down the problems. So, for testing interoprability, we decided to go with tests that would flex the everyday tasks that people perform with their machines and networks.

In addition to these networking tasks that we will be testing, we will also be running what we call 'power-cycle' tests. A discovery was made at a trade show some time ago that if you had multiple machines on a network, and power-cycled (i.e. turned off then back on) one of the machines, it would effectively bring down the network. Since then, that test has become a part of the LGTB suite. This example brings up another way that tests will be incorporated into the suite. The basic tests that we will be doing come out of what we thought would be 'worthy' to test. However, as time goes on, and other potential problem areas are found, we will add tests to look for those problems in the future, to prevent a device from regressing, or to help find a similar problem in other hardware.

Finally, the LGTB has created a 'Testbed Control Interface' (TCI) - a GUI front end for setting up and running tests. This will provide a central control point for the entire testbed, and will allow new tests to be added easily.

After running these tests, a report is generated that will be sent back to the vendors. This report contains information about the test that was run, revision levels of the various pieces involved, information on the test hosts involved, information on the topology of the test (i.e. host-host, host-switch-host, etc...), information on the run of the test, and finally, a summary giving a concise description of the result of the test (passed, failed, good, better, best). A sample report file

is included in appendix F.

III Design of the LLNL Gigabit Testbed

My project for this past semester involved implementing this first round of tests for the testbed, as well as writing the TCI. We decided that it would be best to have a central 'control' system, from which we would configure and run tests on other machines in the testbed. We referred to this machine as the c3 machine (after c3 modules, command, control, & communication, used in the military). The ideal setup would be one where we could bring machines in from a vendor, set them up quickly, run the tests, and return the results to the vendor as quickly as possible. In addition - we wanted to have a system that would package easily and be sent out to vendors to allow them to do their own runs of our tests.

Once we had decided on some form of central control, we then started looking at a number of ways of providing this control. The first method that I looked at, in retrospect a bad idea, involved using PVM (Parallel Virtual Machine) for handling the distribution of test control. We quickly threw out this idea for a number of reasons, including the high overhead of PVM, the fact that it would require high amount of setup and configuration time to install on new machines. In addition, the large size of the PVM system would have made it difficult to distribute the testbed system out to vendors.

The next idea was based on using Tcl (Tool Command Language, pronounced tickle, see appendix B - Tcl), and a distributed processing package for it called Tcl-DP. The idea would be that we would write clients to run on all the machines in the testbed, and use Tcl-DP to distribute information and commands to these clients. However, for a number of reasons not unlike the ones with PVM, we decided this would be a bad idea.

The third idea we worked on, and the first one that we actually implemented tests in used another Tcl extension called expect. Expect is a nifty little extension, that allows us to build expect/response scripts. I.e. we tell the system what we expect to see, and what kind of response to take based on it. See appendix C - The Expect extension for more information on expect The first implementation of the test bed using this system (written over the summer by myself) involved having a tcl/expect client running on both the c3 machine, as well as the test hosts, and involved sending scripts over to the test hosts, and then using expect to run those scripts.

After working with this setup though, it became clear that we would still have some of the problems of PVM and the first Tcl idea, namely, that having to install the Tcl/expect toolkits, as well as our interpreter for them on the client machines made for a much higher setup time than we would have liked.

The final setup - and the one that is in the current implementation of the testbed, was to once again use Tcl/Expect - but this time, only use them on the c3 machine. We would then use expect to manage telnet connections to the test hosts, and it would act like a user, running commands, noting output and such.

This method had a number of advantages. The biggest one is it required only that the Tcl and expect toolkits be installed on and configured for the c3 machine. The only configuration work that needed to be done on the test hosts was setting up a couple of test accounts, and if necessary, installing and configuring the networking cards. Another advantage was that writing a test case would basically consist of figuring out how one would do it if they were going to run the test by hand, thereby greatly speeding up the development cycle for new tests.

One final piece was added to make the testbed into it's current system. It was an extension to Tcl called [incr Tcl], or, the Tcl equivalent of C++. I was able to make use of the modularity

ideas put forth in [incr Tcl] (or itcl) in the final design of the testbed system. Namely, I made use of the object facilities of itcl to facilitate handling of individual test hosts. See appendix D - itcl for more information on [incr Tcl].

IV Implementation of LGTB

The LGTB tests have at their core, a set of itcl classes that I call the Testbed Control System. The TCS provides the basic functionality for handling connections to a test host, running commands on such a host, getting information back from said host, as well as commands for manipulating report files, and finally, for doing logging of test progress.

The TCS centers on an itcl class, called hostClass. A brief definition of hostClass is given here (note: default values and actual method implementations are left out);

```
itcl_class hostClass {
 # Variable
 common hostList
 public ether_hostname
 public ether_ipaddr
 public fc_hostname
 public fc_ipaddr
 public config_file
 public acct_name
 public acct_passwd
 public sys_type
 protected host_id
 protected host_pid

 # methods/procs
 proc getHosts
 method set {var_name}
 method config
```

```
    method open
    method close
    method put {filename {remote NULL}}
    method get {filename {local NULL}}
    method exec {command}
}
```

The idea for this class is that one instance of this class would represent a single host. The variables in the class definition provide information about the host. For example, ether_hostname and ether_ipaddr contain the ethernet hostname and ip address for that host. Likewise, the fc_hostname and fc_ipaddr contain the fibre channel hostname and ip address.

The methods are used to control a host. Open and close are used to open and close the connection to the remote host (this actually involves logging in/logging out of the host - the acct_name and acct_passwd fields are used to allow logging in). Put and get are used to place and retrieve files to/from the test host. Finally, exec is used to execute the given command on the host.

In addition to the hostClass, there is another class in the TCS called reportClass. reportClass basically supplies an interface for handling report file generation. I won't elaborate on it's layout here, but basically, it provides functions for creating a title block, printing up host information, and test topology.

The next piece to the TCS system is a configuration file, currently called hosts.tcl. This file contains itcl code to initialize objects for each host in the testbed. Obviously, this file needs to be updated when new hosts are added to the system, however, this provides a central location from which we can get information about all the hosts in the system. (Note: the Testbed Control Interface, described below, currently provides a graphical interface for viewing info in this file, and will eventually allow for adding/deleting/editing host entries).

The final pieces in the TCS system are the actual tests themselves. Each test is typically a stand-alone Tcl file, containing a function named run_test, some initialization code, and any other support functions that the test write deems necessary. The basic form of a test is:

open connection to host(s) involved in test

transfer any temp files needed for test

issue commands to run test

retrieve output files from test run

place output into report file

V The Testbed Control Interface

The Testbed Control Interface is a GUI front end for the TCS written using yet another extension to Tcl called Tk (more info in appendix E). The front end currently consists of five separate windows. The first window, simply contains a title bar/graphics, and two buttons one to quit the TCI, and the other to run the test in the current configuration. The rest of the windows are (or will) be used to set up the configuration for a test run.

Then, there is a window for selecting a test to run. There is a set of radio buttons along the left side of the window, from which you can select a test. When you select one, a series of fields show up on the right hand side of the window, allowing you to edit the arguments that will be passed to the run of the test.

The next window is the report window. In this window, you can do things like set the destination directory for the test report, as well as the title of the report file. For the report file, you have two options - either a default filename that is constructed based on name, date and a unique ID number - or a user supplied name. In addition to the report window, there is also a

topology window that lets you select the topology of the current testbed setup.

The final window is the host window. It is divided up into two parts. The first part is a list of hosts known to the TCS system. These hosts are picked up in the hosts.tcl file. The user can double click on an item in this list and the information for that host will fill up the other part of the host window. Currently, this is only used for reference information, i.e. to look up information about various hosts. In the future, this window will also allow a user to edit host information, as well as add or remove hosts.

VI The Future of the Testbed - Near and Far

Now that we have this first round of tests implemented and working, we have begun looking at the future of the testbed. Plans for the testbed include increasing the number of tests being run, as well as increasing the scope of existing tests. In addition, we are looking at ways to run multiple tests simultaneously, as well as setting tests up to run repeatedly for long periods of time.

There are also plans to extend the scope of the testbed, namely, starting up tests on i/o devices such as Fibre Channel based drive arrays and such. Currently - we are still in the process of defining just how one goes about testing that.

We are also planning on upgrading the TCI and adding more features to the front end, such as the ability to handle varying arguments of tests, repeating tests, etc...

Finally, in the short term, we are planning on changing our report format to something like HTML - to facilitate using WWW clients (like Mosaic or NetScape) to brouse the reports. In addition to this, we are looking at integrating the GNUPlot plotting package to create graphics illustrating the results of the tests.

In the long term - we hope to get more tests into the testbed, come up with testing plans for

visualization devices and switches, and perhaps start looking into other high speed networking technologies like ATM.

Appendix A - Fibre Channel

What is Fibre Channel? Well - according to the FC-PH Spec, revision 4.1 (page xxxix), Fibre Channel is:

> The Fibre Channel provides a general transport vehicle for Upper Level Protocols (ULPs) such as Intelligent Peripheral Interface (IPI) and Small Computer System Interface (SCSI) command sets, the High-Performance Parallel Interface (HIPPI) data framing, IP (Internet Protocol), IEEE 802.2, and others.

Fibre Channel is a currently evolving standard (ANSI X3T11 committee) describing a high speed network transport for a number of other, higher level protocols. The FC spec is much like, for example, ethernet, in that it defines only what's necessary for sending info over the wire, and covers very lightly, such things as address resolution and such. FC is not designed to be a networking protocol in and of itself (unlike, for example, ATM), rather, FC is designed to be used under another protocol, such as IP (most common usage in networking), SCSI, etc....

Fibre Channel is set to run at bandwidths up to 1 gigabaud, perhaps even 2 if the technology can be pushed. For reference, modern ethernet bandwidth is 10 megabaud, or 0.001 gigabaud.

Fibre Channel is (currently) a point-to-point standard. I.e. there are only two connections on a single fibre, unlike ethernet which can have multiple hosts sharing a single wire.

For more information, Fibre Channel specification documents are available at:

ftp://ftp.network.com/FC

Appendix B - Tool Command Language (Tcl)

Tool Command Language, or Tcl is an extensible scripting language that was developed at Berkeley under the direction of John K. Ousterhout. According to the tcl-faq Tcl is:

> "First, Tcl is a simple textual language, intended primarily for issuing commands to interactive programs ... It has a simple syntax and is also programmable"
>
> "Second, Tcl is a library package that can be embedded in application programs."

Tcl is used in the testbed to provide the framework for the other Tcl based tools that we use (Expect, Tk, and itcl). More information on Tcl is available in the newsgroup comp.lang.tcl, from John Ousterhout's book, Tcl and the Tk Toolkit, and from various sources on the net. A faq about tcl can be retrieved from :

ftp://rtfm.mit.edu/pub/usenet-by-groups/comp.lang.tcl/tcl-faq*

And tcl itself can be retrieved from:

ftp://ftp.aud.alcatel.com:/tcl/ftp.cs.berkeley.edu/

Appendix C - Expect

Expect is one of 3 extensions to Tcl that is used by the TCS. From the Expect man page:

Expect is a program that "talks" to other interactive pro grams according to a script. Following the script, Expect knows what can be expected from a program and what the correct response should be. An interpreted language pro vides branching and high-level control structures to direct the dialogue.

The biggest things that expect adds to the Tcl language, are the ability to spawn off processes to run certain programs, and the powerful expect construct. For example, here is a sample expect script, that does an anonymous ftp session:

```
spawn ftp rtfm.mit.edu

expect {
 { Name*: } { send "ftp\r" }
}

expect {
 { Password*: } { send "myemail@\r" }
}

expect {
 { ftp> } { send "get file\r" }
}

exit
```

The expect construct allows a script writer to set up a series of strings that are 'expected' from the spawned program. The example above is a simple one. There is no reason at all why a single expect command could have a list of multiple strings to wait for. For example, we could

have written the third expect command above as:

```
expect {
 { ftp> } { send "get file\r" }
 { *access denied* } { puts "Drat, we couldn't log in!" }
}
```

More information on expect cat be gotten from the expect man page which comes with the distribution. Expect is available on:

ftp://ftp.aud.alcatel.com:/tcl/extensions

Appendix D - [incr Tcl]

[incr Tcl], or itcl is an object oriented extension to Tcl. From the itcl manpage:

> [incr Tcl] provides object-oriented extensions to Tcl, much as C++ provides object-oriented extensions to C. The emphasis of this work, however, is not to create a whiz bang object-oriented programming environment. Rather, it is to support more structured programming practices in Tcl without changing the flavor of the language. More than anything else, [incr Tcl] provides a means of encapsulat ing related procedures together with their shared data in a local namespace that is hidden from the outside world. It encourages better programming by promoting the object oriented "library" mindset.

For us, the most important item itcl brings to the testbed is the class abstraction. This allows us to group related functions and variables together in an 'object'. This is how the hostClass and reportClass were implemented. An excellent introduction to itcl and how it uses classes is given in the Intro.PS file that comes with the itcl distribution. The distribution can be retrieved from:

ftp://ftp.aud.alcatel.com:/tcl/extensions

Appendix E - Tk

Tk is probably the reason for the widespread success and acceptance of Tcl and friends. Tk provides a very fast, intuitive method of building user interfaces. An extension to Tcl, Tk provides functions for creating various kinds of user interface objects, or widgets, such as buttons, labels, scrollbars, etc...

The appeal and power of Tk lies in it's relative simplicity compared to traditional user interface building. For example, in Tk, to create a label widget, one simply has to do:

```
label .labelOne -text "Hello world!"
pack .labelOne
```

And you have you're label widget. To do something comparable in raw Xlib calls, or even Xt calls would take at least 10 times as many lines of code, if not more.

Also, because Tk, like Tcl is interpreted, it makes for a very fast development cycle, since the tradition holding point of stopping and waiting for a compile has been done away with.

Appendix F - A Sample report file

Below is a sample report file. The first block is the title block, and contains things such as who ran the test, when they ran it, and revision numbers of various portions of the code making up the test. In addition - there will eventually be a description of what the test does included as well.

The next section contains an ASCII representation of the topology for the test. The next two blocks contain information on the machines used, including system stats, OS level, manufacturer, etc...

Finally - the rest of the report contains messages from the test. In this case, all the test returned was a note about what it was doing, and whether it succeeded or not.

```
#Title=============================================================
Test:    Ftp Test
Operator:         Daniel Garcia
Test run at:      Wed Oct 12 18:01:29 PDT 1994
Sequence Number:  25
reportClass:      $Id: reportClass.tcl,v 1.5 1994/10/12 00:11:59 dgar-
cia Exp $
logClass:         $Id: logClass.tcl,v 1.2 1994/07/15 02:22:00 kender
Exp $hostClass:   $Id: tlib.tcl,v 1.7 1994/10/12 00:11:59 dgarcia Exp
$
 ftp.tcl: $Id: ftp.tcl,v 1.3 1994/10/12 00:22:13 dgarcia Exp $

#Topology==========================================================
h-h
#Host info for edward=========================
</lgtb/sysInfo/edwardInfo>
HOSTNAME : edward
OS/OS LEVEL : Unix Whatever
MAIN MEMORY : 160 MB
SWAP SPACE : 76 MB
DISK SPACE : 1458176 Blocks 729088 MB
```

```
/TMP SPACE : 8192 kb total 7776 kb free
#Host info for teller=========================
</lgtb/sysInfo/tellerInfo>
HOSTNAME : teller
OS/OS LEVEL : Unix Whatever
MAIN MEMORY : 320 MB
SWAP SPACE : 36 MB
DISK SPACE : 1458176 Blocks 729088 MB
/TMP SPACE : 8192 kb total 7772 kb free
=============================================================================

Starting ftp test, testFile@edward-fc to teller-fc

testFile transferred succesfully.
=============================================================================
```

Bibliography/References

Expect documentation Don Libes, NIST 1994

Fibre Channel PH Spec Revision 4.1 X3T11 ANSI Committee 1994

Guide to the LLNL Gigabit Testbed Tim Voss 1994

itcl documentation Michael Mclennan, AT&T 1993

Tcl and the Tk Toolkit John Ousterhout 1994 Addison-Weseley

tcl frequently asked questions list Larry W. Virden 1994

In Vitro Synthesis and Purification of PhIP-Deoxyguanosine and PhIP-DNA Oligomer Covalent Complexes

Jenatta Freeman

Alabama A & M University

Lawrence Livermore National Laboratory
Livermore, California 94550

December 14, 1994

Prepared in partial fulfillment of the requirements of the Science and Engineering Research Semester under the direction of Glenn Marsch, Ph.D., Research Mentor, at the Lawrence Livermore National Laboratory.

*This research was supported in part by an appointment to the U. S. Department of Energy Science and Engineering Research Semester (hereinafter called SERS) program administered by LLNL under Contract W-7405-Eng-48 with Lawrence Livermore National Laboratory.

ABSTRACT

2-Amino-1-methyl-6-phenylimidazo[4,5-*b*]pyridine (PhIP) is a heterocyclic amine compound formed when meats are cooked at high temperatures. PhIP damages DNA by forming covalent complexes with DNA guanine bases and is moderately mutagenic. Thus, PhIP is a suspected human carcinogen. In an effort to understand how the binding of PhIP to DNA may cause cancer, it is important to characterize the structures of PhIP-damaged DNA molecules. Our HPLC data support fluorescence and ^{32}P Post-labeling studies which indicate the formation of several species of 2'deoxyguanosine-(dG) or oligodeoxynucleotide-PhIP adducts. The reaction of PhIP with dG resulted in a reddish precipitate that was likely the major adduct, *N*-(deoxyguanosin-8-yl)-PhIP (dG-C8-PhIP) adduct, with a more polar adduct fraction remaining in the supernatant. Reversed-phase HPLC analysis of the adducts in the supernatant revealed the existence of species of much shorter retention times than the dG-C8-PhIP adduct, confirming that these species are more polar than dG-C8-PhIP. At least four adducts were formed in the reaction of PhIP with DNA oligomer. HPLC analysis of the PhIP-DNA oligomer supernatant after butanol extractions revealed four unresolved peaks which spectra had maximum wavelengths between 340 and 360 nm. Though adduct peaks were not completely resolved, there was ~3 minutes interval between the DNA oligomer peak and the adduct peaks. Furthermore, fluorescence emission data of the DNA oligomer-PhIP adduct solution show heterogeneous binding. The more polar PhIP adducts were fraction-collected and their structures will be solved by nuclear magnetic resonance or x-ray crystallography.

INTRODUCTION

PhIP belongs to the amino-imidazoazaarene (AIAs) class and has been isolated mostly from meat foods cooked at high temperatures, e.g. fried beef and pork.[1] Most AIA mutagens identified so far cause mutations in the Ames/Samonella assay and their occurrence may be correlated with the incidence of certain human cancers. PhIP is a natural product of the cooking process which forms at normal household cooking temperature from the condensation of creatine and amino acids in muscle meats. PhIP represents over 70% of the heterocyclic amine carcinogens isolated from foods.[2] This compound is not direct-acting, but is activated *in vivo* to highly reactive intermediates[3] that damage DNA in bacterial and eukaryotic cells. PhIP is moderately mutagenic in *Salmonella typhimurium*[1] and carcinogenic in rodents[4]. Therefore it is a potential human carcinogen,[4] and it is imperative to determine the mechanism of DNA damage by PhIP.

The formation of adducts *in vivo* are considered indicators of carcinogen exposure.[5] The ^{32}P-postlabeling assay, a highly sensitive method for detecting adducts, indicated the formation of PhIP adducts in cynomolgus monkeys fed

PhIP. *In vitro and in vivo* studies using ^{32}P-postlabeling revealed the formation of up to three principal PhIP adducts.[6]

PhIP adducts are formed primarily at the C-8 atom of guanine. One of the major positions where most aromatic amines form DNA adducts. [7] Other food mutagens, such as 2-amino-3-methylimidazo-[4,5-f]quinoline (IQ) and 2-amino-3.8-dimethylimidazo[4,5-f]quinoxaline (MeIQx), formed major adducts at the guanine C-8 and N^2 positions.[8] Furthermore we are interested in determining if other adducts are formed when PhIP covalently binds to 2'dG or oligodeoxynucleotide.

Synthesis and purification of PhIP adducts is the rate-limiting step in the characterization of these compounds. Thus my research involved synthesizing and purifying PhIP covalently bound to deoxyguanosine and DNA oligomer in order to later characterize their structure.

EXPERIMENTAL PROCEDURES

Chemicals

Caution: The heterocyclic aromatic amine PhIP and its derivatives are carcinogenic in rodents and should be handled carefully according to appropriate Environmental Safety and Health protocols. N-hydroxy PhIP (N-OH PhIP) was purchased from SRI International (Menlo Park, CA). The single stranded DNA oligomer, 5'd[(CCTACGCATCC)3'], was synthesized at Lawrence Livermore National Laboratory (Livermore, CA). The 2'deoxyguanosine was purchased from Sigma Chemical Co. (St. Louis, MO).

Activation of N-acetoxy-PhIP

N-OH-PhIP (4.2 mg/ml) suspended in dimethylformamide was derivatized to N-acetoxy-PhIP using a 41.5X molar excess of acetic acid and a 51X molar excess of acetic anhydride. The reaction sample was degassed with nitrogen gas at periodic intervals, kept on ice and stirred during the complete reaction. After this reaction was complete, the adduction reaction immediately followed.

PhIP adduction reaction

The DNA oligomer, 5'd[(CCTACGCATCC)3'], was suspended in citrate buffer, pH 5.0 (10mM citrate, 100mM NaCl, 1mM EDTA) in 5mg/ml aliquots. DNA was reacted with N-acetoxy PhIP in ratio of 2 PhIP/single strand oligomer. The acelylated PhIP solution was added dropwise over 5 minutes. The sample was degassed occasionally and stirred constantly. The reaction continued for 10 minutes after all the N-acetoxy PhIP was added. We noted the formation of red precipitate.

Because the DNA oligomer is highly charged, the oligodeoxynucleotide adduct remained in solution. N-hydroxy-PhIP hydrolysis product was extracted from the supernatant with butanol. The adducts remained in the aqueous phase.

In the PhIP adduction reaction using 2'-deoxyguanosine, polar adducts remained in the supernatant and were extracted with butanol. However most of the major adduct, the dG-C8-PhIP adduct, precipitated out of solution. The

pellet was redissolved in methanol and the hydrophobic adduct was extracted. The red precipitate formed was a bis-azo-PhIP by-product and was discarded. After the reaction ended, the sample was kept in the dark and at -80^{O}C, since it is extremely photo- and heat-labile.

HPLC separation of PhIP-dG adducts

PhIP-dG adducts were purified using a reverse-phase semipreparative C18 phenyl column with a flow rate of 3.2ml/min. Buffer A was 50mM ammonium formate (pH 3.8) and buffer B was acetonitrile. These solvents were continually degassed with nitrogen. Buffer B was increased from 0 to 30%B in 30 minutes, was then maintained at 30%B for 30 additional minutes, and was increased to 100% over an additional 10 minutes. The average injection volume was 250uL. The pellet in methanol was collected using the same conditions except the pH for Buffer A was adjusted to 4.0. The runs were detected at 340, 350 and 360 nm.

HPLC separation of PhIP-DNA oligomer adducts

PhIP-DNA oligomer adducts were separated using a reverse-phase semi preparative polystrene column with a flow rate of 2.5ml/min.. Buffer A was 10mM potassium phosphate (pH 7.0) and buffer B was acetonitrile. Buffer B was increased from 0 to 15% in 15 minutes, then held isocratically at 15% for 20 minutes, then was increased from 20 to 100%B in 5 minutes. The runs were monitored at 340, 350 and 360 nm.

RESULTS

There are two methods which can be used to synthesize PhIP adducts (Fig. 1). Direct adduction of N-hydroxy-PhIP to dG results in lower yield, therefore aceytlation of N-hydroxy PhIP with acetic acid and acetic anhydride produces larger amount of adducts. Nonetheless, the major adduct produced is the dG-C8-PhIP covalent complex.

HPLC purification of the methanol extracted sample (Fig. 2) of the PhIP-dG reaction resulted in mainly one major adduct eluting off the column ~ 48 minutes. The on-line absorbance spectrum (Fig. 3) shows that this adduct has a wavelength maximum and shape characteristic of the major dG-C8-PhIP adduct, which has been studied extensively. The dG-C8-PhIP adduct has a maximum wavelength of 365nm.

In the HPLC separation of the butanol phase of the reaction mixture (Fig. 4), several peaks eluted off the column. Peak 1, the largest and most resolved peak, had a retention time of ~48 minutes when an analytical column was used. In Figure 4, the absorbance spectrum for this peak correlates with the spectrum of the dissolved pellet in methanol. Although the dG-C8-PhIP adduct is relatively hydrophobic and most of it precipitates out in the reaction, it is somewhat polar and a portion remains in the aqueous phase. The other eluates

with shorter retention times eluted off the column at ~33, 34, 38 minutes. These earlier retention times indicated that these species are more polar. The absorbance spectra (Fig. 3) reveal that peak 1 has a wavelength maximum in the 340 nm range and Peak 2 and 3 in the 350 range.

UV/Vis absorbance data (Fig. 5) from the crude reaction mixture revealed that adducts with a maximum wavelength of ~ 346nm were formed. The HPLC profile of the sample monitored at 340 and 365 nm (Fig. 6) revealed four unresolved peaks which have retention times between 14 and 18 minutes. Because of the low resolution of the peaks, the real-time absorbance spectra (Fig. 7) show shoulders and tailing. We analyzed this sample by fluorescence spectroscopy (Fig. 8) to determine how many components were in the mixture. The sample was excited at 340, 350 and 380 nm, emission spectra identified the formation of at least four adducts also.

CONCLUSION

We have succeeded to synthesize and purify large quantities of PhIP adducts to oligodeoxynucleoties and 2'deoxyguanosine. The ^{32}P-Postlabeling and fluorescence spectroscopy data support HPLC results that binding of PhIP to dG and DNA oligomer was heterogeneous. Since we have developed an efficient HPLC-based separation protocol, we will continue purification of these adducts. The major future project involves generating a high-resolution structure of one of the polar PhIP adducts by either nuclear magnetic resonance or x-ray crystallography.

ACKNOWLEDGEMENTS

Special thanks to the Molecular Toxicology group of the Biology and Biotechnology Research Program of the Lawrence Livermore National Laboratory, especially Glenn Marsch, Esther Fultz and Ken Turtletaub.

REFERENCES

1. Felton, J. S., Knize, M. G. (1990) Heterocyclic-amine mutagens/carcinogens in foods, *Handbook of Experimental Pharmacology.* **94**, 471-502.

2. Turtletaub, K. W., Knize, M.G. ,et. al. (1989) The metabolic disposition of 2-amino-1-methyl-6-phenylimidazo [4,5-*b*] pyridine in the induced mouse. *Fd. Chem. Toxic.*, **27**, 667-673.

3. Turtletaub, K. W., Knize, M.G., et al. (1990). Metabolism of 2-amino-1-methyl-6-phenylimidazo [4,5-*b*] pyridine (PhIP) by liver microsomes and isolated rabbit cytochrome P450 isozymes. *Carcinogenesis*, **11**, 941-946.

4. Ito, N., Hasegawa, R., Sano, M., Tamano, S., et. al. (1991). A new colon and mammary carcinogen in cooked food, 2-amino-1-methyl-6-phenylimidazo

[4,5-*b*] pyridine (PhIP). *Carcinogenesis*, **12**, 1503-1506.

5. Huang, G., and Krugh, T.R. (1990). Large scale purification of synthetic oligonucleotides and carcinogen-modified oligodeoxynucleotides on a reverse-phase polystrene (PRP-1) column. *Analytical Chemistry*, **190**, 21-25.

6. Snyderwine, E. G., Davis, C.D., et. al.(1993) ^{32}P-postlabeling analysis of IQ, MeIQx, and PhIP adducts formed *in vitro* in DNA and polynucleotides and found *in vivo* in hepatic DNA from IQ-, MeIQx-, and PhIP-treated monkeys. *Carcinogenesis*, **14**, 1389-1395.

7. Turesky, R.J., Rossi, S.C., Welti, D.H., et. al.(1992). Characterization of DNA adducts formed in vitro by reaction of N-hydroxy-2-amino-3-methylimidazo [4,5-*f*] quinoline and N-hydroxy-2-amino-3,8-dimethylimidazo [4,5-f] quinoxaline at the C-8 and N^2 atoms of guanine. *Chem. Res. Toxicol.*, **5**, 479-490.

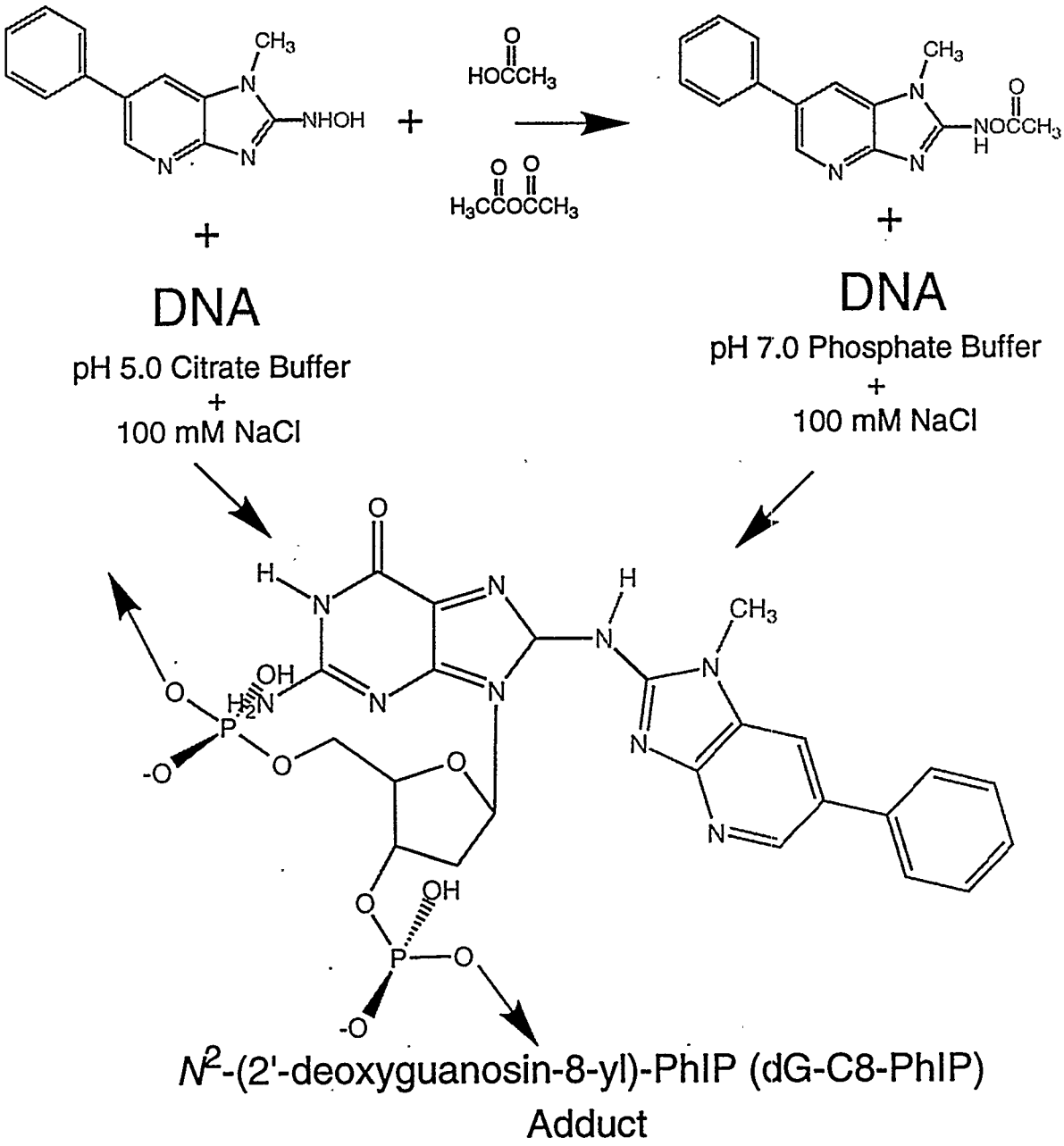

Figure 1. Two methods can be used to synthesize PhIP-dG adducts. Aceylation of N-hydroxy-PhIP results in a higher yield of adducts, the primary adduct formed being the dG-C8-PhIP covalent complex.

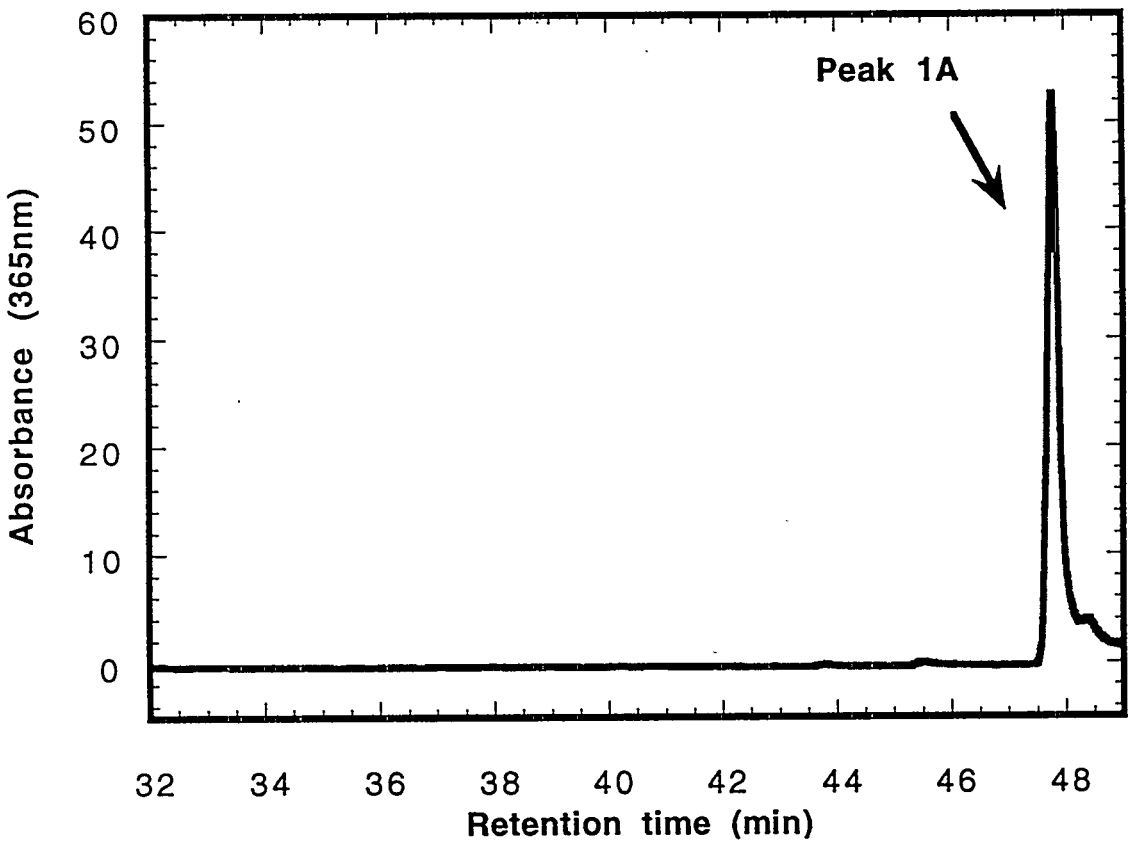

Figure 2. This HPLC chromatogram of the dG-PhIP pellet in methanol show mainly one peak which is the dG-C8-PhIP adduct.

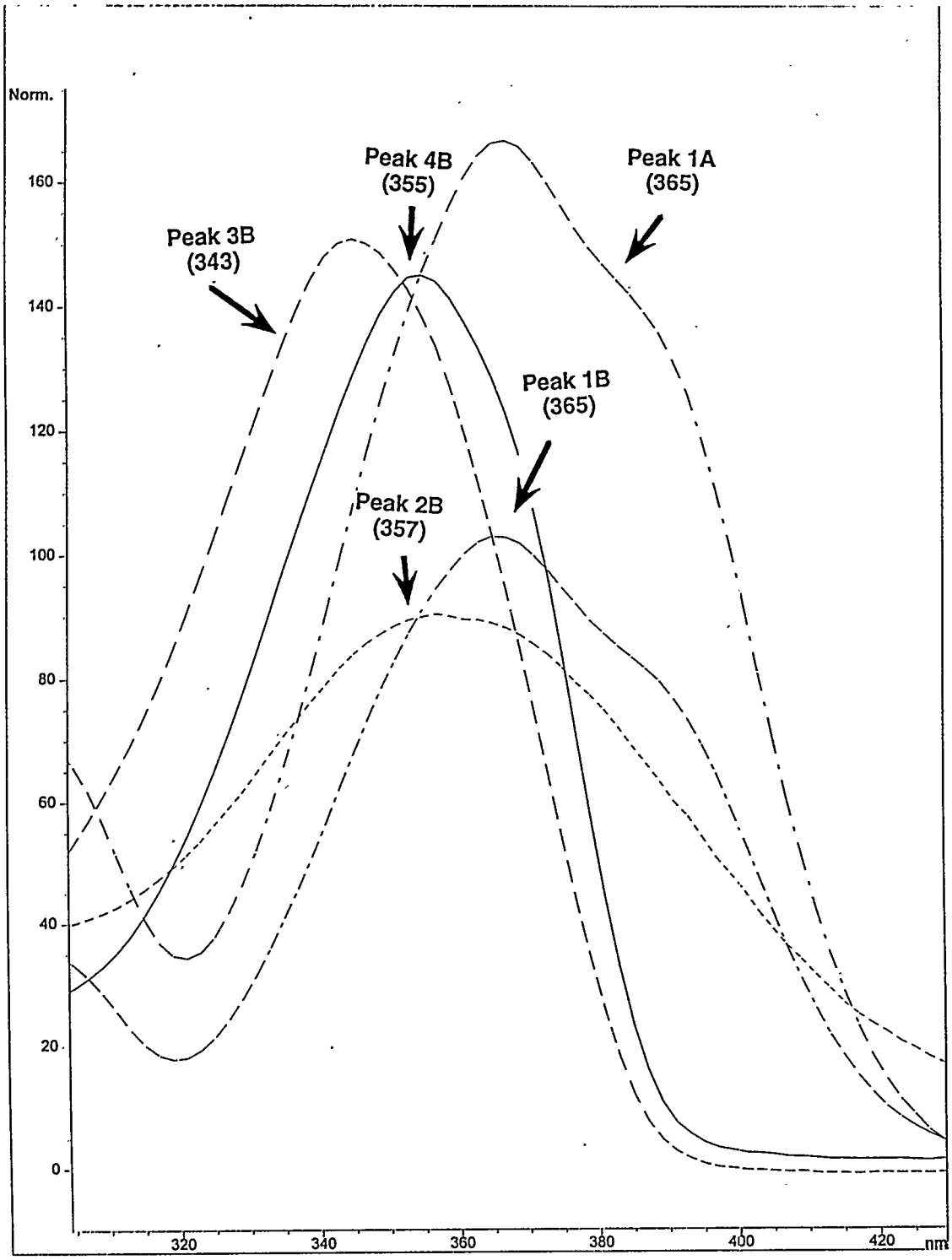

Figure 3. On-line absorbance spectra of the dG adducts from both the pellet and supernatant samples. Both Peaks 1A and 1B have a maximum wavelength of365 nm. The ~ 3-minute difference in retention times of 1A and 1B peaks is due to an analytical column being used in the initial analysis of the methanol-suspended pellet instead of the semi-prep column.

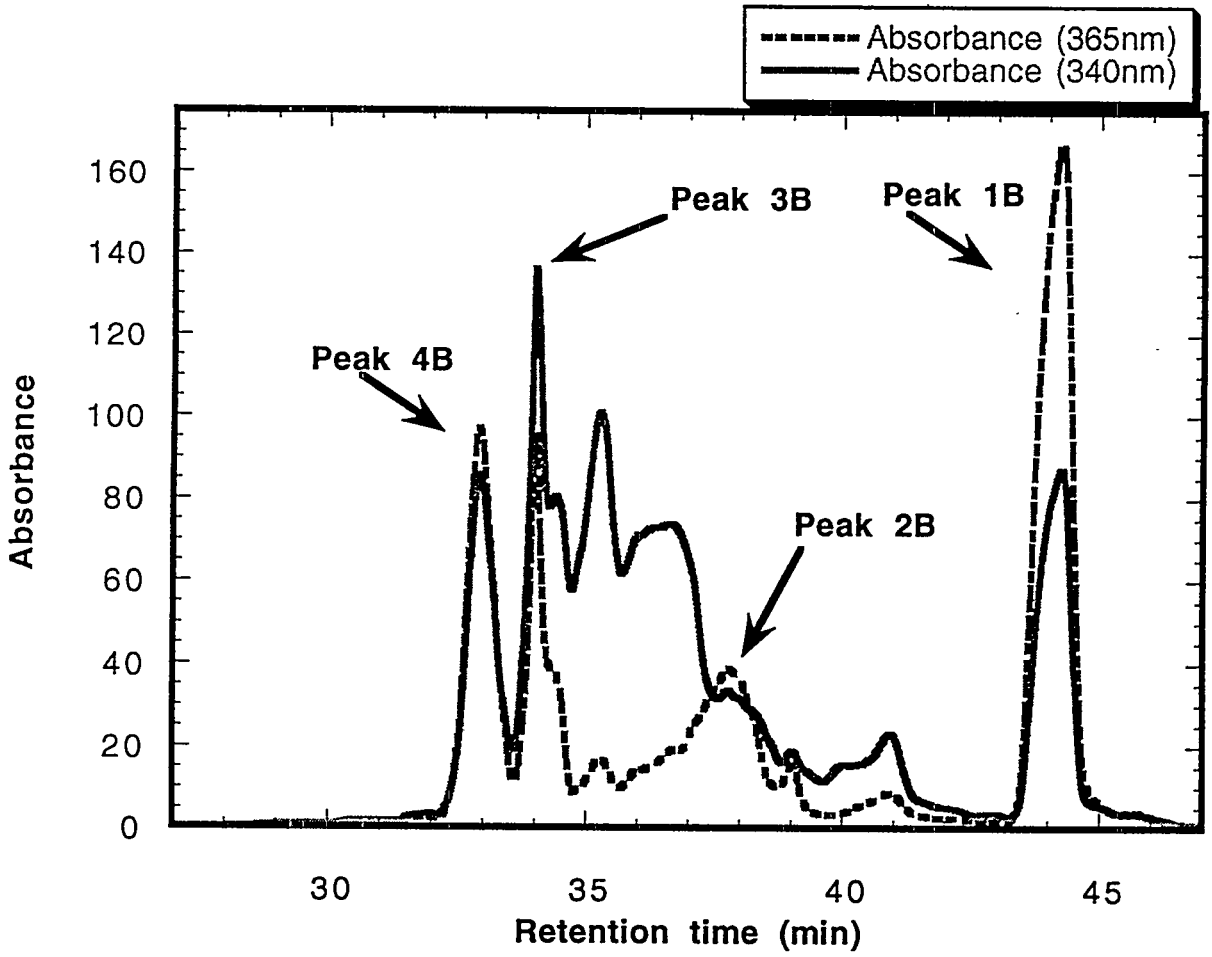

Figure 4. HPLC profile of the butanol-extracted adducts in the supernatant. The retention time and absorbance spectrum of Peak 1B correlates with Peak 1A, it is somewhat hydrophobic and the most of it precipitates out of solution. Peaks 2B, 3B, and 4B have retention times in the 30 minute range, which indicated that they are more polar than the C8 adduct.

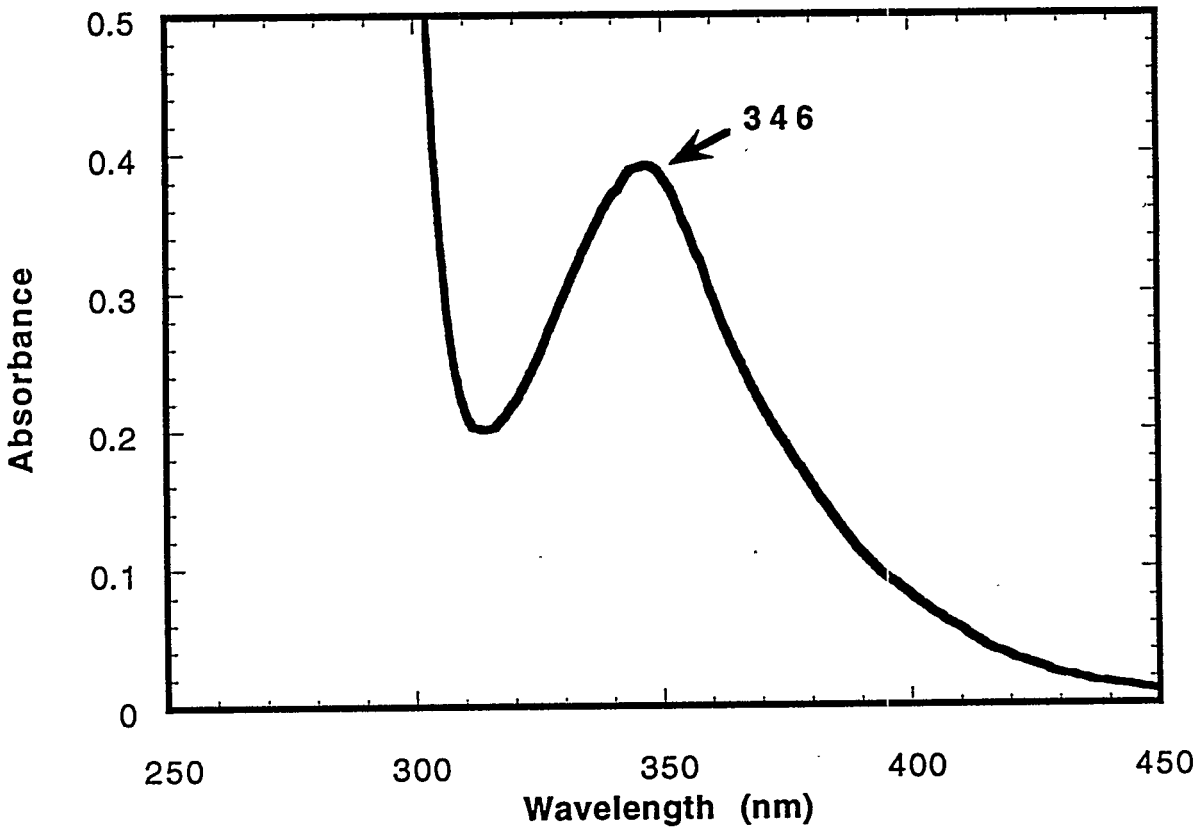

Figure 5. UV/Vis absorbance spectrum of the crude PhIP-DNA oligomer reaction mixture revealed the formation of adducts with a maximum wavelength of 346nm.

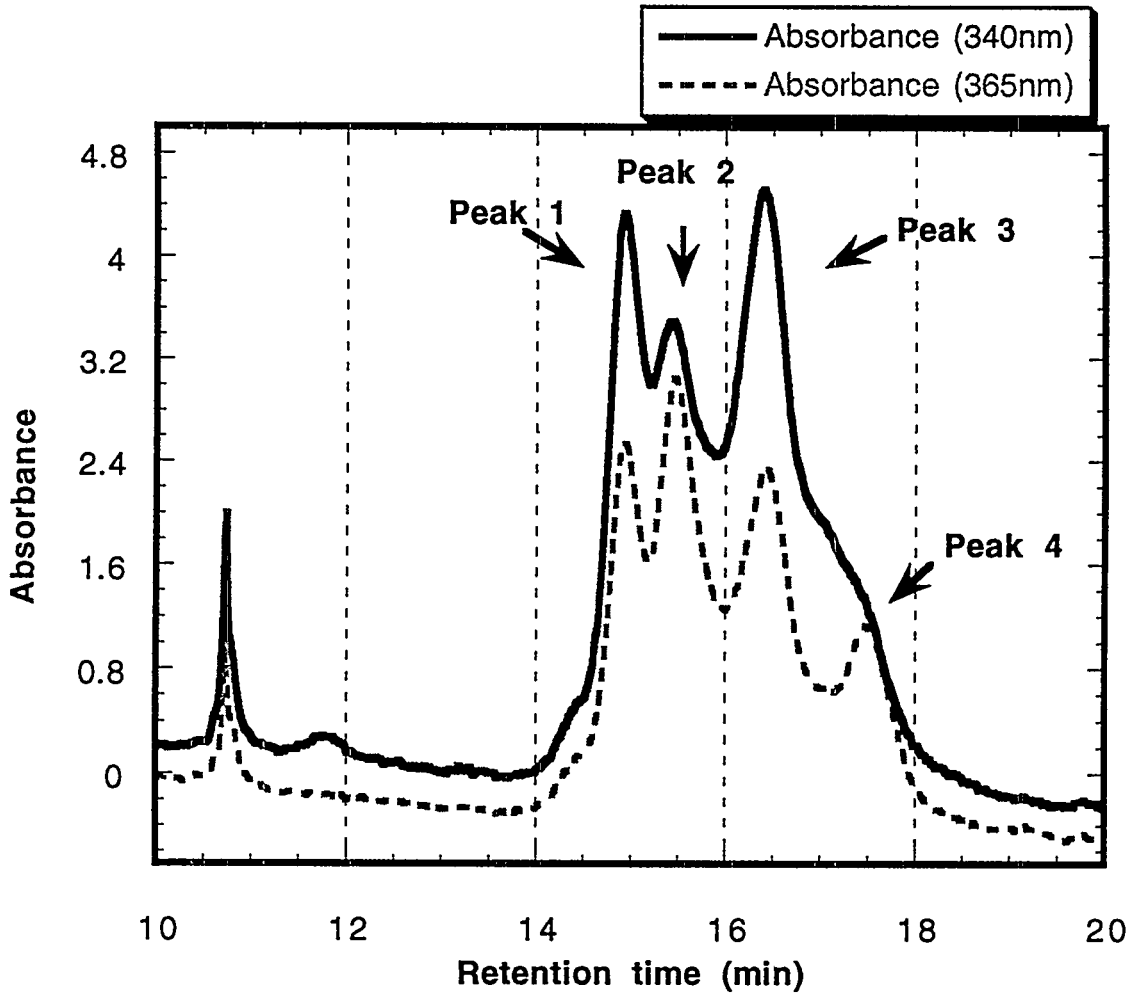

Figure 6. HPLC purification of the DNA oligomer adduct supernatant detected at 340 and 365 nm showed four unresolved peaks with retention times between 14 and 18 minutes.

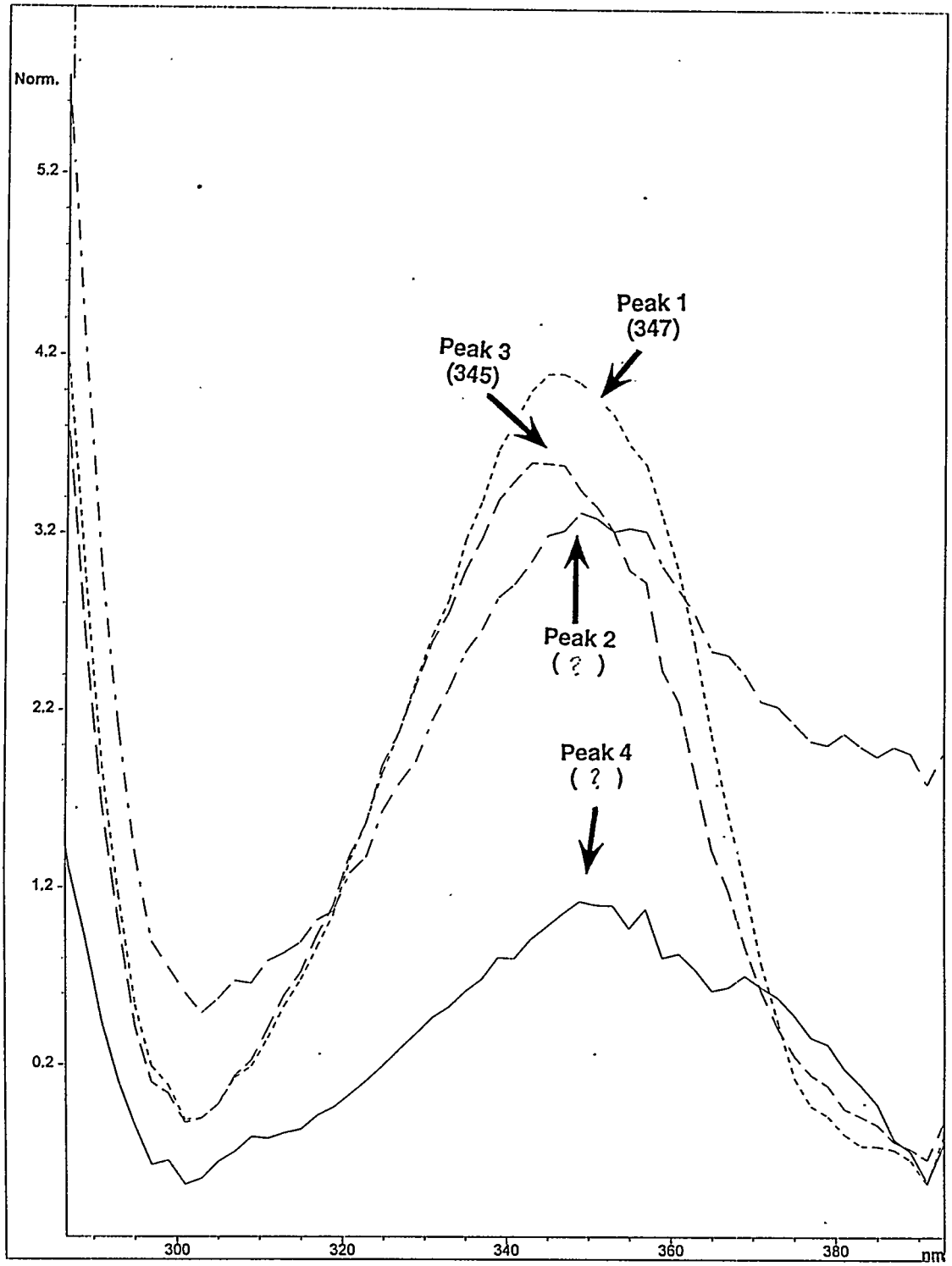

Figure 7. Some of the real-time spectra of the PhIP-DNA oligomer adducts have shoulders and tailing which prevents determining the maximum wavelenghths of some of the adducts.

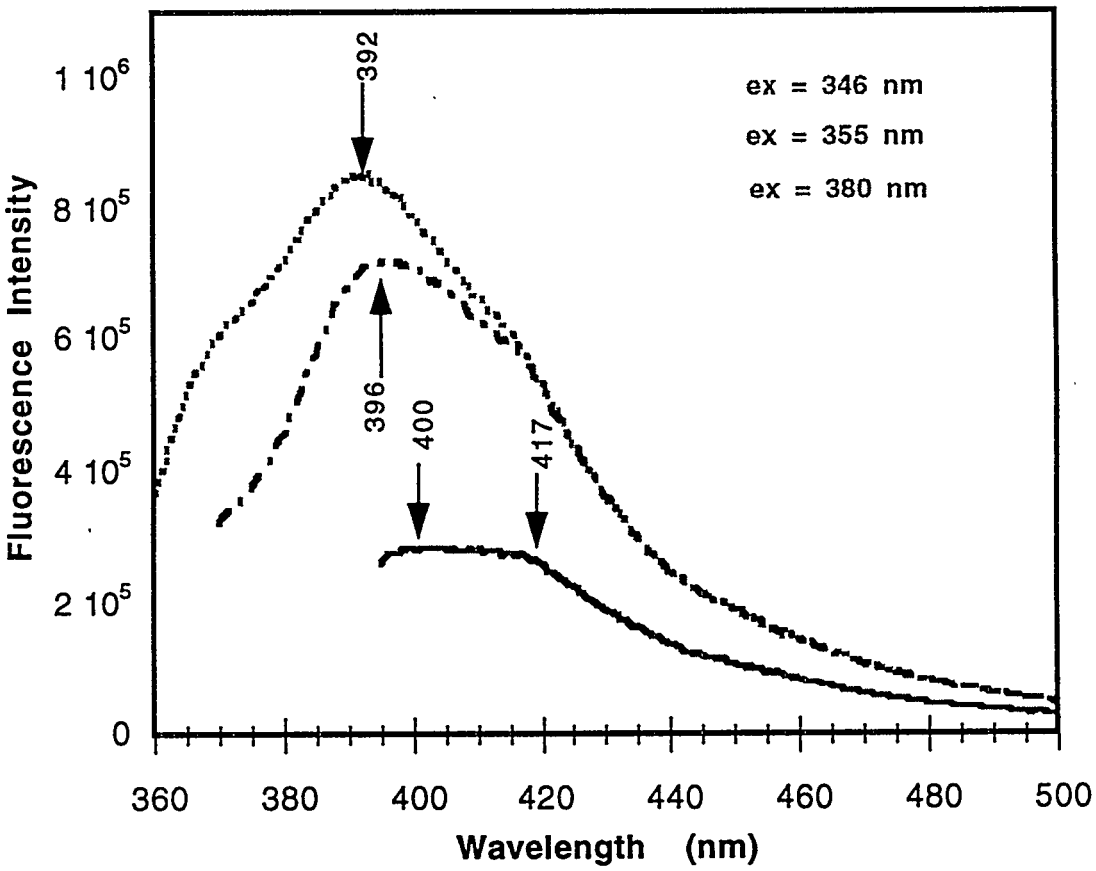

Figure 8. Fluorescence emission spectra of the DNA oligomer-PhIP reaction sample indicated the presence of four adduct species.

Pre-thymic Somatic Mutation leads to High Mutant Frequency at Hypoxanthine-guanine Phosphoribosyltransferase Gene

Jamie Jett
Biology and Biotechnology Research Program
Lawrence Livermore National Laboratory

Abstract

While characterizing the background mutation spectrum of the Hypoxathine-guanine phosphoribosyltransferase (HPRT) gene in a healthy population, an outlier with a high mutant frequency of thioguanine resistant lymphocytes was found. When studied at the age of 46, this individual had been smoking 60 cigarettes per day for 38 years. His mutant frequency was calculated at 3.6 and 4.2×10^{-4} for two sampling periods eight months apart. Sequencing analysis of the HPRT gene in his mutant thioguanine resistant T lymphocytes was done to find whether the cells had a high rate of mutation, or if the mutation was due to a single occurrence of mutation and ,if so, when in the T lymphocyte development the mutation occurred.

By T-cell receptor analysis it has been found that out of 35 thioguanine resistant clones there was no dominant gamma T cell receptor gene rearrangement. During my appointment in the Science & Engineering Research Semester, I found that 34 of those clones have the same base substitution of G=>T at cDNA position 197. Due to the consistent mutant frequency from both sampling periods and the varying T cell receptors, the high mutant frequency cannot be due to recent proliferation of a mature mutant T lymphocyte.

From the TCR and DNA sequence analysis we conclude that the G -> T mutation must have occurred in a T lymphocyte precursor before thymic differentiation so that the thioguanine resistant clones share the same base substitution but not the same gamma T cell receptor gene.

Introduction

Due to the inherent mistakes cells make during DNA replication, any number of individuals' DNA sampled for genetic studies will slightly deviate from the normal genetic code. In the interest of compiling a spectrum of background mutations in a population of normal healthy individuals, Department of Energy and National Institute of Environmental Health Sciences funded a 6 year study to characterize the specific genomic DNA changes within the Hypoxanthine-guanine phosphoribosyl transferase gene of healthy individuals which resulted in a mutant phenotype in individual human T cells. By examining the mutation spectrum of the HPRT gene of human T cells, researchers investigate aspects of somatic mutagenesis such as molecular mechanisms of mutations, consequences of *in vivo* exposure of somatic cells to mutagen agents, and individual susceptibility factors (ie. age or DNA repair). This study of background mutations at the HPRT gene would serve as the control (Burkhart-Schultz 1993) for later molecular studies at the HPRT gene of human populations exposed to possible toxic substances (ie. smoking, chemical toxins, radiation). In order to determine any genomic changes caused by a toxic substance a control population with no previous toxic exposure, but similar living conditions and age groups, is necessary for comparison.

The mutations within the control population are investigated in two ways:

(1) calculating the frequency at which mutations occur within the control population's T cells gives an average mutant frequency for healthy individuals for comparison to the experimental population of toxic exposure.

(2) determining the mutation type that occurs in the control population for comparison to experimental population. Three major types of mutations:

   (i) DNA deletions, large DNA segments or a single nucleotide is missing from DNA chain;

   (ii) DNA insertions, large DNA fragments or a single nucleotide is added to DNA chain; and

   (iii) Base substitution, a single nucleotide is replaced by one of the other 3 possible mononucleotides.

Narrowing the focus from characterizing the background mutations of healthy individuals at the HPRT locus, the control population was divided into two groups, smokers and nonsmokers. These two groups were compared to detect any genetic effects of smoking at the HPRT gene. While studying the effects of smoking at the HPRT gene, a 46 year old male smoker was found to have an exceptionally high mutant frequency. This result generated the question as to whether the high mutant frequency is due to separate occurring mutations, possible from 38 years of smoking 60 cigarettes a day, or to a single mutant cell which passed the mutation on to its daughter cells. We wanted to determine whether this male smoker had a high mutation rate. If so, this condition might pose a special health risk such as a higher risk of cancer. Mutations that alter the expression of a tumor-suppresser gene can increase the chances of cancerous cell development. (Cohen 1991)

HPRT Gene/Protein

The HPRT gene is one of ten phosphoribosyltransferase genes that have had their function and sequence determined. Phosphoribosyltransferase genes code for proteins that catalysis the production of mononucleotides used in DNA synthesis. The HPRT protein salvages degraded nucleic acids by enzymatic hydrolysis, freeing the purines xanthine and guanine for recycling within the cell for future nucleic acid synthesis. In people without the HPRT protein xanthine degrades to uric acid which builds up in the body and may form kidney stones or deposits in other tissues. An accumulation of uric acid may lead to Lesch-Nyhan syndrome with neurological effects of mental retardation, spartic cerebral palsy, choreoathetosis, and aggressive behavior such as self mutilation. (Sculley 1992)

Thoroughly investigated to find more about how the loss of HPRT protein activity associates with Lesch-Nyhan syndrome, the HPRT gene sequence was reported by Jolley et al. (1983) Since the entire genomic and complementary DNA sequence is known, the HPRT gene serves as a reporter gene in studies concerned with effects of external influences on DNA replication and repair. The reason for the wide use of the HPRT gene in genetic studies is three-fold.

- the entire HPRT gene sequence is known
- cells are easily obtained through peripheral blood
- mutant cells are easily isolated using a thioguanine growth media

We can isolate HPRT mutant cells by growing the cells in a thioguanine solution. A cell with functional HPRT protein will incorporate thioguanine into the cellular DNA through the purine salvage pathway and it will kill the cell. Cells with a mutation of the HPRT gene that effects the protein function and efficiency will have nonfunctional HPRT protein and will not incorporate thioguanine into the cell. These mutant cells will continue to live and replicate in a thioguanine growth media while normal lymphocytes with functional HPRT protein will die.

Materials and Methods

Isolation of Thioguanine-resistant Mutant Cells

Peripheral blood lymphocytes from the high mutant frequency outlier were extracted from whole blood samples and mutant frequency is determined as reported in Jones et al. (1993). Individual thioguanine-resistant clones were incubated at 37C at 5% CO_2 and expanded in LAK supernatant-supplemented medium with PHA at 0.1ug/ml. After the number of thioguanine-resistant cells reached $5x10^7$ to 10^8, cells were isolated by centrifugation and lysed using Rossi buffer with 50mM KCl, 10mM Tris-HCl at pH of 8.3, 2.5mM $MgCl_2$, 0.1ng/ml gelatin, 0.45% NP-40 and 0.45% Tween-20. The lysed cells were then refrigerated at 4C.

DNA Amplification

To further investigate the HPRT gene of the isolated thioguanine-resistant mutant cells, we amplified the HPRT gene specific DNA using the polymerase chain reaction (PCR) method. In this method a small amount of DNA from the lysed cell acts as a template from which more copies can enzymatically be made, thus provideing a large amound of gene specific DNA fro further analysis.

Four reagents are required to exponentially amplify a specific DNA sequence.

- original DNA template
- two small DNA segments (primers) that complement separate strands of the original DNA template. These must flank the DNA sequence of interest

- The four deoxyribonucleoside triphosphates (dNTPs): dATP, dCTP, dGTP, dTTP
- Taq polymerase: a heat stable DNA polymerase that reads the original DNA template and places the appropriate dNTP in the DNA copy

By heating the reagent mixture, the original DNA template denatures allowing space for the primers. As the mixture cools the primers align to the original DNA template and adhere to the complementary DNA sequence. The Taq polymerase reads along the original DNA template and joins the next dNTP to the end of the primer. After the Taq polymerase has joined the first appropriate dNTP to the primer, it reads the original DNA template for the next dNTP to be added. The Taq polymerase continues to add dNTPs until it reaches the stop codon located on the original DNA template. The Taq polymerase then detaches from the original DNA template. From these series of events two copies of DNA are made, one copy from each strand of original DNA template.

Then by heating the mixture a second time, the double stranded DNA denatures again and allows space for the primers to anneal to the DNA template. Taq polymerase again adds dNTPs to the primer in a long chain until reaching the stop codon where it detaches from the DNA template. Now there are four strands of DNA to act as template for the third cycle of template denaturation, primer annealing, and Taq polymerase extension. Eight strands of DNA are now available to act as template for the four cycle, as 16 for the fifth cycle, 32 for the sixth cycle, ect. Numerous cycles will yield enough DNA for sequence analysis. Following PCR amplification conditions as set by Gibbs et al. (1989), HPRT exon 3 of 35 thioguanine mutant clones were amplified for DNA sequencing using fluorescently labeled primers.

Sanger-Dideoxy DNA Sequencing Method

In DNA sequencing, the order of each nucleotide of the DNA chain is determined by making many copies of the DNA template but stopping the extention of the chain at certain nucleotides to yield different size DNA fragments. With many copies with varying size, the sequence is determined by looking at the size of DNA fragment at which a nucleotide stopped the extending copy DNA. A reaction must be run for each of the four nucleotides: A, C, G, and T. When pooled together and ordered by size, the ending nucleotide is

fluorescently detected and recorded as the nucleotide in that position of the chain. The nucleotide of the next size fragment is determined and recorded as occupying the position after the first nucleotide. Then the third size fragment's ending nucleotide is determined and recorded as the third nucleotide in the sequence. Every nucelotide of the differing size DNA fragments is determined in the order of size and recorded as occupying a sequential position.

Taq DNA polymerase is used in DNA sequencing to copy an original DNA template, but the Taq polymerase is not allowed to continually add dNTPs until it reaches the stop codon on the original DNA template, but is stopped by special terminating nucleotides to yield many differing sizes of copy DNA.

In the reaction mixture along with the dNTP's there are dideoxyribonucleoside triphosphates (ddNTPs). Taq incorporates these ddNTPs into the growing chain of copy DNA just like dNTPs; but Taq is unable to extend the chain after adding a ddNTP and releases the copy DNA. With numerous cycles it is possible to have Taq polymerase stop at all nucleotides yielding different DNA fragment sizes. These varying copy DNA fragments have a fluorescent label according to the last ddNTP incorporated by Taq into the copy DNA chain. By By examining the ending nucleotide of these differently sized DNA fragments, the nucleotide sequence can be determined.

The reaction mixture is separated by size on an electrophoresis gel, and the identity of the ending ddNTP of each DNA fragment is established when a laser excites the fluorescently label primer which correspondes to the ending ddNTP. Using the ABI 373A DNA Sequencer and the ABI Analysis software the DNA sequence is detected and recorded by a computer. The genomic DNA of 40 thioguanine resistant clones was sequenced to determine the exact mutation in the HPRT gene.

T cell Antigen Receptor (TCR) Analysis

T cells are lymphocytes located in the peripheral blood. It is these T cell's HPRT gene that we study. An analysis of the TCR repertoire in the 35 HPRT mutant clones was done to determine whether the mutant clones had the same TCR markers or not.

Inside the thymus, T cells undergo a T cell receptor gamma gene rearrangement that determines its immunological purpose in the body. A T cell precursor, or stem cell, from the bone marrow enters the thymus and receives

its markers by gene rearrangement. The T cell then exits the thymus. When the T cell is immunologically stimulated it then divides to produce a population of T cells with those same T cell markers.

By examining the TCR markers, we could determine whether the mutation happened in a T cell precursor before differentiation in the thymus or in a T cell line after T cell thymic differentiation. If the mutation occurred in a T cell precursor, the mutant clones isolated would have differing markers because each daughter cell from that mutant T cell precursor would enter the thymus at different times receiving different markers. But if the mutation occurred after thymic differentiation all mutant clones would be daughter cells with the same T cell markers.

Possible Mutation Scenario

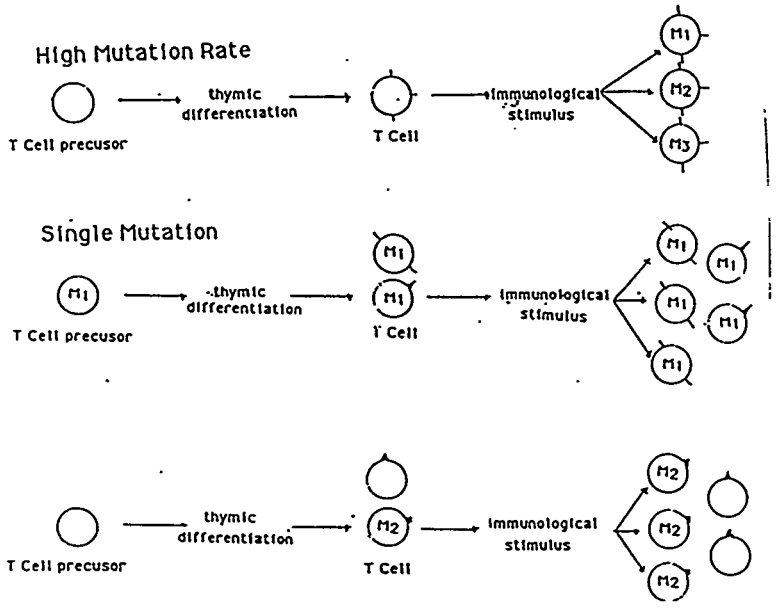

To determine whether or not the mutant clones isolated had the same T cell receptor gene rearrangement and therefore the same markers, another PCR reaction is done. For this PCR reaction several sets of primers are used to amplify the DNA sequence of interest. In this case not the HPRT gene itself, but the T cell receptor gamma gene. That segment of DNA is amplified and observed in an agarose gel to determine if all 35 HPRT mutant clones had the same T cell receptors. If all clones had the same gene rearrangement it could be concluded that all 35 HPRT mutant clones came from the same T cell that divided due to immunological stimulus. But if the mutant clones with identical mutations had differing gene rearrangement then a pre-thymic somatic mutation must have occurred.

Results

In Table 1 labeled "Molecular Analysis of Cloned Lymphocytes of High Mutant Frequency Outlier" provides an overview of the mutant clones studied from the high mutant frequency outlier from the HPRT population study. Listed here are mutant clone identification, HPRT exon band pattern, T cell receptor band pattern, and the genomic DNA mutation found.

HPRT Exon Band Pattern

By PCR amplification, Gibbs et al. (1990), we were able to determine that all 9 exons of the HPRT gene were present in the genomic DNA and that no large deletions had occurred in the HPRT gene.

T cell Receptor Band Pattern

No dominant gamma T cell receptor gene rearrangements as seen by the 13 different T cell receptor band patterns. There were 13 band patterns seen in 17 mutant clones studied using the TCR method.

Genomic DNA Sequence

From sequencing the genomic DNA of 35 thioguanine resistant mutant clones, it was found that 34 mutant clones, of the 35 contained the same base substitution at cDNA position 197 of an thymine where a guanine nucleotide normally would be.

No mutation could be found for the one mutant clone that did not contain the base substitution at cDNA 197 but had the normal genomic sequence for all 9 exons studied.

Table 1

Molecular Analysis of Cloned Lymphocytes
High Mutant Frequency

clone ID	HPRT[1] Multiplex band pattern	T cell[2] receptor pattern	Mutation
1.4A5	normal	1	G_{197} => T[3]
1.4B12	normal	2	G_{197} => T
1.4C1	normal	3	G_{197} => T
1.4C3	normal	4	G_{197} => T
1.4C9	normal	5	G_{197} => T
1.4D11	normal	4	G_{197} => T
1.5E2	normal	6	Wild Type
1.5F11	normal	7	G_{197} => T
1.5G11	normal	1	G_{197} => T
1.5H12	normal	5	G_{197} => T
1.6A3	normal	7	G_{197} => T
1.6B7	normal	8	G_{197} => T
1.6D6	normal	9	G_{197} => T
1.6D7	normal	10	G_{197} => T
1.6D8	normal	11	G_{197} => T
1.6D10	normal	12	G_{197} => T
1.6E8	normal	13	G_{197} => T
2.4C9	normal	ND	G_{197} => T
2.4F2	normal	ND	G_{197} => T
2.4F5	normal	ND	G_{197} => T
2.4F6	normal	ND	G_{197} => T
2.5F2	normal	ND	G_{197} => T
2.5G1	normal	ND	G_{197} => T
2.5H3	normal	ND	G_{197} => T
2.6A6	normal	ND	G_{197} => T
2.6C9	normal	ND	G_{197} => T
2.6E11	normal	ND	G_{197} => T
2.7A5	normal	ND	G_{197} => T
2.8A2	normal	ND	G_{197} => T
2.8A3	normal	ND	G_{197} => T
2.8B3	normal	ND	G_{197} => T
2.8B12	normal	ND	G_{197} => T
2.8C1	normal	ND	G_{197} => T
2.8E5	normal	ND	G_{197} => T
2.8F5	normal	ND	G_{197} => T

[1] An analysis that reveals large gene deletions

[2] An analysis that allows one to compare T cell markers

[3] At nucleotide position 197 an thymine replaces the normal guanine nucleotide

Discussion

During the HPRT control population study a male smoker was found to have an exceptionally high mutant frequency of HPRT mutant cells. The initial concern was if this high mutant frequency of this male smoker was due to a high mutation rate within his lymphocytes. Another concern was if this high mutation rate could posed a possible health risks such as a development of cancerous cells if a mutation occurred in a tumor-suppresser gene. These questions lead to a molecular analysis of his thioguanine-resistant T cells.

We were able to determine by TCR analysis and DNA sequencing of his T cell genomic DNA that the high mutant frequency of this male smoker was not due to a high rate of mutation in his cells but that the thioguanine resistant mutant clones did originated from a mutant T cell that proliferated due to immunological stimulus. From the TCR analysis we concluded that the mutation occurred in a stem cell or T cell precursor before it entered the thymus for T cell receptor gamma gene rearrangement. Since the time frame for this mutation was early in his lifetime, this mutation could not be linked to his 38 years of smoking.

But this might not have been the case, and only through this investigation could we determine that this male smoker was not at any special health risk but has a normal risk of cancer. Every occurrence of a high mutant frequency could be a high mutation rate and only if investigated could a possible health risk be determined.

Acknowledgments

I would like to acknowledge those who participated in this study. Claudia L. Thompson at the National Institute of Environmental Health Sciences for her work in collecting donor samples for the characterization of DNA mutations at the HPRT gene within a healthy population. Cynthia B. Thomas and Bethany Tucker for their work on thioguanine-resistant clone isolation of the characterization study. Cheryl L Strout for the TCR analysis of the male smoker who was a high mutant frequency outlier within the characterization study. .Karolyn Burkhart-Schultz, who performed the molecular analysis of the DNA mutations at the HPRT gene within a healthy population. And the principal investigator, Irene M. Jones.

References

1. Schultz K, Thomas CB, Thompson CL, Strout CL, Brinson E, and Jones IM. Characterization of in vivo Somatic Mutations at the Hypoxanthine-guanine Phosphoribosyltransferase Gene of a Human Control Population. Enviroment Health Perspectives 101.1:68-74 (1993)

2. Cohen SM, Ellweiz LB. Genetic errors, Cell Proliferation, and Carcinogensis. Cancer Res 51: 6493-6505 (1991)

3. Gibbs RA, Nguyen P, Edwards A, Civitello AB, Caskey CT Multiplex DNA Deletion Detection and Exon Sequencing of the Hypoxanthine Phosphoribosyltransferase Gene in Lesch-Lyhan Families genomics 7: 235-244 (1990)

4. Jolly DJ, Okayama H, Berg P, Esty AC, Filpula D, Bohlen P, Johnson GG, Shivel JE, Hunkapillar R. Friedman T Isolation and characterissation of a full-leng expressible cDNA for human hypoxanthine phosphoribosyltransferase. Proc Natl Acad Sci USA 80: 477-481 (1983)

5. Jones IM, Moore DH, Thomas CB., Thompson CL, Strout CL, and Burkhart-Schultz K. Factors Affecting HPRT Mutant Frequency in T-Lymphocytes of Smokers and Nonsmokers Cancer Epidemiology, Biomarkers & Prevention 2: 249-260 (1993)

6. Sculley DG, Dawson PA, Emmerson BT, Gordon R B. A Review of the Molecula Basis of Hypoxanthine-guanine phosphoribosyltransferase (HPRT) deficiency Hum Genet 90: 195-207 (1992).

Jamie M. Jett

535 Caliente Avenue
Livermore, CA 94550
(H) 510-443-4924
(W) 510-423-3627

Goal: To obtain employment in the field of molecular genetics.

Education:
University of Arkansas Fayetteville, AR
Degree: B.S. Chemistry/Biochemistry, May 1994
Major GPA: 3.44 Cum. GPA: 3.61

Work Experience:

Science-Engineering Research Semester Student
Biology and Biotechnology Research Department
Lawrence Livermore National Laboratory
Livermore, CA 94551
8/94 to 12/94
Fellowship working within Irene Jones' Biodosimetry Group on the Somatic Mutations of the Hypoxanthine-guanine Phosphoribosyltransferase Gene. Research experience with automated DNA sequencing, and PCR.

Biomedical Scientist
Biology and Biotechnology Research Department
Lawrence-Livermore National Laboratory
Livermore, CA 94551
5/94 to 8/94
Summer employment within Irene Jones' Biodosimetry Group on the Somatic Mutation of the Hypoxanthine-guanine Phosphoribosyltransferase Gene. Research experience in handling human blood, tissue culture, and PCR.

Lab Technician
Campbell Soup - Residue Laboratory, Fayetteville, AR.
1/94 to 6/94
Itemizing and performing analytical testing on poultry products, such as: Hydrogen Peroxide and Moisture Determination of poultry fat, Organochloride and Organophosphorus pesticides by acetonitrile extraction for feeds, Organochloride and Organophosphorous (acetone extraction) for Litter, Sulfadimethoxine ELISA Quick Test, and Fat Extraction of commercial products. Compiling results on Pesticide Residue Reporting System (PRRS).

Office Assistant
Bureau of Business and Economic Research, Fayetteville, AR
8/90 to 5/94
Duties included numerical data entry and extensive use of the telephone, copy machines, and directing facsimile for the entire Business College.

Special Skills: Research experience with DNA sequencing techniques, ABI automated sequencer and Perkin-Elmer Thermocylcer, two years of classroom experience with protein sequencing, UV Spectrometer, and manual gas chromatography, and one year of work experience with Hewlett-Packard automated gas chromatography.

Coursework/College Experience:

Undergraduate College Courses 8/90 to 12/94
University Chemistry, Organic Chemistry (I &II), Analytical Chemistry
Methods in Organic/Inorganic Analysis, Physical Chemistry (I & II), Inorganic Chemistry, Biochemistry (I& II), Biochemical Techniques, Pathogenic Microbiology, Immunology, University Microbiology

Honors/Awards: Senior Chemistry Scholar Award, Barbara Wertheim Campbell Award, Jacob Sacks Award, Dean's List, and American Chemical Society Achievement Award

Characterization of Thin-Film Multilayers Using Magnetization Curves and Modeling of Low-Angle X-ray Diffraction Data

M. Lane
Emory & Henry College, Emory, VA 24327
A. Chaiken and R.P. Michel
Lawrence Livermore National Laboratory, Livermore, CA 94550

Abstract

We have characterized thin-film multilayers grown by ion-beam sputtering using magnetization curves and modeling of low-angle x-ray diffraction data. In our films, we use ferromagnetic layer=Co,Fe, and NiFe and spacer layer=Si, Ge, $FeSi_2$, and $CoSi_2$. We have studied the effects of 1) deposition conditions 2) thickness of layers 3) different layer materials and 4) annealing. We find higher magnetization in films grown at 1000V rather than 500V and in films with spacer layers of 50Å rather than 100Å. We find higher coercivity in films with cobalt grown on germanium rather than silicon, metal grown on gold underlayers rather than on glass substrates, and when using thinner spacer layers. Finally, modeling reveals that films grown with disilicide layers are more thermally stable than films grown with silicon spacer layers.

Introduction

The discovery of giant magnetoresistance (GMR)[1] has stimulated a great deal of interest in producing a recording head which uses this phenomenon. One way to create GMR is to grow thin-film multilayers with different alternating ferromagnetic metals. This method relies on the fact that the different ferromagnetic metals have different coercive fields. High magnetization, a large difference in coercivities, and high thermal stability are all desirable qualities in films that may be used for magnetic heads. We are interested in studying films of this type using silicon and germanium as the spacer layers and iron, cobalt, and permalloy (NiFe) as the ferromagnetic layers.

Experimental Details

Multilayers were prepared by ion-beam sputtering with a base pressure of $2X10^{-8}$ Torr. Depositions were conducted at a pressure of $1X10^{-4}$ Torr at a rate of .3-.4Å/s. Hysteresis loops were measured using a LakeShore Cryotonics VSM with a 6 kOe magnet. X-ray diffraction measurements were made by a Rigaku X-ray Diffractometer with a rotating anode generator and a copper target. The modeling of the x-ray data was performed as described by Fullerton et al.[2].

Results

We find that higher magnetization can be obtained by growing films at a higher deposition voltage. Figure 1 shows a magnetization curve for two samples grown at different voltages. Films grown at the higher deposition voltage show a 27% increase in magnetization over films grown at the lower deposition voltage. A high magnetization indicates the film is better layered and more closely reflects a perfect superlattice. Roughness, interdiffusion, and formation of non-magnetic compounds lead to a decrease in magnetization. The coercivity of the metal layer was increased by thinner spacer layers, cobalt grown on germanium instead of silicon, and growing the metal on a gold substrate rather than on glass.

Figure 2 shows a magnetization curve for two samples grown on different spacer layers. The coercivity increased by 113% for thinner spacer layers, 100% for cobalt grown on germanium, 594% for cobalt grown directly on gold, and 116% for permalloy grown directly on gold. Figure 3 shows curves for cobalt grown on different substrates.

Table 1 summarizes the results obtained from the growth of (Co30/Si14)X25, (Co30/$CoSi_2$14)X25, (Co29/$CoSi_2$3/Si8/$CoSi_2$3)X25, (Fe30/Si14)X25, (Fe30/$FeSi_2$14)X25, and (Fe29/$FeSi_2$3/Si8/$FeSi_2$3)X20 multilayers. All thicknesses are in angstroms. The table also shows the film morphology before and after annealing.

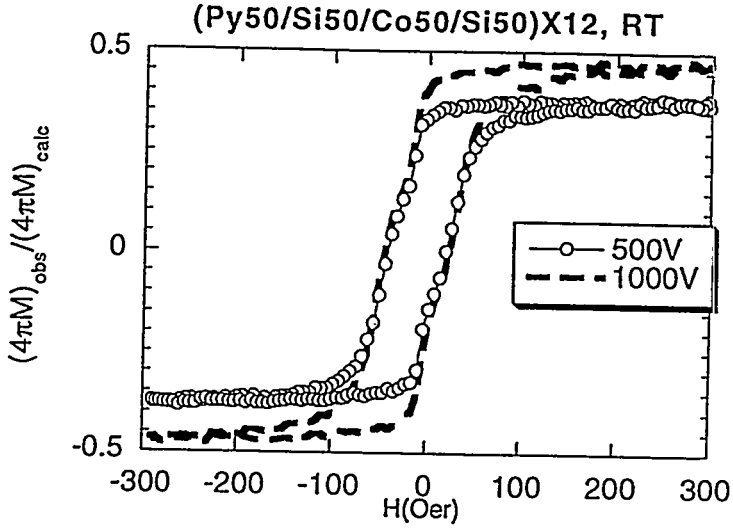

Figure 1: Magnetization curve for samples grown at different voltages.

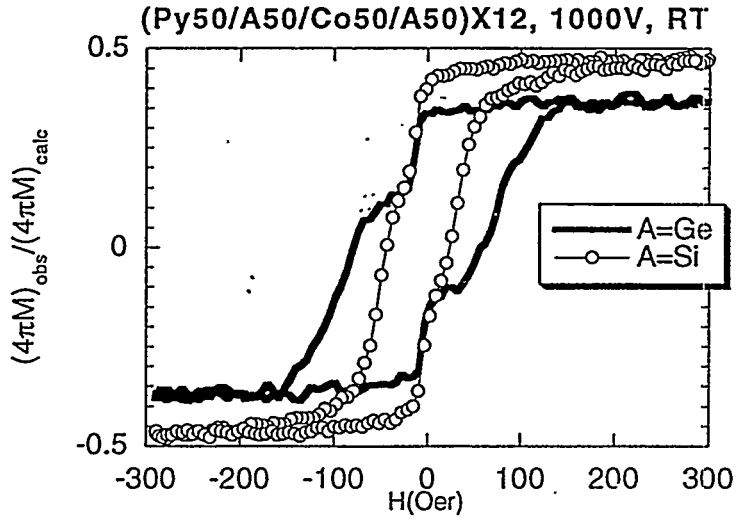

Figure 2: Magnetization curve for samples with different spacer layers.

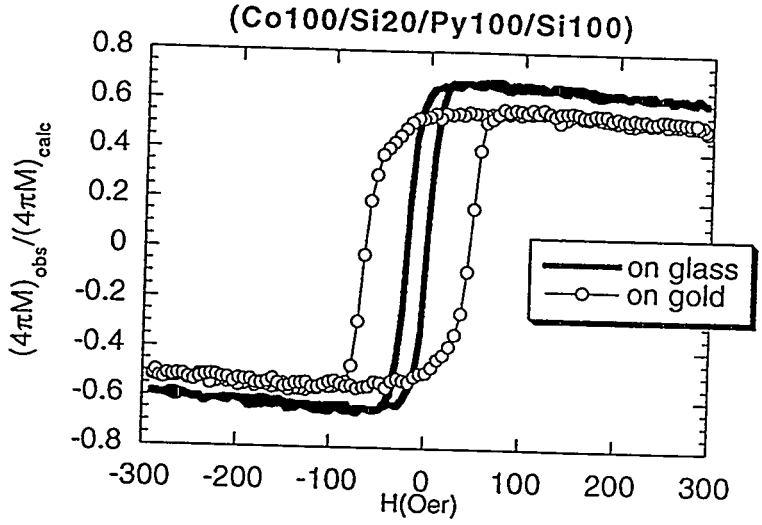

Figure 3: Magnetization curve for samples grown on different substrates.

Sample	Density A	Density B	Modulation	Thick B	Magnetization
$Co/CoSi_2/Si$	.72	1.80	43.9 (43.0)	7.0 (8.0)	.42
$Co/CoSi_2/Si$*	.70	1.80	43.8 (43.0)	7.0 (8.0)	.42
$Fe/FeSi_2/Si$	.71	1.65	42.9 (43.0)	8.0 (8.0)	.74
$Fe/FeSi_2/Si$*	.70	1.00	42.9 (43.0)	7.9 (8.0)	.72
$Co/CoSi_2$	.83	1.30	43.5 (44.0)	14.0 (14.0)	.43
$Co/CoSi_2$*	.83	1.20	44.1 (44.0)	12.0 (14.0)	.44
$Fe/FeSi_2$	.90	1.40	43.9 (44.0)	14.0 (14.0)	.55
$Fe/FeSi_2$*	.73	1.20	43.9 (44.0)	13.9 (14.0)	.62
Co/Si	.75	1.20	38.3 (44.0)	14.0 (14.0)	.37
Co/Si*	.80	1.20	39.3 (44.0)	9.5 (14.0)	.36
Fe/Si	.80	1.70	38.1 (44.0)	14.0 (14.0)	.52
Fe/Si*	.80	1.60	41.9 (44.0)	10.5 (14.0)	.60

Table 1: A=ferromagnetic layer, B=spacer layer, Thickness in Å, *Annealed at 200C for 20 min, Nominal value in parentheses. Column 1 and 2 contain multiplication factors to the electron density rather than the actual densities.

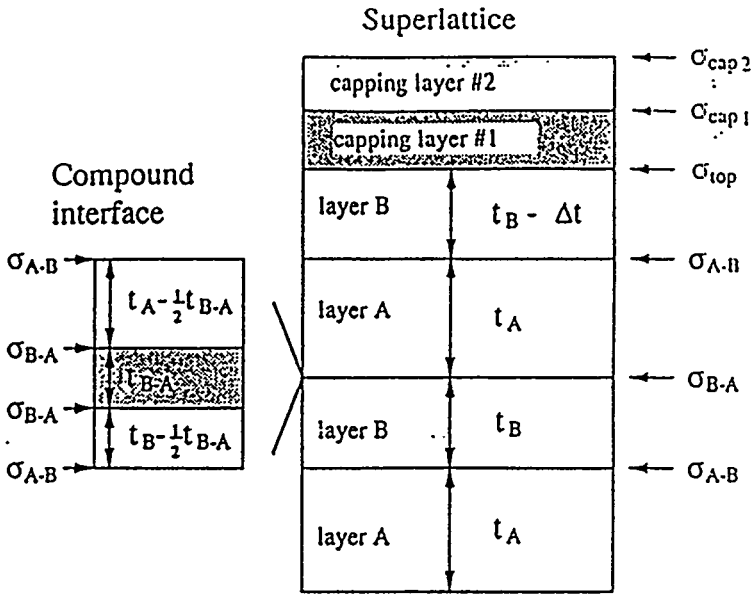

Figure 4: Explanation of parameters for Table 1.

Morphology after deposition

From the table, we see that the electron density for the ferromagnetic layer decreases and the electron density for the spacer layer increases. This is attributable to the diffusion of the metal layer into the amorphous layer containing silicon. This is in agreement with Montcalm et al. which found that molybdenum at a silicon interface was more reactive than silicon at a molybdenum interface.[3] The films with disilicide layers show little or no change in modulation wavelength while the films with silicon-only spacer layers show a smaller modulation wavelength than the nominal one.

Morphology after annealing

After annealing, we find that the electron densities are close to the values after deposition. This indicates the composition of these layers did not change a significant amount. The modulation wavelength for films with disilicide spacer layers does not change but the wavelength for films with silicon-only spacer layers increases. This may be due to growth of metal silicides at the interfaces. The silicon-only films also show a large decrease in the thickness of the spacer layer while the disilicide films show values close to nominal.

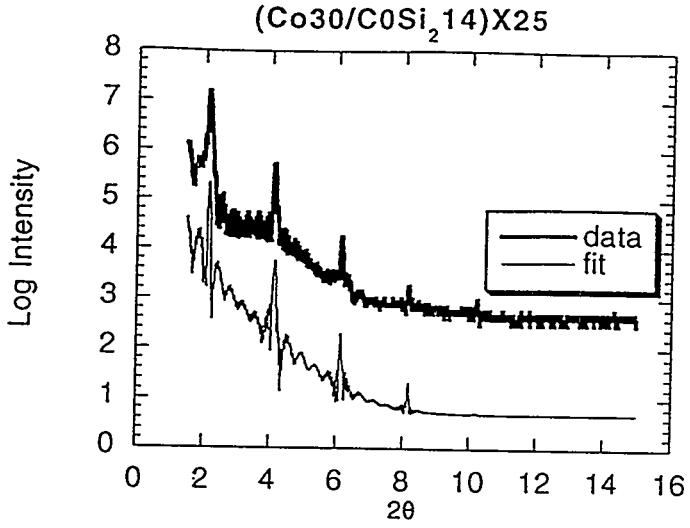

Figure 5: Fit of experimental data.

This is in agreement with growth at the interfaces for the silicon-only films.

Conclusions

Co, Fe, and NiFe multilayers have been grown under different deposition conditions, with different spacer layers, and with different layer thicknesses. We have done annealing studies on films with and without disilicide layers. We find that by varying layer thickness, varying layer materials, and varying deposition conditions a multilayer with higher coercivity and magnetization can be obtained. We also find that multilayers grown with disilicide spacer layers are closer to what would be nominally expected than multilayers grown with silicon only spacer layers. It is also seen that the multilayers with the thin disilicide layers more closely resemble the films with the thick disilicide layer than the film with the silicon-only layer. In the Co films we find the magnetization for the sample with the silicon-only layer to be lower than the magnetization of the other Co films. This is in good agreement with the differences in film morphology of the Co films. No similar relationships can be drawn between the morphology and magnetization of the Fe films yet, but it is an area of future research. We also intend to continue tracking

the thermal stability of both Co and Fe multilayers through more annealing experiments.

We would like to thank Kathy Morse for AFM measurements. Michael Lane was supported by the Department of Energy's Science and Engineering Research Semester. Part of this work was performed under the auspices of the U.S. Department of Energy by LLNL under contract No. W-7405-ENG-48.

[1] M. N. Baibich, J. M. Broto, A. Fert, F. Nguyen van Dau, F. Petroff, P. E. Etienne, G. Creuzet, A. Friederich, and J. Chazelas, Phys. Rev. Lett. 66, 2472(1988).

[2] E. E. Fullerton, I. K. Schuller, H. Vanderstraeten, Y. Bruynseraede, Phys. Rev. B 45, 9292(1992).

[3] C. Montcalm, B. T. Sullivan, H. Pepin, J. A. Dobrowolski, M. Sutton, Applied Optics 33, 2057(1994).

Analysis of Total Least Squares in Estimating the Parameters of a Mortar Trajectory

prepared by

Daniel Leo Lau
Dr. Lawrence C. Ng

Astract. Least Squares (LS) is a method of curve fitting used with the assumption that error exists in the observation vector. The method of Total Least Squares (TLS) is more useful in cases where there is error in the data matrix as well as the observation vector. This paper describes work done in comparing the LS and TLS results for parameter estimation of a mortar trajectory based on a time series of angular observations. To improve the results, we investigated several derivations of the LS and TLS methods, and early findings show TLS provided slightly, 10%, improved results over the LS method.

Problem Statement

We want to measure the performance of Total Least Squares (TLS) in estimating the parameters of a mortar trajectory based on a time series of angular observations.

Introduction

Least Squares (LS) is a method of solving a set of linear equations with more equations than unknowns. In the case of:

$$Ax = B \quad \text{where} \quad A = \Re^{m \times n}, x = \Re^{n \times 1}, B = \Re^{m \times 1} \tag{1}$$

A is the Data Matrix, and B is the Observation Vector. $\Re^{m \times n}$ denotes a matrix of real numbers, $m \times n$ elements in dimension. We rewrite Eq. 1 as:

$$Ax = b + r \quad \text{where} \quad r = \Re^{m \times 1} \tag{2}$$

to model the existence of error in the observation vector. The LS problem is finding a solution x_{ls} that minimizes the equation:

$$\begin{aligned} &\sum_{i=1}^{m} \left[(Ax_{ls})_i - (b+r)_i \right]^2 \\ &\sum_{i=1}^{m} \left[(b)_i - (b+r)_i \right]^2 \\ &\sum_{i=1}^{m} \left[r_i \right]^2 \end{aligned} \tag{3}$$

In rewriting Eq. 1 as:

$$(a+e)x = b + r \quad \text{where} \quad e = \Re^{m \times n} \tag{4}$$

to model error in both the data matrix and the observation vector, the LS problem has a solution x_{ls} that minimizes the equation:

$$\begin{aligned} &\sum_{i=1}^{m} \left[((a+e)x_{ls})_i - (b+r)_i \right]^2 \\ &\sum_{i=1}^{m} \left[(ax_{ls} + ex_{ls})_i - (b+r)_i \right]^2 \\ &\sum_{i=1}^{m} \left[(b + ex_{ls})_i - (b+r)_i \right]^2 \\ &\sum_{i=1}^{m} \left[(ex_{ls})_i - (r)_i \right]^2 \end{aligned} \tag{5}$$

From Eq. 5, we see that the error introduced into the data matrix propagates into the LS solution as ex_{ls}.

The Total Least Squares (TLS) method solves this case where error exists in both the data matrix and the observation vector. Described by Golub and Van Loan [1], we want to find an x_{tls} such that:

$$(a+e_o)x_{tls}=b+r_o \text{ where } \sum_{i=1}^{m}\sum_{j=1}^{n+1}[e|r]_{ij}^{2} \tag{6}$$

is minimized at $e=e_o, r=r_o$. Table 1 summarizes the differences between LS and TLS:

LS	TLS
$Ax=b+r$	$(a+e)x=b+r$
minimize $\sum_{i=1}^{m}[r_i]^2$	minimize $\sum_{i=1}^{m}\sum_{j=1}^{n+1}[e\|r]_{ij}^{2}$

Table 1. Comparison of LS and TLS

An illustration taken from Golub and Van Loan [1], Fig. 1 shows, graphically, the nature of TLS and LS. In this illustration, LS minimizes the vertical distance, and TLS minimizes the perpendicular or absolute distance.

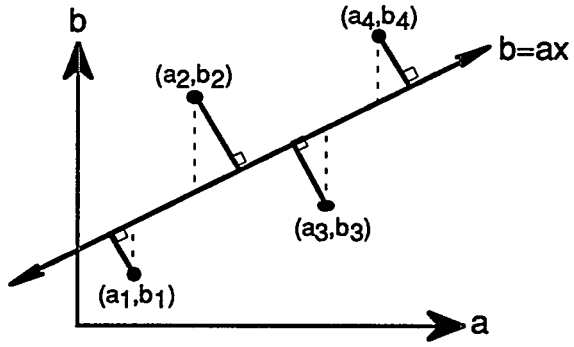

Figure 1. Total Least Squares versus Least Squares

As a further analysis of the TLS problem, Demmel [3] investigated a situation where some of the columns in the data matrix are known exactly, a situation called Constrained Total Least Squares (CTLS). The solution can be summarized as finding the smallest perturbations to a submatrix,

composed of the columns of $C=[A|B]$ that contain error, that lowers the rank equal to the size of the vector x.

Numerical Implementation

For testing, we implemented the LS and TLS algorithms with the use of MATLAB. The following lists, taken from Golub and Van Loan [1 & 2], outline the procedure. Appendix 1 gives a complete listing of the MATLAB code.

LS

- Solve for $C = A^TA$
- Calculate $d = A^TB$
- Solve for G where $GG^T = C$
- Solve for y where $Gy = d$
- Finally, solve for x_{ls} where $G^Tx_{ls} = y$

TLS

- Calculate C from $C = [A\ B]$
- Single Value Decomposition, $U^TSV = svd(C)$
- Calculate $[e_o\ r_o] = -U_{:,n+1}S_{n+1,n+1}[V^T_{1:n,n+1}V^T_{n+1,n+1}]$
- Then solve for $x_{tls} = -T_{1:n,1:n}V_{1:n,n+1}V^{-1}_{n+1,n+1}T^{-1}_{n+1,n+1}$

Experimental Verification

The problem of estimating parameters for a mortar trajectory was setup as follows:

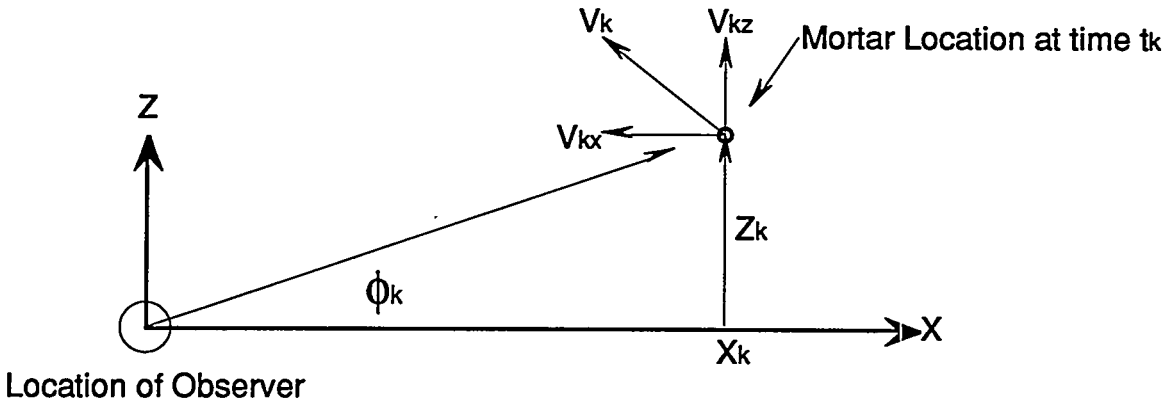

Figure 2. Vector Plot of Mortar Trajectory

We want the parameters Z_o, V_{zo}, X_o, and V_{xo}, the initial conditions. By relating these parameters with the angular observations, ϕ_k, we derived the equation:

$$Z_o + V_{zo}t_k - X_o \tan\phi_k + V_{xo}t_k \tan\phi_k = \frac{1}{2}gt_k^2 \text{ where } k = 1,2,3... \text{ and } g = gravity \quad (7)$$

The TLS algorithm requires a minimum of five observation points, more equations than unknowns. Using Eq. 7, Eq. 1 becomes:

$$\begin{bmatrix} 1 & t_1 & -\tan\phi_1 & t_1\tan\phi_1 \\ 1 & t_2 & -\tan\phi_2 & t_2\tan\phi_2 \\ 1 & t_3 & -\tan\phi_3 & t_3\tan\phi_3 \\ 1 & t_4 & -\tan\phi_4 & t_4\tan\phi_4 \\ 1 & t_5 & -\tan\phi_5 & t_5\tan\phi_5 \end{bmatrix} \begin{bmatrix} Z_o \\ V_{zo} \\ X_o \\ V_{xo} \end{bmatrix} = \frac{1}{2}g \begin{bmatrix} t_1^2 \\ t_2^2 \\ t_3^2 \\ t_4^2 \\ t_5^2 \end{bmatrix} \tag{8}$$

As a first test of TLS and LS, values were generated for the data matrix and observation vector with no noise added. Table 2 lists the results.

Parameter	Value	LS Solution	TLS Solution
Z_o	0	0	0
V_{zo}	50	50	50
X_o	100	100	100
V_{xo}	10	10	10

Table 2. Results for Case of No Error

To model a more realistic case, we added noise, of at most 0.002 radians, to the angular observations, ϕ_k. This creates error in the third and fourth columns of the data matrix. Fig. 3 shows the results after 50 runs using the same parameter values listed in Table 2.

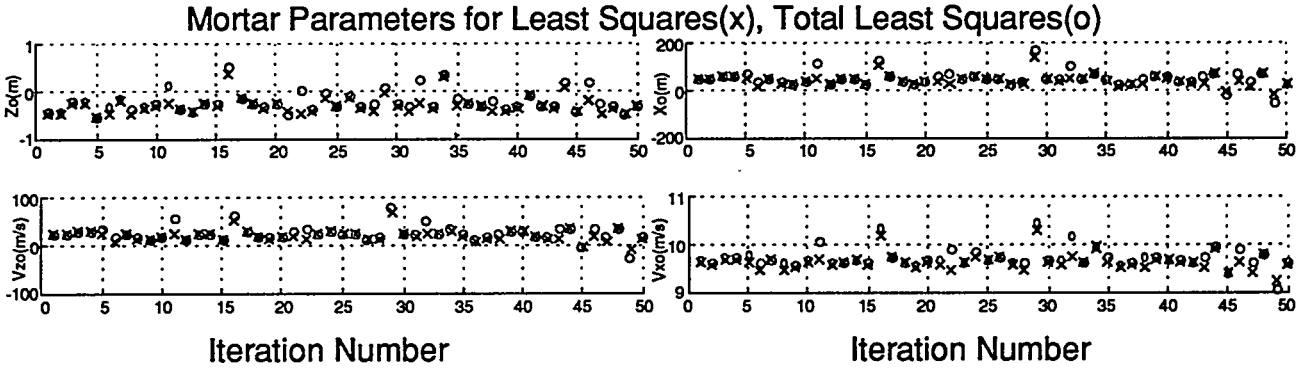

Figure 3. Results of LS and TLS with Error in Angular Observation ϕ_k

The numerical results are listed in Table 3. These numbers are the mean values taken from Fig. 3. Although LS and TLS are within one meter of the original Z_o and V_{zo}, LS offers only 40% signal recovery of V_{xo} and X_o.

TLS improves those results by 10% of the original signal, but that still leaves 50% of V_{zo} and X_o unrecovered.

Parameter	Value	LS Solution	TLS Solution
Z_o	0	-0.2891	-0.2267
V_{zo}	50	20.9674	25.3320
X_o	100	41.1933	50.0860
V_{xo}	10	9.6506	9.7158

Table 3. Results with Error in the Angular Observation ϕ_k

As a demonstration of the significance of these results, Fig. 4 shows the physical interpretation of these values. From the best observation by TLS, the range of the mortar would be roughly 55.9m short of the actual distance.

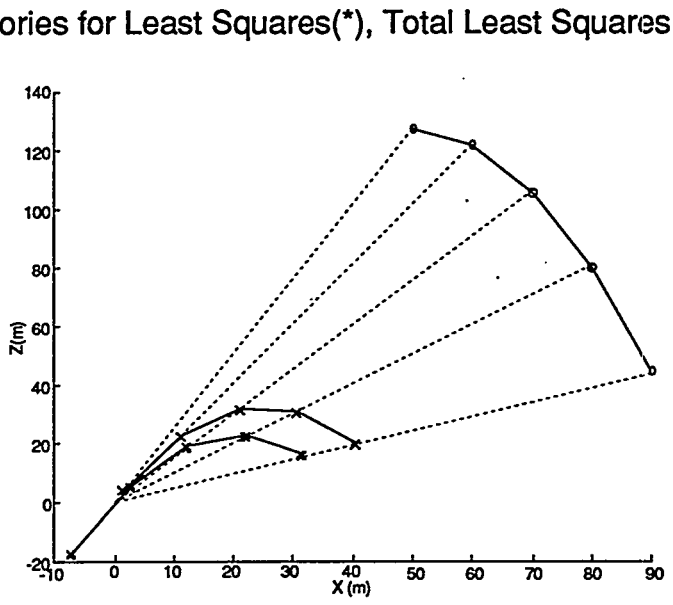

Figure 4. Mortar Trajectories of Actual, LS and TLS Parameters

In using the CTLS method, the results, listed in Table 4, show CTLS gives better results, but these improvements are very insignificant. Put quantitatively, CTLS provides less than 0.01% improvement.

Conclusions

TLS does not offer an accurate, within 10%, solution to the problem of estimating parameters for a mortar trajectory. By giving parameter values 10% closer in some instances, TLS offers a slightly improved solution over

LS. The solution of the TLS problem is one of finding the best-fit solution and not the absolute true answer. We will continue to search for an accurate method of estimating the parameters for a mortar trajectory. Bottom line: TLS is not a solution to this problem.

Parameter	Value	TLS Solution	CTLS Solution
Z_o	0	-0.2267	-0.2261
V_{zo}	50	25.3320	25.3577
X_o	100	50.0860	50.1387
V_{xo}	10	9.7158	9.7161

Table 4. CTLS and TLS Results with Error in the Angular Observation ϕ_k

Bibliography

[1] G.H. Golub and C.F. Van Loan. "An Analysis of the Total Least Squares Problem," SIAM J. Numer. Anal. 17, 1980, pages 883-93.

[2] G.H. Golub and C.F. Van Loan, Matrix Computations, Johns Hopkins Press, Baltimore, MD, 1990, pages 221-31,576-81.

[3] J.W. Demmel. "The Smallest Perturbations of a Submatrix which Lowers the Rank and Constrained Total Least Squares Problems," SIAM J. Numer. Anal. 24, 1987, pages 199-206.

Acknowledgment

This work was completed as part of the Department of Energy's Science and Engineering Research Semester, Fall 1994, at the Lawrence Livermore National Laboratory, in Livermore, California.

Appendix 1. MATLAB Code Listing

```
function [Xtls, Eo, Ro] = tls(A, B, D, T)
%*************************************************************
% TLS(A, B, D, T)
%     Returns the solution to the Total Least Squares problem
%     where errors exist in the data matrix "A" and in the
%     observation vector "B":
%
%                          (A+Eo)Xtls = (B + Ro)
%
%     The algorithm used was taken from G. Golub, and C. van
%     Loan, Matrix Computations, John Hopkins Press,Baltimore,
%     MD, 1989, pages 576-81.
%
% Input Arguments:      A -> Data Matrix
%                       B -> Observation Matrix
%                       D -> Non-singular diag(d1,...,dm)
%                       T -> Non-singular diag(t1,...,tn+k)
%
% Output Arguments:     Eo -> Error in Data Matrix
%                       Ro -> Error in Observation Vector
%                       Xtls -> Total Least Square Solution Vector
%
% Daniel Leo Lau
% November 18, 1994
%*************************************************************

% DETERMINE SIZE OF MATRIX "A" AND "B"
[m,n]=size(A);
k=size(B, 2);

% CHECK FOR IMPROPER MATRIX SIZE
% CONDITION OF ALGORITHM ASSUMES "m" be greater than or equal "n"+"k"
if (m ~= size(B,1))
      fprintf('ERROR! MATRIX DIMENSIONS MUST AGREE...\n');
      fprintf('Number of Rows in "A" must equal number of rows in "B"\n');
      return;
elseif (m < n+k)
      fprintf('IMPRORPER MATRIX SIZE. (#COL)a >= (#ROW)a + (#COL)b');
      return;
end;

% CREATE IDENTITY MATRICES FOR "D" AND "T" IF NOT STATED OTHERWISE
if (nargin == 2)
      D=eye(m);
      T=eye(n+k);
end;

% CALCULATE MATRIX "C"
C = D*[A B]*T;

% PERFORM SINGLE VALUE DECOMPOSITION SO THAT U'CV = S
% MATLAB'S SVD(X) RETURNS WSY' = X AND THEREFORE
% ADDITIONAL TRANSFORMATIONS ARE REQUIRED
```

```
[w S y]=svd(C,0);
if (size(w,1) == size(w,2))
        U=inv(w');              % USE inv() FOR SQUARE MATRIX "U"
else
        U=pinv(w');             % USE pinv() FOR NON-SQUARE MATRIX "U"
end;
if (size(y,1) == size(y,2))
        V=inv(y');              % USE inv() FOR SQUARE MATRIX "V"
else
        V=pinv(y');             % USE pinv() FOR NON-SQUARE MATRIX "V"
end;

% PERFORM ROW AND COLUMN PARTITIONING TO SIMPLIFY LATER EQUATIONS
U1=U(:,1:n);
U2=U(:,n+1:n+k);
V11=V(1:n,1:n);
V12=V(1:n,n+1:n+k);
V21=V(n+1:n+k,1:n);
V22=V(n+1:n+k,n+1:n+k);
S1=S(1:n,1:n);
S2=S(n+1:n+k,n+1:n+k);

% CALCULATE ERROR IN "A" AND "B" ON THE CONDITION THAT
% THE Nth DIAGNOL BE GREATER THAN THE N+1st DIAGNOL OF "S"
if (S(n,n) > S(n+1,n+1))
        w=inv(D)*(-U2*S2*[V12'   V22'])*inv(T);
        Eo=w(:,1:n);
        Ro=w(:,n+1:n+k);
end;

% PERFORM ROW AND COLUMN PARTITIONING TO SIMPLIFY "Xtls" EQUATION
T1=T(1:n,1:n);
T2=T(n+1:n+k,n+1:n+k);
if (size(V22,1) == size(V22,2))
        Xtls=-T1*V12*inv(V22)*inv(T2); % USE inv() FOR SQUARE MATRIX "V22"
else
        Xtls=-T1*V12*pinv(V22)*inv(T2); % USE pinv() FOR NON-SQUARE MATRIX "V22"
end;

return;
```

```
function Xls = lsq(A, B)
%*************************************************************
% LS(A, B)
%           Returns the solution to the Least Squares problem
%           where errors exist in the observation vector "B":
%
%                       (A)Xls = (B + Ro)
%
%           The algorithm used was taken from G. Golub, and C. van
%           Loan, Matrix Computations, John Hopkins Press, Baltimore,
%           MD, 1989, pages 221-33.
%
% Input Arguments:      A -> Data Matrix
%                       B -> Observation Matrix
%
% Output Arguments: Xls -> Least Square Solution Vector
%
% Daniel Leo Lau
% November 21, 1994
%*************************************************************

C=A'*A;
d=A'*B;
R=chol(C);
G=R';
y=pinv(G)*d;
Xls=pinv(G')*y;

return;
```

```
function [Xctls, dD] = ctls(A, B, r, s, d, t)
%*************************************************************
% CTLS(A, B)
%           Returns the solution to the Constrained Total Least Squares problem
%           where errors exist in some of the columns of the data matrix, A:
%
%                       (A + Eo)Xctls = (B)
%
%           The algorithm used was taken from J.W. Demmel (1987). "The
%           Smallest Perturbations of a Submatrix which Lowers the Rank
%           and Constrained Total Least Squares Problem," SIAM J. Numer.
%           Anal. 24, 199-206.
%
% Input Arguments:      A -> Data Matrix
%                       B -> Observation Matrix
%                       r -> Reduced Rank Sought After
%                       s -> Number of Column with Error
%
% Output Arguments:     Xctls -> Constrained Total Least Squares Solution Vector
%                       dD -> Error Matrix
%                       d & t -> Weighting Matrices
%
% Daniel Leo Lau
% November 21, 1994
%*************************************************************

% DETERMINE SIZE OF MATRIX "A" AND "B"
[m,n]=size(A);
k=size(B, 2);

% DETERMINE IF d & t ARE SPECIFIED
if (nargin == 6)
      T=d*[B A]*t;
else
      T=[B A];
end;

% DIVIDE MATRIX T INTO C, NO ERROR, AND D, WITH ERROR
C=T(:,1:s);
D=T(:,s+1:k+n);
[U S V]=svd(C);       % PERFORM SINGLE VALUE DECOMPOSITION

RKc=rank(C);          % DETERMINE RANK OF SUBMATRIX C
U'*T;
C1=ans(1:RKc,1:RKc); D1=ans(1:RKc,RKc+1:k+n); D2=ans(RKc+1:m,RKc+1:n+k);
[u si v]=svd(D2,0);
temp=zeros(1,size(u,2));
for i=(r-RKc)+1:size(diag(si),1)
      temp(i)=si(i,i);
end;
dD2=-u * diag(temp) * v';
temp=zeros(size(D));
temp(RKc+1:m,:)=dD2;
dD=U*temp;
W=[C D+dD];
```

```
Xctls=pinv(W(:,2:n+k))*W(:,1);
return;
```

Determining the *In situ* Water Content of The Geysers Graywacke of Northern California

Alice Marsh
University of Montana
Mentors: Brian Bonner and Chantel Aracne Ruddle
Earth Sciences Division
Lawrence Livermore National Laboratory
December 16, 1994

Abstract

The water content, porosity and permeability measurements of the Northern California Geysers rocks are used to predict the lifetime of the geothermal resource, which provides 10% of Northern California's electricity. The Geysers rock was drilled from defunct well SB-15-D, and some cores were sealed in aluminum tubes to preserve the *in situ* water content. These cores were sent to the Lawrence Livermore Laboratory to measure the water content. Humidity measurements were taken of the air around a one and a half foot encased core, recovered from a depth of 918.9 feet. Over a seven day period, the humidity reached almost 100% indicating that the air around the core was saturated in water vapor. We believe the sealing method is effective, preserving the *in-situ* water content. To measure water content, I will use Archimede's principle to determine the density of the core before and after drying in an oven. Ultrasonic measurements will be taken of the core upon removal from aluminum tube to determine the change of p-wave velocity with change in water content. Water in the pores increases the effective compressibility of the rock therefore increasing the p-velocity. The measured p-wave velocities can then be used in the field to determine *in-situ* water content. Three dimensional x-ray images will be used to determine the deviations from average density within individual cores. Since the density depends on water content as well as mineralogy, images can show the location of pore fluid and drilling mud. Archimede's principle, humidity detection, ultrasonics and x-ray scanning are viable methods to measure the *in-situ* water content and pore water distribution in the graywacke.

Introduction

The Geysers geothermal plant in Northern California, the largest of its kind in the world, provides 10% of Northern California's power. Total production of The Geysers plant, established in the 1960's, began at 1990 MW, but steam decline has decreased

production to 1400 MW. Due to the steam decrease, LLNL and other interested groups are analyzing the geothermal rocks in order to predict the future performance and improve steam quality. Two projects have been proposed: 1000 ft continuous core retrieval of Geysers graywacke, the predominant rock, from defunct well, SB-15-D and later, a three year injection test into the same well to determine fluid flow paths using tracers. Every 100 ft of drilling, alternating 1.5 or 5 ft cores with diameter of 3.5 in. were enclosed in aluminum tubes to prevent water loss and immediately sent to the Lawrence Livermore National Lab for analysis. Approximately ten sealed cores were sent to the Lab. The objective of the coring project is to measure the liquid water content, porosity and permeability of the geothermal reservoir graywacke using density measurements, ultrasonics and x-ray tomography and radiography. These measurements will then be used to predict the future performance of the resource and improve steam quality.

Background

The rock cores recovered from well SB-15-D are "highly fractured, heavily veined, but weakly altered Franciscan graywacke with minor argillite."(Hulen, 1994) The graywacke's origin appears to be turbiditic as indicated by the graded beds, load structures and the interbedded argillite, a dark organic-rich shale which exhibits flame structures into the graywacke. An unfractured argillaceous graywacke caps the reservoir graywacke and prevents the steam from dissipating into the air. A felsite intrusion, at an elevation of -5000 ft, lies below the graywacke. Circulating ground water is heated to steam by the felsite intrusion. The reservoir has a volume of 650 cubic km and a thickness of 2000-2500 ft at an upper elevation of approximately -1500 ft. The steam pressure in the reservoir is 500 psi and at a temperature of approximately 235 C.

The Geysers plant uses a direct steam system because of the dry-steam reservoir. (See Figure 1) Dry-steam reservoirs are rare, and only three exist in the world: The Geysers, Yellowstone and Lassen. After removing contaminants, the steam from the reservoir travels through a system of pipes to a steam turbine. The expanding steam rotates the turbine shaft which powers the electric generator. The exhaust steam is

condensed and used either as cooling water and/or reinjected into the reservoir.(Adapted from Braun and McCluer, 1993.)

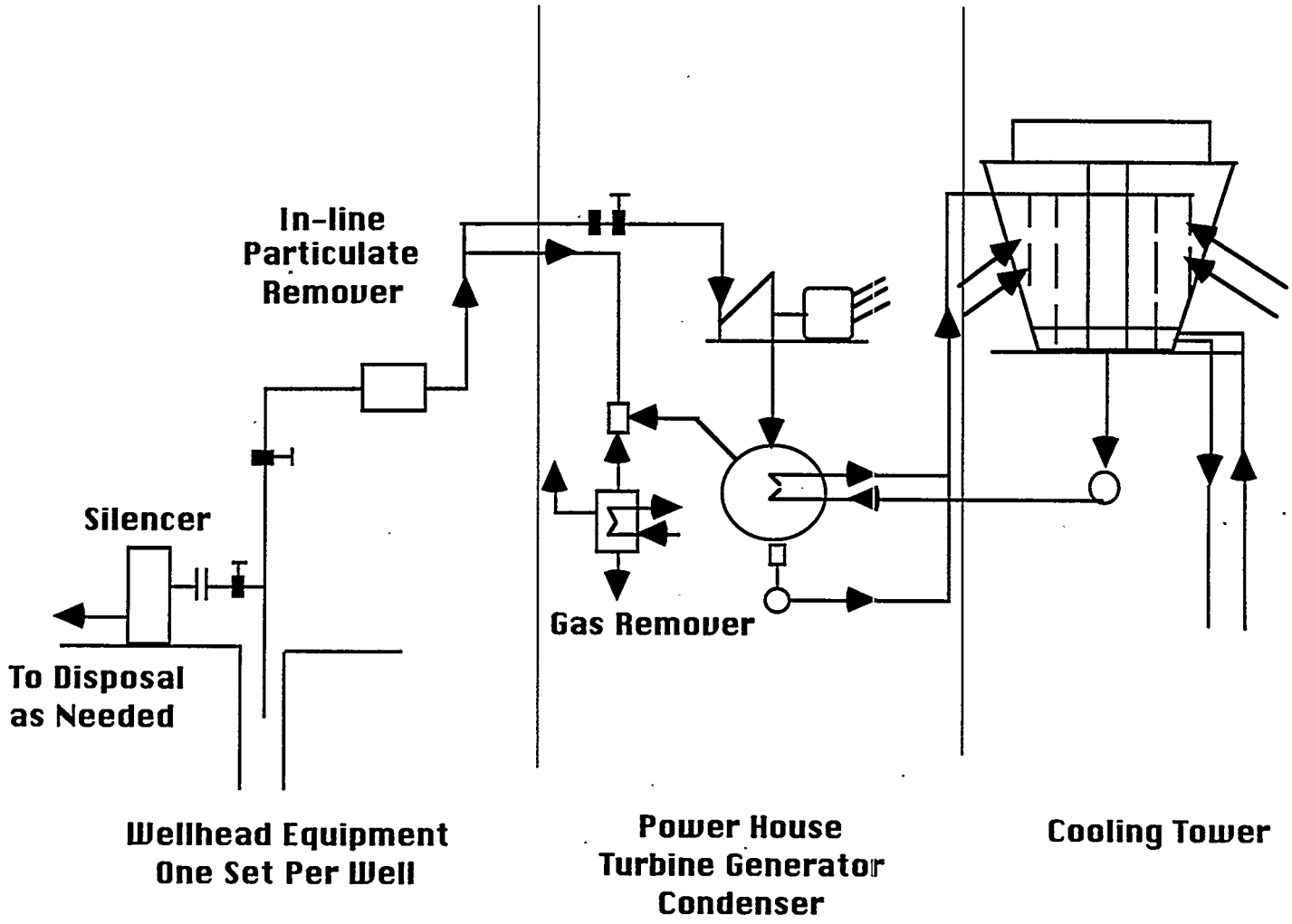

Figure 1: Dry steam geothermal plant.

Methods and Approach

The *in-situ* water content is an important characteristic of The Geysers graywacke because it tells us how much water resides in the pore spaces. We can compare the water content of the cores with changing depths and use these measurements for field seismic studies. Therefore we can characterize The Geysers reservoir with increasing depth.

Humidity Detection

The humidity detection apparatus was used to determine if the sealing of the recovered cores was effective. To do this, we measured the vapor saturation around the core in the aluminum tube. I helped design and build the apparatus.(Figure 3) First we glued a plastic tube to the aluminum lid. In the center of the tube Chantel drilled a hole in the aluminum. When drilling was completed we inserted the humidity probe and sealed it to the plastic tube with acupucky. Over a week period the humidity was checked. The humidity increased rapidly at first and then steadily increased until it reached approximately 100%.(See Figure 4) We performed this experiment on a one and a half ft core recovered from 918.9 ft, and we will use the graph as a comparison model for humidity experiments on deeper cores.

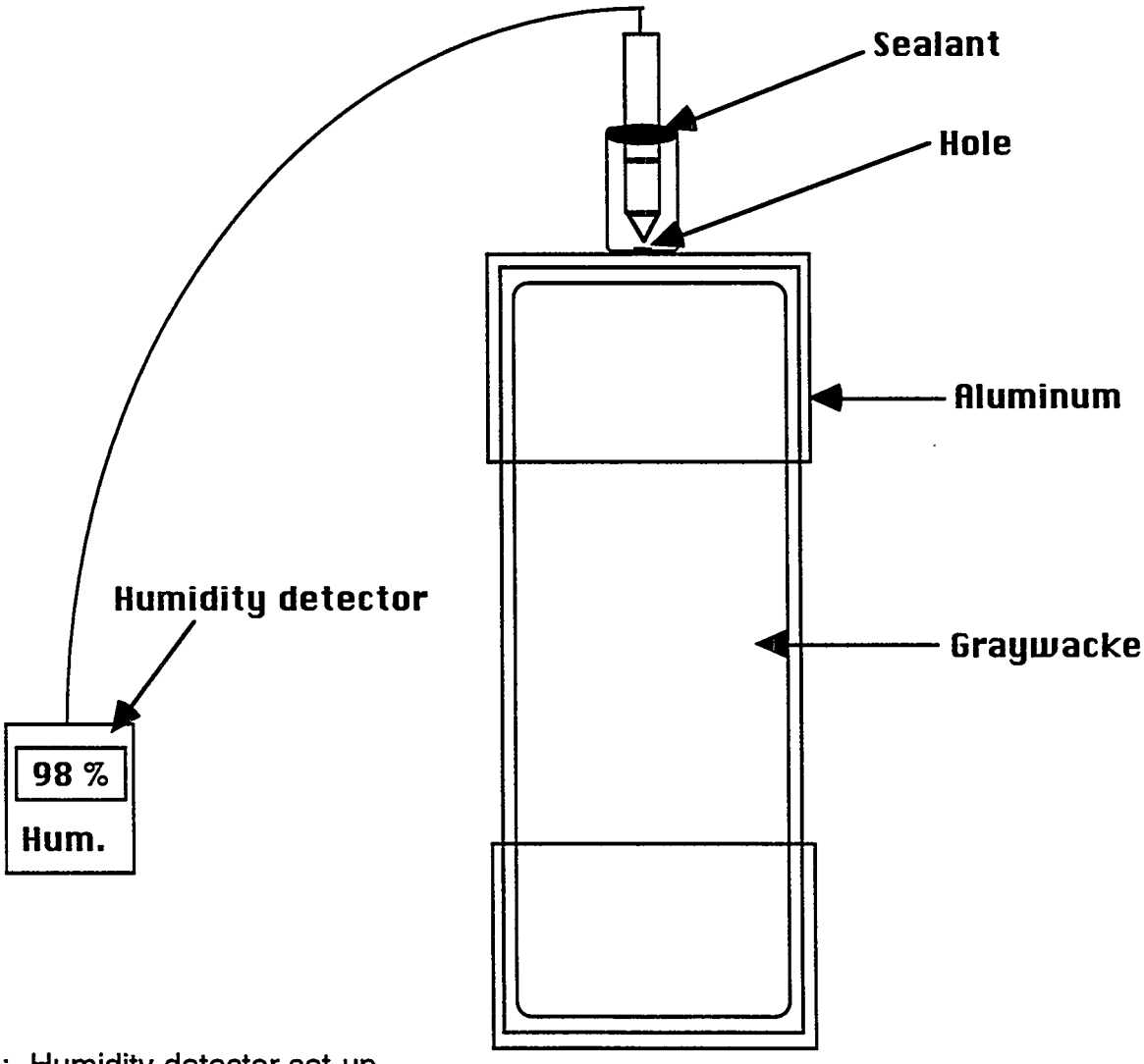

Figure 3: Humidity detector set-up

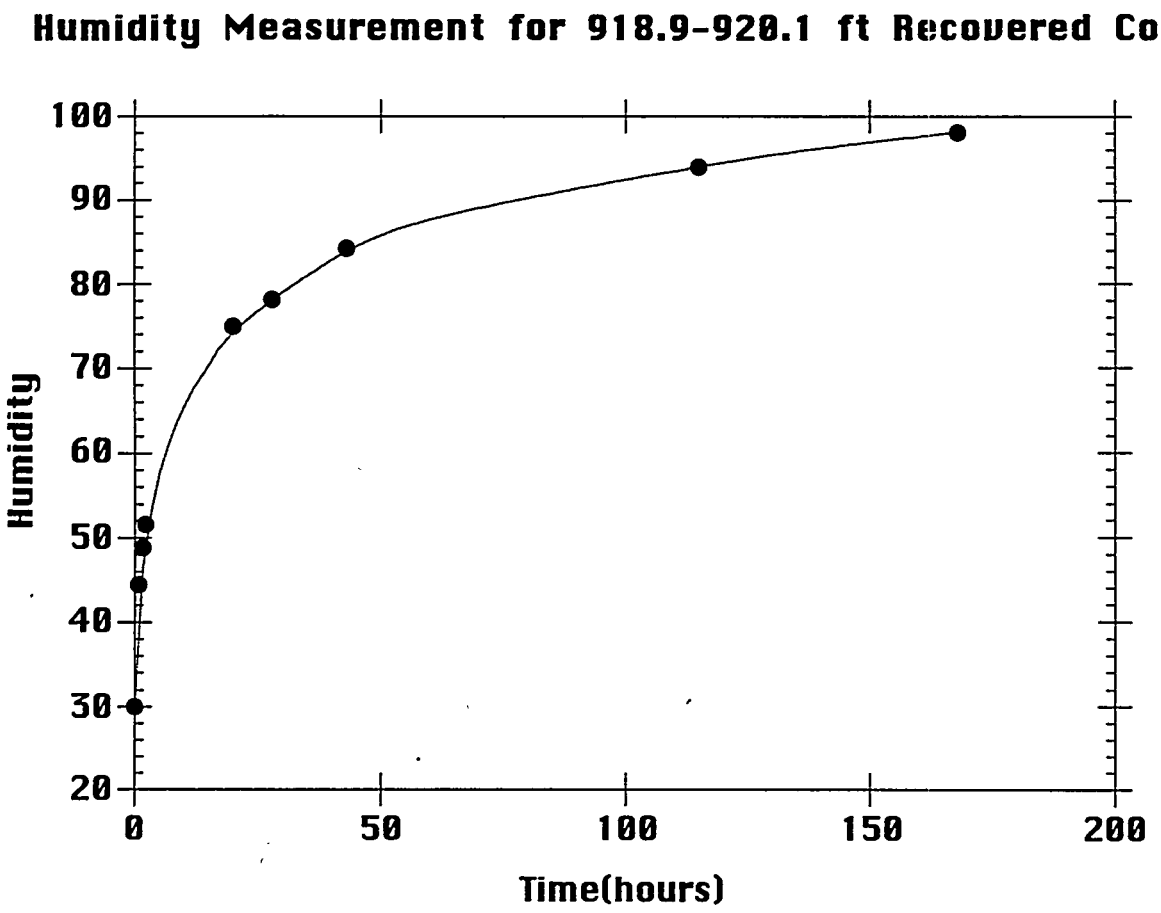

Figure 4: Humidity graph

Archimede's Principle

One way to measure the *in situ* water content of the graywacke core is to measure density using Archimede's principle. By placing the rock in a bucket of water, a volume of water will be displaced equal to the volume of the rock. Using the volume and the measured mass of the rock, the rock's density can be calculated. I designed and fabricated the apparatus to measure the volume of a sample.(Figure 2) To ensure maximum water displacement the two tubes were glued at 90 degrees to each other and, the water was filled to the upper edge of the tube connected to the bucket before I put the sample in the apparatus.

When the core is removed from the aluminum tube, I immediately will weigh the sample and measure the volume in the apparatus. Then the core will be dried out in an oven until the water content of the core is 0%. The core will be coated with a water seal to prevent water infiltration. Again weight and volume measurements will be taken. The

difference between the two measurements is the water content. The measurements will be performed on all cores retrieved, beginning with the 918.9 ft core.

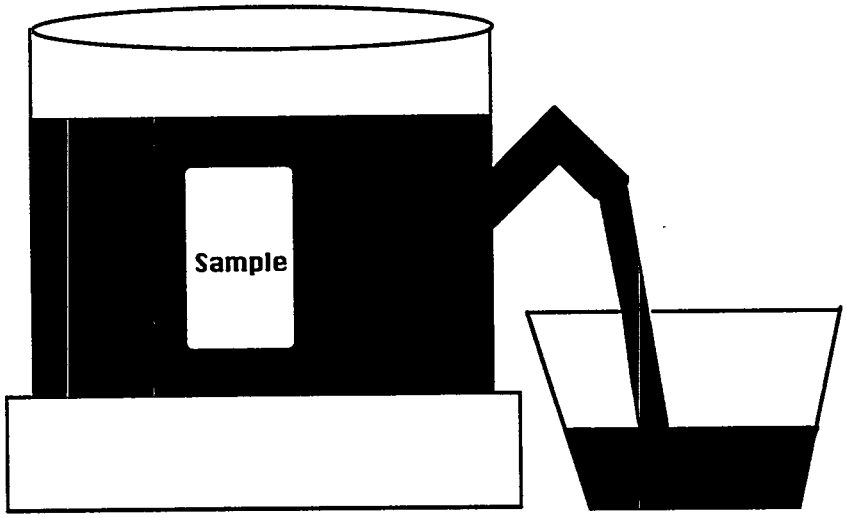

Figure 2: Archimede's principle

Ultrasonics

Using ultrasonic pulses on a rock sample of known length, the p-wave(compression) velocity can be determined.(Figure 5) A pulse generator triggers the timer and emits a high frequency electrical pulse to a piezoelectric transducer where the electric pulse is converted to a compressional mechanical pulse. This pulse travels through the rock sample and is converted back to an electric pulse by the piezoelectric receiver. The electric pulse is amplified and received by the digital oscilloscope which measures the time. The length of the sample divided by time gives the p-wave velocity.

P-waves are sensitive to water content: generally the higher the water content, the higher the velocity. First I will remove the core from the aluminum canister and weigh it. I will then place the rock between the transducers as illustrated in Figure 6 and measure the velocity. I will then evacuate and saturate the graywacke core to 100% water saturation and again place between the transducers. I will take continuous measurements of the velocity and the weight until velocity and weight remain constant. I will graph time vs. velocity and water content vs. velocity. This data can then be used in field seismic studies to determine the water content of the steam reservoir at different

depths. I have not measured the velocities of the cores yet, but I calibrated the oscilloscope by measuring the p-wave velocity of steel samples.

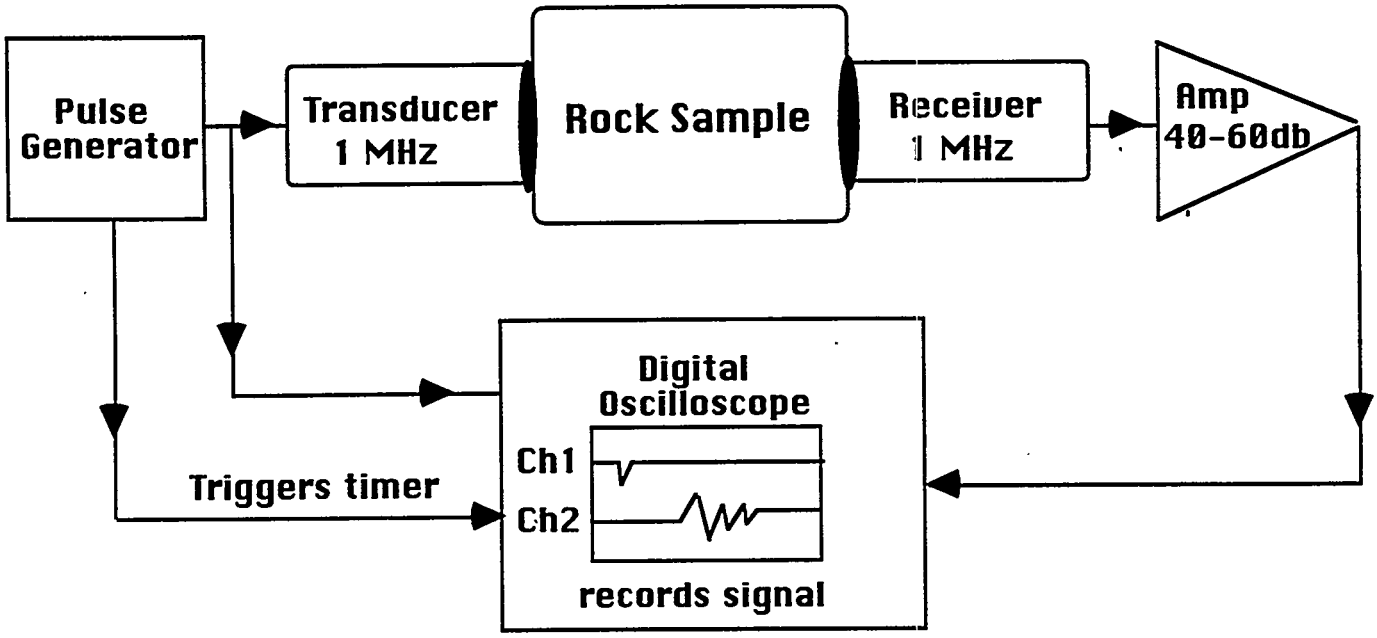

Figure 5: Ultrasonics set-up

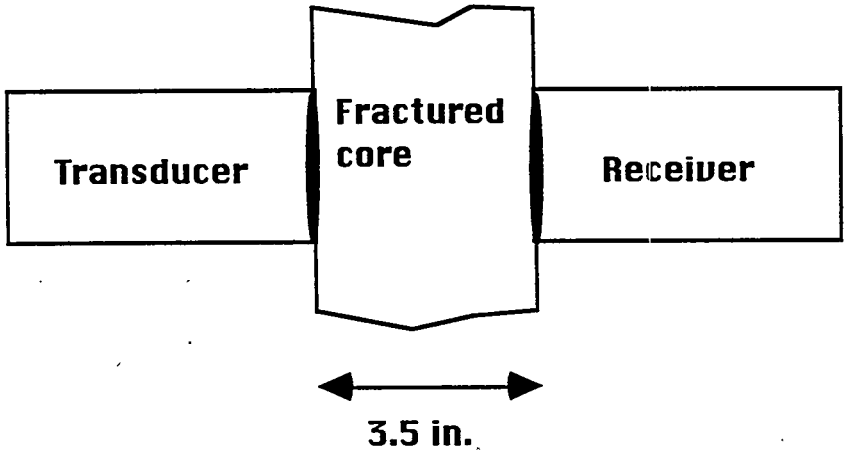

Figure 6: Fractured 3.5 in. diameter core(each recovered core has diameter of 3.5 in.)

Radiography and x-ray Computed Tomography

Radiography and x-ray computed tomography are used to study the *in situ* water content as well as the water distribution in The Geysers graywacke. Radiography is the

method of capturing images on a photograph.(Figure 7) The rotating sample is irradiated and depending on the density or thickness of the components of the sample the x-rays are absorbed differently. Tomography is an x-ray method that looks at one particular plane of an object, similar to a cross-section.(Figure 8) Once the camera captures the image, the picture is loaded into a computer and developed with software. X-rays are absorbed by an object depending on density: the greater the density, the greater the absorption of the x-rays.

All sealed cores, about ten, received at the Lab were irradiated. Included in this paper is the radiographs of cores recovered from 875.9 feet and 1420.5 feet.(Figure 9 and 10, respectively) Note: higher numbers on the image represent deeper part of core. The shallower core has substantially more fractures than the deeper core. We do not know if the fractures are filled with water or minerals. We will dry out the cores in an oven to remove all water from pores. Again the cores will be irradiated. We will then compare the two images for differences. Figure 11 is a computed tomographic image of the core recovered from 1420.5 ft(a slice through Figure 10). To the right center of the image is an asymmetric fold. The edges of the image are lighter than the center raising the question of drilling mud infiltration.

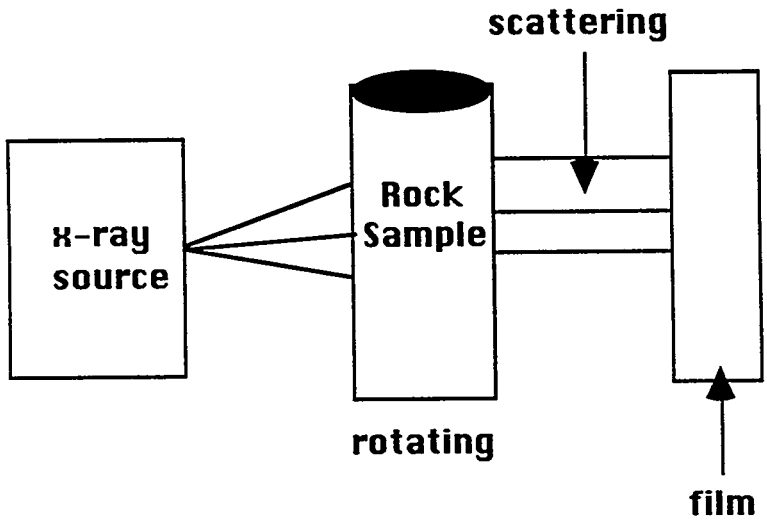

Figure 7: Radiography set-up

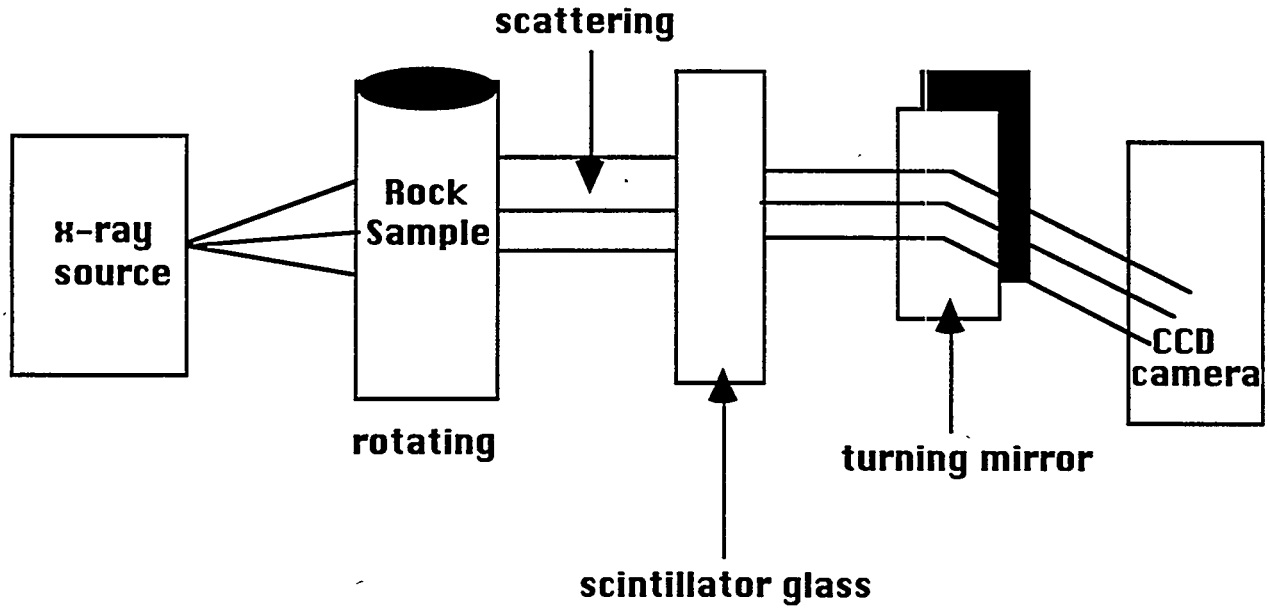

Figure 8: X-ray tomography set-up

Conclusion and Future Research

Density measurement using Archimede's principle, ultrasonics, radiography and x-ray computed tomography are viable methods for measuring and analyzing the water content of The Geysers graywacke. With the measured *in situ* water content and x-ray images, the reservoir graywacke can be characterized to use in predicting the lifetime of the reservoir. From the humidity detection experiment we discovered that the 918.9 ft core was sealed properly, and no water vapor escaped. Experiments need to be performed on the other cores to test the effective sealing. The cores remain in the aluminum casing to prevent water loss. The first core to be analyzed is one of the shallowest at 918.9 feet of depth. Using the density device and ultrasonics, we will measure the water content of this shallow core first. Measurements will be taken of all recovered cores, and hopefully we will be able to develop a detailed picture of The Geysers reservoir.

Figure 9

Run 7

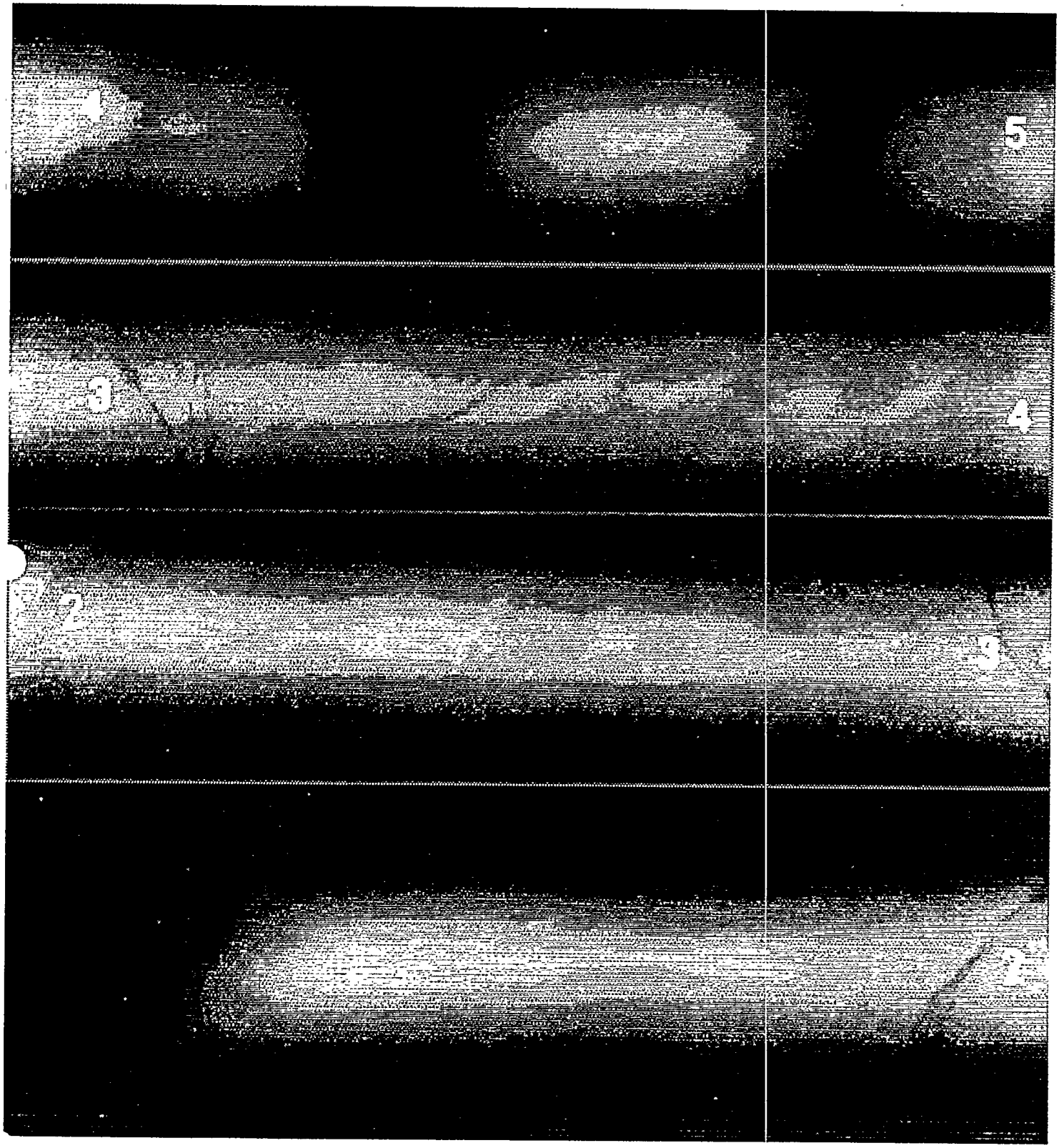

figure 10

Run 68

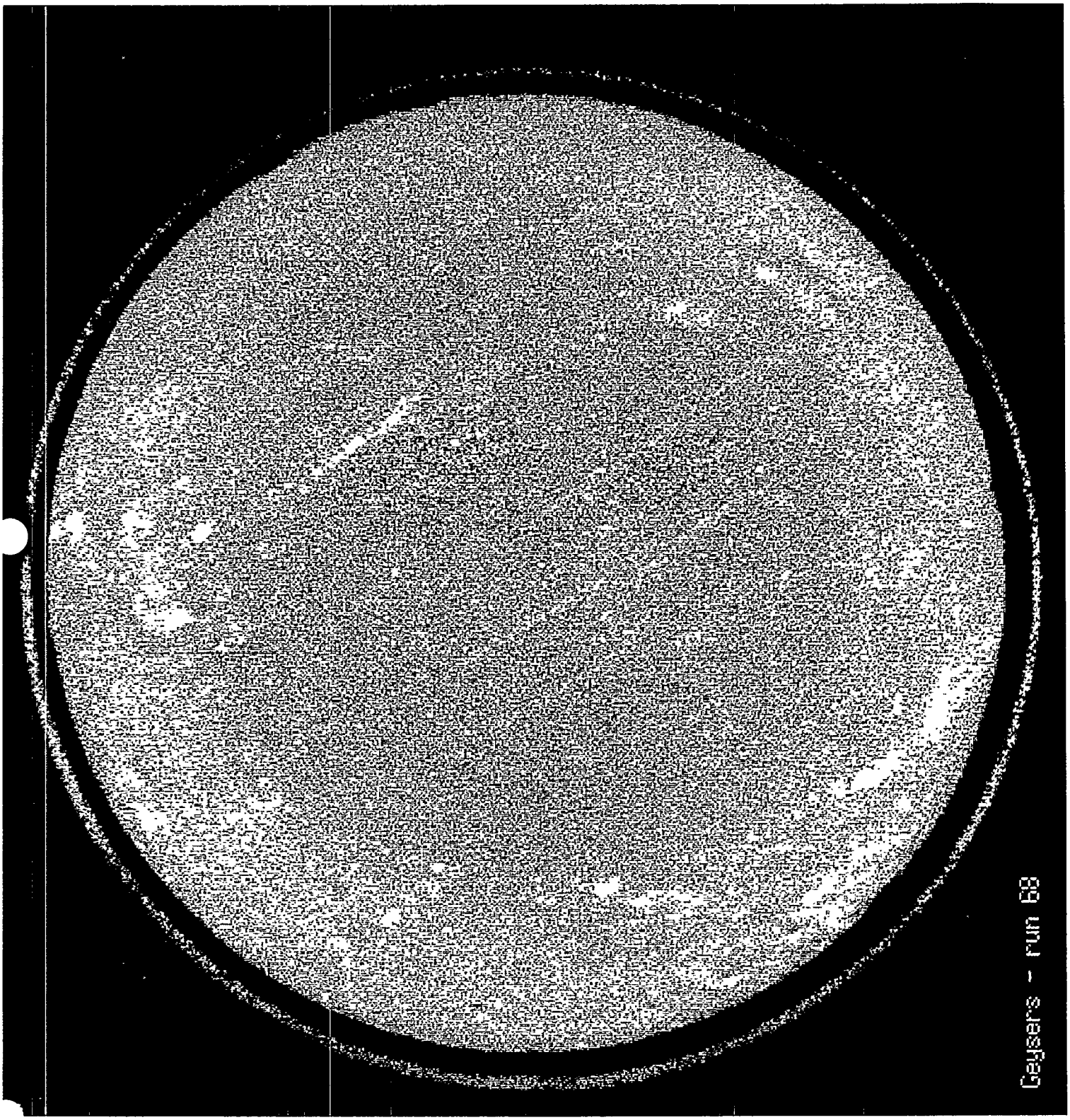

Figure 11

References

Braun, Gerald W. and McCluer, H. K. "Pete," 1993, Geothermal Power Generation in United States: Proceedings of the IEEE, vol. 81, p. 434-448.

Giancoli, Douglas C., 1991, *Physics, Third Edition:* Prentice-Hall, Englewood Cliffs, New Jersey.

Hulen, J. B., and Nielson, D. L., 1994, *Sample Handling, Field Procedures and Curation Guidelines for The Geysers Coring Project:* University of Utah Research Institute, Earth Science Laboratory Report.

Hulen, Jeff, November 11, 1994, *The Geysers Coring Project: Progress Report, Sept. 3 to Nov. 11, 1994.* : University of Utah Research Institute, Salt Lake City.

Rinehart, John S., 1980, *Geysers and Geothermal Energy:* Springer-Verlag, New York.

Roberts, J., Bonner, B., and Schneberk, D., 1994, Determining Water Content and Distribution in Reservoir Graywacke from the Northeast Geysers with X-ray Computed Tomography: Lawrence Livermore National Laboratory, Livermore, Ca.

The DSET Tool Library:

A software approach to enable data exchange between climate system models

Joe McCormick
California State University, Chico
Lawrence Livermore National Laboratory

ABSTRACT

Climate modeling is a computationally intensive process. Until recently computers were not powerful enough to perform the complex calculations required to simulate the earth's climate. As a result standalone programs were created that represent components of the earth's climate (e.g.Atmospheric Circulation Model). However, recent advances in computing, including massively parallel computing, make it possible to couple the components forming a complete earth climate simulation.

The ability to couple different climate model components will significantly improve our ability to predict climate accurately and reliably. Historically each major component of the coupled earth simulation is a standalone program designed independently with different coordinate systems and data representations. In order for two component models to be coupled, the data of one model must be mapped to the coordinate system of the second model. The focus of this project is to provide a general tool to facilitate the mapping of data between simulation components, with an emphasis on using object-oriented programming techniques to provide polynomial interpolation, line and area weighting, and aggregation services.

The DSET Tool Library:

A software approach to enable data exchange between climate system models

Joe McCormick
California State University, Chico
Lawrence Livermore National Laboratory

December 14, 1994

Mentors:
John Ambrosiano,
Lawerence Livemore National Lab, Global Climate Research Division

Celeste Matarazzo,
Lawrence Livermore National Lab, Computation Organization

Table of contents

Abstract

Climate modeling is a computationally intensive process. Until recently computers were not powerful enough to perform the complex calculations required to simulate the earth's climate. As a result standalone programs were created that represent components of the earth's climate (e.g.Atmospheric Circulation Model). However, recent advances in computing, including massively parallel computing, make it possible to couple the components forming a complete earth climate simulation.

The ability to couple different climate model components will significantly improve our ability to predict climate accurately and reliably. Historically each major component of the coupled earth simulation is a standalone program designed independently with different coordinate systems and data representations. In order for two component models to be coupled, the data of one model must be mapped to the coordinate system of the second model. The focus of this project is to provide a general tool to facilitate the mapping of data between simulation components, with an emphasis on using object-oriented programming techniques to provide polynomial interpolation, line and area weighting, and aggregation services.

1. Introduction

For over 20 years people have been asking questions about global warming, holes in the ozone, the effects of deforestation, and other questions that deal with the future global climate. These questions are impossible to solve manually, so computer models were created that would predict the earth's climate for hundreds or thousands of years. Historically, because of computational limitations, it was not possible to create one model that could represent the entire earth climate. Instead several different models were created representing specific elements of the earth's climate. Example models include Atmospheric Global Circulation Model (AGCM), Ocean Global Circulation Model (OGCM), and Land Surface Model. Each model is designed as a standalone program.

As development of these models continues they are reaching the limits of their reliability and accuracy, because they typically are run independently. In standalone, the models use simple methods to calculate values at their borders, where they should be interacting. An example of a border value is the sea surface temperature (**Figure 1**). Both the AGCM and OGCM influince the temperature of the ocean at the surface. Realism demands the component models be coupled, where coupling is defined as a dynamic interaction of models exchanging data at their borders. Once the models are coupled all of the information needed to calculate the border values, like sea surface temperature, accurately and reliably will be available.

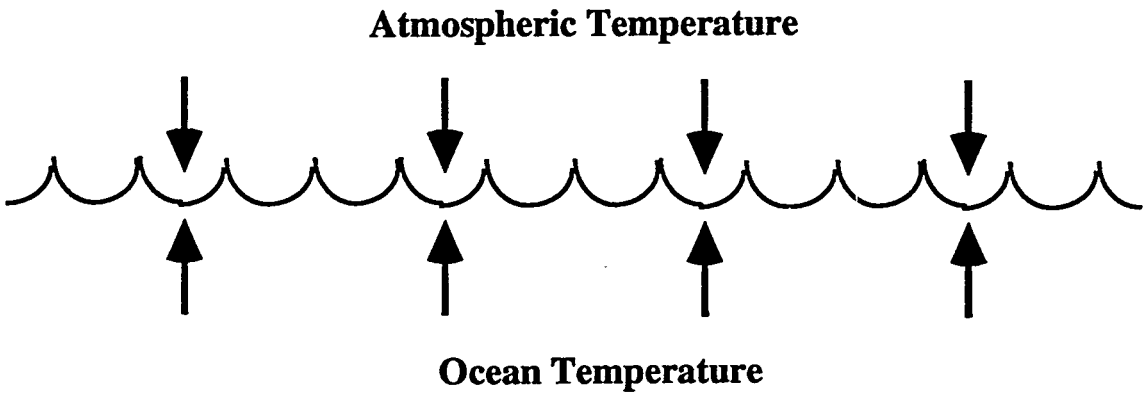

Figure 1. The sea surface acts as the border between the ocean and the atmosphere. Both the ocean and the atmosphere contribute to the temperature of the ocean surface.

Two things are necessary for coupling to be reasonable. First, we need fast computers that can perform the needed calculations in a reasonable amount of time. The computer time required to run a coupled version of the AGCM and OGCM for a 100 year prediction on a Cray C-90 is estimated to be 2000 hours. If 256 of the processors in a MEIKO or T3D are used the computer time requirements are estimated to drop below 400 hours. Second, we need a systematic method for coupling. One aspect of coupling is the exchange of data between models. Our project is to develop a code library that will provide the tools necessary to map data back and forth between models.

Since the component models were developed independently they each have there own way of representing their data. A particular representation is chosen for a given model based on consideration of computer time verses accuracy. Therefore some interpolation step is generally required for coupling.

Coupling can be thought of in two forms, tight and loose. A tight coupling can be used when the data representations of the models are the same. In a tight coupling data values are passed directly between the models. Loose coupling is needed when the data from a model must be transformed before it is usable by another model. The ocean, atmosphere link is an example of the latter.

To implement our library we decided to use object-oriented development techniques to create a systematic tool set for coupling. (Refer to Object-oriented Analysis and Design With Applications by Grady Booch for a discussion on object-oriented development.) The name we gave the code library is DSET. Packaging information in objects allows us to perform loose coupling systematically because the individual models will not need to know any information about another model's data representation. Also, the object-oriented design allowed us to make the DSET library flexible enough to accommodate many different data representations: gridded, ordered, tree, and scattered.

The DSET library is implemented in C rather than C++ for performance and portability reasons. This library will be required to run on a variety of platforms ranging from single processor machines to distributed work stations to 256 processor parallel machines. C++ code has been proven to run slower than code designed using object-oriented techniques and implemented in C. Also, the standards for C++ compilers are not as well developed as the C standards.

Currently the DSET library is capable of mapping data between any two rectangular coordinate systems up to four dimensions and can be accessed by either C, C++, or Fortran programs. Four methods are available to pass information: direct, polynomial interpolation,, integral weighting, and aggregation. This paper will cover the DSET library objects and give a simple program example showing how to use the DSET library.

2. Objects

This section describes the objects in the DSET library. Each object has a brief description about the physical object that it represents followed by a list of attributes and methods. Following the name of each attribute is its data type in parentheses. These conventions also apply:

AXIS	-Objects are capitalized and italicized.
name	-Attributes are lower case and italicized.
NORM	-Methods are capitalized.
target	-Instance variables are lower case bold.

2.1 AXIS

An *AXIS* represents a portion of the real number line. It is used to define the independent variables on a single dimension of a coordinate system. The attributes define the number, location, and values of the independent variables. The methods allow the access to the independent variables using either actual or relative values. For example, an *AXIS* knows that on a periodic domain defined between 0 and 2π the points $3\pi/2$, $7\pi/2$, $11\pi/2$, ... are all equal.

2.1.1 Attributes:

name(string)	-The name used to identify the *AXIS*.
num_nodes(integer)	-The number of nodes on the *AXIS*.
node_array(real)	-The array of node locations along the *AXIS*. The nodes must be in increasing order. At least one element of the *node_array* must be in the first period of the domain. Also, the distance between the first and last elements must be less than the

distance between *domain_min* and *domain_max*. **(Figure 2.)**

domain_min(real)	-The minimum domain value.
domain_max(real)	-The maximum domain value.
boundary_cond (flag)	-A flag telling if the *AXIS* is periodic or bounded.
window_min(real)	-The first node in *node_array*.
window_max(real)	-The last node in *node_array*.

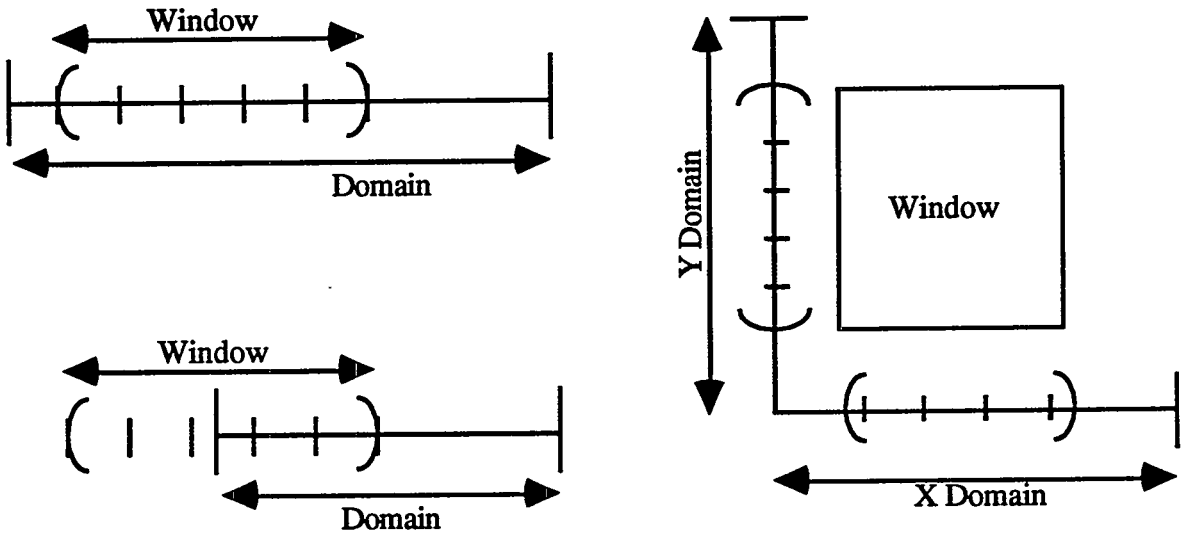

Figure 2. It is not necessary for the nodes to cover the entire domain on an *AXIS*. Also, it is possible for the node to extend beyond the first period of the domain.

2.1.2 Methods:

DEFINE_AXIS	-The *AXIS* constructor.
MID_LOCAL	-Locates the mid-point between two nodes.
NORM	-Moves a point to the first period of the domain.
FIND_CLOSEST_NODE	-Locates the node closest to any point.
FIND_INTERVAL	-Locates the nodes to the left and right of any point.
LOC	-Finds the node in *array_node* corresponding to any integer on a periodic *AXIS*..
NORM_INDEX	-Gets the array index for a node in *array_node* that corresponds to any integer on a periodic *AXIS*.

2.2 *GRID*

The *GRID* object represents a multidimensional coordinate system made up of the Cartesian cross products of the *AXIS* objects it contains.

2.2.1 Attributes:

name (string)	-The name used to identify the *GRID*.
shape (flag)	-The shape of the coordinate system. The shapes that have been implemented are spherical, geographic, and flat.
num_dimens (integer)	-The number of dimensions in the coordinate system. The legal range of values is 1 to 4.
axis_array (*AXIS*)	-An array containing *num_dimens AXIS* objects.

2.2.2 Methods:

DEFINE_GRID	-The *GRID* constructor.
AREA	-Calculates the area of a cell given its boundaries.
COVERED_AREA	-Calculates the overlapping area of two cells given their boundaries.

2.3 *DATA_ARRAY*

A *DATA_ARRAY* contains the values for the dependant variables. The attributes of a *DATA_ARRAY* help describe how to access the array.

2.3.1 Attributes:

name (string)	-The name used to identify the *DATA_ARRAY*.
data_array (void)	-A multidimensional array containing the values of the dependant variables.
type (flag)	-Defines the type of data stored in the array. Both reals and integers are valid data types.
num_dimens (integer)	-The number of dimensions in *DATA_ARRAY*. The legal range of values is 1 to 4.
num_elem_array (integer)	-The number of data elements in each dimension.

2.3.2 Methods:

DEF_DATA_ARRAY	-The *DATA_ARRAY* constructor.
GET_ARRAY_VAL	-Retrieves a data element from a *DATA_ARRAY.*
PUT_ARRAY_VAL	-Places a data element in a *DATA_ARRAY.*

2.4 *DSET_OBJECT*

The *DSET_OBJECT* puts the values of the dependant variables in a *DATA_ARRAY* on top of the independent variables of a *GRID.* In order to put a *DATA_ARRAY* on top of a *GRID* they must have the same dimensionality. Also they must also have the same number of nodes in each dimension. The methods for a *DSET_OBJECT* perform the loose coupling between climate models. In the cases that tight coupling is applicable the *DSET_OBJECT* or *DATA_ARRAY* can just be passed from one model to another.

2.4.1 Attributes:

DATA_ARRAY (string)	-The name of the *DATA_ARRAY* to place on top of a *GRID.* This is also the name used to identify the *DSET_OBJECT.*
GRID (string)	-The name of the *GRID* to lay the *DATA_ARRAY* on.

2.4.2 Methods:

DEFINE_DSET	-The *DSET_OBJECT* constructor.
INTERP_POINT	-The interpolation algorithm relies on Chebychev's polynomial interpolation functions to determine the value of a target node from a source *DSET_OBJECT.*
INTERP_DSET	-Performs point interpolation from a source *DSET_OBJECT* to a target *DSET_OBJECT.*
AREA_WEIGHT_CELL	-Area weighting calculates a weighted average value for the target cell from the overlapped source cells. Note: Each *AXIS* node is defined as a cell center with cell wall at the mid-point between its neighboring nodes. Also, this method has also only been implemented for one and two dimensional objects. (**Figure 3.**)

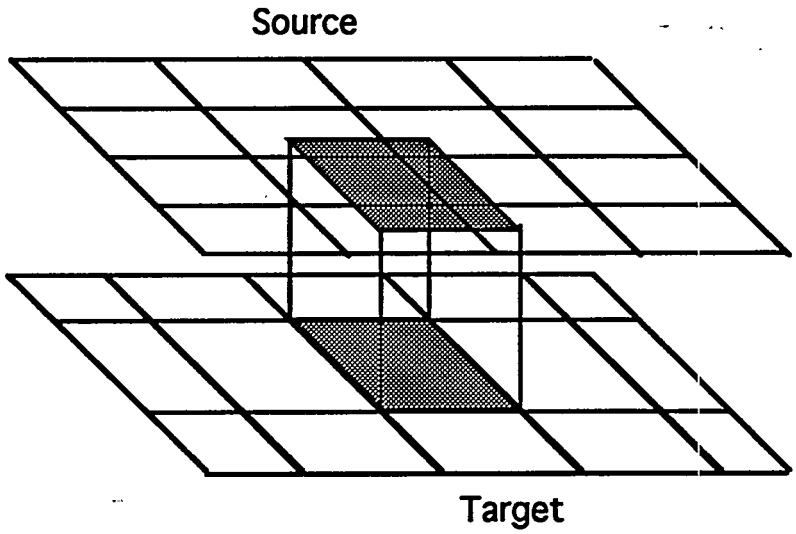

Figure 3. The source cells that are overlapped by the target cell.

AREA_WEIGHT_DSET -Performs integral weighting to map data from a source *DSET_OBJECT* to a target *DSET_OBJECT*. At this point integral weighting has only been implemented for only one and two dimensional objects.

AGGREGATE_CELL -Aggregation assigns the discrete value of the source cell that covers the largest area of the target cell. Aggregation is used when the data represents discrete types such as vegetation types: grass lands, desert, or forest.

Example: The total area of a source DSET_OBJECT covered by a target cell is 20 and the area of the source is distributed as follow:

Area	Aggregate
1	Ocean
5	Forest
5	Brush
10	Desert

because the largest area is covered by desert the target cell would receive desert as its value.

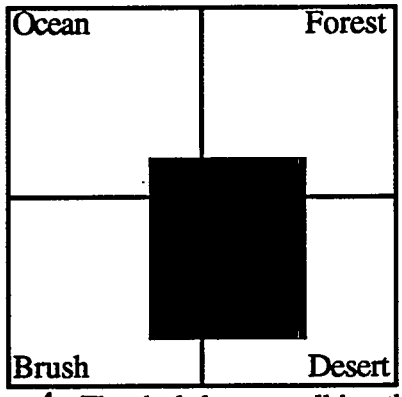

Figure 4. The shaded target cell has the most area in the Desert source cell.

We defined each *AXIS* node to be a cell center with cell wall at the mid-point between its neighboring nodes. At this point aggregation is only available for two dimensional objects.

AGGREGATE_DSET -Allows discrete data types to be mapped from a source *DSET_OBJECT* to a target *DSET_OBJECT*.

3. Example

This is a simple program that maps the data on a source coordinate system to a target coordinate system using linear interpolation and area weighting. The source coordinate system is defined on the real interval [0,8] in both the X and Y directions. The target coordinate system is defined for X and Y on the real interval [2,4]. Both the target and source have five nodes on each axis. The output from the program is after the code. The program is written in C but could also have been written in Fortran. The complete program and output is in Appendix A.

3.1 Code

The header file `dset.h` must be included in any C or C++ program that uses the DSET library. The `dset.h` file contains the definitions for the valid flag constants: *DATA_ARRAY.type*, *GRID->shape*, and *AXIS->boundry_cond.*

```
#include "dset.h"
```

This block of code defines the constants that will be used to create the target and source objects. `NUM_NODES` is used to define the number of nodes along each axis of the target and source coordinate systems. In this example all of the coordinate axes contain five nodes. The window and domain of the source in both dimensions will be the interval [0,8] on the reals. For the target window and domain the interval [2,4] on the real line will be used in both directions.

```
#define NUM_NODES 5
#define SOURCE_WINDOW_MIN 0.0
#define SOURCE_WINDOW_MAX 8.0
#define SOURCE_WINDOW SOURCE_WINDOW_MIN,SOURCE_WINDOW_MAX
#define SOURCE_DOMAIN SOURCE_WINDOW
#define TARGET_WINDOW_MIN 2.0
#define TARGET_WINDOW_MAX 4.0
#define TARGET_WINDOW TARGET_WINDOW_MIN,TARGET_WINDOW_MAX
#define TARGET_DOMAIN TARGET_WINDOW
```

The memory for the data arrays and the axis arrays must be created and initialized before it can be used by the DSET library.

```
main()
{
  double source_data[NUM_NODES][NUM_NODES];
  double target_data[NUM_NODES][NUM_NODES];
  double source_axis_array[NUM_NODES];
  double target_axis_array[NUM_NODES];
```

```
make_axis_array(source_axis_array,SOURCE_WINDOW,NUM_NODES);
make_axis_array(target_axis_array,TARGET_WINDOW,NUM_NODES);
source_data = fill_array(NUM_NODES,SOURCE_WINDOW,NUM_NODES,
                         SOURCE_WINDOW);
```

A call to the functions `init_dset` is required to initialize the lookup tables, open the error output file, and other run time support for the DSET library objects.

```
init_dset();
```

The following section shows the function calls that create the target and source objects. First an *AXIS* is defined. Then the *AXIS* is used to define a *GRID*. A *DATA_ARRAY* object is created. Finally the *GRID* and *DATA_ARRAY* are combined to form a *DSET_OBJECT*.

```
DEFINE_AXIS("source axis",NONUNIFORM,BOUNDED,LINEAR,NUM_NODES,
            source_axis_array[0],source_axis_array[NUM_NODES-1],0.0,
            source_axis_array,SOURCE_DOMAIN);
DEFINE_GRID("source grid",FLAT,DEGREE,2,"source axis","source axis");
DEF_DATA_ARRAY("source",DOUBLE,source_data,2,0,NUM_NODES,0,NUM_NODES);
DEFINE_DSET("source","source grid");

DEFINE_AXIS("target axis",NONUNIFORM,BOUNDED,LINEAR,NUM_NODES,
            target_axis_array[0],target_axis_array[NUM_NODES-1],0.0,
            target_axis_array,TARGET_DOMAIN);
DEFINE_GRID("target grid",FLAT,DEGREE,2,"target axis","target axis");
DEF_DATA_ARRAY("target",DOUBLE,target_data,2,0,NUM_NODES,0,NUM_NODES);
DEFINE_DSET("target","target grid");
```

After the objects needed by the DSET library are created they can be used to perform complicated tasks with a single function call. The following two lines of code use linear interpolation and area weighting to estimate values from the source to the target *DSET_OBJECTS*.

```
INTERP_DSET("target","source");
AREA_WEIGHT_DSET("target","source");
```

Before the end of a program that uses the DSET library the function CLOSE_ERROR_OUT must be called. CLOSE_ERROR_OUT closes the DSET output files and performs other clean up operations on the DSET objects.

```
  CLOSE_ERROR_OUT();
}
```

3.2 Input and Output

For the sample program above the source data array was filled with the following values:

```
source defined on [0,8]X[0,8]
4.000   9.000   14.000   19.000   24.000
3.000   8.000   13.000   18.000   23.000
2.000   7.000   12.000   17.000   22.000
1.000   6.000   11.000   16.000   21.000
0.000   5.000   10.000   15.000   20.000
```

Here is the program output after interpolation from source to target.

```
target defined on [2,4]X[2,4] interpolated from source
7.000   8.250   9.500   10.750   12.000
6.750   8.000   9.250   10.500   11.750
6.500   7.750   9.000   10.250   11.500
6.250   7.500   8.750   10.000   11.250
6.000   7.250   8.500    9.750   11.000
```

This is the program output for area weighting from source to target.

```
target defined on [2,4]X[2,4] area weighted from source
7.000   7.000   9.500   12.000   12.000
7.000   7.000   9.500   12.000   12.000
6.500   6.500   9.000   11.500   11.500
6.000   6.000   8.500   11.000   11.000
6.000   6.000   8.500   11.000   11.000
```

4. Conclusion

The DSET library is a useful tool for coupling models with different grid representations. Though far from comprehensive, (supporting at present only rectalinear grids.) the foundation for development is well established. The DSET library presently contain enough utilities to couple models that comprise the global climate system applications, the application for which it was intended. The object-oriented design of the library makes it possible to be expanded in the future to accommodate any model. This last section will cover some of the ways the DSET library is presently being expanded and could conceivably be expanded in the future.

The current version of the DSET library does not perform integral weighting, polynomial interpolation, or aggregation fast enough for the amount of information passed in coupled climate models. Presently, each time models want to share information, the relationship between their coordinate systems must be recalculated. Determining the relationship between coordinate systems consumes over 50% of the time taken to perform any of the information passing algorithms. To speed these algorithms up we have introduced a new object named *CHANNEL*. A *CHANNEL* stores the information about the relationship between two *GRID* (i.e. coefficients, interaction lists, etc.) objects for integral weighting, interpolation, and aggregation. The first tests have shown that using a *CHANNEL* make the method AREA_WEIGHT_DSET over 75% faster. The time savings due to the *CHANNEL* object should be enough to make the overhead for climate model coupling acceptable.

Some additions to the library that build on the existing methods would help round out the library. The method VOLUME_WEIGHT_DSET could be developed from AREA_WEIGHT_DSET to perform integral weighting on three dimension coordinate systems. Also, AGGREGATE_DSET can be expanded to work with one and three dimensional *DSET_OBJECT*s.

The development for the DSET library is only beginning and the possibilities for expanding the library are limitless. One direction we are investigating for expanding the DSET library is developing tool sets that are not based on rectalinear coordinate systems. Some examples of data representations we have considered are curvalinear coordinate systems, spherical coordinate systems, tree structures and scattered data. Also, we are considering a DSET library designed to run on parallel computers. We are continually reevaluating the DSET objects in order to expand the functionality of the library.

5. Appendix A -Sample Code

This is the complete code and output for the sample program presented above.

```
#include "dset.h"

#define NUM_NODES 5
#define SOURCE_WINDOW_MIN 0.0
#define SOURCE_WINDOW_MAX 8.0
#define SOURCE_WINDOW SOURCE_WINDOW_MIN,SOURCE_WINDOW_MAX
#define SOURCE_DOMAIN SOURCE_WINDOW
#define TARGET_WINDOW_MIN 2.0
#define TARGET_WINDOW_MAX 4.0
#define TARGET_WINDOW TARGET_WINDOW_MIN,TARGET_WINDOW_MAX
#define TARGET_DOMAIN TARGET_WINDOW

double *fill_array(num_x,min_x,max_x,num_y,min_y,max_y)
     int num_x;
     double min_x;
     double max_x;
     int num_y;
     double min_y;
     double max_y;
{
  double *F;
  int i,j,k = 0;
  double x = min_x;
  double y = min_y;
  double del_x = (max_x - min_x) / num_x;
  double del_y = (max_y - min_y) / num_y;

  BA_DIM2D(F,double,num_x,num_y);

  for (i=0; i < num_y; ++i)
    for (j=0; j < num_x; ++j)
      {
      F[k] = k;
      ++k;
      }
  return(F);
}

void make_axis_array(array,min,max,num_x)
     double array[ ];
     double min;
     double max;
     int num_x;
{
  int i;
  double del_x = (max-min)/(num_x-1);
  double x = min;

  for(i=0; i < num_x; ++i)
```

```
    {
      array[i] = x;
      x += del_x;
    }
}

void make_data_sets(source_data,target_data)
      double *source_data;
      double *target_data;
{
  static double source_axis_array[NUM_NODES];
  static double target_axis_array[NUM_NODES];

  make_axis_array(source_axis_array,SOURCE_WINDOW,NUM_NODES);
  source_data = fill_array(NUM_NODES,SOURCE_WINDOW,NUM_NODES,
                           SOURCE_WINDOW);

  DEFINE_AXIS("source axis",NONUNIFORM,BOUNDED,LINEAR,NUM_NODES,
              source_axis_array[0],source_axis_array[NUM_NODES-1],0.0,
              source_axis_array,SOURCE_DOMAIN);
  DEFINE_GRID("source grid",FLAT,DEGREE,2,"source axis","source axis");
  DEF_DATA_ARRAY("source",DOUBLE,source_data,2,0,NUM_NODES,0,NUM_NODES);
  DEFINE_DSET("source","source grid");

  make_axis_array(target_axis_array,TARGET_WINDOW,NUM_NODES);
  BA_DIM2D(target_data,double,NUM_NODES,NUM_NODES);

  DEFINE_AXIS("target axis",NONUNIFORM,BOUNDED,LINEAR,NUM_NODES,
              target_axis_array[0],target_axis_array[NUM_NODES-1],0.0,
              target_axis_array,TARGET_DOMAIN);
  DEFINE_GRID("target grid",FLAT,DEGREE,2,"target axis","target axis");
  DEF_DATA_ARRAY("target",DOUBLE,target_data,2,0,NUM_NODES,0,NUM_NODES);
  DEFINE_DSET("target","target grid");
}

void output_results(target_data,source_data)
     double target_data[NUM_NODES][NUM_NODES];
     double source_data[NUM_NODES][NUM_NODES];
{
  int i,j;

  printf("source defined on [0,8]X[0,8]\n");
  for (i=NUM_NODES; i > 0; --i)
    {
      for (j=0; j < NUM_NODES; ++j)
      printf("%5.3f  ",source_data[i][j]);
      printf("\n");
    }

  printf("\n\n\n");
  printf("target defined on [2,4]X[2,4] interpolated from source\n");
  for (i=NUM_NODES; i > 0; --i)
    {
      for (j=0; j < NUM_NODES; ++j)
```

```
      printf("%5.3f  ",target_data[i][j]);
      printf("\n");
    }
  printf("\n\n\n");
}

main()
{
  double source_data[NUM_NODES][NUM_NODES];
  double target_data[NUM_NODES][NUM_NODES];

  init_dset();

  make_data_sets(source_data,target_data);

  INTERP_DSET("target","source");
  output_results("target","source");

  AREA_WEIGHT_DSET("target","source");
  output_results(target_data,source_data);

  CLOSE_ERROR_OUT();
}
```

```
source defined on [0,8]X[0,8]
4.000   9.000   14.000   19.000   24.000
3.000   8.000   13.000   18.000   23.000
2.000   7.000   12.000   17.000   22.000
1.000   6.000   11.000   16.000   21.000
0.000   5.000   10.000   15.000   20.000


target defined on [2,4]X[2,4] interpolated from source
7.000   8.250   9.500   10.750   12.000
6.750   8.000   9.250   10.500   11.750
6.500   7.750   9.000   10.250   11.500
6.250   7.500   8.750   10.000   11.250
6.000   7.250   8.500   9.750   11.000


source defined on [0,8]X[0,8]
4.000   9.000   14.000   19.000   24.000
3.000   8.000   13.000   18.000   23.000
2.000   7.000   12.000   17.000   22.000
1.000   6.000   11.000   16.000   21.000
0.000   5.000   10.000   15.000   20.000
```

```
target defined on [2,4]X[2,4] area weighted from source
7.000   7.000   9.500   12.000   12.000
7.000   7.000   9.500   12.000   12.000
6.500   6.500   9.000   11.500   11.500
6.000   6.000   8.500   11.000   11.000
6.000   6.000   8.500   11.000   11.000
```

Nanomechanical properties of SiC films grown from C_{60} precursors using atomic force microscopy

Kathryn Morse
Engineering Department
Colorado School of Mines
Golden, CO 80401

M. Balooch, A. V. Hamza, and J. Belak
University of California
Lawrence Livermore National Laboratory
Livermore, CA 94550

ABSTRACT

The mechanical properties of SiC films grown via C_{60} precursors were determined using atomic force microscopy (AFM). Conventional silicon nitride and modified diamond cantilever AFM tips were employed to determine the film hardness, friction coefficient, and elastic modulus. The hardness is found to be between 26 and 40 GPa by nanoindentation of the film with the diamond tip. The friction coefficient for the silicon nitride tip on the SiC film is about one third that for silicon nitride sliding on a silicon substrate. By combining nanoindentation and AFM measurements an elastic modulus of ~300 GPa is estimated for these SiC films. In order to better understand the atomic scale mechanisms that determine the hardness and friction of SiC, we simulated the molecular dynamics of a diamond indenting a crystalline SiC substrate.

Introduction

Microelectromechanical systems (MEMS) field is growing rapidly now that the technology is present to create and use these silicon-based devices.[Howe] Sensors, actuators, resonators, and even motors, a few microns in size, are examples of the devices that have been manufactured using standard silicon processing technology. The MEMS act as the microtechnology interface between electronics and the physical world. This technology will be a driver in the ever expanding use of microtechnology in modern society.

Currently these devices are manufactured from silicon and polysilicon. The operating life of some of these devices is limited (somewhat severely) by the wear properties of the contacting surfaces. The silicon with its native oxide used in demonstration devices wears quickly, and limits the use of these devices. Friction characteristics of the silicon produce wear via energy deposition [41].

Silicon Carbide is a possible solution to this friction and wear problem. Silicon carbide has a very high hardness and high elastic modulus, suggesting it would have low friction coefficients and excellent wear properties. Producing MEMS devices requires the processing technology for manufacturing microcomponents to be incorporated in the structure. Thus, incorporating SiC in MEMS devices requires a silicon carbide technology capable of producing or coating microcomponents.

Recently, the growth and manufacture of microcomponents of SiC by a technique compatible with present silicon processing technology has been demonstrated by Balooch and co-workers [hamza, balooch]. Briefly, the properties of the fullerene C_{60} are used to react the C_{60} with silicon selectively at substrate temperatures between 950 and 1200 K. The selectivity results from the much higher reaction probabilities for C_{60} with silicon than with silicon dioxide. This film can be easily coated on the Si gears, or whole objects can be turned into SiC with this new method of growing SiC thin films [1]. These thin films can be patterned easily to either fabricate these devices or coat them precisely.

Patterned SiC films can be produced by making use of the high reaction probability of C_{60} with silicon at surface temperatures greater than 950 K and the negligible reaction probability for C_{60} on silicon dioxide at surface temperatures less than 1200 K[8]. The

silicon dioxide layer is patterned using standard lithographic techniques to produce areas of silicon and areas of silicon dioxide. Then in ultra-high vacuum (UHV) the sample is heated to 1200 K to clean off the native silicon oxide on the silicon areas. The surface is heated to 1100 K and exposed to C_{60} to grow the SiC thin film. The sample is then removed from UHV and placed in concentrated HF acid to remove the silicon dioxide film.

Because of its favorable properties, and ease of patterning, there are many applications for this thin film from C_{60}. Microsensors located in car engine cylinders to regulate the air/gas mixture, making the engine more efficient, would be useful in the automotive industry. SiC micro sensors can withstand the harsh environment. Currently, accelerometers in hard disk drives, that lock the head in place when the drive is falling, are made from silicon. Upon impact some of the locks fail and the head hits the disk. These locks could be made from the potentially harder, stronger SiC. As these disk drives get smaller and smaller with the growth of technology, the sliders for the hard disk drives are getting smaller too. They could easily be patterned and constructed to any size with SiC. Once the mechanical properties are known, many applications can be found for thin film SiC grown via C_{60}.

In order to justify the new material for these devices, the mechanical properties must be better than the current silicon. The mechanical properties that must be improved for longer life of the devices, are the coefficient of friction, hardness, and the elastic modulus. We measured these properties with modified AFMs and a Nanoindenter. In this report, we describe the three types of AFMs and the Nanoindenter used. We will also describe the film and the mechanical properties, hardness, elastic modulus , coefficient of friction, and the porosity of the film.

Background

C_{60}

We grow SiC thin films from C_{60} precursors. C_{60}, also known as "Buckyballs" after the architect Buckminster Fuller, is a new stable form of carbon first produced in gram quantities in 1990. The structure of the ball mimics soccer balls composed of 60 carbon atoms that form 12 pentagon and 20 hexagon faces. See Figure 1. C_{60} is a one nanometer diameter cage and is stable in this form up to temperatures of 950K. Above this temperature the balls open and become reactive [balooch]. We use temperatures above

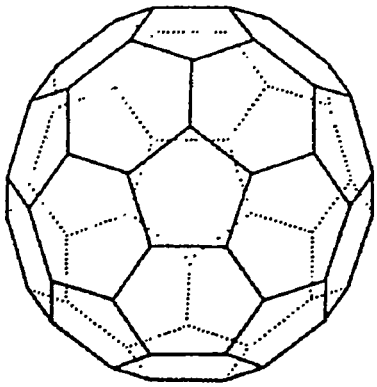

Figure 1 - C60 or 'buckyballs' have 60 carbon atoms that form 12 pentagon and 20 hexagon faces.

950K when growing SiC, so the C_{60} opens and reacts with a silicon surface to form SiC [hamza].

Process

The setup and procedure for growing SiC from C60 precursors are described by Hamza and Balooch [1, hamza]. Our SiC is grown in a vacuum chamber at 10^{-9} torr. A silicon wafer is heated to 1250 Kelvin and an Auger electron spectra (AES), Figure 2, ensures a clean surface. The knudsen cell filled with C_{60} powder is heated by the spectra-mat button heater, and the C_{60} sublimes. See the setup in Figure 3. The balls travel through the pin holes of the cell and onto the surface of the heated silicon sample. The high temperature silicon allows the C_{60} balls to open and react with the surface to form SiC. Another AES, Figure 2, indicates the SiC surface is stoichiometric, meaning there is one carbon atom for one silicon atom. The sample is then removed from the vacuum chamber and is ready for measurement of the film mechanical properties.

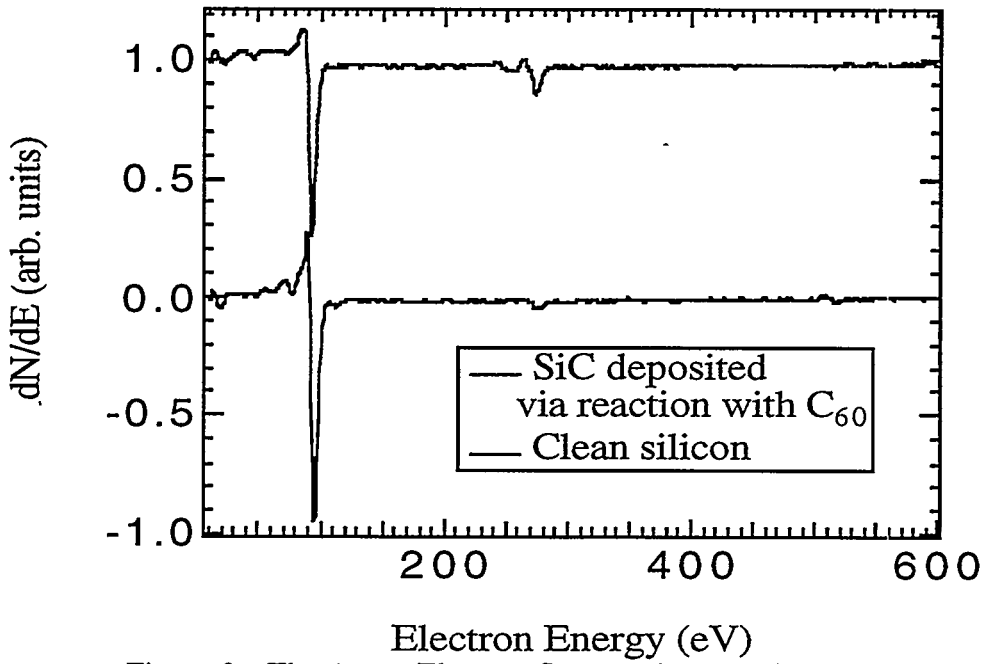

Figure 2 - The Auger Electron Spectra shows a clean silicon surface with few impurities. Slightly offset is the AES for the stoichiometric SiC of our film.

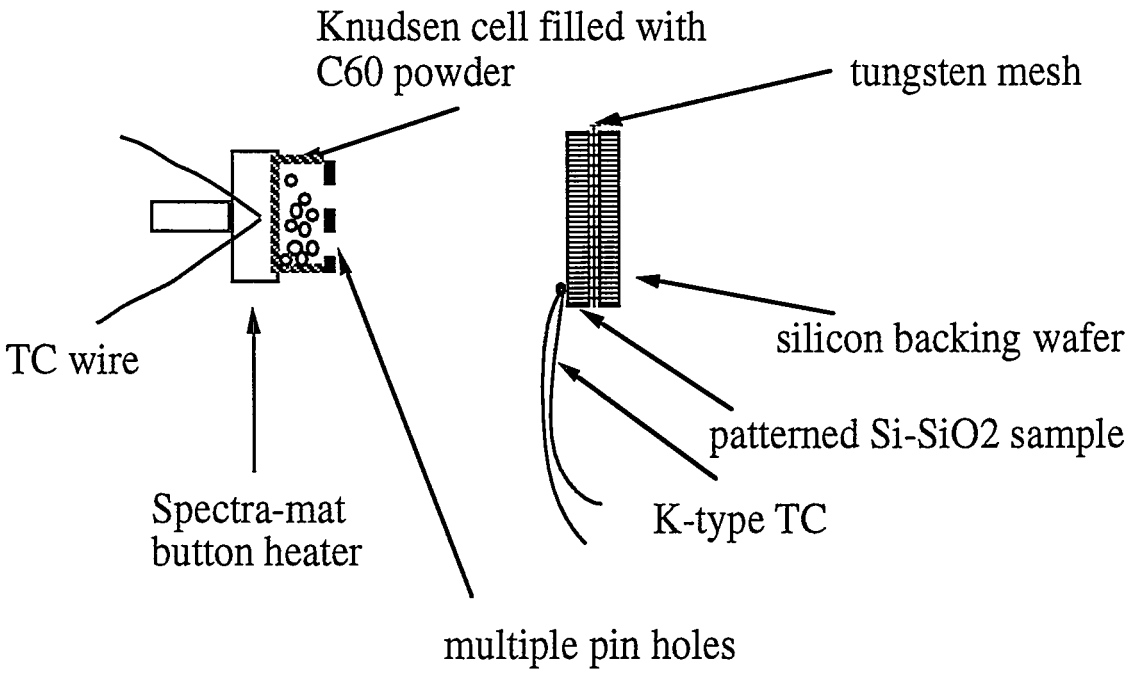

Figure 3 - The setup in the vacuum chamber to grow SiC from C60 precursors consists of a Spectra-mat button heater that heats the buckyballs to sublimation, and a Knudsen cell that holds the C60 powder with a pin hole screen to direct the C60 at the sample. The sample is mounted with a tungsten mesh heating element and a silicon backing wafer to reflect the heat from the mesh. A thermocouple measures the sample temperature.

Properties of SiC

The bulk properties of SiC will also characterize the thin SiC films. SiC is resistant to high temperatures and radiation. Because of its high dielectric strength, devices made from SiC can operate at higher power and higher frequency than standard silicon devices. Some unique properties of SiC thin films grown from C_{60} precursors include, easy patterning and growth at 950-1200 K, a lower temperature than conventional SiC coatings (1300-1800K).[58,42]

Atomic Force Microscope

In 1986, Bennig, Quate and Gerber [Bennig] invented the atomic force microscope (AFM) to study non conductive surfaces. Today, the AFM is one of the most widely used tools for real-space near-atomic resolution surface analysis. The AFM is easily modified for different applications. Low temperature AFMs and ultra high vacuum (UHV) AFMs ensure cold or clean environments to scan samples. Some AFMs have

samples that move under a still cantilever, and others have cantilevers that move over a still sample. AFMs can image surfaces, image the friction of surfaces, image elastic modulus of a surface using force modulations, and can indent surfaces with a stiffer cantilever. Cantilever movement detection has advanced as well. Methods to detect cantilever motion include piezoresistance[3], laser deflection[4,5], interferometry[5,6], and even quantum mechanical tunneling[Beenig].

A conventional open atmosphere AFM has a small cantilever beam with a sharp tip at one end. The tip is lowered to the sample and imaging is done in one of two modes, contact or non-contact mode. In contact mode the tip will slowly approach the surface of the sample and will softly touch the top atoms of the sample. The force that the tip exerts on the sample is smaller than the forces holding the atoms of the sample together, thus the sample is barely damaged while imaging. As the tip scans the sample the repulsive forces between the sample atoms and tip atoms causes the tip to deflect while encountering changes in topography of the sample. During non-contact mode the tip doesn't actually touch the sample surface, it just 'feels' the attractive force of the surface atoms pulling the tip. This leaves a gap of 50-100 A between the tip and the sample. This stiffer cantilever vibrates at a resonating frequency, which is kept constant while scanning the surface by moving the tip height according to the changes in topography.

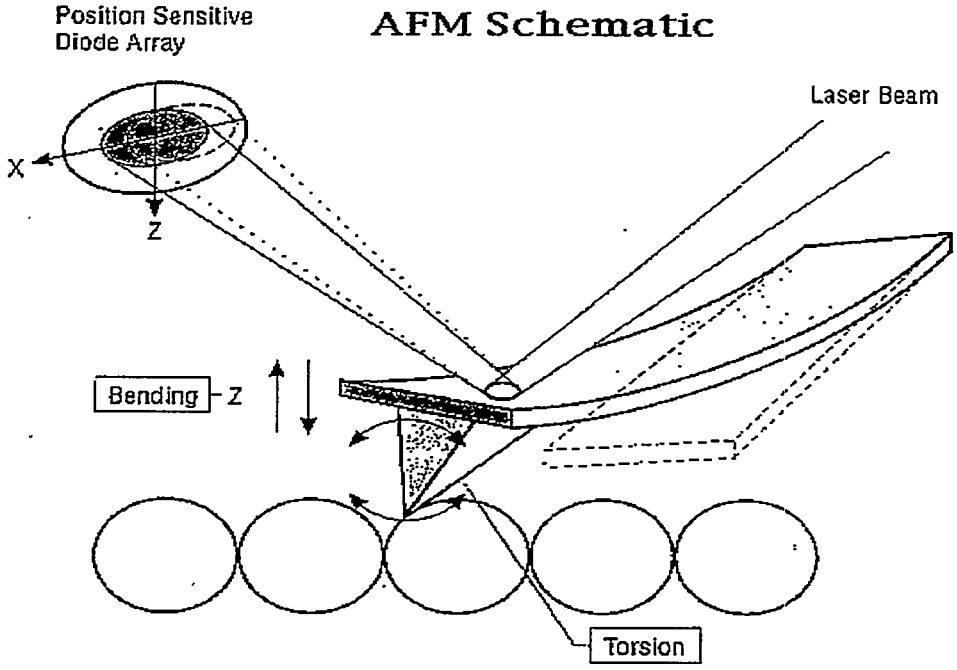

Figure 4- The deflection is measured by the changes in the reflected trajectory of a laser beam. This laser beam strikes a detector made of four diode detectors that allow the measurement of its position in two independent directions (normal and horizontal)

Both modes on the conventional AFM detect changes in the tip height by reflecting a laser beam on the back of the cantilever and reflecting it to a photo diode. This method is called laser beam deflection. The photo diode is divided into four quadrants, enabling it to measure vertical displacement as well as torsional displacement with the accuracy of a few angstroms. From this, the AFM can image the surface and image the coefficient of friction of the surface. See Figure 4 for a schematic of a conventional AFM.

Experiments

Friction

We used three different types of AFMs and a Nanoindenter to determine the mechanical properties of the SiC thin films. We used a Digital Instruments, conventional large stage AFM Nanoscope III to measure relative coefficients of friction between the silicon nitride tip and a SiC pattern on a silicon substrate. This open air AFM has a tip made of silicon nitride with a spring constant, k, equal to 0.1 N/m. Laser beam deflection is used to detect the cantilever deflection, reflecting a laser off the back of the cantilever and into a photo diode. The four quadrant photo diode on our conventional AFM allows it to measure torsional movement of the tip. While scanning the sample, the tip is deflected in a torsional manner due to the friction between the tip and the surface. Thus, the amount of torsional deflection dictates how high the friction of the surface is. To measure the relative coefficient of friction between two materials, they must be scanned by the AFM at the same time. To do this we pattern our SiC film with the method previously described. The resulting sample shown in Figure 4, has a SiC 'A' on a silicon background.

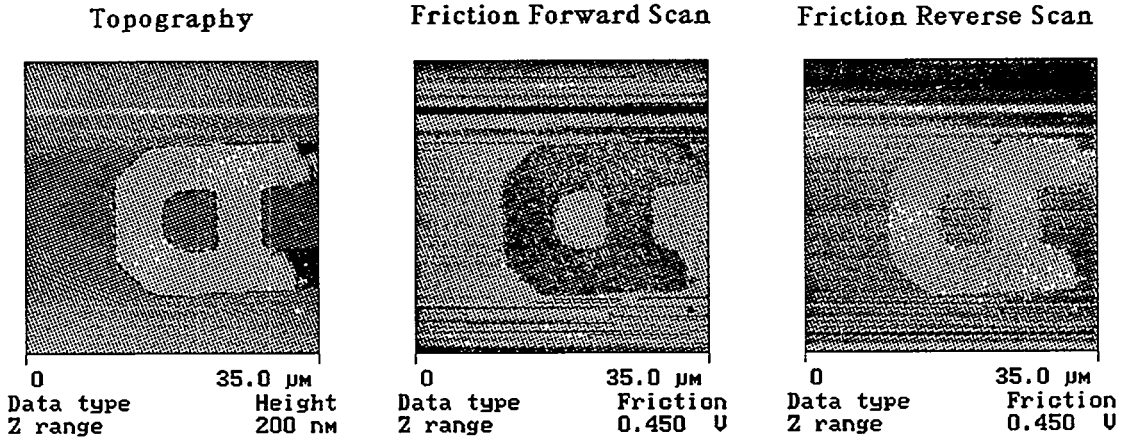

Figure 5 - The first plot is a profile of the surface across the middle of the 'A'. On the next plot the relative coefficient of friction is measured as the distance between the forward trace and the reverse trace. The friction of the SiC 'A' is about half the friction of the silicon.

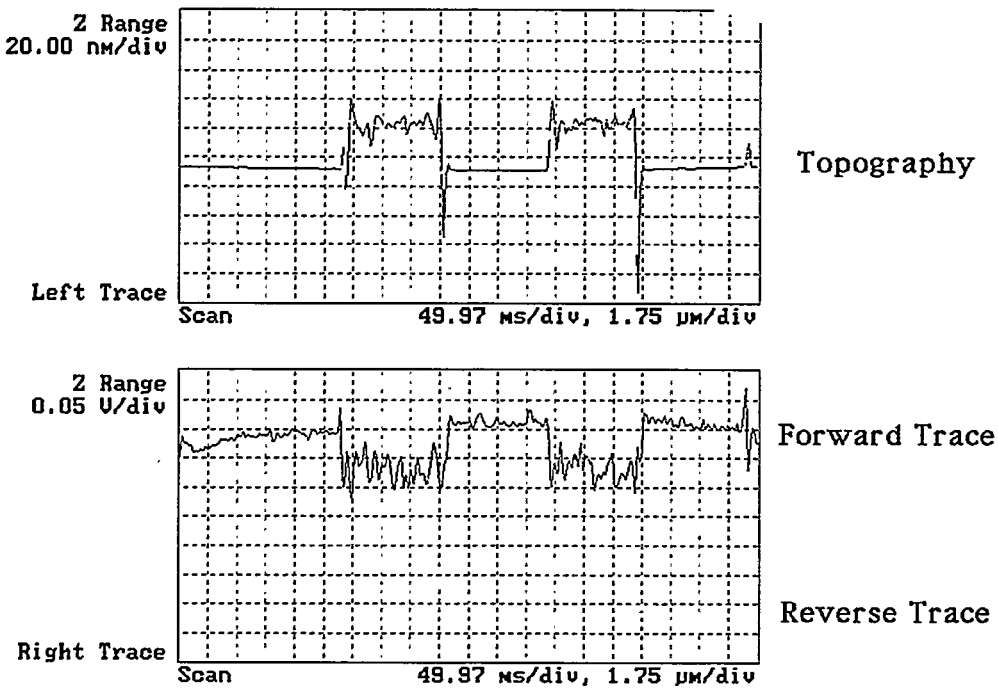

Figure 6 - The AFM images height and coefficient of friction. The left picture is the topography and the next two are the relative friction going forward and reverse. With a uniform pattern the friction pictures should be exactly opposite in color.

The AFM images topography and coefficient of friction. In Figure 5 the left picture is the topography and the next two are the relative friction during forward and reverse scans. With a uniform pattern the friction pictures should be exactly opposite in color. A cross-section of the image results in a graph of the relative friction coefficient versus distance, Figure 6. The first plot is a profile of the surface across the middle of the 'A'. The next plot shows the forward and reverse friction scans as the amount of deflection of the tip. For example, the forward scan graph indicates that the SiC 'A' has a lower surface friction because it is closer to tip equilibrium. By combining the forward and reverse friction scans, the relative friction can be found as the distances between the two directions. Without calibration, these images are only a plot of relative coefficients of friction.

From the graph, the relative coefficient of friction between the SiC 'A' and the silicon nitride tip is about half the friction of the neighboring silicon and tip. Other images show that the friction of SiC can be up to one third that of the silicon.

There are limits to the accuracy of the friction images. Sometimes the rapid change in height topography effects the friction image. When the tip encounters a step on the

sample surface, spikes are seen on the graph during the transition up and down each step. The friction graph in Figure 5, exhibits this problem. The patterned 'A' is higher than the substrate, and corresponding spikes are seen on the graph at the edges of the steps. Two sliding parts could also exhibit adhesion, the breaking and joining of asperities on the two materials and ploughing, the actual displacement of material. [Blau]. Thus, the surface quality can have an effect on friction. Since we are focusing on the relative friction between two materials, adhesion is not a problem and if present would just increase the friction scans. While not observed, water or other contaminants present on the surface can cause an error. We operate the AFM in repulsive mode so that attractive forces due to water are not observed in the image. Increasing the force on the tip from 10^{-9} to 10^{-8} N shows no change in the relative friction images, so the coefficient is independent of applied force in our images.

Hardness

The hardness of our SiC thin films is found two ways. In one, a modified tip on an AFM enables us to indent the surface of the sample for a hardness test. The tip in use from Advanced Film Technology Inc. (Japan) has a diamond microtip with a radius of 100 nm which is mounted on a gold-plated stainless steel leaf spring. The spring constant of this cantilever that we used is 3000 N/m. The spring constant of our cantilever, and k can vary from 100 to 5000N/m by adjusting the length of the cantilever. The second method of finding the hardness of our SiC film is the Nanoindenter.

Advanced Film Technology Inc. provides a spring constant, k, for the cantilever 10 mm in length. Then we calculate the change in k as the length of the cantilever changes. The following equation is used:

$\omega = 4 P c^3 (1-\upsilon^2) / (bt^3E)$

$P = k \omega$

ω = deflection	P = applied force	c = effective length	k = spring constant
υ = poisson's ratio	b = width	t = thickness	E = elastic modulus

Using the modified tip, the maximum force on the tip is measured while surface penetration takes place. Then, we image the indented surface on a conventional AFM, because it has higher resolution. The triangle indentations are seen on the image and the projected area is measured. Figure 7 shows the indention in SiC. Figure 8 shows the indent on the silicon sample with native oxide. From this the hardness is simply calculated as the maximum force divided by the projected plastically deformed area.

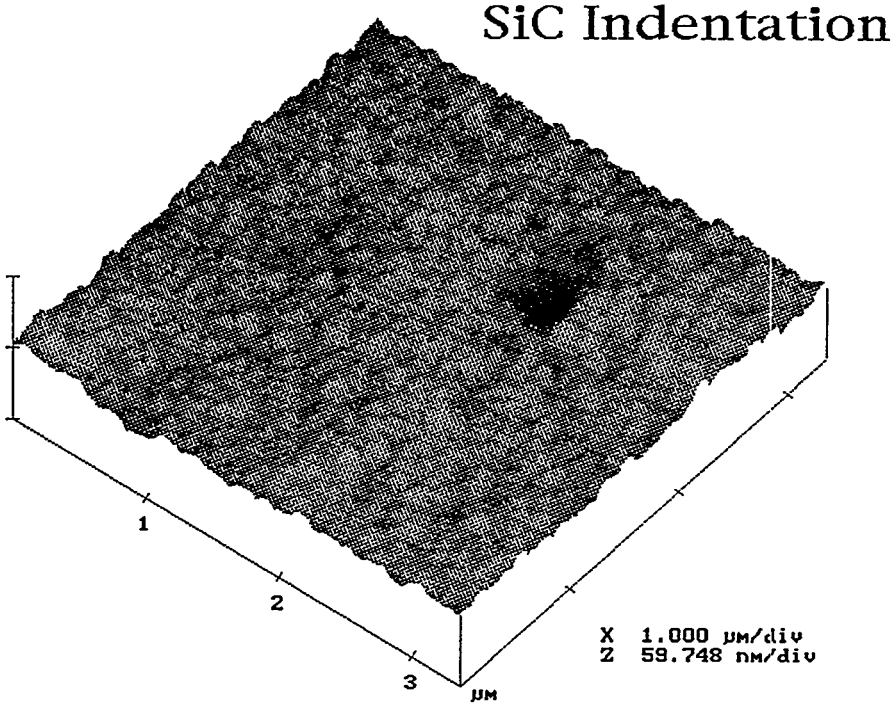

Figure 7 - The SiC film grown is indented with the Nanoindenter and is imaged here with the AFM. The bluryness of the picture indicates that the tip is dull and needs replacement. The hardness of this particular sample was 26 GPa.

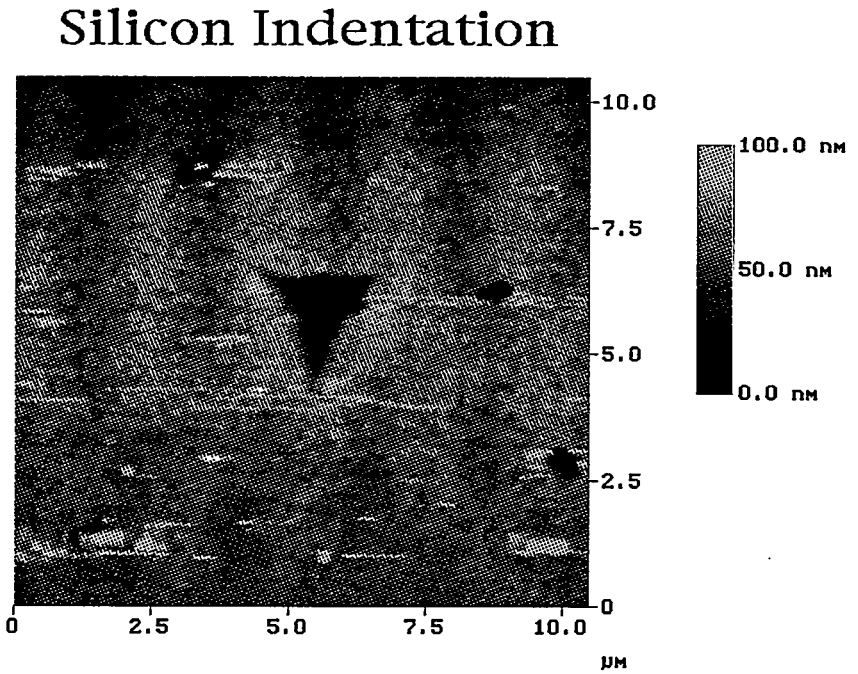

Figure - 8 This silicon sample has a very thin film of SiC on it. The sample was indented through the film with the Nanoindenter and then imaged with the AFM. The hardness of the silicon was calculated to be 16 GPa, just a little harder than (111) silicon which is 14 GPa and (100) silicon which is 11 GPa.

Measuring the hardness with the Nanoindenter is a similar process. The tip is indented into the surface and the maximum force is recorded. The hole is imaged with the conventional AFM, the area is measured, and the hardness calculated.

Our calculations show that the hardness of our films is 26 GPa with values ranging up to 40 GPa for a crystal boundary indention. The hardness of the silicon (110) that we indented was 14 GPa.

The variations in hardness of our film could be due to the grain size of the growth. The grains are large, about .3μm so, when indenting, we do not know if the indent is on a grain boundary or in the middle of a grain. It is also likely that we could push grains aside while indenting, or indent on a dislocation. A better understanding of these variations is now being pursued.

The image of the indent and the measurement of the area, are other sources of error in the hardness calculation. Our tip has a radius of 90 nm. Imaging a small hole, or a dramatic change in height, often images the tip instead of the actual hole. [8] This is called tip architecture[8] This means that the hole image could be off by 45nm in any one direction. This would result in a 20% error in hardness calculation. When the indention takes place, material is displaced on the sides of the hole. This extra material reduces the accuracy of the area measurement. Also, during imaging this material could be pushed into the hole, leading to an inaccurate measurement. Repeated imaging of our sample did not change the size of the indentation, therefore, we do not asses any error in hardness due to the movement of material. The edges of the hole are the only important features in the hardness calculation, and no change was noticed in those areas. Also, the hardnesses are effected by the substrate. Even though our indentations do not exceed 20 percent of the film thickness, the substrate effects could still be present, which can lower the hardness. Considering these factors the overall estimated uncertainty is calculated to be ±30 %.

Modulus

The elastic modulus of our SiC thin film is found two ways. It is calculated absolutely with the Nanoindenter, and is imaged relatively with the Digital Instruments Force Modulation AFM.

The Nanoindenter will indent a sample to find the hardness and elastic modulus. To indent the surface, force is applied to the top of the tip with the magnet and a loading coil. The tip is supported by suspending springs and the deflection is measured by the capacitance displacement gages. See Figure 9 for a Nanoindenter schematic.

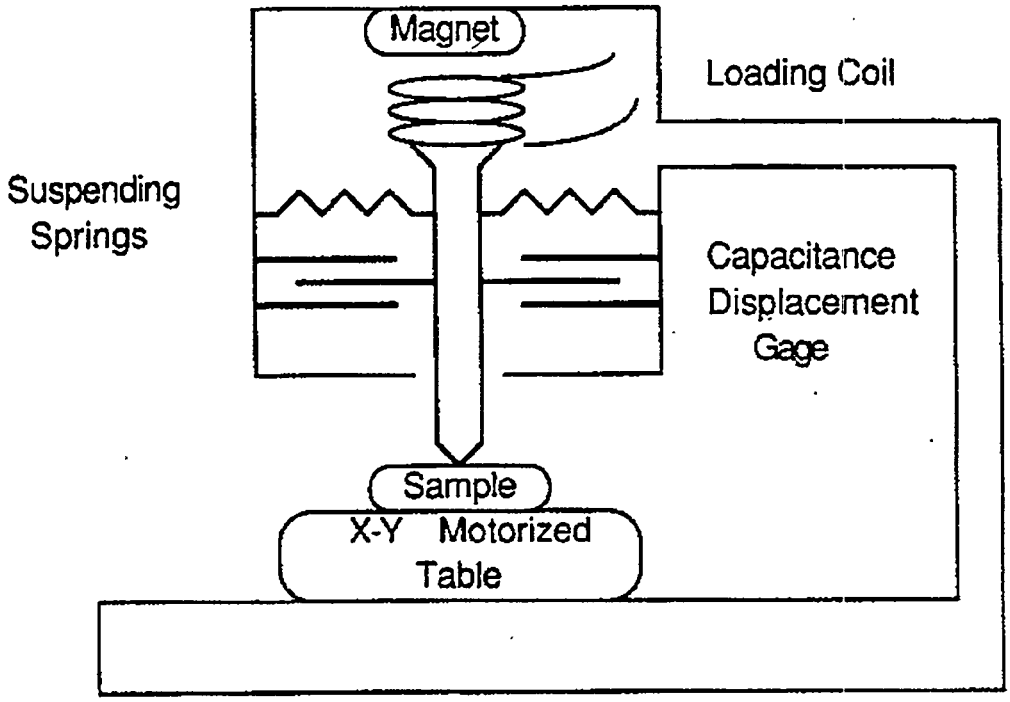

Figure 9 - A schematic of the Nanoindenter shows the magnet and loading coil that apply the force on the tip, the springs that support the tip, and the capacitance deflection gages that monitor the tip deflection.

Software controls the tip force and gathers force versus deflection data during the indentation. The Nanoindenter plots the force versus displacement data. Loading and unloading curves are seen in the plot, Figure 10. The slope of the unloading curve from that plot is the stiffness that is used in calculating the modulus. The contact radius is also needed to calculate the elastic modulus of our film. To obtain this information, the holes from the indentations are imaged with the conventional AFM, and the contact radius is estimated from the images.

The following equations are used to calculate the elastic modulus of our SiC films.
Modulus Calculation:

$S = 2*a*E_r$

$1/E_r = (1-\nu^2)/E + (1-\nu_0^2)/E_0$

S: stiffness

E_r: effective modulus

E: modulus of SiC film (unknown)

E_0: modulus diamond tip

a: contact radius

v: Poisson's ratio for SiC film

v_0: Poisson's ratio for diamond tip

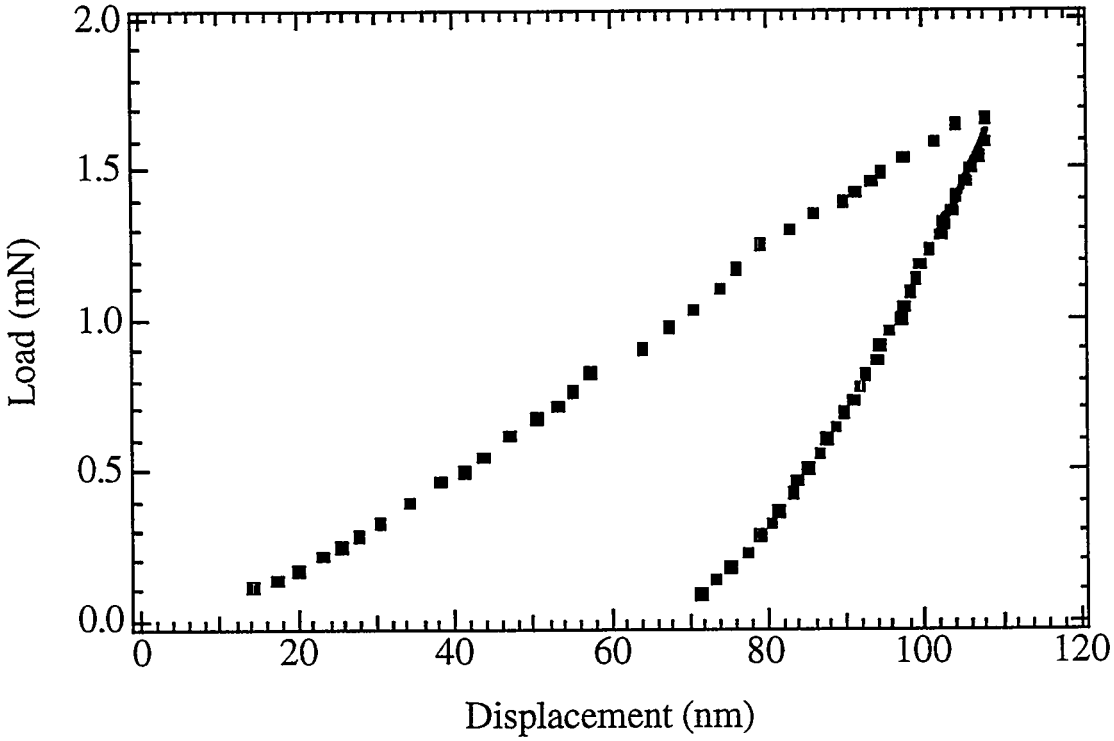

Figure 10 - This is an example of the force versus displacement plot used to calculate the elastic modulus of our SiC film. A second order polynomial was fit to the initial slope of the unloading curve on this plot. The derivative was taken of the polynomial and the resulting slope is the stiffness of the film.

The results of the Nanoindenter show that the SiC film is 310 GPa ± 10 %. The ten percent error takes into account the following uncertainties.

The modulus calculation from the Nanoindenter data has some uncertainty. There is some error in the fitting of the unloading curve with the polynomial. The number of points included in the fit can change the answer. We found the slope to vary from 0.07 to 0.05 mN/nm which is about 25% error. The other uncertainties are the contact radius (±10%) and the estimate of Poisson's ratio. $\upsilon = 0.19$ [Blau] It is not necessary to know Poisson's ratio very accurately to get a good estimate of the modulus.

Digital Instruments manufactures an AFM that can measure relative elastic modulus of a sample. This AFM does what's called 'Force Modulation Imaging'. During scanning of the surface, the tip vibrates at a resonating frequency while in contact with the sample

material. The modulus of the material dictates the amplitude of the vibration. A soft material (low elastic modulus) will have lesser effect on the cantilever, thus resulting in a smaller amplitude. While a stiffer material will cause the cantilever to bend, increasing the deflection signal, increasing the amplitude of the vibrating tip. Figure 11 illustrates the force modulation imaging. An image of the relative amplitudes will show the relative elastic modulus of the surface scanned. Without calibration this machine cannot measure absolute elastic modulus.

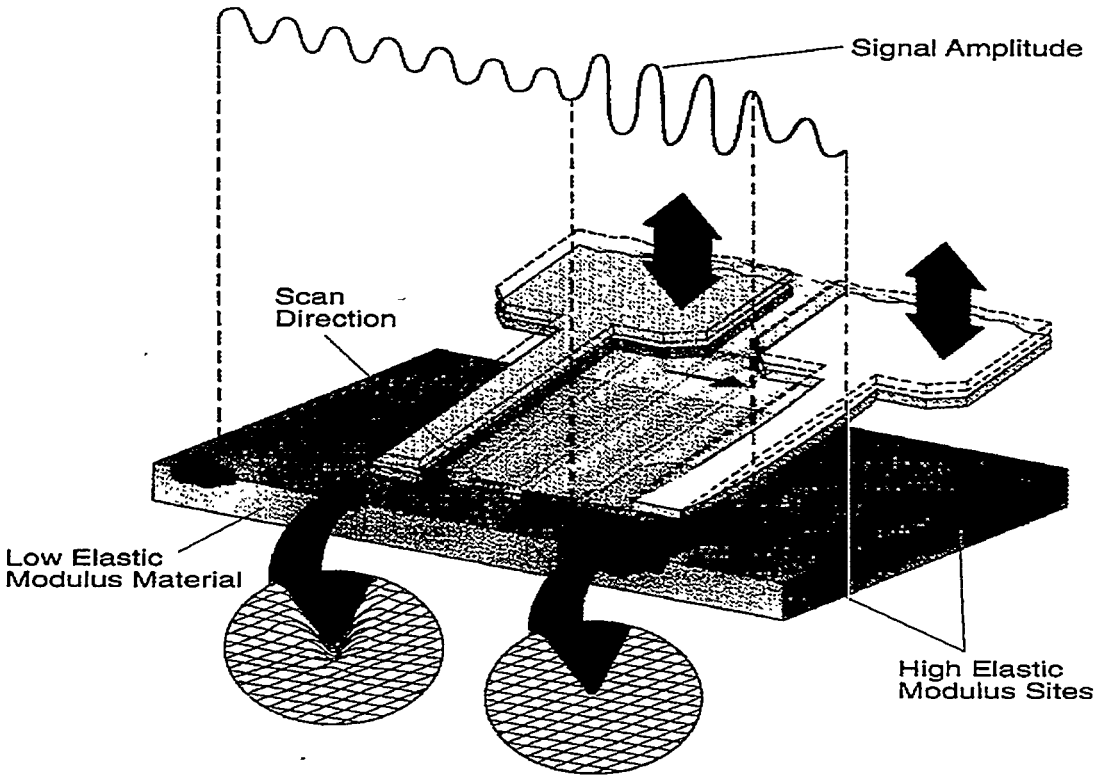

Figure 11 - The schematic of the Force Modulation AFM illustrates how the tip is absorbed by softer more elastic materials and bounces off harder materials while vibrating. Imaging with the amplitude of the vibration will show the relative elastic modulus of the surface. (Digital Instruments)

We used the Digital Instruments Force Modulation AFM to image the elastic modulus of our SiC thin film. The film imaged had a dot of SiC on a silicon substrate. The image, Figure 12, shows a rough topography image on the right side, and a modulation image on the left. The SiC dot is clearly a lighter color, therefore the SiC does have a higher elastic modulus, just as we calculated.

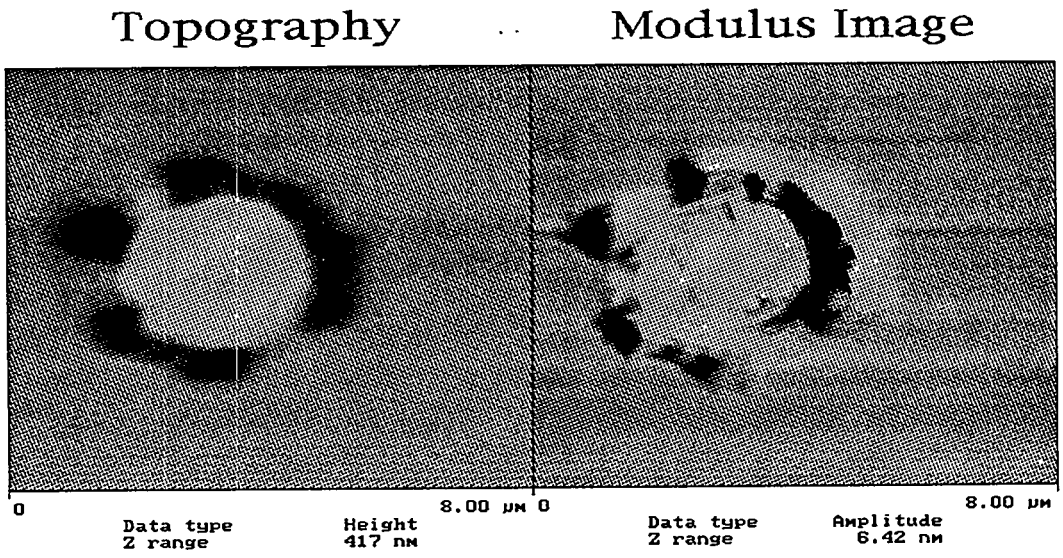

Figure 12 - The force modulation AFM images the topography and the modulus in one scan. The left image is the topography of a SiC dot on a silicon substrate. The right image is the force modulation image, and shows that the SiC dot has a higher elastic modulus than the surrounding silicon.

Porosity

To find the quality of our SiC thin film grown from C_{60} precursors, we are measuring the porosity. This measurement will help us to determine how our film is growing and if certain factors, such as temperature, contribute to the quality of our film.

To find the porosity of our SiC film the initial thickness of a silicon wafer is measured before exposure to C_{60}. We then grow a SiC thin film using the procedure already presented. The film is then popped off the sample and the thickness of the wafer is measured. From this, we can find the amount of silicon that was converted to SiC. Assuming the film is stoichiometric SiC, the amount on carbon in the film is known also. The thickness of the film that was popped off is measured and the final porosity is calculated. Balooch [9] further describes this process. On the same type of SiC thin films he calculates a porosity of 17%.

The following equation is used to calculate porosity from the measurement of the elastic modulus of our film.

$E/E_0 = 1\text{-}1.9P + 0.9P^2$ $\quad E = 310$ GPa (our film) $\quad E_0 = 448$ GPa (bulk)

These calculations show that the porosity of our film is 18%, very close to Balooch's findings. This percent indicates that we have a good film, and we can now explore different deposition techniques for a more dense film.

Molecular Dynamics Modeling

Molecular Dynamics Modeling of SiC Indentation

In order to gain a clearer understanding of the atomic-scale processes taken place at the SiC surface when indented by a very small tip, we performed a series of molecular dynamics simulations indenting a diamond-like tip into the SiC (100) surface. Molecular dynamics modeling is very simple in principle. The response of a material to an external force, for example indentation of the surface, is evaluated by following the response of every atom in the material.
We solve the Newtonian equations of motion (Force = mass * acceleration) for every atom, with the forces derived from a model of how the atoms interact with one another. These forces are ultimately due to the covalent and other types of bonds that form between atoms, a proper description of which requires a quantum mechanical solution. Solving the quantum mechanics directly during a molecular dynamics simulation has only recently become possible and is currently limited to very small systems (a few hundred atoms) for very short times (a few picoseconds). To overcome these limitations approximate models that mimic the quantum mechanics have been developed. One such model that accurately represents the covalent bonding in SiC is the bond-order model due to Jerry Tersoff [ref]. This is the model we used in our simulations.

In practice we can not simulate all of the 10^{23} atoms in a material so we devise special boundary conditions that allow us to simulate a process with minimal effects with a much smaller number of atoms. On present generation high-performance workstations, like our cluster of IBM RS/6000's, we can simulate tens of thousands of atoms for up to nanoseconds of simulation time. Massively parallel computers allow us to simulate much larger systems, up to hundreds of millions of atoms, though the time scales at still limited to at most ten nanoseconds. The boundary conditions used in our simulations is shown schematically in Figure 13. The surface consists of many layers (32 in our SiC simulations), the bottom-most few are held rigid. Along the sides the problem is periodically reproduced to effectively emulate an infinite surface. All of the non-rigid

surface atoms are held at room temperature. The tool atoms are also rigid but move in concert into the surface at a constant velocity. We used indentation velocities of 430, 43, and 4.3 m/s. Slower velocities are not possible due to the length of simulation time. The tool is composed of carbon atoms on a diamond lattice. We cleave (in the computer) the diamond along the (100), (010), and (001) planes to make a triangular tip shaped like the edge of a cube. A few atoms are removed from the tip to make it slightly blunted. Further details concerning boundary conditions and the application of molecular dynamics modeling to tribological processes may be found in a recent dedicated issue of the MRS Bulletin on Nanotribology.[10]

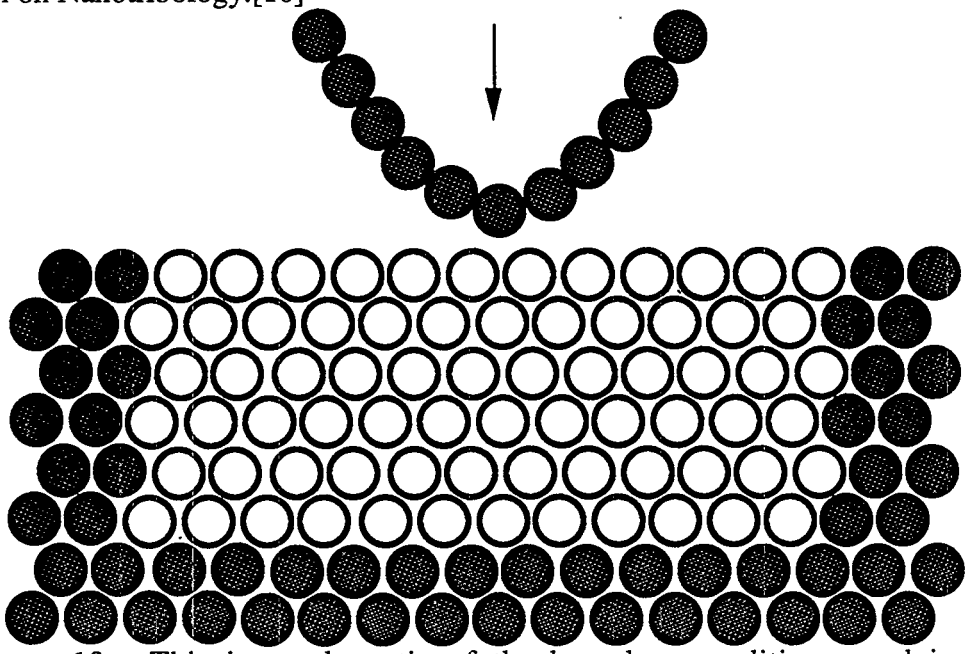

Figure 13 - This is a schematic of the boundary conditions used in our simulations. The bottom few blue sample atoms and the tip atoms are held rigid during simulation. The white surface atoms that are non-rigid are held at room temperature during the simulation.

SiC crystallizes into the same lattice structure as diamond with Si and C atoms alternately replacing the C atoms in diamond. Prior to running any indentation simulations we asked how well the Tersoff bond-order model represents the SiC structure. We found that the model prefers a lattice constant of 0.4316nm at room temperature, which is slightly smaller that the experimental value of 0.4348nm. We used 0.4316nm to construct our surface for the indentation simulations. The basic unit cell contains 8 atoms in 4 layers, with each layer alternating between being pure C or pure Si. We replicated this basic unit cell 8 times in the z direction and 12 times in the x and y directions. This made a surface cell containing 9216 atoms with dimensions 5.1792nm in x,y and 3.4528 in z. We allowed the surface to "reconstruct" and come to equilibrium at room temperature prior to starting the indentation simulation. The reconstruction consists of neighboring atoms (in

the (110) direction) coming together to form rows of dimers. The Tersoff bond-order potential does this spontaneously.

Two snapshots from our simulation with a Si terminated surface (we did simulations for both when the top-most surface layer was all Si and for when it was C) and an indentation velocity of 43m/s are shown, Figures 14, and 15. The surface dimer rows and the shape of our triangular diamond-like tip can be seen in these snapshots. The first snapshot is prior to the start of the indentation and the second is for an indentation of about 1nm. The Si atoms are colored by their local coordination, i.e. by the number of atoms they are bonded to. The C atoms are colored gray. Green corresponds to the four-fold coordination found in the equilibrium diamond lattice. Yellow means three fold and red is two-fold. The dimer rows are colored yellow and red. In the second snapshot we clearly see the plastic flow of the SiC material up the sides of the diamond-like tip. Some of the atoms in the high stress region under the tip are colored blue. This indicates a coordination greater than four. We need to further analyze the structure in this region to see wether the material has transformed into another phase (like the six-fold phase of Si at high pressure) for some other mechanism is taking place.

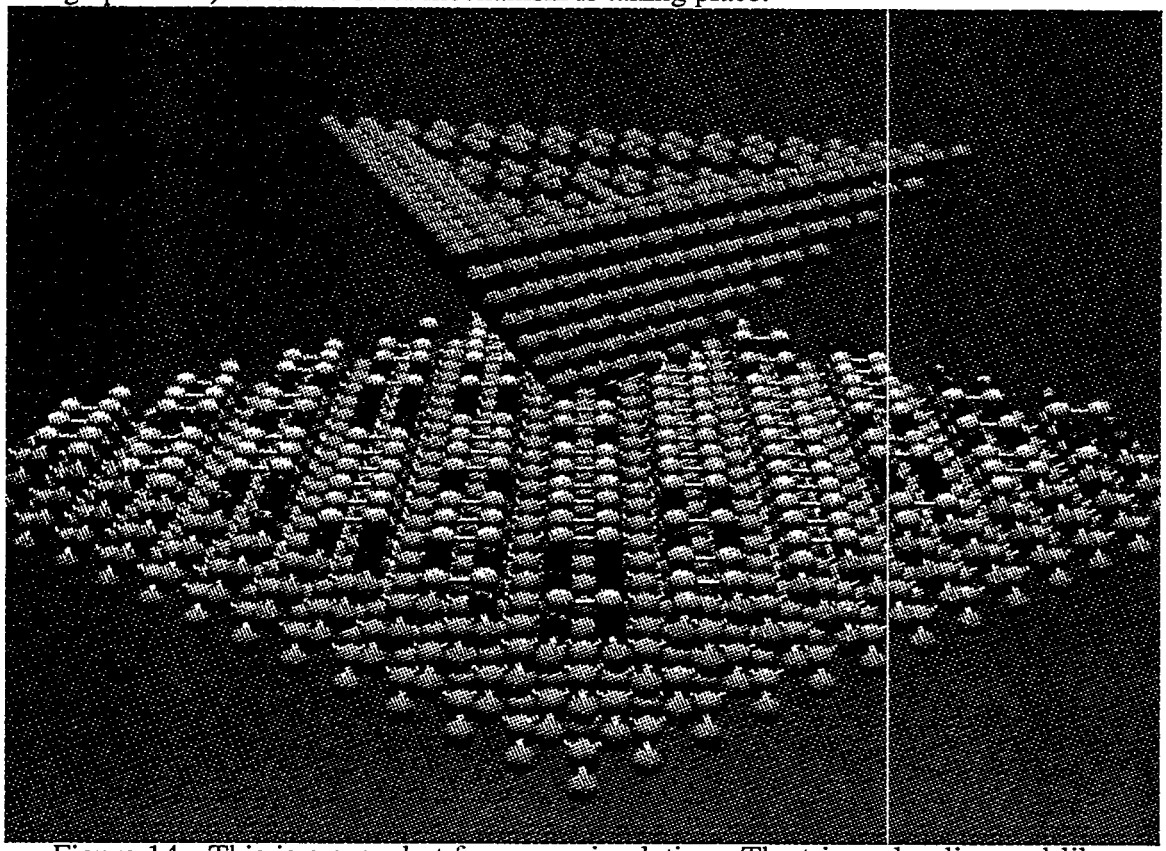

Figure 14 - This is a snapshot from our simulation. The triangular diamond-like tip can be seen, as well as the dimer rows on the sample surface. No indentation has taken place yet at this point in the simulation.

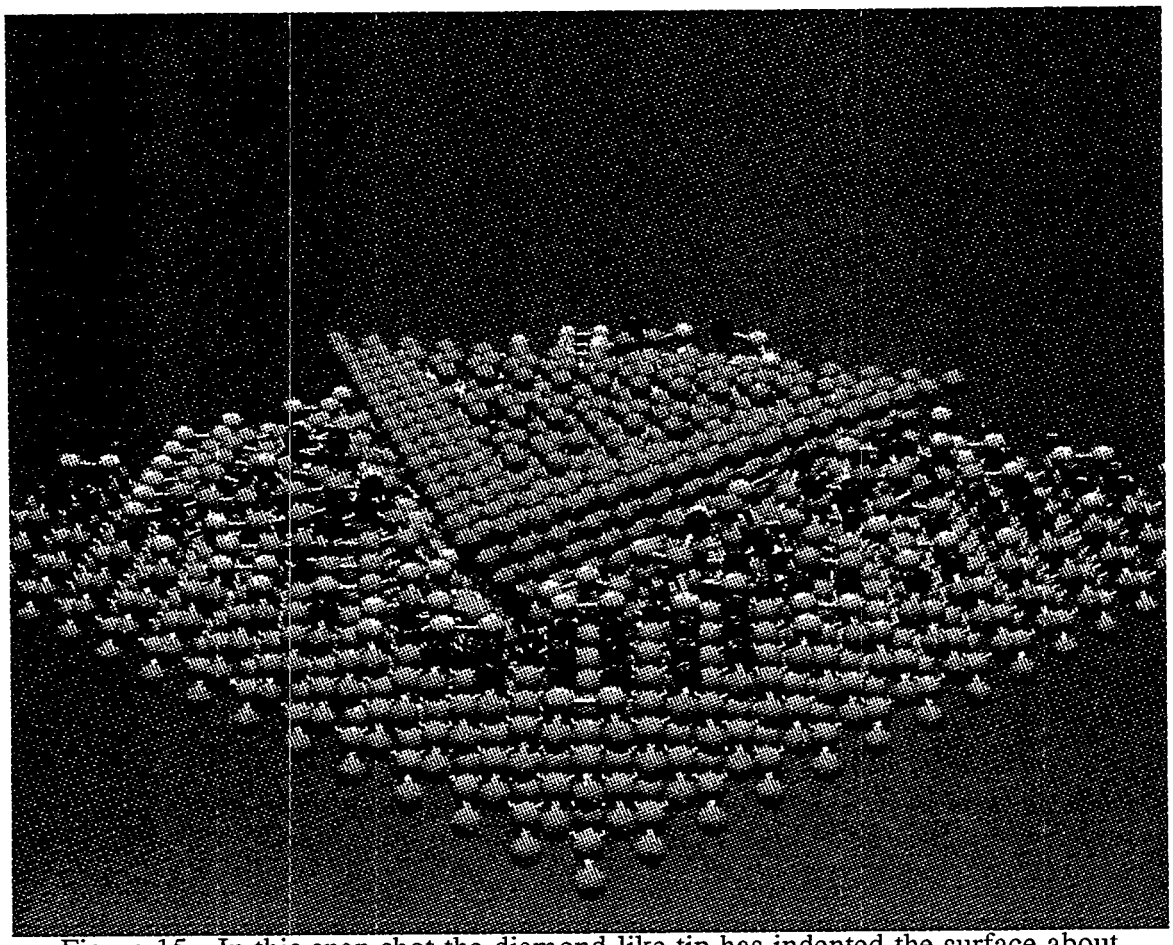

Figure 15 - In this snap shot the diamond-like tip has indented the surface about 1nm. We can see the plastic flow of the SiC material up the sides of the tip.

The data is more easily related to experiment by examining the loading curve. The loading curves for indentation rates of 430 and 43 m/s are shown in Figure [16]. The two curves are almost identical for small indentation but the slower rate shows smaller loads for large indentations. This slight dependence on indentation rate may mean that our 43m/s simulation may not represent the equilibrium process. We will know the answer to this issue when our 4.3m/s simulation finishes. The curves show some interesting features. The initial response of the surface is elastic and the first plastic "yielding" occurs at an indentation of 0.4nm. The curve is characterized by several of these yielding/reloading events that occur with a spacing of about 0.25nm. The process appears to be a build-up of stress until a critical value is reached, at which time the material starts to flow plastically. But the mechanism of this plastic flow seams to be such that the amount of material that has "transformed" is limited such that the stress builds up again over the next 0.25nm. We need to further analyze the data to make these ideas concrete.

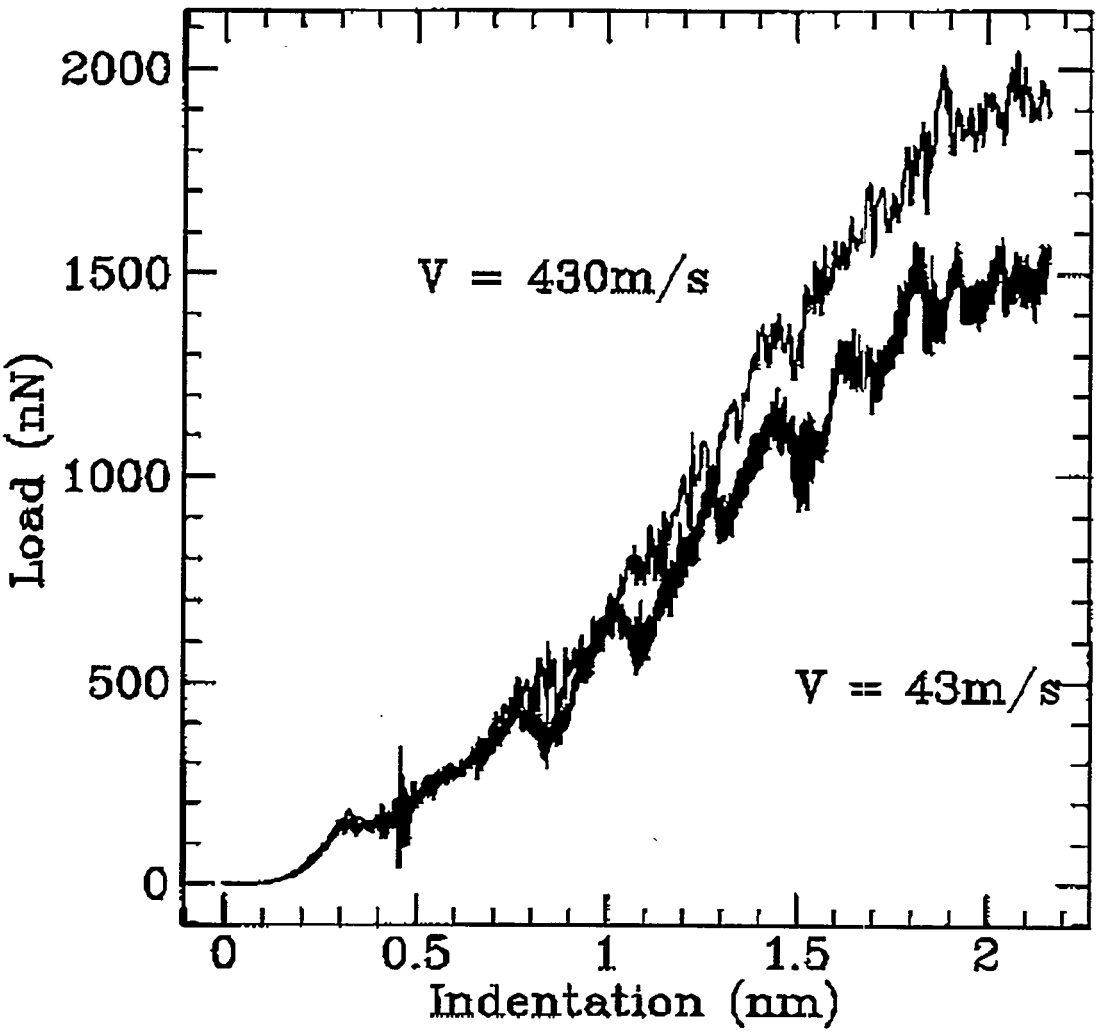

Figure 16 - The loading curves for indentation rates of 430 and 43 m/s are shown. The two curves are almost identical for small indentation but the slower rate shows smaller loads for large indentations.

The hardness is defined to be the load divided by the area of contact. We can estimate the area of contact from the geometry of our tool. For indentations larger than the tip radius, the area is approximately (9/2) I^2 where I is the depth of the indentation. From the loading curve we find H = 111GPa at I=1nm, and H=85GPa at I=2nm, with an estimate of the error at about 30%. This value is somewhat larger than the experiments. The discrepancy may be due to: the defect-free nature of our simulated surface; the small size of our simulation an the rigid lower boundary; or the fast rate of indentation. We are currently running a simulation at 4.3m/s to further examine the rate dependence and plan to start a large simulation to examine the dependence on system size.

Results

Table of Results

The following is a table of our test results performed on an SiC film grown from C60 precursors:

	Hardness	Modulus	Friction	Porosity
Our SiC	26-40 GPa	308 GPa	3X less than Si	18%

A comparison between our film and some other films:

	Hardness	Modulus	Friction
Our SiC	26-40 GPa	310 GPa	1/2-1/3 silicon
Silicon (110)	14 GPa	190 GPa	2-3X SiC
Cree SiC	25 GPa		
Bulk SiC [Tong]	30 GPa	448 GPa	
SiC [El Khakani]	30 GPa	240 GPa	

The table shows that SiC that is made by chemical vapor deposition (CVD) (Cree) and plasma enhanced chemical vapor deposition (PECVD) (El Khakani) both have very similar properties to our film with C60.

Bulk SiC does show a higher modulus of elasticity. We feel that this difference is the effect of the substrate while indenting the film.

Conclusion

Three different types of AFMs and a Nanoindenter were used to find the mechanical properties of SiC thin films grown from C60 precursors. The conventional AFM with a silicon nitride tip was used to image the relative coefficient of friction between SiC and the tip, and silicon and the tip. To find the elastic modulus of our SiC film, the Nanoindenter was used to indent the film and plot the force versus displacement. From this graph we calculated the elastic modulus of our film. A Digital Instruments Force Modulation AFM, was used to find the relative elastic modulus of SiC on silicon.

Hardness was calculated by indenting the film with a modified diamond tip on the AFM. We then imaged the surface with a conventional AFM. From these images, we calculated the hardness of the SiC thin film.

The results of these tests show that SiC films that are made with C60 precursors have a hardness of 26 GPa. Friction measurements reveal a 2 to 3 times lower coefficient of friction between the silicon nitride tip and silicon carbide, than between the tip and plain silicon. The Nanoindenter calculation shows that SiC films have an elastic modulus of 310 GPa. The force modulation verifies that the islands of SiC are stiffer than the surrounding silicon wafer. The porosity of our film was calculated to be 18 percent.

These results are favorable for the use of SiC thin films for MEMS to increase their wear properties and life expectancy. The mechanical properties of this film are better than those for silicon that is currently used. We hope that this new material can open doors into the micro-mechanical world, and applications that have not been previously considered.

Acknowledgments

The work was performed under the auspices of the USDOE at Lawrence Livermore National Laboratory, contract # W-7405-ENG-48.

References

1. R.T. Howe, R.S. Muller, K.J. Gabriel, and W.S.N Trimmer, IEEE Spectrum July 1990 p.29-35.
2. G. Binnig, C.F. Quate, Ch. Gerber, Physics Review Letters 1986 p.56.
3. M. Tortonese, R.C. Barrett, C.F. Quate, Applied Physics Letters, V.62 No.8 22 Feb 93 p.834-836.
4. M. Kageshima, H. Yamada, K. Nakayama, H. Sakama, A. Kawazu, T. Fujii, M. Suzuli, Journal of Vacuum Science and Technology B 11(6) Nov/Dec 1993 p.1987.
5. C.A.J. Putman, B.G de Grooth, N.F. van Hulst, and J. Greve, Ultramicroscopy 42-44 1992 p.1509-1513.
6. D. Sarid, P. Pax, L. Yi, S. Howells, M. Gallagher, T. Chen, V. Elings, and D. Bocek, Review of Scientific Instruments 63 (8) August 1992 p.3905.
7. P. J. Blau, Wear 162-164 1993 p.102-109.

8. K.L.Westra, A.W Mitchell, and D.J. Thomson, Journal of Applied Physics 74 (5) 1 Sept 1993 p. 3608-9.
9. M. Balooch, A.V. Hamza, Journal of Vacuum Science and Technology B Nov/Dec 1994.
10. J. Belak, Material Research Society Bulletin May 1993.
11. J. Tersoff, Physical Review V.39 No.8 15 March 1989 p.5566-5568.
12. L. Tong, M.Mehregany, L.G.Matus
14. M.A. El Khakani, M. Chaker, A. Jean, S. Boily, J.C. Kieffer, M.E. O'hern, M.F.Ravet, and F.Rousseaux, Journal of Material Research V.9 No.1 Jan 1994 p.96.
15. A.V. Hamza, M.Balooch, M. Moalem, Surface Science 317 1994 p.L1129-L1135.

Advanced Information Technology: Building Stronger Databases

David Price

Lawrence Livermore National Laboratory

Fall 1994 Science and Engineering Research Semester

Abstract

This paper discusses the attributes of the Advanced Information Technology (AIT) tool set, a database application builder designed at the Lawrence Livermore National Laboratory. AIT consists a C library and several utilities that provide referential integrity across a database, interactive menu and field level help, and a code generator for building tightly controlled data entry support. AIT also provides for dynamic menu trees, report generation support, and creation of user groups. Composition of the library and utilities is discussed, along with relative strengths and weaknesses. In addition, an instantiation of the AIT tool set is presented using a specific application. Conclusions about the future and value of the tool set are then drawn based on the use of the tool set with that specific application.

History of AIT

Advanced Information Technology(AIT) is descended from a program called Business Planning System(BPS). BPS is a personnel management, planning, and cost tracking system developed at Lawrence Livermore National Laboratory. It was originally designed to use Query Language (QUEL) to manipulate an Ingres Database Management System (DBMS). Much of the underlying code of BPS was redesigned to use Structured Query Language (SQL) rather than QUEL and was made somewhat DBMS platform independent. This new version of BPS is becoming AIT.

The majority of the AIT tools are modified versions of similar functions in the original BPS framework. Although tested in a more limited form, they have yet to be evaluated in a larger full scale application. Constructing a pervasive application from the ground up will give us a good feeling for the strengths and weaknesses of the AIT tool set.

We have chosen to test AIT by building a new application for the Software Distribution Engineering Services(SDEs) organization. SDEs maintains a contract for all Digital Equipment Corporation (DEC) software licensing and documentation purchased at LLNL. The underlying data is stored using the Ingres DBMS and is accessed through Applications By Forms (an Ingres menu tree generator and application builder), Query By Forms (a data entry mechanism) and Report Writer (a report generating facility). The SDEs DEC database is fairly old and for one reason or another certain issues were either not addressed by the database designers or simply not implemented. We shall first examine the lowest level framework of the application, the menu tree, then we shall incorporate data integrity and validation, on-line help, user groups and reporting facilities into our evaluation of the AIT tool set and the existing SDEs application.

The Primary Menu Tree

The user interface employed by SDEs is built by Applications By Forms (ABF), a software package provided with Ingres. ABF constructs a menu tree from a catalog of menu definitions. The end result is a menu driven program that allows the user to either call a user frame to open a submenu or start an operating system shell script, call a report frame to execute a Report Writer script, or call a Query By Forms (QBF) frame to initiate a data entry unit. No attempt was made to implement on-line documentation for the SDEs DB, although the facilities exist within ABF. In some instances user frames in the SDEs application execute OS scripts whose only function is to independently run reports that could have been started by report frames. Ingres and ABF do not have the capability of linking tools together. For example, one QBF frame cannot start up a different QBF frame or begin an OS script. No steps are taken in the creation of the application to control user access to specific portions of the menu tree. (Although table level restrictions are enforced) The final package is a loose conglomeration of calls to independent prepackaged Ingres tools, in which the users are free to roam wherever they please. Its design is inefficient in that many steps are taken to produce an end result and training new users is prolonged due to a lack of on-line help.

User interfaces constructed by ABF is a separate entity that controls the underlying database applications. This approach is used by other designers as well [440, Pap]. AIT treats the user interface as an integrated extension of the underlying software packages. When an AIT application is being built, a primary menu table (PMT) is constructed. Each tuple in the PMT contains a menu option's name, the name of it's parent node, which type of option it is, which user groups may access it, and the name of the function to execute if the option is selected. A routine traverses the table and constructs the final menu tree. Each menu is defined as the set of all menu options whose parent nodes are identical. Once a menu is defined, a code generator produces a script that links into a help library for each menu option. In the specific case of data entry screens,

the code generator also builds functions that link into the referential integrity and data validation mechanisms. The generator is also capable of creating the ability to start a separate menu option while executing the current one. This allows one data entry unit to instantiate another, if the need arises. The final program is a tightly interconnected series of menus, controlling user access and maintaining consistent data.

Referential Integrity

When the AIT code generator constructs a data entry screen, it links into a referential integrity mechanism. Referential integrity implies "if a relational table has a foreign key, then every value of that foreign key is either null or matches a value in the relation table in which that foreign key is a primary key." [49, Sto] Put simply, if data in one column is repeated in more than one table, and that data is changed in some way, the modification must be propagated to all tables containing copies of that data. Many DBMSs do not provide support for referential integrity, that task is left to application programs.[123-4, Haw] This leaves the implementer responsible for maintaining the integrity of the database. The version of Ingres used by SDEs does not support referential integrity, however there is an additional application available at significant cost, which is capable of enforcing data integrity.

The SDEs designers left referential integrity in the hands of the user. This has caused a fair amount of additional work for system and application managers. For example, the unique product identifier (UPI) appears as a key in several tables in the SDEs database. Should DEC one day decide to change a UPI, that change would have to be made in the SDEs database as well. If I as a database manager, change the value of the old UPI in all but one table then my database contains invalid data. I may have simply forgotten about a table or it might have been left out of the system's documentation. Either way, the database considers there to be two different product identifiers. Let us further assume that the table I have neglected contains the UPIs, and their monthly costs. If I were to run a report asking for system names, the products they ordered, the

cost of those products, and a total charge for a particular month, it will return invalid incorrect totals. The report will pull the UPI out of two tables, one containing the system names and products purchased, and the other with products and their prices. Since the UPIs in those tables differ, a join based upon matching product identifiers will fail to include tuples with the updated UPI. That product will not appear in the report, and its price will not be included in the total system charge. I must then spend time trying to figure out why this product is not appearing in the reports as it should. This extra work would be avoided if referential integrity were implemented

AIT contains the means of allowing applications to enforce referential integrity. A referential table is created when the database is initially constructed. The table has four columns, source table, source field, target table and target field. Every time an update is performed on a column, a search for the effected table and field is performed in the referential table. The change is then duplicated in the target field of the target tables paired with the source table and field. All instances of changes in one table that must be reflected in other tables are listed in the referential table. Suppose we have two tables, one containing a list of personnel and their office numbers, and the other containing departments and department leaders. If an employee gets married and changes their name, that change is made in the personnel table. The system then searches for a source table named personnel and a source field called name. A match is found. The target table, department, and target field, dept_leader, are then changed exactly as the source table field was. Note that it is not required for the altered fields to have the same heading, in this case, one was titled name and the other dept_leader.

When data entry screens are instantiated, the code generator, when instructed to, inserts routines that access the referential integrity unit. This allows the designer to clearly state that the rules of referential integrity must be upheld when data is modified in each particular field of every data entry screen.

Data Validation

Referential integrity is not the only requirement for solid data entry, data must be validated as well. There are no means available to validate the data entered into the SDEs DB. ABF constructs a call to a QBF frame, which is capable of manipulating tuples in either one table or a join of tables. QBF was mainly designed to perform simple maintenance of the data, not to enter large amounts of data into several tables. There are no structures available to guarantee the uniqueness of data or the existence of data in other tables. The only data checking performed by QBF is to insure the type of data being entered into a field are correct. That is to say QBF makes sure there are no dates entered where dollar amounts are expected.

Once a data entry screen has been created by AIT, and links to referential integrity have been made, the code generator starts implementing data validation. Application builders may specify which fields must contain elements from separate tables. When instructed by the designer, the code generator produces functions that check for the existence of new data in specified tables. These function will raise a flag if that search fails and ask the user if they wish to change their input or create a new entry in the other table. If the user decides to create a new entry, the function will automatically bring up the data entry screen for the second table. Designers may also select fields to contain unique data items (i.e. table keys). In that case, the dynamically created functions check for existence of a new piece of data in the table which it is being entered. If the item is not unique, the function will produce an error message and force the user to re-enter a unique value.

On line help

Once the data entry units are complete the menu tree builder begin to link into the On-line help mechanisms. On line help is a means of providing the user with information about what they are working on while they are working on it. Rather than searching through stacks of manuals to locate a singular menu option or table field, a user may simply press a key and be

presented with description of the current menu node and the elements contained within.

ABF provides the means to incorporate on-line documentation into the applications it constructs. The designers of the original SDEs application chose not to use it. There is no real user manual for the system either. This drastically increases the amount of time required for new users to become familiar with the application. The problem is compounded by the confusing or misleading report, table and column names found in the SDEs DB. For example, the report maintmonthbill produces a billing report for a fiscal month, and the report maintmonthcharge produces a cost transfer for a fiscal month. These report names are very similar, and new users have a tendency to confuse the two. On-line documentation would quickly provide the user with a distinction between the two reports.

After the primary menu tree has been build by AIT, three levels of on-line help are linked into the program. They are menu and field level help as well as user manual generation. Menu level help provides the user with a description of the currently selected menu option and if need be, an sample of the output from selecting that option. For example, if I were working in a sub menu and came across the option to run the maintmonthbill report and did not know what that report did, I could simply press the help key. This would give me a brief description of the maintmonthbill report. If I were still uncertain of the nature of the report, I could ask for sample output.

Field level help provides information about particular fields in data entry screens. For example, if were entering data into a table and did not know the purpose of the field labeled "beginning", I could call up the on-line help and it would tell me that beginning refers to the date that the customer wants the license to become active.

AIT provides a routine that will construct a user manual. It traverses the primary menu tree and builds a collection of screen images and all on-line help associated with each screen. That information is then formatted and a table of contents is calculated and pretended to the manual. The

manual my either be sent to a text file, displayed at the computer screen or printed to paper. These three types of help have the potential of facilitating the training of new users and lessening the reliance on printed documentation. However, if the field descriptions or menu examples are meaningless, on line help can be more of an annoyance than a feature. For example, if the description of a date field, named "beginning", consists of "This is the beginning date." then no useful information is being presented to the user, and the entire purpose of on-line help is defeated.

User Groups

The SDEs application uses table level validation as its only method of controlling user access in the database. If a user can execute the menu tree for SDEs then he can view every menu and every option of that menu. Table level restrictions are still enforced, that is the user cannot have access to the tables required to run a particular menu option. Each time a new table is created in the SDEs DB, each user must be granted privileges to that table. When a new user enters the system, he or she must be given access to all of the tables they will be manipulating. This is a very sloppy means of applying security.

One method of improving upon this security scheme it to create an access control matrix as proposed by Fernandez et al. [68-72, Fer] Their approach requires a user rights table. It is populated by tuples containing a user name, a table name, an action and a predicate. When a user attempts to manipulate a table, a search is made in the rights table for the user name, target table and action desired. If such a tuple is found, then the predicate is validated. A predicate may contain the hours during which a user has rights to a table. If the predicate is true, the action is performed. This method is stronger than the one employed by SDEs, but it still suffers from the problem granting rights on new tables to all users and granting appropriate rights to a new user. However, the scope of the difficulty is greatly reduced because the user rights are contained in a table. A copy of an existing user's privileges with the new user's name may be inserted into the rights table. A much more versatile security mechanism is employed by AIT.

User groups are set up when AIT applications are constructed. A particular group consists of all users with the same access rights to the database. When a new user is brought into the system, their name is entered into the appropriate user group. This grants them access to all the tables they will need with one command, rather than several separate statements. Furthermore, every tuple in the primary menu tree table contains the name of the user groups that may access that particular option. When a user moves into a sub menu, only the options available to his or her group are listed. This prevents the general population from entering the sections of the database that only administrators need to use. Table level restrictions are also implemented for all groups. When an action is attempted on a table, a search is performed on a group rights table. If a tuple containing the user's group and the attempted action on the target table is not found then the action is not permitted.

Report Generation

AIT and SDEs use the same report generation system, namely Report Writer. The only difference it that AIT provides a fairly thick wrapper around the report mechanism. In the SDEs application, a user chooses to run a report from a menu, they are then prompted for information required and the report is run. Upon completion of the report, the user may print the report to a text file or send it to a line printer.

The same basic procedure is followed by AIT. After the user inputs the specific information for a report, they are asked when the report is to be run and if it is should be done singly or in a batch of reports. If batch mode is selected, the user has the option of prepending a table of contents to the final batch. Users may then select the final destination of the report. They have a choice of either a text file, a line printer or the computer screen. Once all of this information is gathered the report request is queued to run. The options of batch mode and setting the time of execution allow for greater flexibility in the report generator.

Conclusions

Advanced Information Technology provides a strong solution to all of the listed deficiencies in the SDEs application. We have proposed methods for guaranteeing referential integrity, validating data entry, providing an on line help facility in a new SDEs application. There are also methods in the AIT package to construct a much tighter, closely interwoven menuing system that takes advantage of the validation, integrity and help functions. The tool set also expands upon the existing reporting mechanism employed by SDEs. Future work on AIT includes removal of platform dependencies and the implementation of a Graphical User Interface.

Bibliography

[Fer] Database Security and Integrity

E B Fernandez, R C Summers and C Wood 1981 Addison Wesley

[Haw] Database Analysis and Design

I T Hawrszkiewycz 1991 Macmillan

[Pap] Relational Database Management, a systems level approach

M. Papazoglou W Valder 1989 Prentice Hall

[Sto] The Ingres Papers

M Stonebraker 1986 Addison Wesley

The Design of an Automated Electrolytic Enrichment Apparatus for Tritium

prepared for:

Bryan Bandong, Howard Hall, Steve Kreek, and Ann Ruth
and
Radiation Analytical Sciences Section
Environmental Monitoring and Analysis Division
Isotope Chemistry Division
LLNL, University of California

prepared by:

Jeffrey Lawrence Myers
University of Washington
U.S. Department of Energy Science and Engineering Research Semester Student

University of California
Lawrence Livermore
National Laboratory

RAS
Radiation
Analytical
Sciences

Fall 1994

Jeffrey Lawrence Myers
Lawrence Livermore National
Laboratory
P.O. BOX 808, L-231
Livermore, California 94551

December 14, 1994

Science and Engineering Research Semester (SERS)
Radiation Analytical Sciences Section (RAS)
Isotope Sciences Division (ISD)
Environmental Monitoring and Analysis Division (EMAD)
LLNL
P.O. BOX 808, L-231
Livermore, California 94551

SERS/RAS/ICD/EMAD:

I am writing in response to your request for a report describing my project at Lawrence Livermore National Laboratory as a SERS participant. I appreciate you allowing me this opportunity to work with one of the finest institutions in the nation.

This report entitled, The Design of an Automated Electrolytic Enrichment Apparatus for Tritium represents not only my recommended design of an automated system for enviornmental analysis but also a background discussion on tritium. My proposed design, titled AEES - Design II, is gravity based. The design was completed keeping in mind project goals of reliability, safety, minimum cost, and time efficiency.

I feel all feasible options were considered before making my design recommendation. If you have any question regarding, The Design of an Automated Electrolytic Enrichment Apparatus for Tritium, please contact me by e-mail, jmyers@stein.u.washington.edu or by phone at 206-827-5677. I have enjoyed working with Lawrence Livermore National Laboratory and especially with RAS Section and hope that this design proves to be a building block in the process of automating the entire tritium enrichment process.

Sincerely,

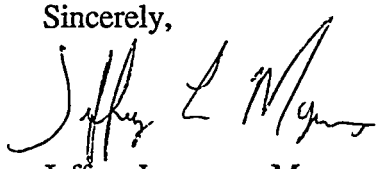

Jeffrey Lawrence Myers
University of Washington
ASCE Vice President
SERS Student

The Design of an Automated Electrolytic Enrichment Apparatus for Tritium

prepared for:

Bryan Bandong, Howard Hall, Steve Kreek, and Ann Ruth
and
Radiation Analytical Sciences Section
Environmental Monitoring and Analysis Division
Isotope Chemistry Division
LLNL, University of California

prepared by:

Jeffrey Lawrence Myers
University of Washington
U.S. Department of Energy Science and Engineering Research Semester Student

University of California
Lawrence Livermore
National Laboratory

Radiation Analytical Sciences RAS

Fall 1994

The Design of an Automated Electrolytic Enrichment Apparatus for Tritium

Jeffrey Lawrence Myers

University of Washington

Lawrence Livermore National Laboratory
Livermore, California 94550

December 14, 1994

Prepared in partial fulfillment of the requirements of the Science and Engineering Research Semester under the direction of Bryan Bandong, Research Mentor, at the Lawrence Livermore National Laboratory.

This research was supported in part by an appointment to the U.S. Department of Energy Science and Engineering Research Semester (hereinafter called SERS) program administered by LLNL under Contract W-7405-Eng-48 with Lawrence Livermore National Laboratory.

The Design of an Automated Electrolytic Enrichment Apparatus for Tritium

EXECUTIVE SUMMARY

The Radiation Analytical Sciences Section at Laboratory at Lawrence Livermore National Laboratory performs analysis of low-level tritium concentrations in various natural water samples from the Tri-Valley Area, DOE Nevada Test Site, Site 300 in Tracy, CA, and other various places around the world. Low levels of tritium, a radioactive isotope of hydrogen, which is pre-concentrated in the RAS laboratory using an electrolytic enrichment apparatus. Later these enriched waters are analyzed by liquid scintillation counting to determine the activity of tritium. The enrichment procedure and the subsequent purification process by vacuum distillation are currently undertaken manually, hence being highly labor-intensive. The whole process typical takes about 2 to 3 weeks to complete a batch of 30 samples, with a dedicated personnel operating the process.

The goal is to automate the entire process, specifically having the operation PC-LabVIEW™ (9) controlled with real-time monitoring capability. My involvement was in the design and fabrication of a prototypical automated electrolytic enrichment cell. Work will be done on optimizing the electrolytic process by assessing the different parameters of the enrichment procedure. Hardware and software development have also been an integral component of this project.

After reviewing and participating in the entire operation of the present electrolytic enrichment process, it became apparent that a quicker procedure was needed in order to satisfy the demand of tritium counts. Several designs were studied considering reliability, safety, time, and cost. These designs narrowed to two after which one was recommended.

This design, titled AEES - Design II, includes complete control of the enrichment equipment and instrumentation, data collection, analysis, archiving, and reporting while satisfying all of the design requirements.

A key feature is that Design II is expected to reduce the process time per enrichment cell by more than 50% thereby substantially reducing costs. In addition, the reliability of the recommended design supersedes all other designs. The design is simplistic in that gravity will be the basis for delivering the desired amount of water sample into an enrichment cell. At a given time interval, water will be dispensed from a storage vessel until the level sensor at the 50 mL mark is activated. This process will continue until the total volume of sample water is depleted. The enrichment process will continue until the 5 mL level sensor is activated after which the whole cell enrichment process will stop and the user will be alerted that the cell has been fully enriched via the software program LabVIEW™.

Currently most of the apparatus needed to satisfy complete automation has been ordered and is awaiting instillation at LLNL. The Pentium - based PC, LabVIEW™ software, thermocouple, external DAQ units, and the DC power supplies are presently being tested and prepared for installation. The solenoid valves and the dual point level switch non-contact ultrasonic level sensor will have to be ordered and tested. The programming of LabVIEW™ to tailor the existing electrolytic enrichment has started and the first stage water bath temperature monitoring is complete. The first stage also included programming the automated temperature monitoring virtual instrument panel. The second and third stages programming and testing has begun but are not completed. These stages will include the final writing of the LabVIEW™ code which will automate the DC power supplies and control the filling of the enrichment cells. Then total assembly and testing of the design can be completed, including full scale and multiple - unit fabrication.

Table of Contents

List of Figures

List of Acronyms and Abbreviations

A	Amps
ADP	Bus computer plug in card
AEES	Automated Electrolytic Enrichment System
AT - 16	16 bit transformer
Bq	Becquerel (1Bq = 2.703E-11 Ci)
CD-ROM	Compact Disk - Read only Memory
Ci	Curie (Ci = 3.7E10 disintegration's/second)
cpm	Counts per minute
DAQ	Data acquisition
DC	Direct current
DRAM	Dynamic RAM
DTR	Disk to buffer
EBq	$1EBq = 10^{18}$ Bq
g	Grams
GBq	$1\ GBq = 10^{9}$ Bq
GLP	Good laboratory practice
GPIB	General Purpose Interface Bus
GW	Giga Watt
HP - IB	Hewlett Packard - Internal Bus
HPLC	High Pressure Liquid Chromatography
IDE	Integrated drive electronics
ITC - 16	16 bit computer interface
ISA	Industrial standard architecture
KB	Kilo Byte
keV	Kilo electron volts
L	Liter
LLNL	Lawrence Livermore National Laboratory
MB	Mega Byte
mCi	$1mCi = 10^{-3}$ Ci = 37 MCi
mL	Mili Liter
PBq	$1\ PBq = 10^{15}$ Bq
PC	Personnel computer
pCi	$1\ pCi = 10^{-12}$ Ci = 0.037 Bq
PCI	Peripheral component interconnect
QA	Quality assurance
QC	Quality control
RAS	Radiation Analytical Sciences
RAM	Random Access Memory
TBq	$1\ TBq = 10^{12}$ Bq
SIMM	Single In-line Module Memory
UNSCEAR	United Nations Scientific Committee on the Effects of Atomic Radiation
US	United States
USSR	Union Soviet Socialist Republic

The Design of an Automated Electrolytic Enrichment Apparatus for Tritium

INTRODUCTION

During the past 75 years, instrumentation for analytical chemistry has evolved from simple measuring devices to sophisticated, microprocessor controlled, intelligent systems. This evolution has allowed laboratories to meet the challenges of increased sensitivity, lower detection limits, and specificity for an expanded number of analyses, as well as address problems of escalating sample loads and a shortage of skilled, knowledgeable personnel. It has also expanded the role of the analyst from that of a bench chemist to one of coordinating several laboratory operations.

Frequently, laboratory personnel are aware that more powerful tools, such as personal computers (PC) exist. Many are not quite sure how to best automate their laboratories around their PC. In the laboratory, a PC can be used for data collection, data analysis, and reporting and chart generation. However, even while the computer is controlling an experiment, it can also be used to interpret the results and design more experiments under a multi - tasking mode of operation.

The present day thrust at Lawrence Livermore National Laboratory's Radiation Analytical Sciences Section is toward the automation and microprocessor control of many of the laboratory operations. Henceforth, The Design of an Automated Electrolytic Enrichment Apparatus for Tritium project was launched. This project cascades into further investigation and design of an automated system, in which total control of all equipment,

monitoring, reporting, data collection, analysis, and archiving in the electrolytic enrichment and vacuum distillation stages is done by a personal computer. This would give the analyst total control of all processes with "the touch of a button." Once installed and on-line this automated procedure will effectively reduce the laboratory time associated with each analysis, decrease the cost per enrichment cell sample, reduce the chances for human error, and minimize the amount of waste produced in the laboratory. In addition, the intelligent computer interface frees the analysts to work on other duties or programs.

Currently, Desert Research Institute, Reynolds Electrical & Engineering Company, Environmental Protection Agency, and Lawrence Livermore National Laboratory have set up an Enriched Tritium Working Group to enhance precise data generation in environmental tritium monitoring. These laboratories use electrolytic enrichment to acquire measurements of low-level tritium concentrations in natural water samples. These laboratories all use similar manually - controlled enrichment processes thus justifying the cause to automate the entire enrichment process since it would be of great benefit and savings to these organizations if they could obtain results more rapidly.

This report is intended to explain the design procedure of the automated electrolytic enrichment apparatus. A brief background on tritium is given to acquaint the reader as to why testing of tritium is done and how measurements are accomplished. Secondly, the requirements for the automated design and their effects on the recommended design are discussed. Thirdly, the materials needed for the automation of the enrichment apparatus and their prospective costs are projected. Two potential designs are evaluated against design criteria by which the preferred design is established. Finally, this report will review the implementation procedure needed to fully automate this process as well as the expected results if the design proceeds as planned.

BACKGROUND

Tritium (^3H) is a radioactive isotope of hydrogen with an atomic number of 1 and atomic weight of 3. It decays with emission of an electron, also called a ß - decay to form ^3He:

$$^3H \text{ ----> } ^3He + e^-$$

Its half-life is 12.35 years. This means that tritium cannot be stored in pure form for extended time periods because 5.6% of the tritium decays annually. The physical and chemical characteristics of tritium are almost the same as hydrogen. Tritium gas burns in oxygen to form tritiated water. It exchanges with hydrogen atoms in organic compounds. Tritium gas is known to diffuse through container walls. Because tritium atoms are three times heavier than hydrogen (^1H), the specific gravity of T_2O or HTO is heavier than that of H_2O, and its boiling point is slightly higher than that of H_2O. The diffusion rates and chemical reaction rates, such as in electrolysis, of tritium compounds are often slower than those of hydrogen compounds due to the increased mass.

The maximum energy of electrons emitted from tritium decay is 18.6 keV, which gives a maximum track length of 6 mm in water (nearly equivalent in human tissue). And because human skin is composed of the epidermis, which is 20-100 mm thick, there is no cause for concern. The target cells for skin cancers and skin damage of other types are present at the basal layer of the epidermis and in the dermis. Thus, electrons emitted from tritium outside of the body could never reach these targets. In other words, electrons from tritium can inflict damage on humans only when tritium is present inside the body (e.g. by ingestion or inhalation). This also implies that most commonly used monitors such as film badges (which are used at LLNL), thermoluminescence dosimeters or pocket ionization chambers are ineffective for detection of tritium in the body. The means to monitor tritium in the

body is a bioassay of urine, blood, or water vapor from expelled air by liquid scintillation counting.

The most common chemical form of tritium in the environment is tritiated water. Incorporation of tritiated water into the human body can occur by three pathways:

- tritiated water vapor in air can be taken into the body via the lung through respiration.
- tritium in fluids and foods can be ingested orally and absorbed through the gastrointestinal tract.
- tritiated water or its vapor can be absorbed through the skin.

Tritium stays in the body in tritiated water and tritium-labeled organic molecules. Tritium, when incorporated into the body, has a biological half-life of 9.7 days to 450 days (1).

Sources of Natural Tritium

Discovery of natural tritium is relatively new. The search for the origin of ^{3}He in the atmosphere led to the discovery of cosmic ray produced tritium. Tritium as free hydrogen in dry air was detected by Harteck and Faltings in 1950, and tritium in surface water was found in heavy water, concentrated from lake water in Norway (1).

The continuous presence of tritium in the earth's environment means that tritium could be produced continuously in the environment, counterbalancing the loss of tritium by its nuclear decay. Major tritium production in nature is from nuclear reactions of atmospheric atoms with cosmic rays in the upper atmosphere, as follows:

$$^{14}N + n \text{ ---> } ^{3}H + ^{12}C$$

$$^{16}O + n \text{ ---> } ^{3}H + ^{14}N$$

$$^{14}N + p \text{ ---> } ^{3}H + \text{products}$$

$$^{16}O + p \text{ ---> } ^{3}H + \text{products}$$

A very minor fraction of natural tritium is produced in the earth's crust from the neutron capture reaction of ^{6}Li in rocks, where neutrons would be provided by spontaneous fission of uranium, and by the (μ ,n) reactions (2).

The United Nations Scientific Committee on the Effects of Atomic Radiation (UNSCEAR) estimated the tritium inventory in natural occurrence to be about 1.0 - 1.3 EBq by assuming near equilibrium. The global inventory of tritium in 1990, including manufactured sources, is illustrated in Figure 1, where its quantity and annual rate are shown in units of EBq (10^{18} Bq) and EBq y^{-1}, respectively.

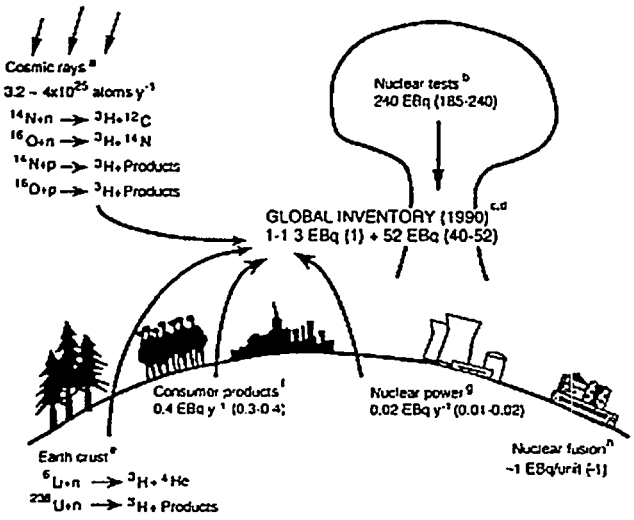

Figure 1 - Global inventory of Tritium (1)

Injection of tritium by nuclear bomb tests into the earth's environment

Since the first bomb test by the U.S. in 1952, various radionuclides have been released into the atmosphere, one of them being manufactured tritium. A series of hydrogen bomb test beginning in 1945 released large quantities of tritium each year until the elimination by the U.S. and U.S.S.R. of atmospheric nuclear weapons testing in 1963. Tests were done after the cessation and it was discovered that the total amount of tritium injected into the earth's atmosphere was manufactured 185 - 240 times the natural tritium (3). UNSCEAR estimated that the amount of tritium released into the environment by 1982 was 6,500 MCi by fusion and 0.15 MCi by fission explosions. If tritium is assumed to decrease only by radioactive decay during 30 year increments, the tritium level from the nuclear tests would be about 40 - 52 times the natural tritium in 1990. (Figure 1)

Bomb tests resulted in radioactive contamination of the earth's environment, but gave scientists opportunities to use tritium in oxide form, HTO, tritium in gas form, HT, and T - methane as radioactive tracers for the study of the kinetics of water, hydrogen, and methane in the environment on a global scale. For example, movements of ocean currents and their vertical mixing, retention time of ground water or lake water, mixing of ground water with rain water, and the exchange rate of atmospheric water vapor between northern and southern hemispheres have been investigated (4).

Release of tritium from nuclear facilities during normal operation

Since 1952, a major portion of the global inventory of tritium has resulted from the release of large amounts of manufactured tritium into the environment from nuclear weapons testing, nuclear power production, and industrial, commercial, and research uses of tritiated compounds.

In 1987, 417 nuclear power stations in 26 countries generated 298 GW of electricity (3). In light water reactors, tritium was produced by ternary fission of the nuclear fuel and from neutron activation of lithium and boron. In heavy water reactors, neutron activation of deuterium was the main source of tritium, exceeding that from ternary fission. The annual production of tritium would be calculated to be about 5.9 MCi by the ternary fission and 10 MCi from the deuterium activation (3). Tritium released into the environment from these reactors was estimated to be 0.62 MCi.

In the case of an incidental release of a puff of tritium gas (HT) from a tritium handling facility, the serious effects can come from human exposure to tritium when in the form HTO. Tritiated water (H_2O) is a greater concern because it is 25,000 times more radiotoxic to humans than HT. This raises the question of how conversion of HT into HTO can occur. First, the conversion can take place by oxidation in air, second, by the exchange reactions with H_2O; third, by photochemical oxidation in air, and finally by oxidation in soil and plants.

Tritium and consumer products

The amount of tritium used for self - luminous light sources in the U.S. was about 400 PBq in 1978, equivalent to tritium produced by light - water power reactors of the country (5). The tritium content of dial paint per watch was up to 740 kBq (6). The thickness of a watch case was sufficient to absorb beta particles from tritium. However, tritiated water or tritiated organic compounds evolved slowly from the paints and could be absorbed by humans through inhalation or skin absorption (3). In the 1960s, seven major paint makers were found to show tritium activities in their urine. Two heavily contaminated persons died of aplastic anemia. Because of their previous records of handling other radioisotopes, it was not possible to attribute their cause of death solely to tritium.

Tritium problems

There is little data on tritium induced health injury in humans, therefore, risk estimation has to be based on animal and cellular experiments with tritium. Such experiments have shown that acute exposure to tritiated water induced carcinogenisis, fetal malformation, mutagenesis, animal death, or killing of hematopoietic stem cells. Because there are few experimental data available, further studies are definitely needed for assessing health risks from tritium under continuous exposure.

Tritium leakage, waste disposal, and public acceptance

Tritium is easily spread into the environment and humans. Several incidences of tritium leakage from tritium facilities showed that tritium of several PBq imposed little health risk. However, if tritium leakage of a much larger quantity would occur, health risk would become of concern.

The other major problem is waste disposal. Some waste, like tritiated water, of high activity may be subjected to concentration and reutilization. That which cannot be reutilized may be solidified for permanent storage. Other waste; for example tritium contaminated powders and materials and tritium contaminated parts of machines and instruments, which occupies a large volume with low tritium activity would need to be stored under constant surveillance. Tritiated water could be diluted and released into the ocean or stored for decay. All types of disposal may become a problem perhaps not because of health risk but because of lack of public acceptance. Therefore, we should be prepared to meet these issues of public perception of risks for the future use of fusion energy, in which tritium plays a major part in the process.

In summary, we covered a brief background on tritium, why tritium is measured, and how it has and is being injected into our environment in the preceding sections. What follows is a discussion of the procedures.

OVERALL CURRENT PROCEDURE FOR TRITIUM MEASUREMENT

The overall procedure for tritium analysis first includes the initial log in of the various sample numbers, names, and locations. After the necessary sample I.D. book keeping, the initial distillation process is begun, using 250 mL of sample followed by the electrolytic enrichment stage. After enrichment has been completed and approximately 5 mL are left in the enrichment cell, the actual water sample is distilled out of the enrichment cell and placed into a dewar flask for vacuum distillation. After vacuum distillation the tritiated water samples are pipetted into minivials where they are then put in the liquid scintillation counters for activity determinations.

Distillation

Distillation is the principle method for purifying liquid compounds. In this process a compound, in our case water, is vaporized. The vapor is condensed, and the liquid is collected in a separate container. Distillation is done first because it is a useful technique for separating a liquid from impurities that have different boiling points or that are not volatile. Also, the initial distillation phase is performed so there is no interference with subsequent procedures.

In order for a liquid to distill, it must be heated to boiling or near boiling. As the liquid is heated its vapor pressure increases until it boils. The boiling point of a liquid is when the temperature at which its vapor pressure equals atmospheric pressure.

Electrolytic Enrichment

The fact that there are very low tritium activities in waters of all kinds found in nature makes it necessary to enrich the tritium in many samples to be measured. This can be achieved by electrolysis of the water until only a very small fraction of the original volume, containing a large part of the initial tritium, remains (Figure 2). Tritium, being heavier than hydrogen or deuterium has a much slower electrolysis rate and hence are broken down (into O_2, HT, or T_2) much slower, thus essentially remaining in solution. Hydrogen and deuterium are evaporated out of the enrichment cell leaving a form of concentrated tritium. The electrolysis is performed in an alkaline solution, with NaOH serving as the electrolytes.

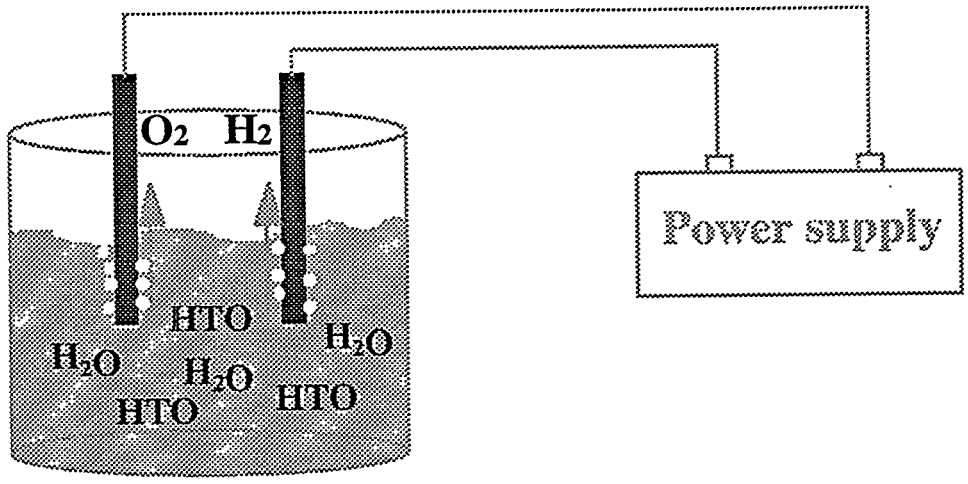

Figure 2 - Electrolysis Process inside an Enrichment Cell

Experience has shown that the concentration of the hydroxide has to be between about 1 and 20% (7). Between each stage the sample has to be distilled for reduction of the concentration of hydroxide. Also, a knowledge of the relationship between the enrichment of deuterium and that of tritium is of the greatest importance for tritium measurements in unknown samples.

The enrichment cell (Figure 3) has been designed to retain most tritium possible and to release all other isotopes throughout enrichment. The lowest, narrow part of the cell has a capacity of about 3 - 5 mL. The total volume up to an upper index mark is about 50 mL. Iron and nickel are used respectively for the cathode and the anode and are kept in position by suitable indentations in the glass and the Teflon baffle plates. The connecting leads support the two Teflon baffle plates which also trap droplets during electrolysis and final distillation. A 250 mL drop funnel, which serves as a sample reservoir, is mounted on the top of the cell.

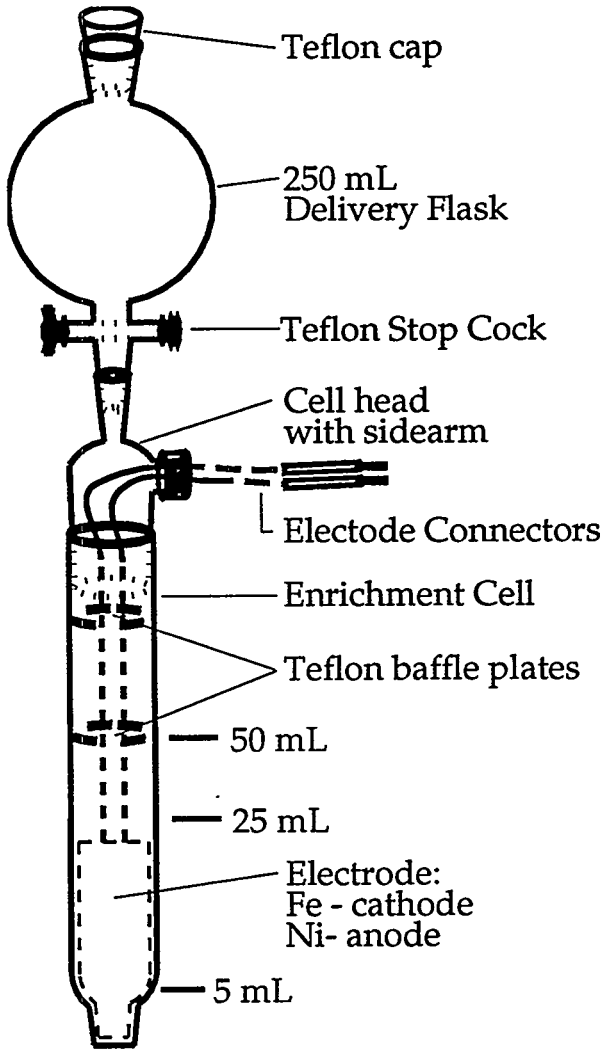

Figure 3 - Enrichment Cell Setup

Usually, in a 250 mL natural water sample, about 50 mL is charged into the cell, and 0.6 g of sodium hydroxide is added. After immersion of the cell in a water bath up to slightly below the ground joint, the remaining portion of the sample is charged into the drop funnel. The water bath is kept at around 5° Celsius by a refrigeration unit, and the temperature read by a regular mercury - in - glass thermometer. This reduces evaporation loss, which would lower the recovery yield of the heavy isotopes during the electrolysis. The electrolysis takes place with 3.0 A controlled by a DC power supply. The temperature of the liquid

should never be more than 0.5 degrees higher than that of the cooling water. In 24 hours the volume decreases to about 25 mL, and by turning the stopcock of the drop funnel a fresh portion of the samples is added up to the 50 mL mark, and the electrolysis is continued. The electrolysis rate is somewhat time dependent on the particular sample. After roughly eight to nine days the sample volume is 25 mL. When this volume or less remains, the current is lowered to about 0.3 A, provided by the same power supply. Within about six days the liquid level is down to the beginning of the narrowest part of the cell, the remaining water quantity being about 2.5 g, after which the electrolysis is terminated.

Vacuum Distillation

Before the sample is distilled the enriched sample is neutralized with carbon dioxide to form Na_2CO_3, to prevent large amounts of hydrogen from being bound in the NaOH. This is performed by removal of the cell head with the sidearm (Figure 3), and the introduction of a thick brass tubing reaching to the bottom, and bubbling carbon dioxide through the liquid at a fixed speed until Na_2CO_3 participates out. After neutralizing the sample, the cell is connected to a distillation head and immersed in a dewar flask kept at around -80° Fahrenheit by dry ice/alcohol mixture. The system is cautiously evacuated while the water freezes out in the trap. The lower half of the electrolysis cell is heated gradually with an electric pad to about 200 degrees Celsius, and the distillation is performed at 60 milli torr, for several minutes. Careful checks have shown that this procedure recovers 99 + or - 1% of the total hydrogen in the concentrate (7).

Liquid Scintillation

Liquid scintillation is the most common procedure for measuring tritium in discrete water samples. The water samples to be analyzed are mixed with a liquid scintillation solution,

called a cocktail, in a scintillation vial. Standard scintillation vials have a capacity of 20 - 24 mL, but smaller vials, called mini vials, are also used if sensitivity is not a problem. Typical water to cocktail ratios are of 1:5 to 1:15 are used in routine applications, however, for low - level counting, special cocktail are used that permit ratios of up to 10:10. In a liquid scintillation counter, the prepared sample is placed between two photomultiplier tubes. The beta radiation in the sample interacts with the scintillation, resulting in several photons being eventually emitted. The summed height of the pulses from the two photomultipliers is proportional to the energy of the beta particle. These counters are run in coincidence mode in order to distinguish photon pulses from photomultipler noise and environmental background. Most LSC counting systems are based on commercially available counters using commercially available cocktails. Our systems utilize the Packard TR/XL 2500 Series.

Typical performance of a regular liquid - scintillation counter is a background of 1 - 3 cpm over the ^{3}H window with a tritium counting efficiency in water of 35 to 55%, depending on sample composition and sample size. The corresponding detection limit is on the order of 200 Bq L^{-1} for a 1 mL water sample counted for 10 minutes. An additional working standard is utilized, when samples require enrichment, to account for the effects of the enrichment process on the sample. The counting rate is a measure of the tritium activity concentration. The liquid scintillation counting method's sensitivity at LLNL (with a counting time of 100 minutes) is generally 0.10 pCi/mL.

Recent developments in background correction and compensation techniques made possible through improved signal processing technology, both with electronic hardware and software analysis, have greatly improved the performance of commercial liquid scintillation spectrometers. As with all of these four procedures, more complete information can be

obtained from manufacturers of specific products and from LLNL's RAS Section Tritium Analysis in Water Samples procedures manual.

AUTOMATED SYSTEM REQUIREMENTS

When considering the design of the automated electrolytic enrichment procedure many issues arise invoking the necessity to produce a set of requirements to which our design can be fabricated. The requirements we have set for the automated system are as follows:

- **Environmentally Safe**
- **Cost Effective**
- **Optimum Automation capability**
- **User-Friendly Software**
- **Fail-Safe mechanism included**
- **Expansible**
- **Keep as much as existing applicable chemistry apparatus as possible**
- **Eliminate cross-contamination of sample**
- **QA/QC and GLP Protocols included**
- **Reliability**

Environmentally Safe

At LLNL, in the RAS section, environmental and occupational safety is a major concern. The final automated electrolytic enrichment procedure for tritium must pose no greater risk to personnel than the previous traditional method, and if at all possible, should be safer.

Cost Effective

As with all projects, the desire to achieve the best results with the lowest cost to LLNL is paramount. The majority of money will likely go into the purchasing of equipment to automate the entire enrichment and vacuum distillation stages. The list breakdown of activities involved are as follows:

- Design
- Engineering Support
- Procurements
- Assembly and Development
- Inspection and Testing
- Training
- Maintenance and Operation

There are also cost increases that can arise from a variety of sources, including the following:

- Cost risk, where vendor quotes or other cost bases may change; or
- Schedule risk, where additional costs may be required to maintain or accelerate activities to support overall project schedule.

It is hoped that this project will go forth without any unforeseen events. Of course, cost effectiveness will depend on the final design chosen and the time it takes to begin the desired design.

Optimum Automation Capability

Optimum automation is preferred to ensure the ease of use, fast processing, and the most efficient automated electrolytic enrichment procedure for tritium. Any particular phase in this enrichment procedure that can be automated should be automated, therefore an extensive look must be presented to warrant that no particular aspect is left out.

User-Friendly Software

Any software system for automating a laboratory must be powerful and flexible, yet easy to use. Many people with different technical skill levels and knowledge of scientific measurements might use the same system. Therefore, having an interactive user interface as well as thorough error checking is very important. The system must be flexible enough so it can be easily adapted for use in new experiments and used to acquire data from new instruments or sensors as they are added. An automated system must also provide analysis capabilities for scaling measurements, comparing data sets, and characterizing data, as well as, archiving, and reporting (8). Finally and most importantly, a system should be able to interface with other systems so that data can be directly shared between laboratories or from a laboratory to an affiliated office.

The key to creating a custom virtual instrument is the software. Powerful and flexible, yet easy to use software tools must be incorporated that communicate with a variety of DAQ (data acquisition) boards, signal conditioning modules, GPIB (general purpose interface bus) interfaces, and serial ports. The software must also include sophisticated analysis functions for processing data, and calculating statistics and trends, and should include functions to present the data in meaningful ways. Data presentation includes everything from displaying data in a variety of two and three dimensional charts and graphs and writing the data to disk in any file format, to printing the data as high quality reports.

Virtual instrumentation is the control of an instrument through a virtual control device. In other words, virtual instruments appearance and operation imitates actual instrumentation. Virtual instrumentation has many advantages over traditional data acquisition and control solutions. Hardware modules can be combined such as plug in boards and signal conditioning components and high level software modules for data acquisition, analysis, and presentation, into a powerful but flexible PC - based system. Also, different instruments from different manufactures can be added or removed. The analysis functions can be combined with the DAQ functions to obtain real time results, instead of saving the acquired data to file and analyzing them later with a different package. Combined with the graphing, data logging, and printing capabilities of virtual instrumentation software, they provide a user interface for a powerful acquisition and analysis tool.

Virtual instrumentation is also cost effective because the same set of tools can be used to develop several systems rather than requiring a different dedicated instrument for each type of measurement. With virtual instrumentation, it is possible to choose the function needed to acquire data from any source, analyze the data, and present the results. Modular hardware components can measure a wide variety of signals, but the software is the key to virtual instrumentation (8).

Fail-Safe mechanism

In order to insure a safe laboratory operation, a fail - safe mechanism must be built into either the software or the hardware, preferably both. Since LabVIEW™ does have many special safe guards within the program, the only concern is that of the manual override controls. These are available and will be utilized in case of an extreme emergency. The controls are clearly marked in the laboratory, thus, any person could completely shut down the enrichment procedure if an accident were to occur.

Expansible

The entire system must be expansible to guarantee that more enrichment cells can be utilized at any one time. Also, if the analyst desires that a new technological measuring device be connected to the existing apparatus, then that should be possible. Furthermore, even if another experiment was to be performed, it is hoped that our system would be able to handle not only its primary purpose of automating the enrichment process, but that of another experiment too.

Keep as much of existing applicable chemistry apparatus

To keep costs from escalating too high, it is desirable that little of the existing enrichment apparatus be changed. Not only would cost be lowered but time saved. The analyst would not have to deal with learning a new procedure for setup or have to maintain the current equipment any differently.

Eliminate cross-contamination of sample

Because the enrichment process is dealing with low-level concentrations of tritium in natural water samples, the samples that are concentrated in the enrichment cells must be prepared carefully in order to receive an accurate and exact measurement. No cross-contamination is acceptable. This factor is very important when deciding between various designs.

QA/QC and GLP Protocols

LLNL - RAS will establish, implement, and maintain quality assurance, quality control and good laboratory practice protocols. These are essential for providing a state of the art laboratory. Under these plans a work - management system provides a systematic means

for achieving technical objectives, ensuring safety, demonstrating that requirements have been met, preventing costly errors and delays, and meeting desired requirements. QA is an integral part of the management of the project.

Reliability

There should be no apprehension about the reliability of the design. To be able to count on a particular design is what LLNL-RAS is looking for. Dependability and the capability of reproducing results of successive trials is what LLNL-RAS is aiming for. When the laboratory is asked to enrich a few hundred samples, our system needs to be able to complete this task within the desired time. Any malfunctions or unreliable equipment will slow down that process, creating a less efficient laboratory. Reliability is one of the most important aspects of this design.

AUTOMATED SYSTEM COMPONENTS

The equipment needed to automate the enrichment phase is by far the most expensive aspect of this project, thus, it is necessary that these materials be understood in detail along with their current cost to LLNL. The materials needed to automate the electrolytic enrichment process for tritium are as follows:

- Personal Computer (AT, 586, etc.)
- External DAQ Units
- Internal Temperature Monitoring DAQ board
- DC Power Supplies
- LabVIEW™ software
- Temperature Monitoring Device

- Solenoid Valves
- Dual Point Level Switch Non-Contact Ultrasonic Level Sensor

A PC 586 / 60 MHz Intel Pentium - based microcomputer is being utilized for the automated electrolytic enrichment procedure for tritium. This particular computer was the most cost effective PC on the market that satisfied our need for speed, time, memory, and the amount of DAQ board units that will be needed for this project. The following list describes a few necessary features within the Gateway 2000 P5-60:

- Intel 60 MHz Pentium microprocessor
- Intel Verified: Upgradable
- 256KB SRAM cache, 15 ns
- 8MB RAM, 70 ns DRAM SIMMs, expands to 128 MB on the system board
- Double-speed CD-ROM drive
- 540MB IDE hard drive with 64KB mulitsegmented cache, 12 ms access time, 17MB/second DTR (disk to buffer)
- PCI Enhanced IDE Interface
- PCI local-bus graphics accelerator with 1MB
- 15" CrystalScan color monitor
  1080 x 1024 in interlaced mode
- Battery-backup clock/calendar
- 4 16 - bit ISA slots, 2 32 - bit PCI slots and 1 PCI/ISA slot
- Desktop case

- 1.44MB 3.5" diskette drive
- 124 - key AnyKey programmable keyboard

All these features make up our PC that is in the process of being integrated into our automated enrichment procedure. This PC's expansibility, reliability, and cost best satisfies our design requirements.

The external DAQ units are called ITC-16 ISA Bus Computer Interfaces and were obtained from a company known as Instrutech Corporation. The cost per unit is approximately $2000 each. These two data acquisition units will be used to acquire signals from the ultrasonic level sensors and DC power supplies. The AT-16 ISA bus computer board plugs directly into the PC - ISA slot and has many different features. These features include a varying number of analog input channels, analog output channels, digital input and output channels, and counter/timers. By using DAQ units the maximum flexibility is available for our measurement needs. In other words, new applications can be easily adapted by adding more boards or simply accessing additional channels to increase the number of channels, isolate the channels from noise or from each other, or even provide amplification or filtering. And because the inside of most computers is very noisy, an external signal conditioning box is optimal. A device driver has been supplied by the vendor and an ADP-16 cable adapter box, which is only for PC's with Pentium microprocessors.

The internal temperature monitoring DAQ board will come from National Instruments. The parts being ordered are specifically for temperature monitoring. The actual DAQ unit is specified ATM M10 16XE50 and costs roughly $1000. A terminal block must also be purchased with the DAQ board in order for there to be an interface for the wires to connect to. This terminal block is specified SC 20 70 and costs $300. This

DAQ unit is very similar to the DAQ units explained above but is exclusively for monitoring, not control of, the temperature system. Another added benefit of this internal DAQ board is that it is already compatible with LabVIEW™, therefore, no drivers are needed.

The DC power supplies are made by Hewlett - Packard and cost around $2500 each. The technical name for this product is the HP-IB DC Power Supply Series - 664xA, 665xA. There are three currently ready for hookup. The new power sources will supply a constant 3 amps DC to the system during the entire enrichment process. The new HP Power Sources will be able to "talk" directly to the PC, unlike the current power supply, creating a concatenated automated system. Drivers will have to be purchased through National Instruments so that this step can be optimized. The existing power sources are supplied by unshielded cables which makes them severely outdated. The new HP amperage units will be much more energy efficient and easy to adapt into the enrichment cells.

LabVIEW™ software from National Instruments is a highly-rated graphical programming system for instrumentation. LabVIEW™ is the single most important component of the design. It costs nearly $2,000 and is revolutionizing the automation industry. This software product, can accomplish all that was discussed previously in the software requirement section and meets and exceeds all design requirements. LabVIEW™ is also a major reason why automating this procedure will reduce the time associated per enrichment cell by 50%. Complete control and storage of all data will be kept through LabVIEW™. Instead of paper being shuffled from hand to hand to computer data will be directly saved into files on the PC hard disk. This information on hard disk can then be accessed by anyone through their own personal computer. Past data history can be seen within seconds rather than having to "hunt" through boxes of papers Thus, LabVIEW™

was chosen to be implemented in the automation of the enrichment procedure. To see a preview of the working virtual instrument and code for the water bath temperature monitoring, see Appendix E.

The temperature monitoring devices will be purchased from Cole-Parmer Instrument Company. The two parts needed are a thermocouple and an extension cable that will hook up directly to the National Instruments terminal block. The thermocouple or immersion probe will cost $60 while the extension cable will cost $20 for 25 feet of cable. An immersion probe was chosen because the thermocouple must be submerged in the water tank. A type T cable and extension cable are necessary because of the temperature range at which the enrichment process takes place. There are different types of cables depending on the temperature range selected to be measured.

Solenoid valves are needed to control the opening and closing of the storage funnels. Basically, the solenoid valve takes the place of the current stopcock (Figure 2). The solenoid valve will be microprocessor controlled, therefore is unequal to any other present device and again, concatenates the automation concept. The cost of one solenoid valve is $200.

The dual point level switch non-contact ultrasonic level sensor will be positioned above the enrichment cell and will sense when the liquid level is at a designated mark in the cell. A level sensor works through an electronic signal that is transmitted to the ITC - 16 ISA Bus Computer Interface by the transmitter - transducer in the sensor. The control unit in turn, through relay contacts, will instruct the solenoid valve to open and the sample water will be delivered into the enrichment cell. When the amount of liquid has been delivered, the solenoid valve will close and the cycle will be repeated to the user's designation. The dual point level switch non-contact level sensor will also be monitored

and controlled by the PC for ease of operation. Also, the use of non-contact sensors will eliminate possible contaminant introduction into the cell. The cost of a dual point level switch non-contact ultrasonic level sensors is approximately $1,200.

THE DESIGN

The objective of the design stage was to facilitate the best manner in which to allow the user to operate the enrichment apparatus in a reliable, time efficient, and safe way. The design of the automated electrolytic enrichment procedure for tritium was definitely the most time consuming aspect of the project. A month was taken in narrowing down the many different designs into two attractive designs. After another three weeks of further investigations between the initial two major designs, one was favored over the other using the selection criteria previously discussed. However, to be confident, a fully integrated pilot-scale model of each design will be built for bench - top testing. Only then will a final design will be absolute. This report purports to provide a recommendation. First, the design not recommended, titled AEES (Automated Electrolytic Enrichment System) - Design I, will be discussed briefly after which the design favored, AEES - Design II, will be explained and justified.

AEES - Design I

The basis to AEES - Design I (Appendix B) is a HPLC (high pressure liquid chromatography) metering pump. Recalling the procedure explained previously, the pump will, in essence, deposit approximately 25 mL of the aqueous sample into the enrichment cell every time the level sensor at the 25 mL mark is activated. This will continue until all the sample water is drained form the storage funnel. Then, after the 5 mL ultrasonic level

sensor is activated the individual cell system will shut down and the user will be notified via the computer screen interface.

AEES - Design II

Gravity, instead of a pump, is the basis for depositing the desired amount of sample into the enrichment cell (Appendix B). At a given time interval, specified by the user, sample water will be dispensed from the storage funnel until the level sensor at the 50 mL mark is activated. This process will continue until the storage water is depleted. The process of enrichment will continue until the 5 mL mark is activated.

Why AEES - Design II ?

The main reason AEES - Design II was selected was because it facilitated the best manner in which to allow the user to operate the enrichment apparatus. AEES - Design II best meets the design requirements stated earlier. For instance, reliability, safety, cost effectiveness, expansibility, cross-contamination, and less modification are all requirements which are better satisfied through AEES - Design II:

- ***Reliability***: Reliability was a major consideration when making the design recommendation because the reliability of a project is one of the most important factors to RAS. Admittedly, both designs are reliable, but AEES - Design II has a better controlled aspect. Because AEES - Design II is run with an internal clock within the PC, the user can depend on knowing exactly when a cell is going to be filled. AEES - Design I has no control over when the pump dispenses the water sample into the cell. Also, AEES - Design II is simple. AEES - Design II is more similar to the existing setup which has been reliable for the last 25 years. The user will not have to learn new or complicated procedures associated with setup/takedown or control wise. All in all, a

simple system is a reliable one and will give the same results on successive trials. Further reasons listed below explain why AEES - Design II is more reliable.

- ***Safety***: The safety issue is an important aspect here at LLNL. Therefore, great time was given in considering designs and safety. Both designs are relatively safe, the only questions arise when a constituent of the system malfunctions or does not perform as expected. It was determined that the pump and the sensors have the same probability of failure, therefore a harder look at both systems were necessary. It became apparent that a pump, with all the tubing that would be necessary to relay the water samples from one place in the lab to another, could be dangerous and requires extensive maintenance. AEES - Design II involves no tubing and would remain as close to the present situation as is possible. Therefore, regarding the safety issue, AEES - Design II has a clear advantage.

- ***Cost***: The cost to obtain the base equipment, or the equipment that both designs will use regardless of which design is chosen is roughly $18,000. The cost per cell for Design I, which would include the metering pump and tube relays, is approximately $2505 where AEES - Design II is near $1400 with no further equipment to purchase. Also, looking at the entire picture, there would be a cost to train the analyst conducting the enrichment procedure. AEES - Design II would involve less training, or less "out of the laboratory time," due to its simple nature and similarity to the present enrichment procedure. Therefore, AEES - Design II, using gravity instead of a metering pump is more cost effective than AEES - Design I (see Appendix C).

- ***Expansiblity***: In terms of adding more equipment or new measurements during enrichment, AEES - Design II is better. For instance, in order to add a few more enrichment cells to the existing setup with AEES - Design I, another pump would have

to be ordered, costing around $1,000 each. AEES - Design II could be expanded without additional equipment having to be ordered. Only LabVIEW™ would have to be adapted and as stated previously, that would present no problem.

- ***Cross-contamination***: AEES - Design II would involve no more cross-contamination than is already present, where AEES - Design I would involve the use of plastic tubing relaying water. Plastic tubing is difficult to clean and has a greater possibility of contamination to samples. In that regard, the plastic tubing would have to be replaced each time a new sample is to be enriched. Because the tritium concentration in the natural water samples are so low, all precautions must be made. No additional contamination factors should enter into the automated design. The cross-contamination factor in AEES - Design I is higher than AEES - Design II.

- ***Modifications***: A substantial new amount of equipment will be needed with AEES - Design I as compared with AEES - Design II. AEES - Design II would use the same equipment with minor modification to the storage funnel, where a solenoid valve would be added. AEES - Design I, would need new storage funnels, or the current one modified severely. Also, the present laboratory setup would have to be adjusted and rearranged so to fit metering pumps and tubing. Lastly, as discussed before, new tubing would need to be replaced each and every time a sample is enriched. Installing new tubing would create an immense increase in setup time. AEES - Design II would involve less modifications.

For the above reasons AEES - Design II has been chosen to be implemented. AEES - Design II, is preferred to AEES - Design I because of its superiority in reliability, safety, cost, expansibility, cross-contamination, and modification capability.

FUTURE PLANS

The next step to automate the electrolytic enrichment procedure for tritium is to fully install and program all components of LabVIEW™. Presently, the temperature monitoring system for the water bath has been fully implemented, including programming and setup. The ITC-16 ISA Bus Computer Interfaces must be completely installed together with the PC. Driver software should be installed onto the PC so that the ITC-16 and the PC can communicate. The last AT-16 ISA bus computer plug in card must also be installed. Once installed the HP-IB Power Supply units must be setup to the enrichment tank, for amperage connection to the enrichment cells, and then connected also to the PC with a driver. After all connections have been made the enrichment cells with ultrasonic level sensors can be hooked up to the solenoid valves which will be controlled by the ITC-16 units. After all initial hook ups have been completed the programming of LabVIEW™ can be consummated. This will entail some time and experience with LabVIEW™. The analyst foreseen to be using the automated procedure for tritium should be a key factor when creating the virtual instrument. The automated control panel should fit to his or her needs as a laboratory analyst. The tentative final setup flowchart of the whole procedure can be seen in Appendix D.

ANTICIPATED RESULTS

If the design of the automated electrolytic enrichment apparatus for tritium is implemented, it will be shown that this automated procedure will effectively reduce the laboratory time associated with each analysis by 50% and minimize the cost per enrichment cell while

maintaining a safe, if not safer, workstation. In addition, the intelligent computer interface will free the analyst to work on problems associated with existing technologies and develop new applications. It will help the LLNL - RAS Section electrolytic enrichment laboratory if implemented, and also create more accurate and consistent data. Unlike the present, we will have complete control of the equipment, data collection, analysis, archiving and reporting of enrichment data in one computer instantaneously. Also, if the project goes as planned it will be the first of its kind in the world, no one else has yet to attempt to automate the electrolytic enrichment apparatus for tritium.

CONCLUSION

Complete control of the electrolytic enrichment apparatus for tritium will occur if AEES - Design II and the above requirements are implemented. The design phase of this project consisted of 3 full months over which much thought and laborious work was done. The future success of the project is based upon timing and funding. If dedicated employees have the time to pursue this project and if funding is available, finalization is possible. The enrichment laboratory will cut the time per enrichment cell by 50%. This reduction in time will ultimately reduce the cost of measuring tritium concentrations more than offsetting the development costs. In summary AEES - Design II is a simple, reliable, safe, and cost effective design that should be implemented in order to reduce costs and time. Another four to nine months with the present people working on the project is essential for its completion. Automating this particular project will be very beneficial to the RAS Section at LLNL and I am proud to have been given an opportunity to participate in its design.

References

(1) Shigefumi Okada and Noriyuki Momoshima, "Overview of Tritium: Characteristics, Sources, and Problems," Health Physics Society, 1993, 593 - 726

(2) Kaufman, S.; Libby. "The natural distribution of tritium," Phys. Rev. 93: 1337 - 1344; 1954

(3) United Nations Scientfic Committe on the Effects of Atomic Radation. New York: United Nations; UNSCEAR 1977 Report; 1977a: 54 - 55

(4) National Council on Radation Protection and Measurements. 2nd ed. Bethsda, MD: NCRD; Report No. 58; 1985: 368

(5) Brown, R.M. A Review of Tritium Dispersal in the Enviorment. 1989: 557 - 576

(6) National Council on Radiation Protection and Measurement. Bethesda, MD: NCRP; Report No. 62: 1979

(7) H.G. Ostlund and E. Werner, The Electrolytic Enrichment of Tritium and Deutrium for natural Tritium Measurements. Volume I, Internal Atomic Energy Agency, Vienna: 1962: 97 - 98

(8) Crystal Doubrava and Meg Kay, "Advanced laboratory applications of PC's," American Laboratory, 1982: 29 - 33

(9) National Instruments. 1993. LabVIEW™. Version 3.01. Computer software.

Appendix A:
Pictures of Procedures

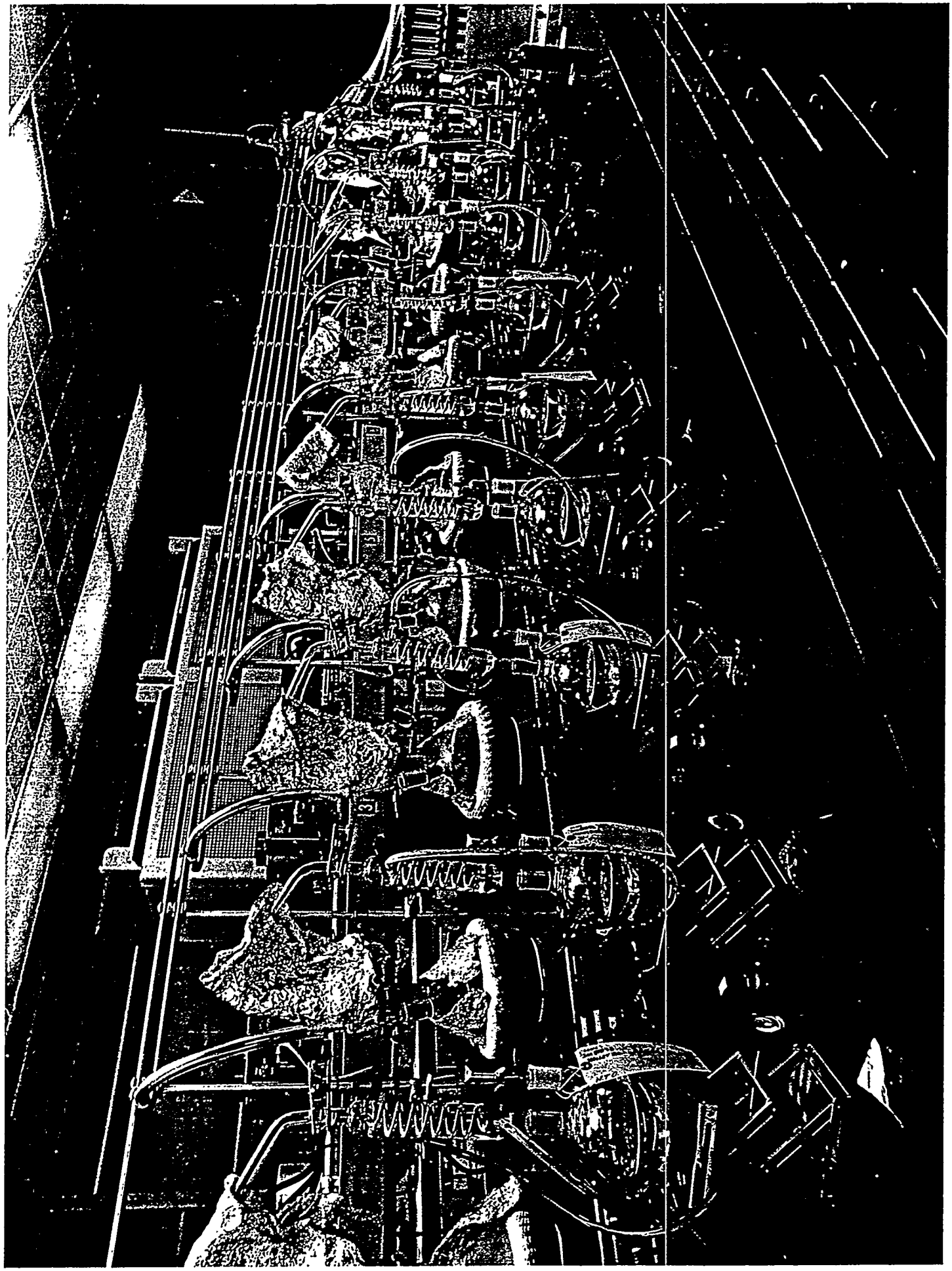

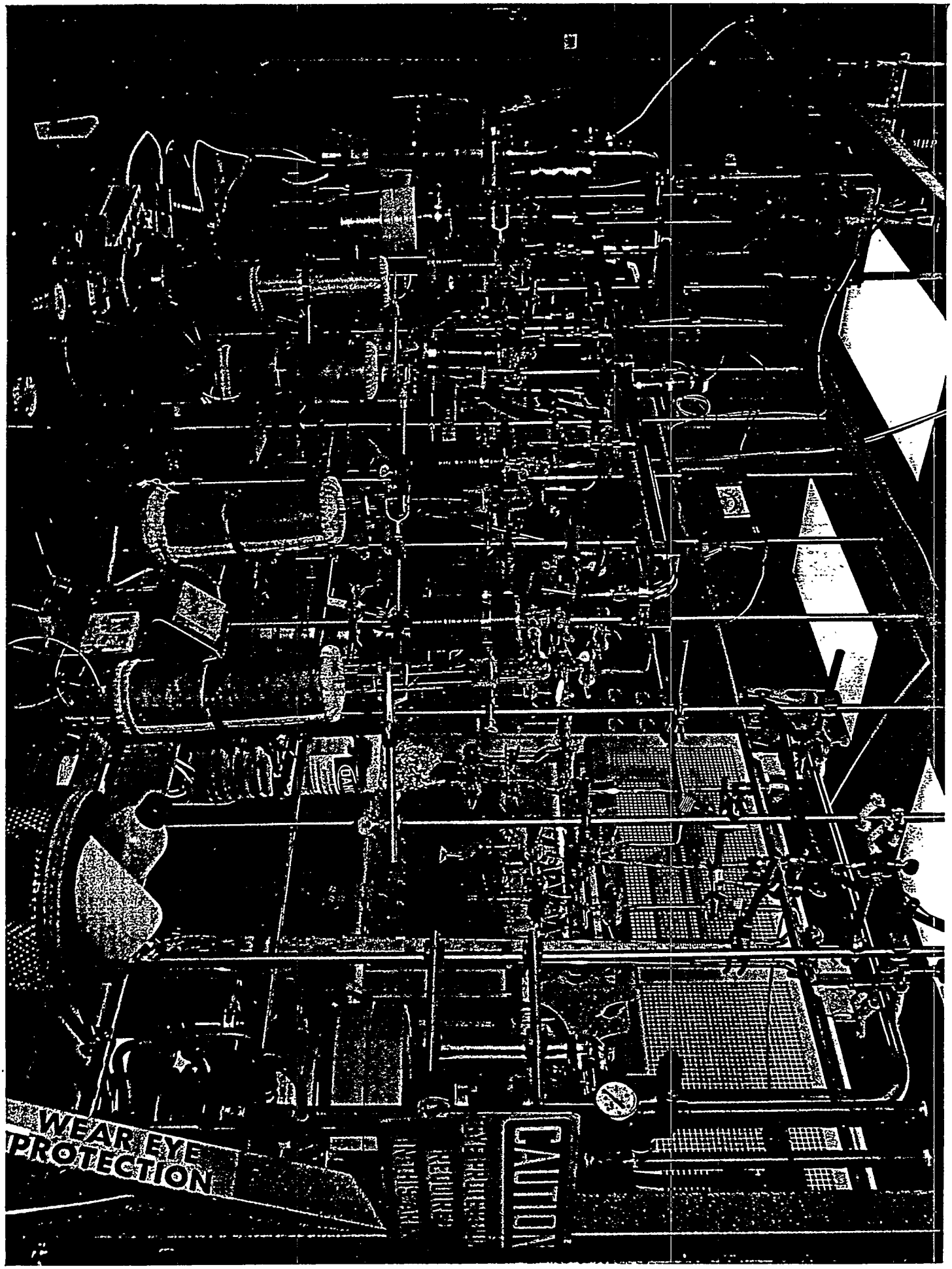
WEAR EYE
PROTECTION
CAUTION

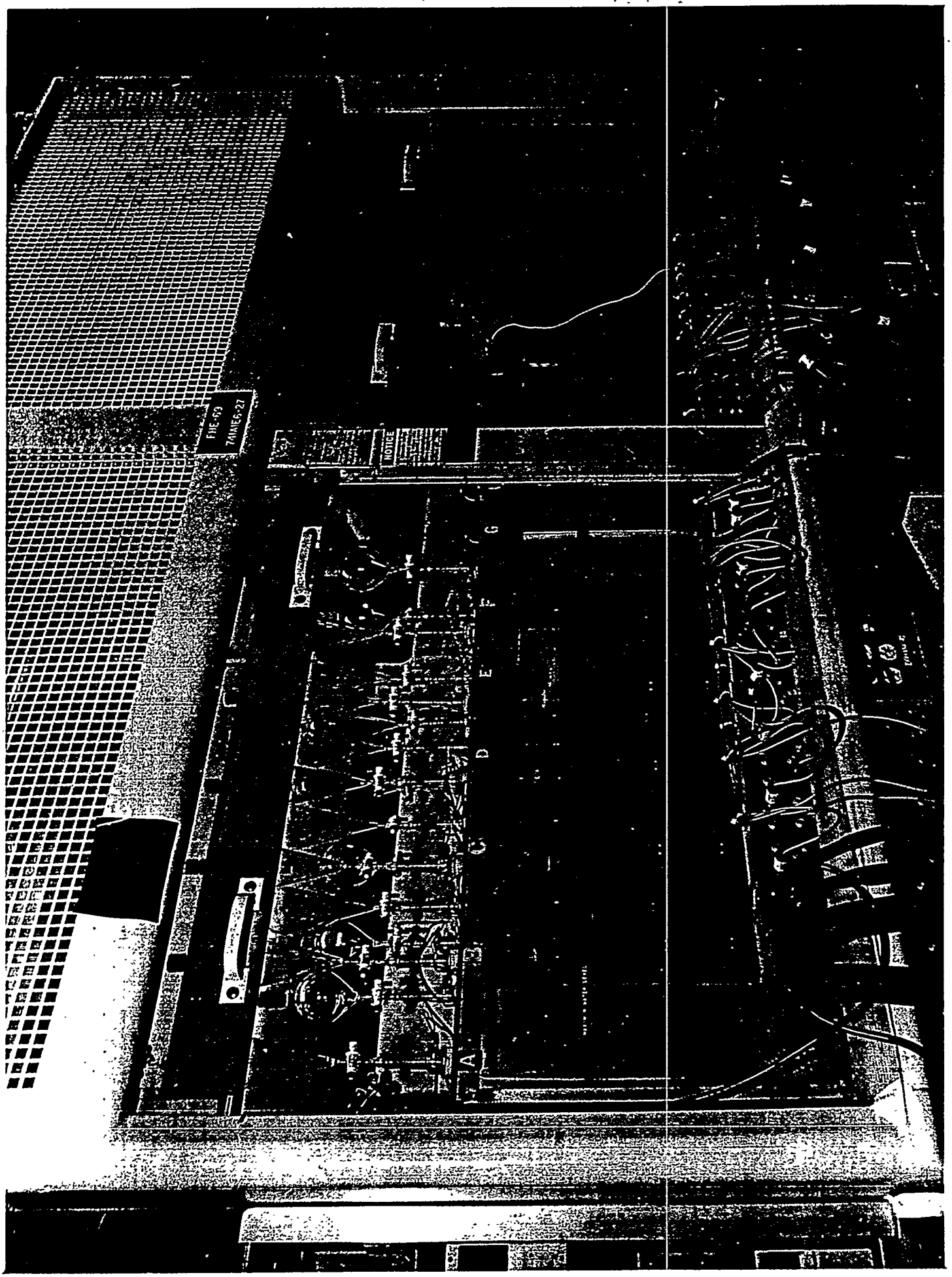
FIRE-69
ZMAIE6-27
NOTICE

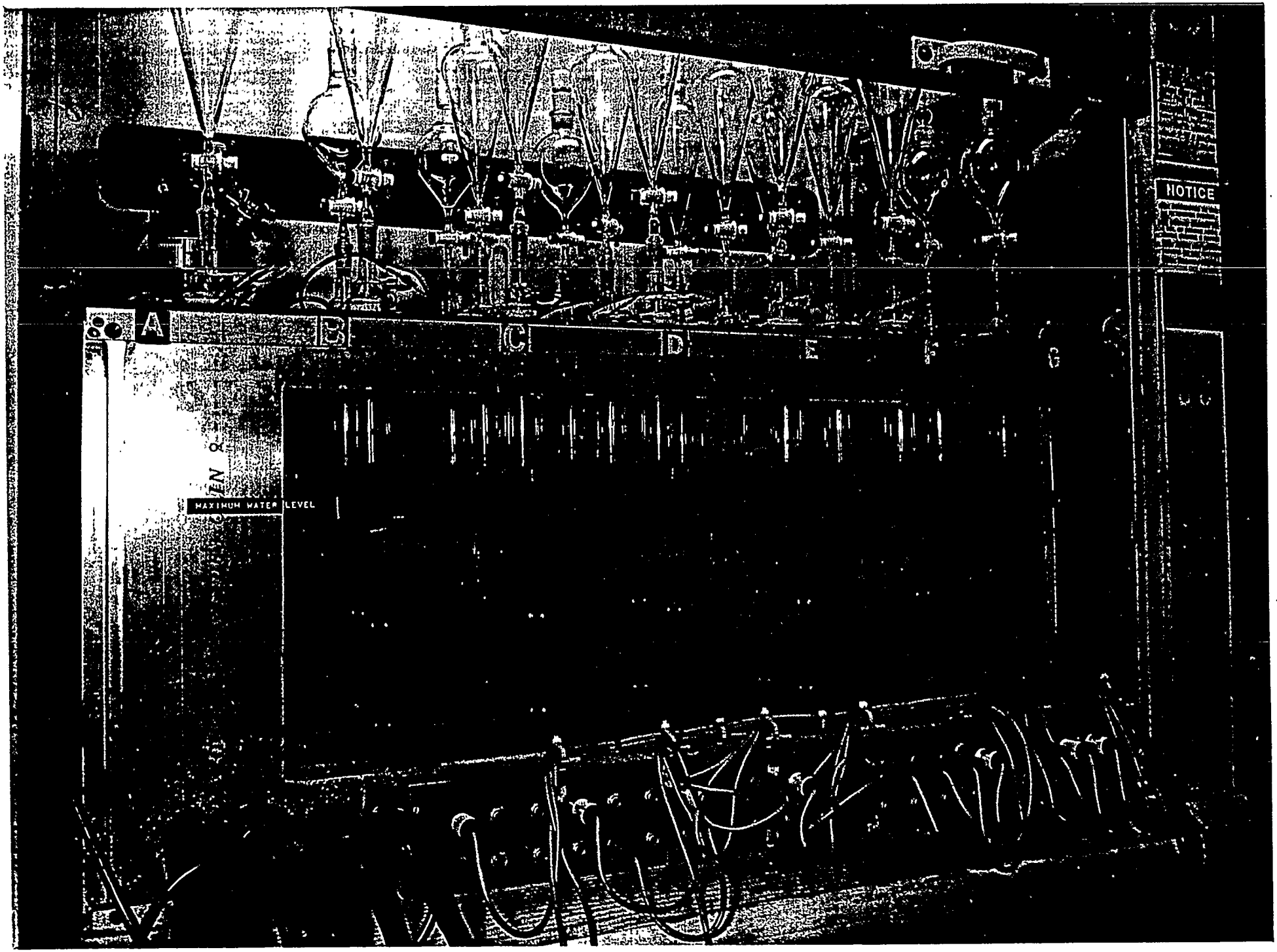
NOTICE
A
B
C
D
E
MAXIMUM WATER LEVEL

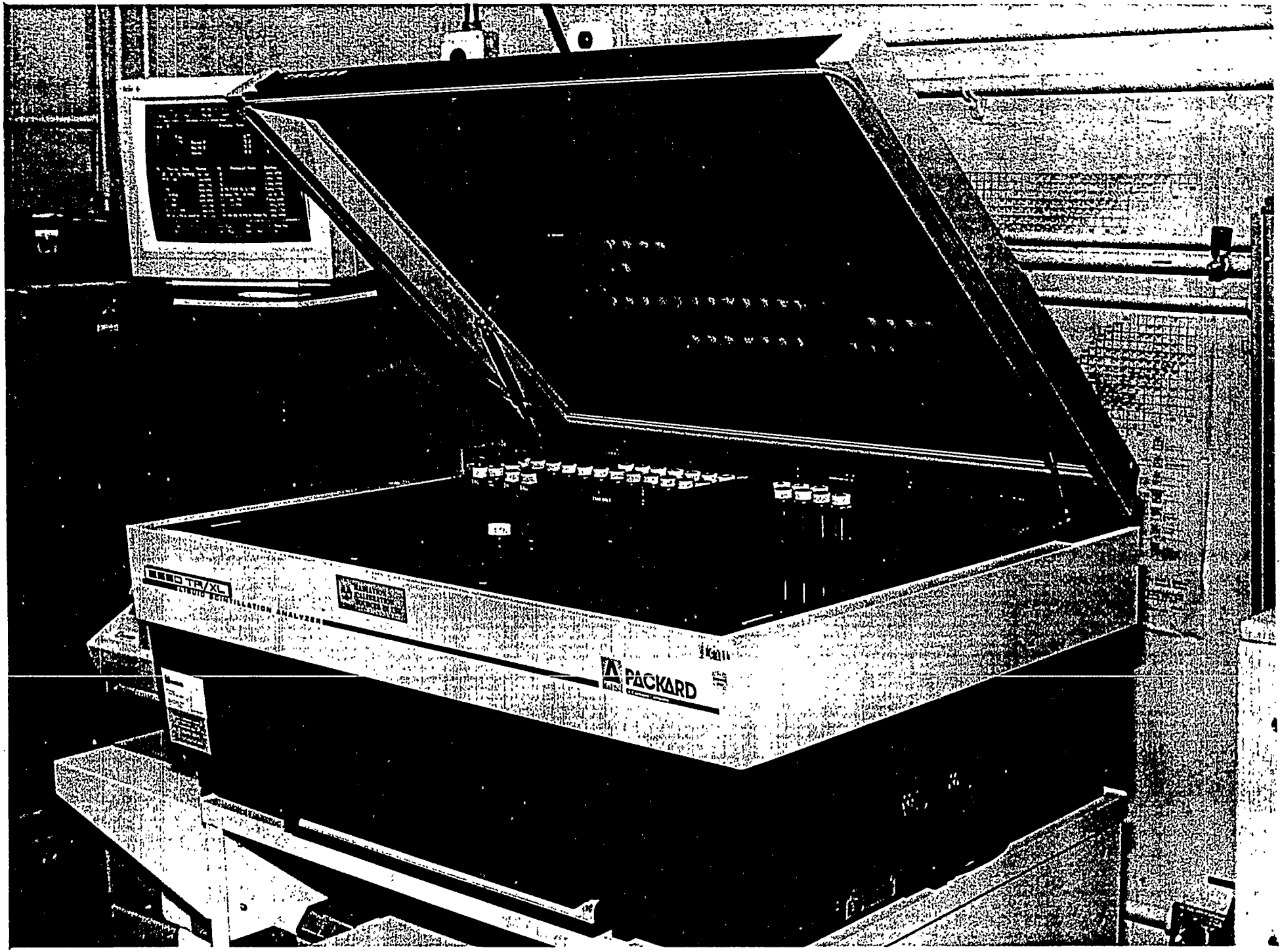
TA/XL
PACKARD

Appendix B:
Flowcharts
Design I
Design II

DESIGN I

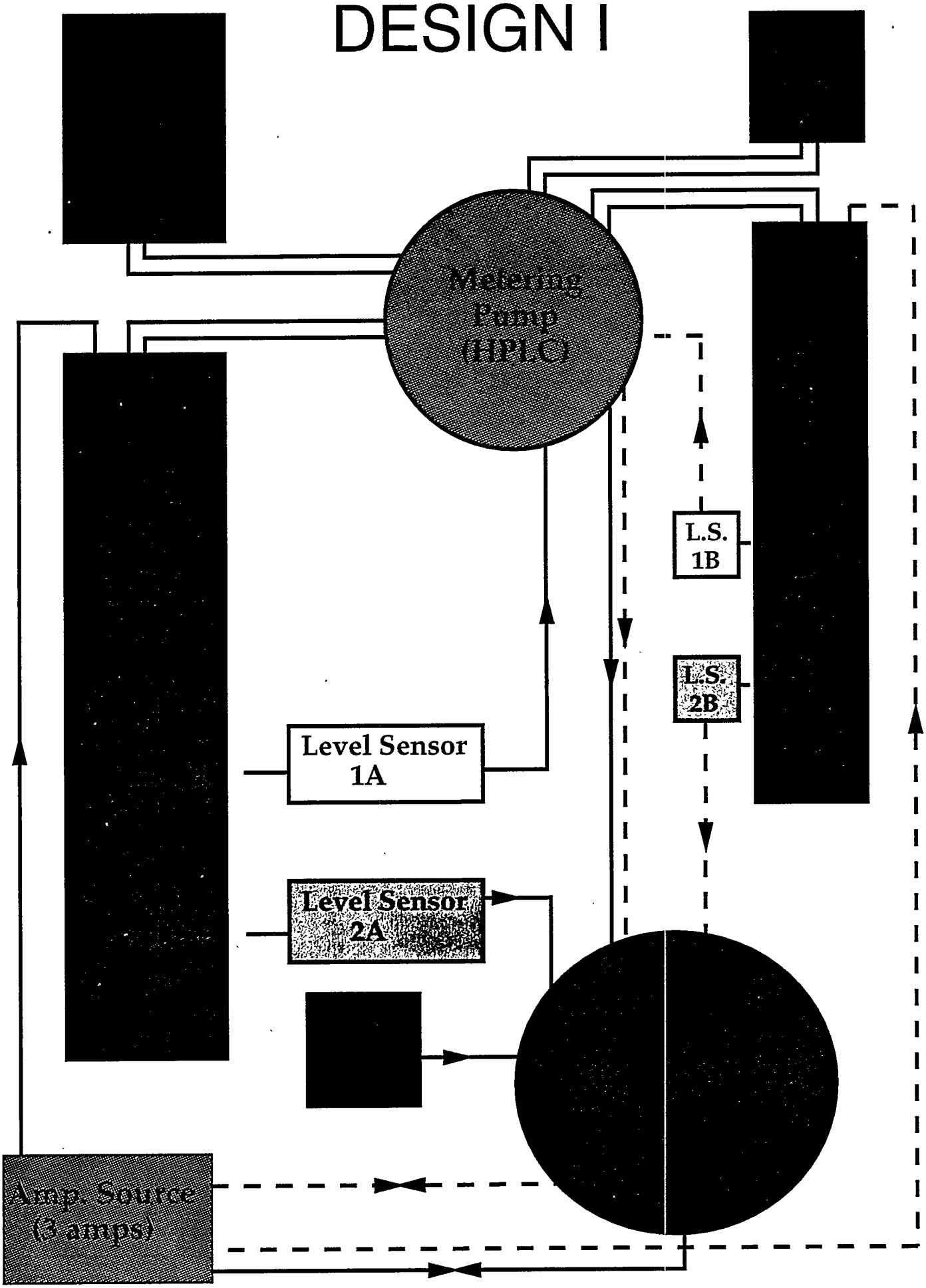
Metering Pump (HPLC)
L.S. 1B
L.S. 2B
Level Sensor 1A
Level Sensor 2A
Amp. Source (3 amps)

DESIGN II

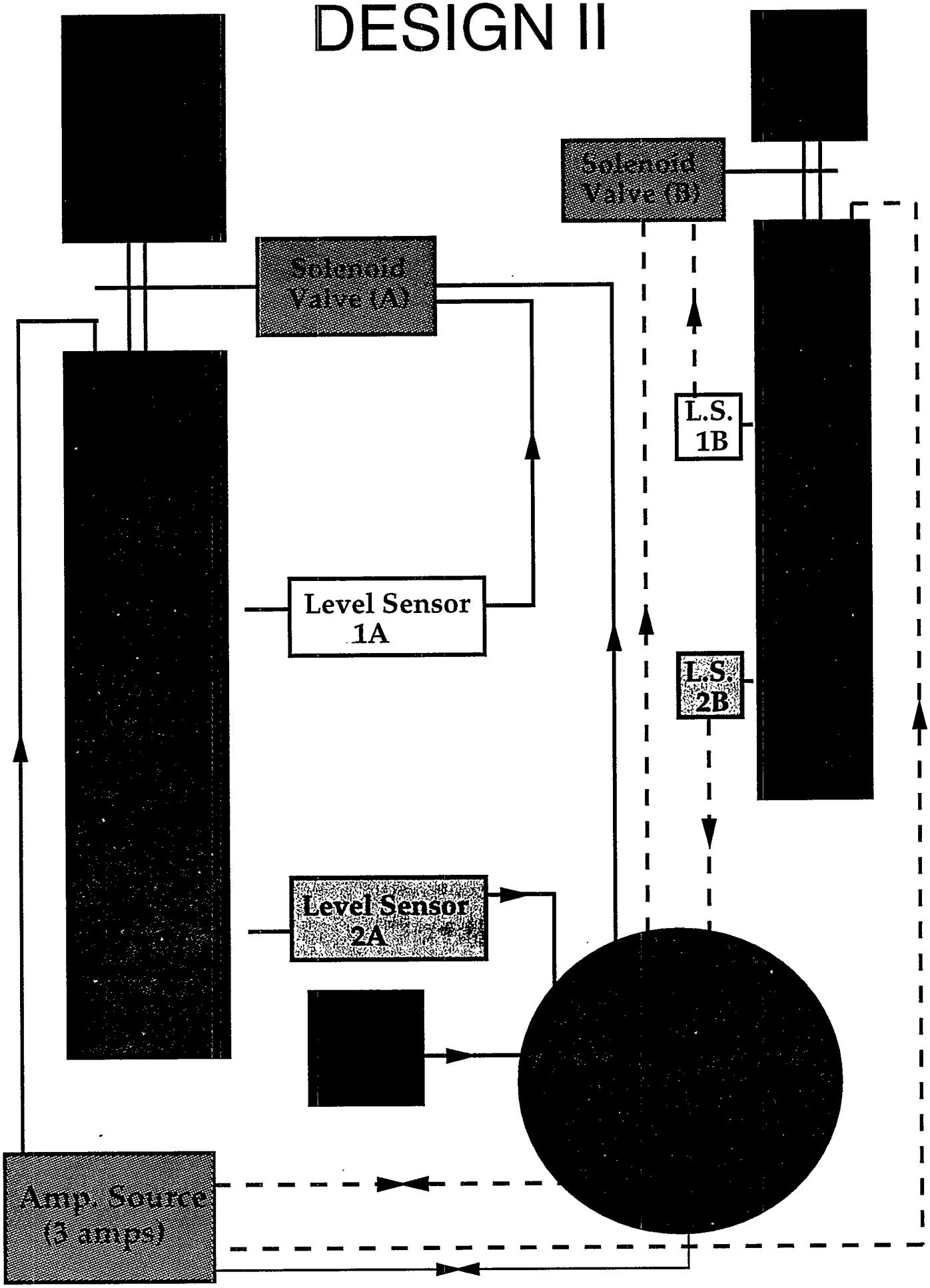
Solenoid Valve (B)
Solenoid Valve (A)
L.S. 1B
Level Sensor 1A
L.S. 2B
Level Sensor 2A
Amp. Source (3 amps)

Appendix C: Cost Breakdown

Cost Breakdown Analysis

BASE EQUIPMENT

Gateway 2000 P5-60	$2,000
External DAQ Units ($2,000 each)	$4,000
Internal Temperature Monitoring DAQ board	$1,000
Terminal Block	$300
Amperage Units ($2,500 each)	$7,500
LabVIEW software	$2,000
Temperature Monitoring Device	
Immersion Probe	$60
Extension Cable	$20
Solenoid Valve	$200
Dual point level switch non-contact ultrasonic level sensor	$1,200
TOTAL	**$18,280**

PER ENRICHMENT CELL

AEES - Design I

Pump up/Pump down relays	$55.00
Chemical Metering Pump	$1,100
Solenoid Valve	$200
Level Sensor	$1,200
TOTAL	**$2,555**

(Note: pump relays would have to be replaced every enrichment cell cycle, which means buying new ones every time. This factor is not included in the breakdown)

AEES - Design II

Solenoid Valve	$200
Level Sensor	$1,200
TOTAL	**$1,400**

Appendix D:
Final Flowchart
of Design II

DESIGN II
(in detail)

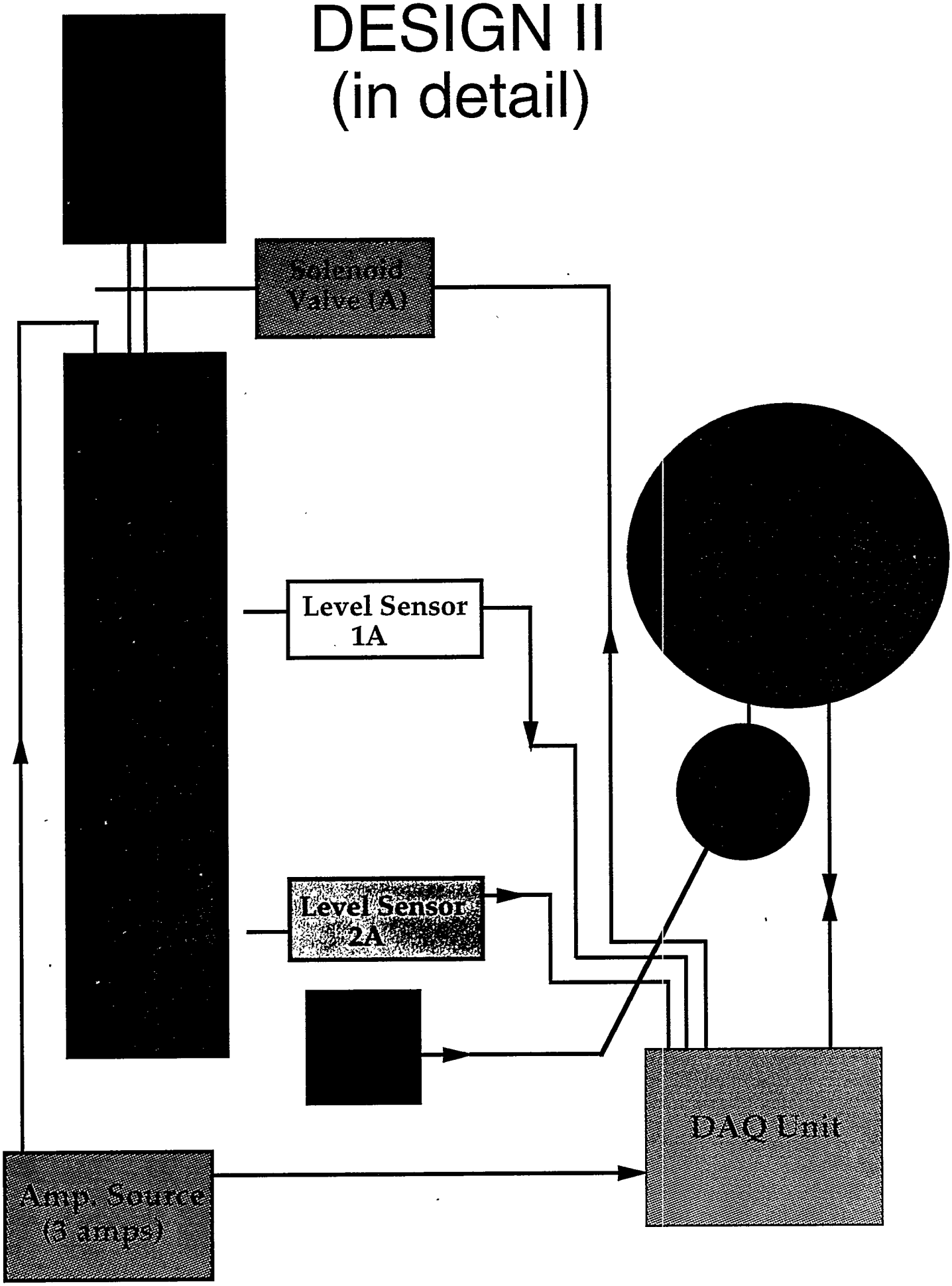

Appendix E:
LabVIEW - Temperature Monitoring:
Virtual Instrument and Code

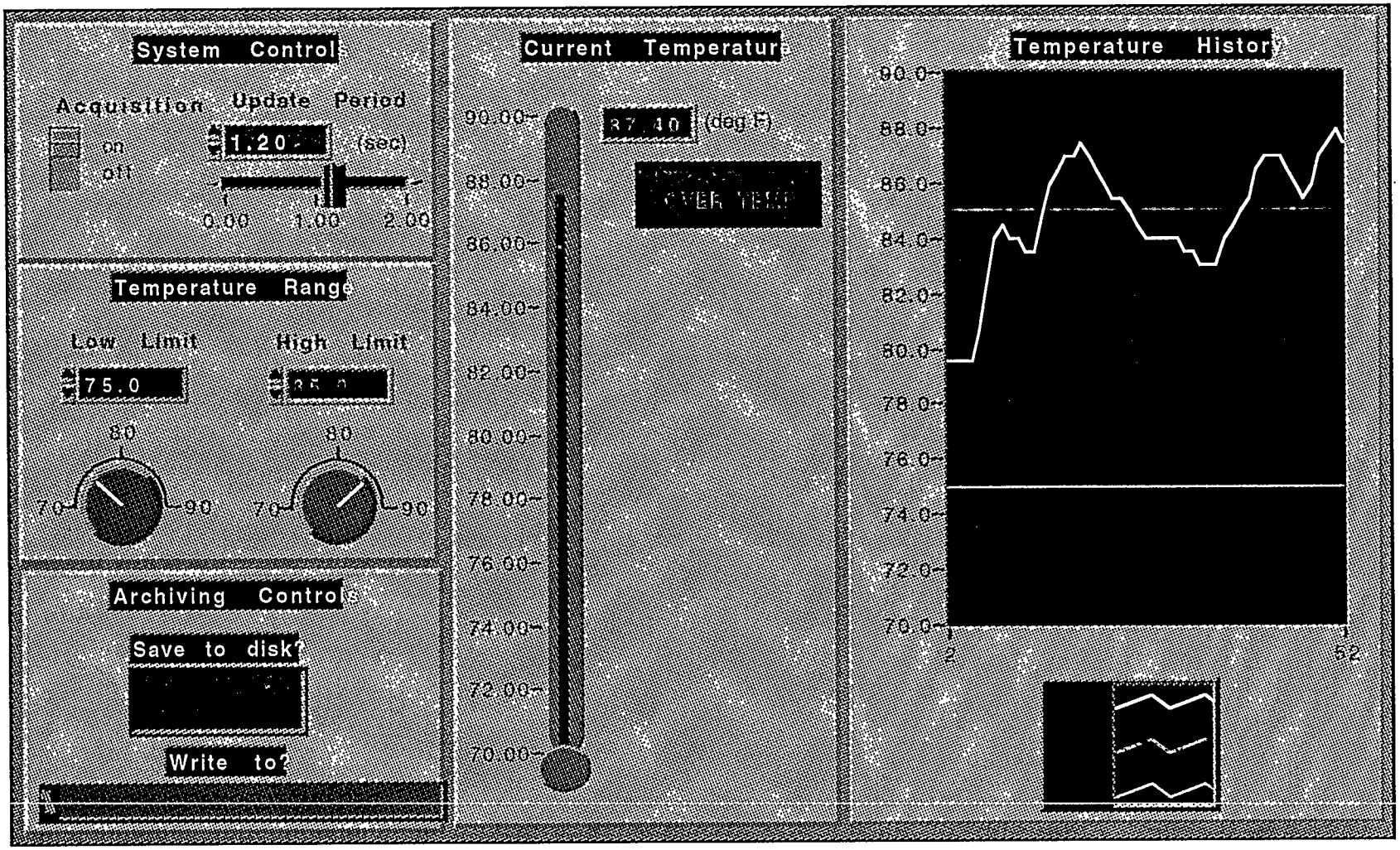
System Controls
Acquisition Update Period
on
off
1.20
(sec)
0.00
1.00
2.00
Temperature Range
Low Limit
75.0
High Limit
80
70
90
Archiving Controls
Save to disk?
Write to?
Current Temperature
87.40
(deg F)
90.00
88.00
86.00
84.00
82.00
80.00
78.00
76.00
74.00
72.00
70.00
Temperature History
90.0
88.0
86.0
84.0
82.0
80.0
78.0
76.0
74.0
72.0
70.0
2
52

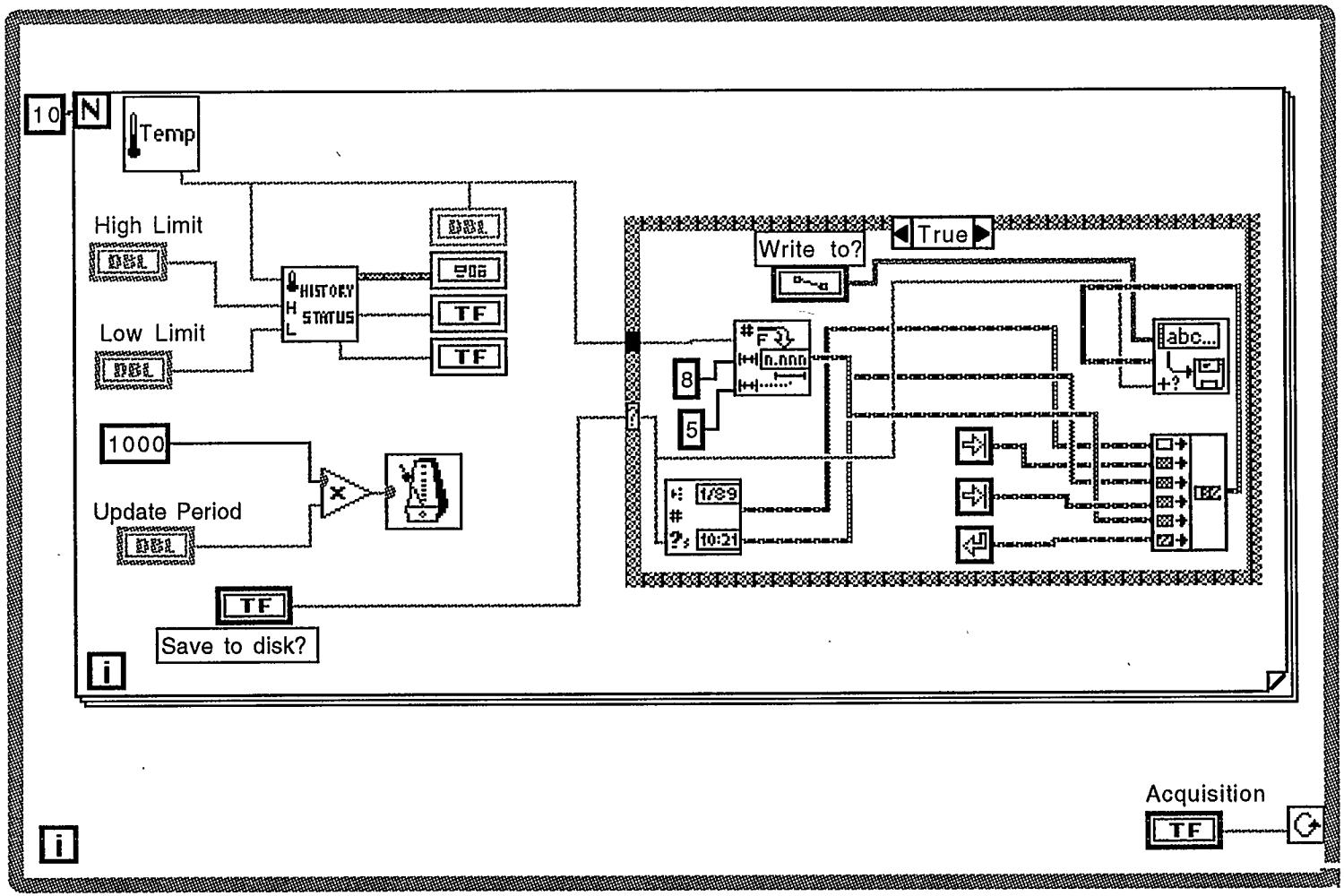
10
N
Temp
High Limit
DBL
Low Limit
DBL
HISTORY
H
L
STATUS
DBL
TF
TF
1000
Update Period
DBL
TF
Save to disk?
i
Write to?
True
8
5
1/89
10:21
abc...
TF
Acquisition
i

Fluvial Terrace Dating Using *In Situ* Cosmogenic ^{21}Ne

Ed Sexton[1] and Marc Caffee[2]

[1]Department of Geological Sciences, University of Illinois at Chicago, IL 60607
[2]Lawrence Livermore National Laboratory, L-397, P.O. Box 808, Livermore, CA 94551

Abstract

Through the analysis of cosmic-ray produced radio-genic and stable nuclide concentrations, specifically ^{21}Ne, we hope to date certain geomorphic features located along the tributaries of the Colorado River in the Eastern Grand Canyon and the Rainbow Plateau located in Utah. During the Quaternary, the Colorado River system was fed by glacial melting and run-off from the Wind River and Colorado Mountain Ranges. Past periods of aggradation allowed the emplacement of terrace features from debris flow activity. By dating such features we can further constrain the timing of key events such as river down cutting, terrace genesis/exposure age, and rates of surface erosion. Knowing the age and elevation of each terrace we can determine an average rate of down cutting of this river system. This, in turn, will offer information regarding alpine glaciation which is a sensitive indicator of global climate change. Studying the relative concentrations of these isotopic species in surface rocks can be useful in researching glacial periodicity and the relationship between solar activity and climate.

Introduction

Our Earth is continuously bombarded by high-energy cosmic rays originating from outside the solar system. These galactic cosmic rays (GCR), greater than 1 GeV, upon striking atmospheric atoms and molecules produce a cascade of secondary particles. This shower of secondaries produce through spallation reactions and neutron capture a number of stable (^{21}Ne and ^{3}He) and radio-isotopes (^{10}Be, ^{14}C, ^{26}Al, and ^{36}Cl). The relative production rate of cosmogenic ^{21}Ne has been determined fairly accurately using the available data on cosmic ray neutrons (1). This production rate is dependent on the target element as depicted in Table 1 from Lal 1991(2), and based on the petrology of the terraces/debris flows. In this study, we are only concerned with spallation production off of the silicon target element yielding cosmogenic neon. Because the oxygen distribution in silicon tetrahedron of quartz is very uniform we expect the production rate to be invariant.

TABLE 1
Approximate production rates of the three stable isotopes of neon at sea-level, latitude > 60°

Target element	Nuclide Production rate (atom / g yr)		
	^{20}Ne	^{21}Ne	^{22}Ne
Mg	8.0×10^{1}	1.1×10^{2}	
Al	2.8×10^{1}	2.4×10^{1}	
Fe	2.2×10^{-1}	2.4×10^{-1}	2.3×10^{-1}
Si	3.3×10^{1}	1.8×10^{1}	2.0×10^{1}

Sample Localities

Geographic areas that are being researched are located in two areas; the first located in the eastern Grand Canyon, between Lee's Ferry and Unkar Creek. Down-cutting of the Colorado River punctuated by periods of stasis results in multiple terraces in which the lowest levels are the youngest. These surfaces come about through erosion of local rocks, mainly chert. There exists at least five levels which range in age from < 2000a to 140-180ka.

The second region lies on high-level pediment surfaces on the Rainbow plateau south Lake Powell, where the terraces are mantled by debris flows from Navajo Mountain. These terraces form several families of different topographic elevation and ages. Canyon cutting has isolated these terraces from the source region of colluvium, thereby preventing further deposition. For the lower and younger surfaces of the sequence, the geomorphic age is confirmed by the cosmogenic nuclide measurements on Navajo sandstone boulders which mantle the terrace. Cosmogenic radio-nuclide ages of the terraces, conducted by Caffee and Finkel, range from about 15ka to > 250ka (3).

Analytical Techniques

Sampling techniques involve chemical pre-treatment as listed in Kohl and Nishiizumi 1992. Samples were crushed and sieved to a uniform grain size and separated from rock fragments by hand picking and magnetic separation. Acid leachant of HNO_3 and HF were subjected to a battery of samples (THA-4a,b, d) ranging in time of 0 to 72 hours while heated. Comparing leach to non-leach samples we noticed very little change in ^{21}Ne concentrations, varying «10%. We conclude that for our samples that the leaching process is not an important step in chemical pre-treatment.

We crushed the rock-samples in a unit flooded with dry nitrogen in order to release a possible trapped non-cosmogenic component of neon in quartz inclusions. By restricting the interaction of the atmosphere with our sample we gain additional time in the pumping down procedure when we load the sample into the crucible. This also limits the amount of impurities released into the mass spectrometer. From this procedure we noticed a negligble reduction in neon concentration, but have decided to keep it a part of the sample preparation for constancy.

Samples range from 0.26g to 0.31g and are loaded into an aluminum boat. Once loaded into a crucible (Molybdenum), we heated at 0, (150)200, 600, and 800°C temperature steps. We see a 99% release of cosmogenic Ne (Ne_c) in the 600°C heating interval as verified by the current research (4, 5).

We follow a long process of filtering and purifying the sample gas in order to isolate neon and helium isotopes. After the heating, the sample gas encounters a sublimation-titanium pump which aids in trapping hydrocarbons. Also a hot Cu/CuO trap oxidizes the gas forming hydrocarbons and catalyzes the CO molecule to CO_2. Once exposed for 15 minutes, the gas is moved to two liquid nitrogen finger (-198°C) where Xe, Kr, Ar, Co_2 phases are separated from the gas. Collection time for this part of the procedure is 50 minutes. Two SAES getters help remove the CO2 from the system. Right before the gas is let into the VG 5400 Noble Gas Mass Spectrometer, a

cryogenic separation of He and Ne help increase the sensitivity and concentration of neon. The freezing point of He and Ne, although not sharing the same excitation energies, differ by 10°C. Through many air calibrations we have pin-pointed the temperature at which the most neon is released with the least amount of argon. We can analyze the helium component of the sample gas and pump it away (roughly 200k counts/second for air calibrations and $1X10^6$ counts/sec for sample gas). This feature enables us to freeze every atom of Ne onto the cryogenic charcoal finger which delivers a 5X sensitivity in comparison to air calibrations not exposed to cryogenic separation..

Isotopic analyses were made on a VG 5400 mass spectrometer with an electron multiplier. All values in table 2 were corrected for interference peaks ($^{44}CO_2$, ^{40}Ar, ^{42}HC, etc.), instrumental effects, and machine blank background levels (6). Ratios and Ne_C represent a best-fit exponential extrapolation to time = 0, which is the y-intercept of time versus counts using Igor Pro graphing tool.

Table 2
Sample characteristics.

A	B	C	D	E	F	G	H	I	J	K	L	M	N	O	P
label	filename	21/20(init)	22/20(init)	20Ne counts/sec	20Ne sigma	sensitivity	weight (g)	20Ne atoms/gram	20Ne sigma	21Ne atoms/gram	22Ne atoms/gram	08e atoms/gram	21/10	22/10	21/22
AR	(0.00345) + (0.10357)														
a	rf-93-8 150c 1dec94.neo	0.00397	0.10085	2.3092E+04	338.46	4.2X10+5	0.2664	3.6410E+10	6.3515	1.8950E+07	0		4.29E+06	4.4172E+00	0.00E+00	
A	rf-93-8 600c 3dec94.neo	0.00405	0.10376	3.3920E+04	7387.15	4.2X10+5	0.2664	5.3477E+10	1.1646	5.6147E+07	9.77E+06		4.29E+06	1.3088E+01	2.28E+00	5.7448E+00
				5.7012E+04				8.9887E+10		7.5697E+07	9773508				
b	rf-93-9 150c 5dec94	0.00404	0.11005	2.9384E+04	125.94	4.2X10+5	0.3034	4.7737E+10	2.046	2.8174E+07	9.18E+06		4.66E+06	6.0458E+00	1.97E+00	3.0654E+00
B	rf-93-9 600c 5dec94.neo	0.00388	0.10407	3.1946E+04	2661.03	4.2X10+5	0.3034	4.4226E+10	3.958	1.8130E+07	2.21E+07		4.66E+06	3.8906E+00	4.75E+00	8.1925E-01
				6.1332E+04				9.1963E+10		4.6304E+07	3.13E+07				1.4784E+00
c	rf-93-12 150c 6dec94.neo	0.00376	0.10531	1.6628E+04	136.27	4.2X10+5	0.2745	2.5747E+10	2.085	7.9817E+06	4.54E+09		9.30E+05	8.5825E+00	4.68E+03	1.7581E-03
C	rf-93-12 600c 6dec94.neo	0.00426	0.10822	2.2548E+04	118.14	4.2X10+5	0.2745	3.4499E+10	1.8125	2.7070E+07	1.60E+08		9.30E+05	3.0075E+01	1.73E+02	1.7434E-01
				3.9376E+04				6.0246E+10		3.5682E+07	4.79E+09				7.6486E-03
d	the-4a 200c 16nov94.neo	0.00365	0.10107	2.2760E+04	226.44	4.2X10+5	0.3236	9.5590E+09	9.51	1.9120E+06	0		3.20E+06	5.9750E-01	0.00E+00	0.0000E+00
D	the-4a 600c 16nov94.neo	0.00355	0.106	3.4387E+04	9488.25	4.2X10+5	0.3236	4.4631E+10	1.23	4.3530E+06	1.09E+08		3.20E+06	1.3603E+00	3.39E+01	4.0094E-02
				5.7147E+04				5.4160E+10		6.2660E+06	108570000				5.7705E-02
G	the-4b(48hr)II 600c 23nov94.neo	0.00372	0.10417	4.4145E+04	279.07	4.2X10+5	0.3246	1.6749E+10	6.446	1.5426E+07	3.43E+07		3.21E+06	4.8056E+00	1.07E+01	4.4998E-01
g	the-4b(48hr)II 150 23nov94.neo	0.00327	0.10663	1.2944E+04	49.82	4.2X10+5	0.3246	5.7120E+10	3.611	0.0000E+00	5.13E+07		3.21E+06	0.0000E+00	1.60E+01	0.0000E+00
				5.7090E+04				7.3868E+10		1.5426E+07	8.56E+07				1.8015E-01
h	(2)rf-93-12@600 18dec94.neo	0.00367	0.10404	1.0878E+05	4269.24	1.7X10+5	0.2915	6.2272E+10	2.4898	1.3690E+07	2.93E+07		9.30E+05	1.4720E+01	3.15E+01	4.6757E-01
H	(2)rf-93-12@600 18dec94.neo	0.00235	0.1004	1.6886E+04	105.34	1.7X10+5	0.2915	9.9058E+09	6.1416	0.0000E+00	0		9.30E+05	0.0000E+00	0.00E+00	0.0000E+00
				1.2376E+05				7.2178E+10		1.3690E+07	2.93E+07				4.6757E-01
I	rf 93_14@600 18dec94.neo	0.00388	0.10962	1.3914E+05	2018.77	1.7X10+5	0.2671	8.8560E+10	1.285	3.8970E+07	5.36E+08		3.70E+06	1.0532E+01	1.45E+02	7.2741E-02
i	rf 93_14@600 18dec94.neo	0.00345	0.0862	4.1140E+03	28.21	1.7X10+5	0.2671	1.8680E+08	1.28	0.0000E+00	0		3.70E+06	0.0000E+00	0.00E+00	0.0000E+00
				1.4328E+05				9.0747E+10		3.8970E+07	5.36E+08				

Results

As depicted in Figure 1, a three isotope plot illustrates air calibration measurements with sample gas analyzed at the 200 and 600°C heating increments. The star indicates the isotopic air inventory, black dots depicting air calibrations, and samples as boxes. An average of the air calibration measurements is marked as 1, which strongly deviates from the actual set of ratios. The difference between this average and air is a mass bias in which the spectrometer discriminates neon abundance. This measurement is subtracted from sample plots in order to remove this machine effect. It is possible that this effect is due to the multiplier over-analyzing the 21 peak or perhaps under-analyzing the 20 peak.

Samples do not cluster around the air-point which means spallogenic or otherwise produced neon is being analyzed. As taken from Neirdmann, et al (1993), we can associate neon production to either spallogenic or nucleogenic origin. Nucleogenic contribution will illustrate a trend towards the lower right section of the graph, depicted as N, whereas spallation reactions follow a slope of 1.2 from air (5). Once we have calculated an average of nucleogenic contribution of ^{21}Ne we can then correct ^{21}Ne abundance to strictly spallation related.

Figure 1
A three isotope plot of Rainbow Plateau samples. Note that small caps refer to lesser temperature step where the large caps signify high heating.

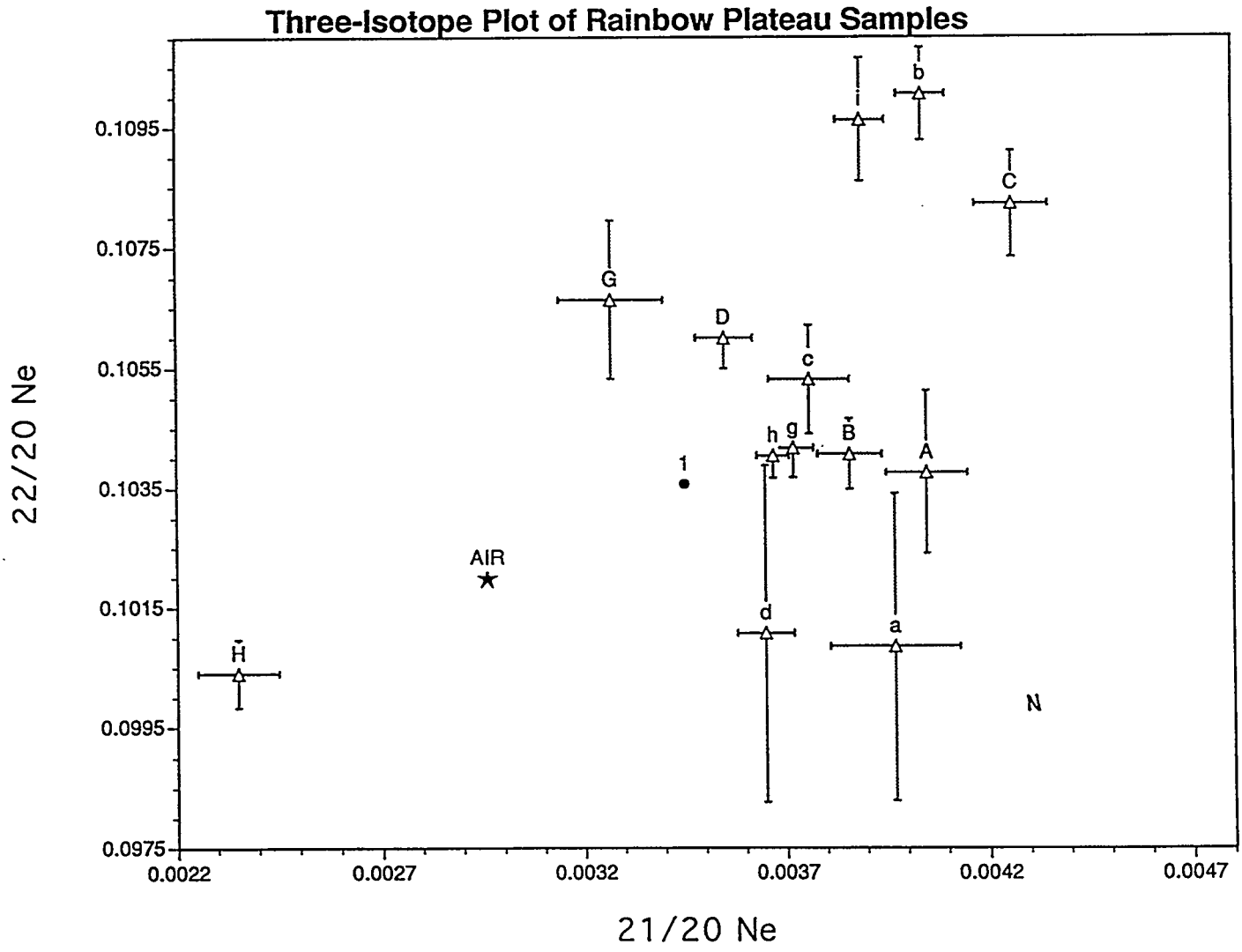

$^{44}CO_2$ Correction Factor

As seen in *appendix A*, slow scans of the neon region during a mass spectrometer blank. Because of interference peaks at the mass 22, which is equivalent to the mass 44 double charge. ^{20}Ne had 200 cts/s and from Podesek's isotopic compositional data for noble gases in air we know the 20:22 ratio to be 0.1020. This yields us with 20 cts/s for the 22-region but we see 110 cts/s. Assuming that the 90 extra counts are $^{44}CO_2^{++}$, we see a ratio of $^{44}CO^{2+}/^{22}CO_2^{+}$ = .00138. This is the correction factor that we use to precisely measure ^{22}Ne.

It is important to point out the same principal operating at the mass 20 region. The ^{20}Ne peak can be increased from a double charged argon ($^{40}Ar^{++}$) species. We choose not to make a correction for this isobaric interference based on that fact that our sample gas consistently measures for ^{20}Ne in the 200k range. This dwarfs the $^{40}Ar^{++}$ influence, which at best allots for 1% of the peak height. Although no correction is made for the $20^{+}/40^{++}$, careful attention is paid to argon levels during analyses.

Conclusion

When making noble gas mass spectrometric measurements, many corrections and chemical separations need to take place. Low machine blanks, mass interference corrections, and machine effect adjustments must be accurately done when one is counting atoms. We have shown that a spallogenic component does exist in terrace rocks of the Utah and Grand Canyon regions. We have also documented a nucleogenic source of ^{21}Ne propagating from alpha/neutron reactions from the decay of U/Th. Noble gas mass spectrometry holds many answers to geomorphic dating and correlation's regarding paleo-climate modeling and solar modulation cycles.

Works Cited:

(1) Finkel, Robert C., and Caffee, Marc W., Geochronology of Downcutting In The Colorado River System, AGU abstract submittal, 1994.

(2) Lal, D., Cosmic ray labeling of erosion surfaces: in situ nuclide production rates and erosion models, Earth and Planetary Science Letters, 104, pp 424-439, 1991.

(3) Lal, D., and Peters, S. Cosmic ray porduced radioactivity on the earth in: Handbuch der Physik, Vol. XLVI/2, Springer, Berlin, pp. 551-612, 1967.

(4)Nierdmann, S., et al. Cosmic-ray Produced ^{21}Ne in terrestrial quartz: the neon inventory of Sierra Nevada quartz separates, Earth and Planetary Science Letters, 125, pp341-355, 1994.

(5) Nierdmann, S., et al. Mass spectrometic identification of cosmic-ray produced neon in terrestrial rocks with multiple neon components, Earth and Planetary Science Letters, 118, pp65-73, 1993.

(6) Podesek, Isotope Geochemistry. 1990.

Appendix A

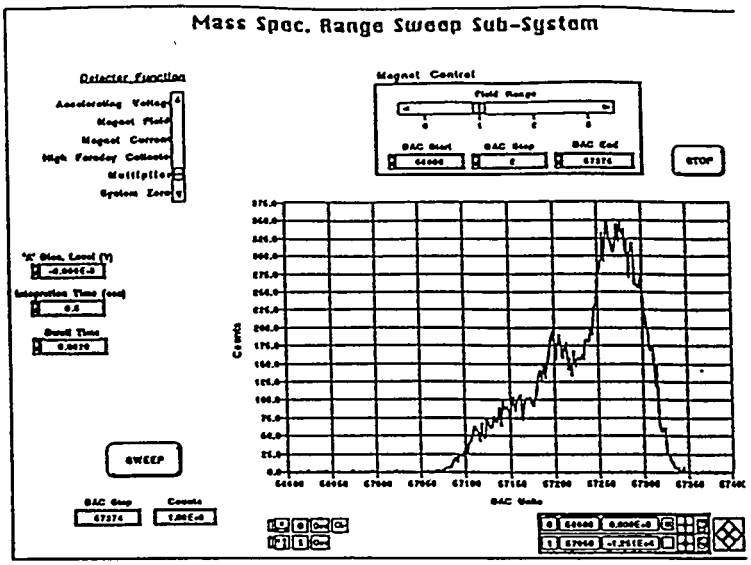

Figure 1-a Air calibration scan of ^{20}Ne peak at 0.1 second integration time. The middle spike is the result of when peaks overlap. ^{20}Ne is at a DAC centerpoint of 57160 and $^{40}Ar^{++}$ is located at a DAC setting of 57275.

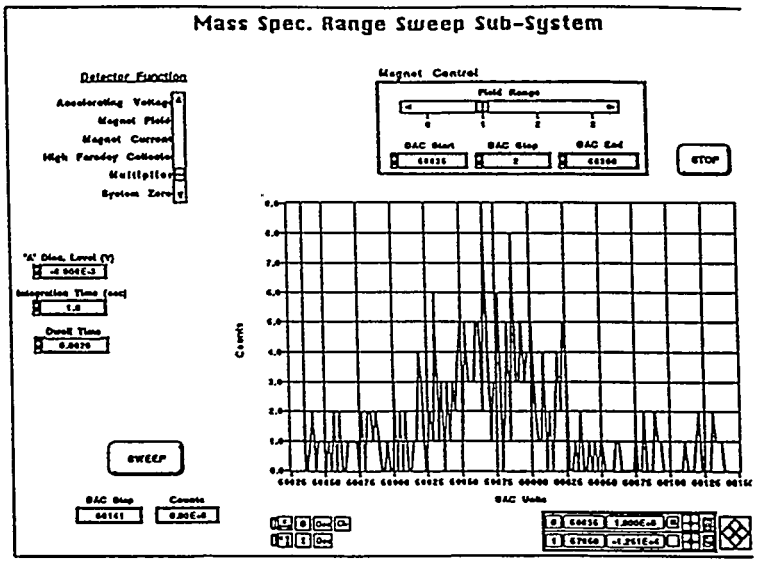

Figure 1-b ^{21}Ne scan showing low machine blank, which demonstrates a constant ratio of $^{21/20}Ne$ 0.00296.

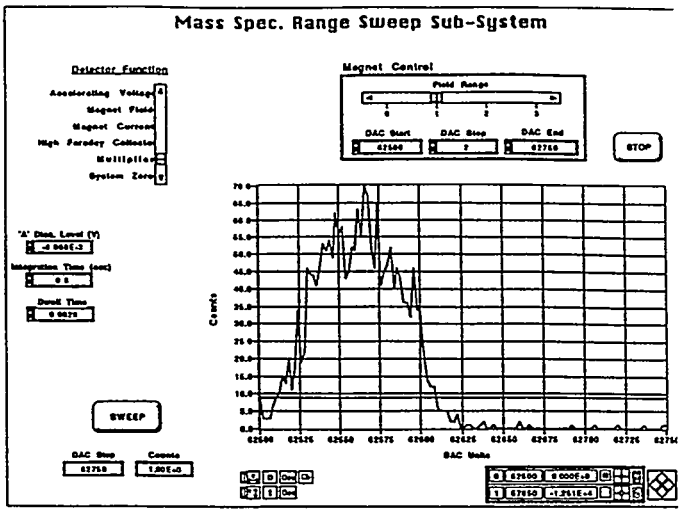

Figure 1-c ^{22}Ne peak with contribution from $^{44}CO_2$.

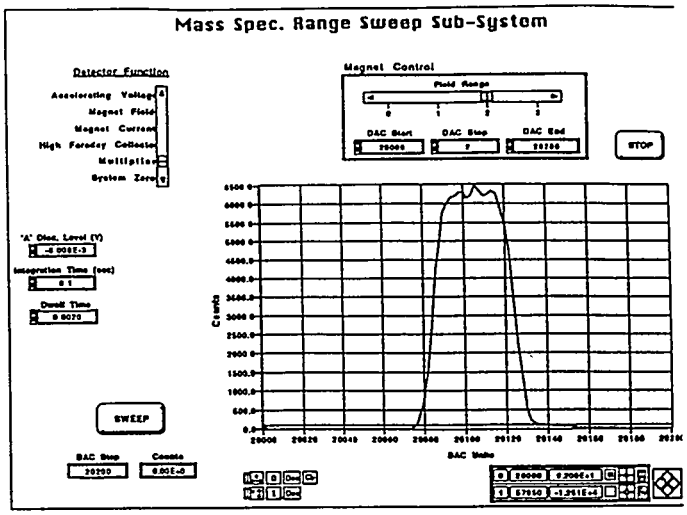

Figure 1-d $^{44}CO_2$ peak.

Computer-Aided Mapping of Stream Channels Beneath the Lawrence Livermore National Laboratory Super Fund Site

by

Mike Sick, Environmental Restoration Division, LLNL, P. O. Box 808, L-528, Livermore, California 94550, (510) 422-9202

ABSTRACT

The Lawrence Livermore National Laboratory (LLNL) site rests upon 300-400 feet of highly heterogeneous braided stream sediments which have been contaminated by a plume of Volatile Organic Compounds (VOCs). The stream channels are filled with highly permeable coarse grained materials that provide quick avenues for contaminant transport. The plume of VOCs has migrated off site in the TFA area, making it the area of greatest concern. I mapped the paleo-stream channels in the TFA area using SLICE an LLNL Auto-CADD routine. SLICE constructed 2D cross sections and sub-horizontal views of chemical, geophysical, and lithologic data sets. I interpreted these 2D views as a braided stream environment, delineating the edges of stream channels. The interpretations were extracted from Auto-CADD and placed into Earth Vision's 3D modeling and viewing routines. Several 3D correlations have been generated, but no model has yet been chosen as a best fit.

Introduction: The LLNL site, and TFA specifically, is underlain by 300-400 feet of highly heterogeneous alluvium that has been interpreted as a braided stream environment (See Figure 1). A braided stream is a broad sheet of water flowing over non-cohesive sediments that breaks up into a network of interconnected channels (See Figure 2). The sediments at the LLNL site show a great deal of spatial variation which make precise characterization of the subsurface difficult. However, to optimize the speed and efficiency of the site remediation, more precise characterization is required.

The SLICE program, developed by Bob McPherrin for the Environmental Restoration Division (ERD) at LLNL, creates an easy and efficient environment for geologic characterization. Using SLICE, a geologist can view well data in several forms A) Traditional vertical cross sections (See Figure 3: A-A') B) Sub-horizontal plan or map views and (See Figure 4: SLICE 6) C) Fence Diagrams, showing a 3D perspective (See Figure 5). The SLICE program is time efficient, allowing for more iterations than traditional mapping methods. SLICE also allows for easy communication between Auto-CADD and the Earth Vision modeling software.

Methods: Vertical cross sections and plan view SLICEs were made in the TFA area. The plan view Slices were defined with an attitude of N15E, 1 from a depth of 70 feet to 180 feet and were constructed at 5 foot intervals. Cross sections A-A' (See Figure 3) and B-B' (See Figure 6) were generated and their traces can be viewed on Figure 6. The stream channels were delineated using the lithologic data expressed on the plan view SLICEs (see Figure 4) and the geophysical and chemical data found on the vertical cross sections (see Figure 3). Once mapped, the stream channels were extracted as X, Y, Z data points with an associated property value that was based upon my SLICE interpretations. The data points were funneled into the Earth Vision software for visualization and further modeling. The models presented below only contain data from 80 to 95 feet.

Observations: I found that the 3D visualization generated in EV honored the conceptual braided stream model. Figure 7, entitled "evpdatnewpnts.2.3grd" represents a reasonable fit to the data given to EV and is compatible with the braided stream model. The red isocontour represents the interpreted center of the stream channels and the yellow represents their edges. The red volumes are the most likely places to find the highly permeable sediments of interest to LLNL environmental geologists.

Figure 8, entitled "3rdtrynewcat.3grd", displays only the "missing" information from Figure 8, thus showing those areas that do not represent the highly permeable stream channel environment. These volumes are the least likely places to find highly permeable sediments. Future wells can be screened to avoid these intervals.

Conclusions and Future Work: The 3D models presented above represent reasonable fits to data that I fed to EV. If the geologic interpretations that I made using the SLICE program are sound, then accuracy becomes an issue of model refinement.

Refinement will be pursued at both ends of the modeling process. On the input end, addition SLICES will be created, interpreted, and fed into EV. On the output end, modeling parameters can be varied to construct 3D models which more closely honor the data given to EV. A well refined model will provide an accurate and easy to use tool for well sighting.

Figure 1: Geologic Map of LLNL site with highlighted TFA study area

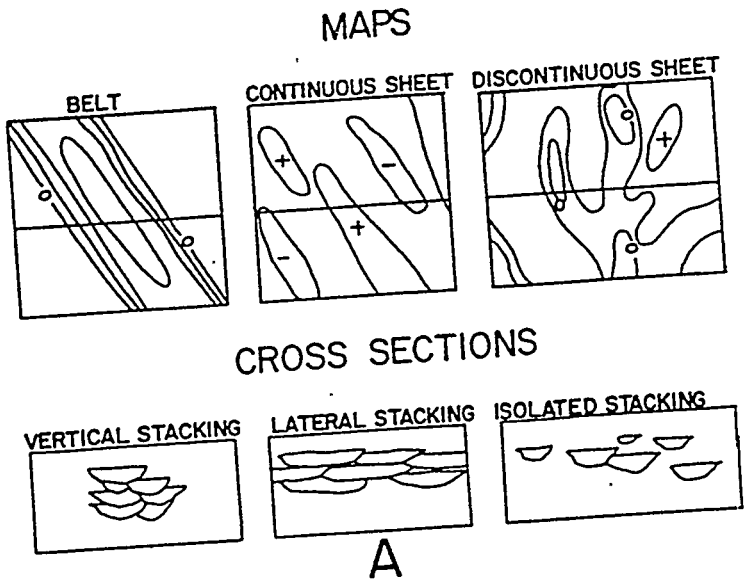

Generalized geologic map of the southeast Livermore Valley

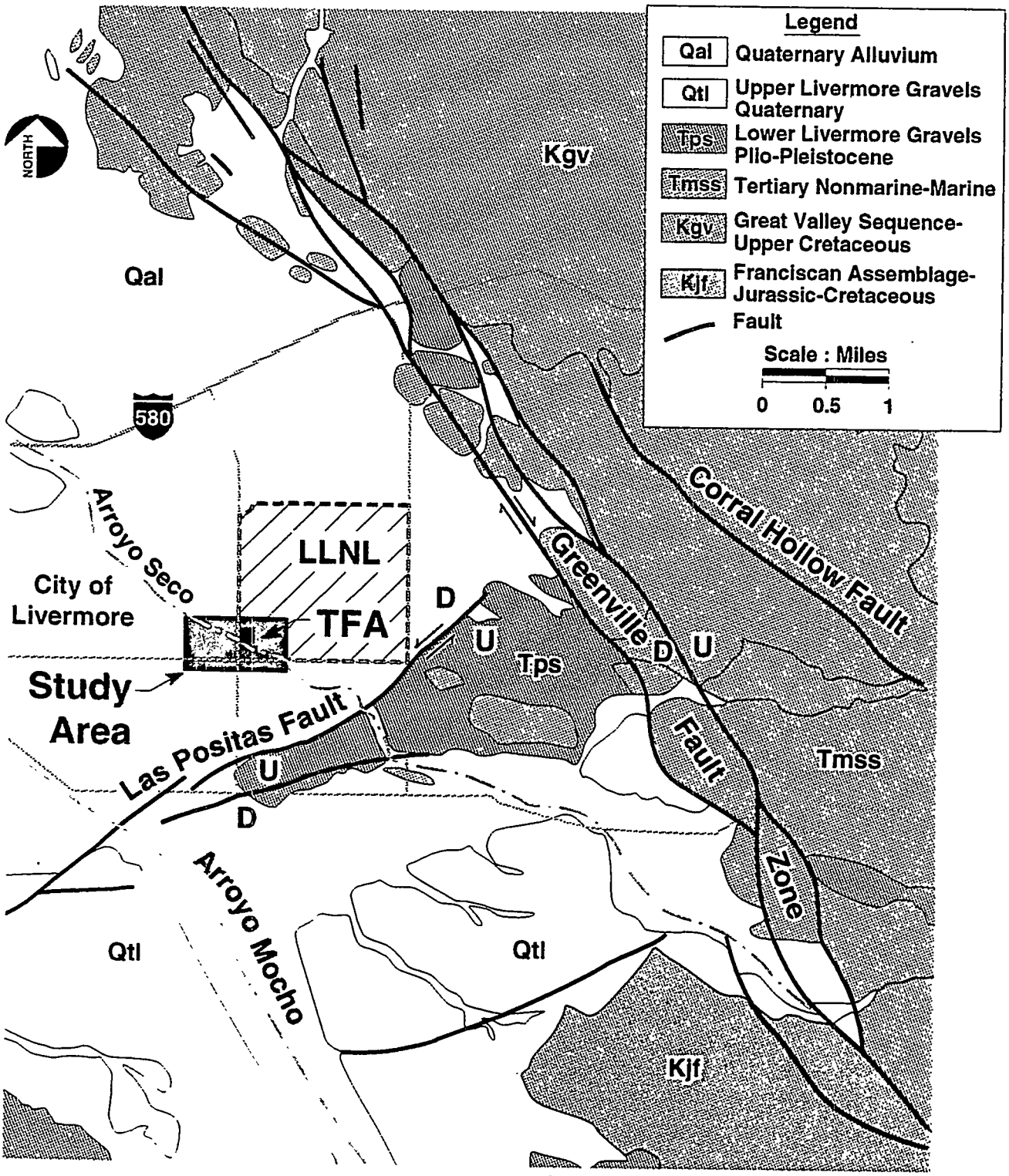

Figure 2: Generalized cross section and map view of a braided stream

8/17/94

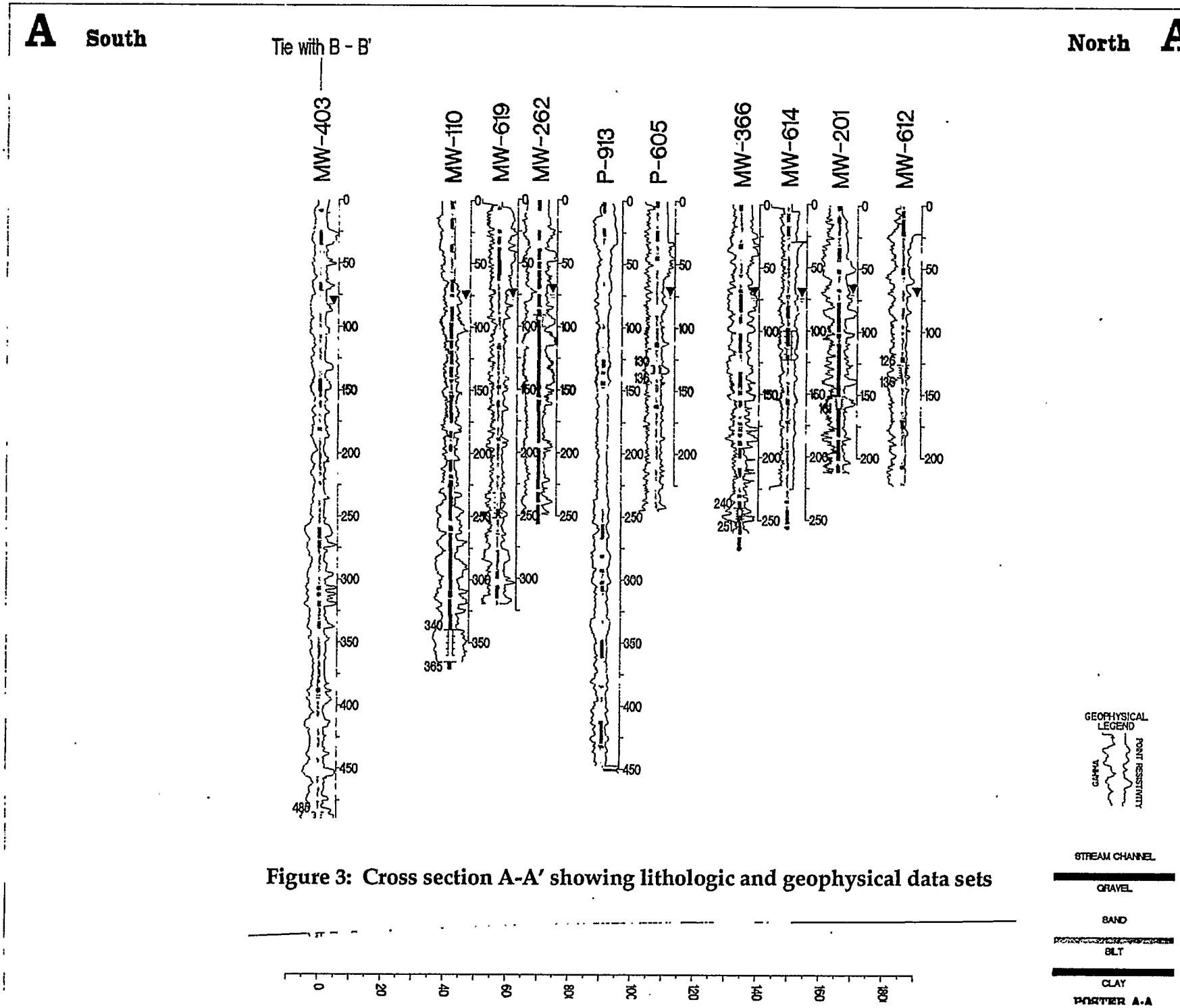

Figure 3: Cross section A-A′ showing lithologic and geophysical data sets

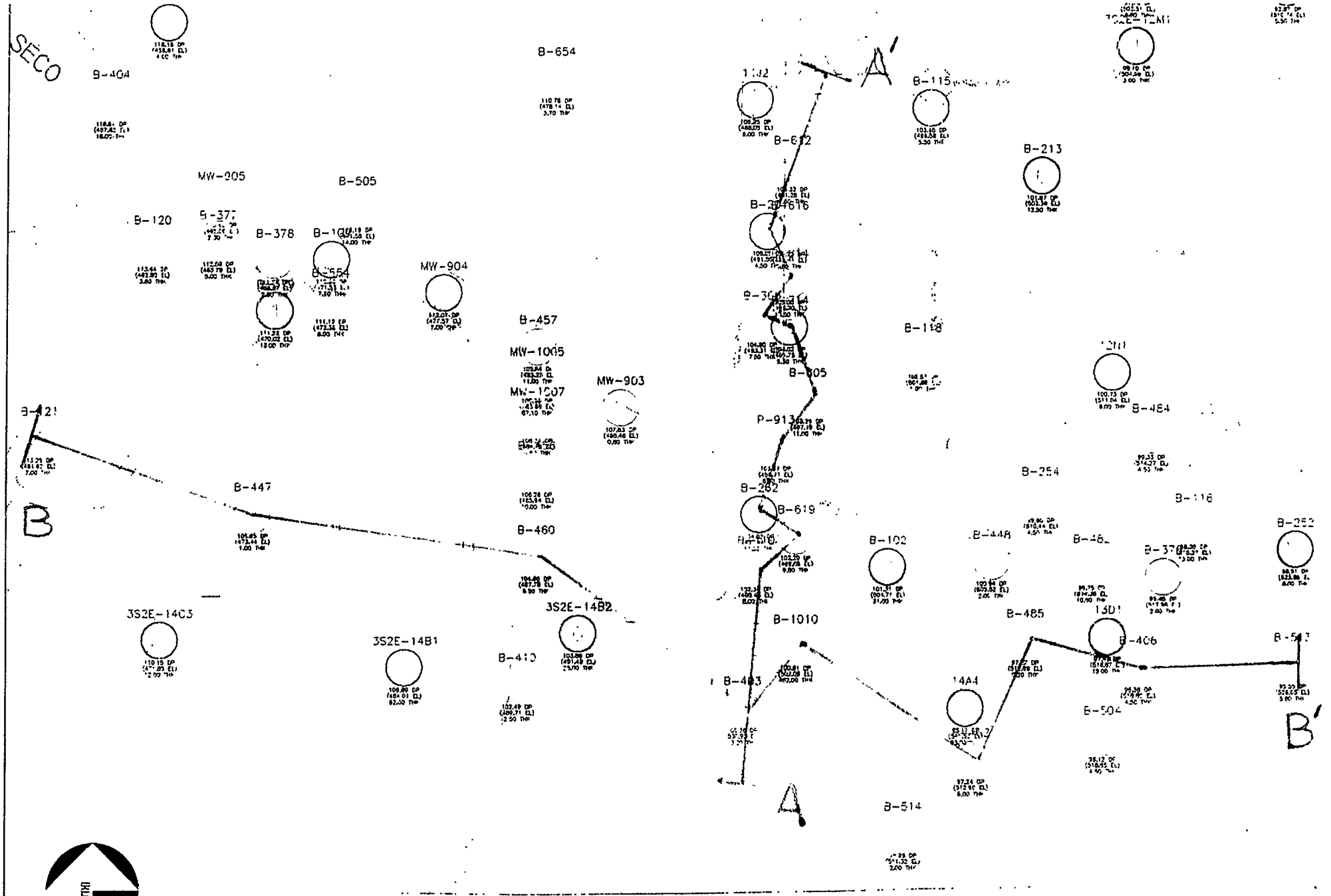

Figure 4: Map view SLICE with interpreted stream beds shown in grey and and cross sections A-A′ and B-B′ shown in green

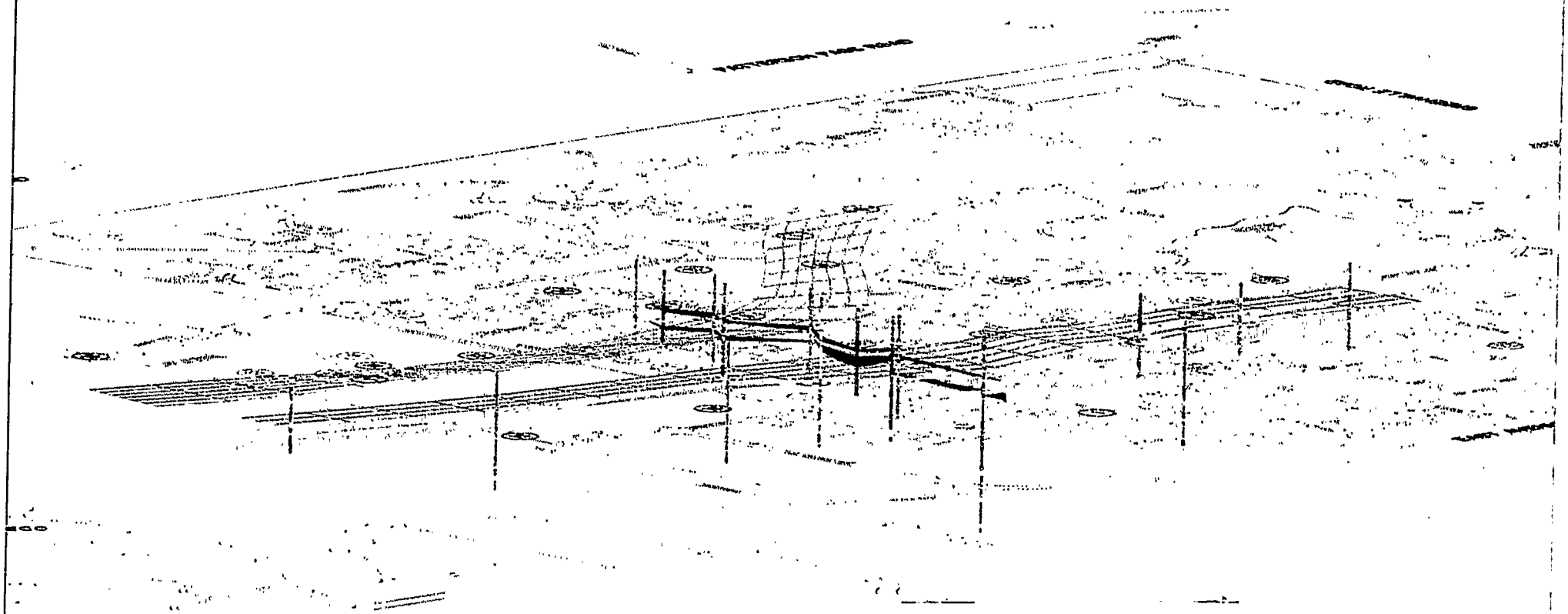

Figure 5: Fence diagram showing combination of cross-section and SLICE interpretations

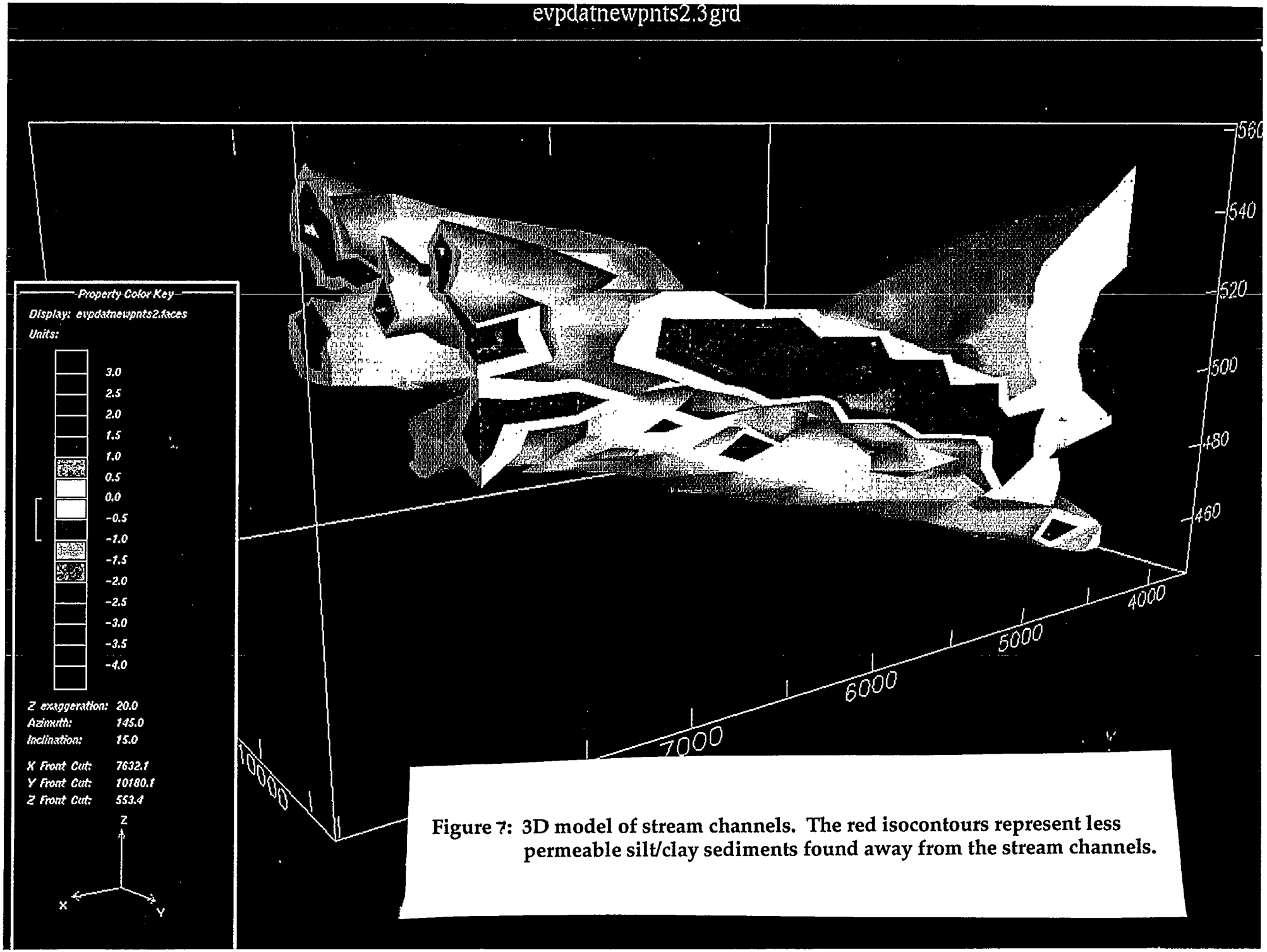

Figure 7: 3D model of stream channels. The red isocontours represent less permeable silt/clay sediments found away from the stream channels.

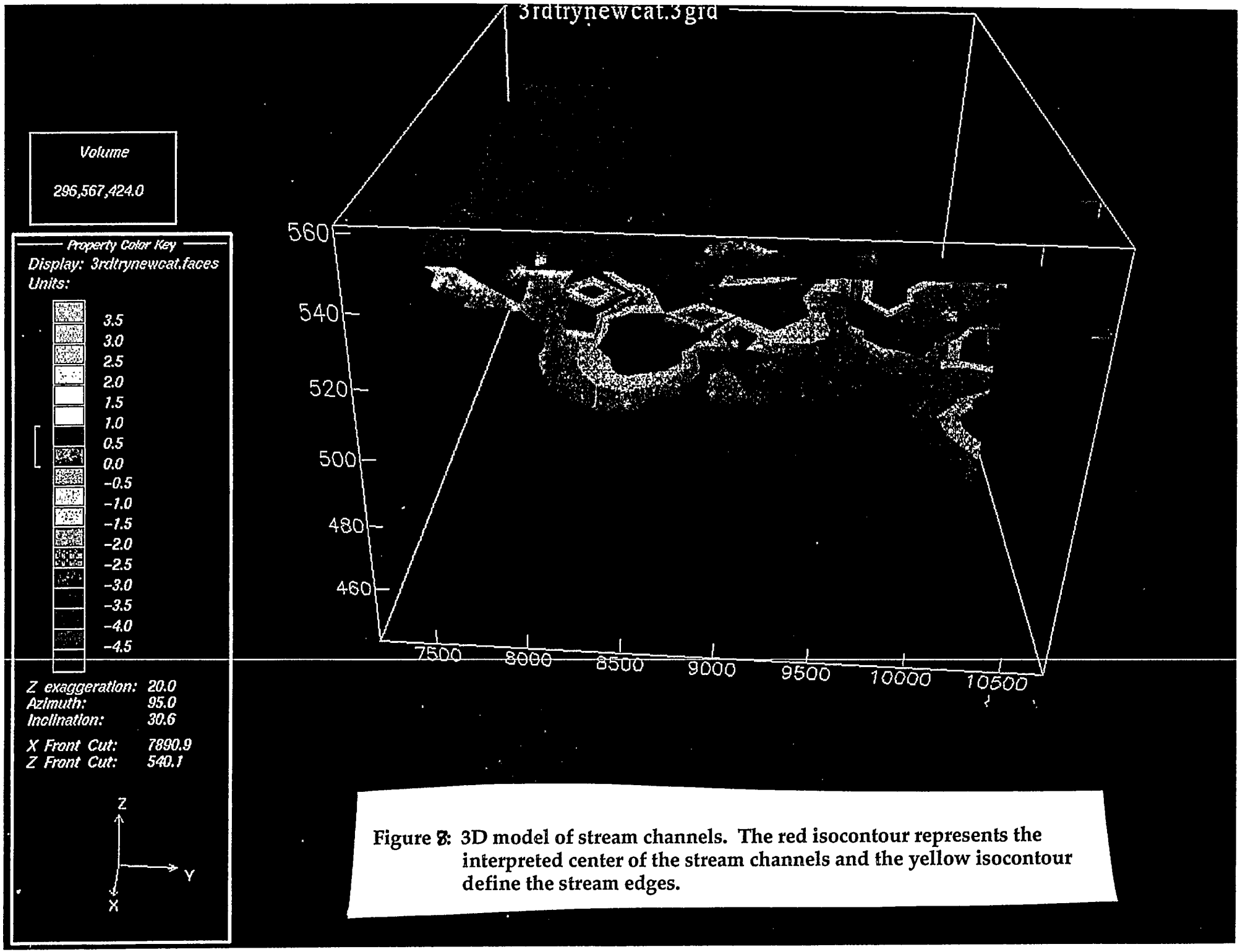

Figure 8: 3D model of stream channels. The red isocontour represents the interpreted center of the stream channels and the yellow isocontour define the stream edges.

X-ray Spectroscopic Technique for Energetic Electron Transport Studies in Short-Pulse Laser/Plasma Interactions

Teresa E. Tutt

Rensselaer Polytechnic Institute

Lawrence Livermore National Laboratory
Livermore, California 94550

December 14, 1994

X-ray Spectroscopic Technique for Energetic Electron Transport Studies in Short-Pulse Laser/Plasma Interactions

Abstract

When a solid target is irradiated by a laser beam, the material is locally heated to a high temperature and a plasma forms. The interaction of the laser with plasma can produce energetic electrons. By observing the behavior of these "hot" electrons, we hope to obtain a better understanding of Laser/Plasma Interactions. In this work we employ a layered-fluorescer technique to study the transport, and therefore the energetics, of the electrons. The plasma forms on a thin foil of metallic Pd which is bonded to thin layer of metallic Sn. Electrons formed from the plasma penetrate first the Pd and then the Sn. In both layers the energetic electrons promote inner (K) shell ionization of the metallic atoms which leads to the emission of characteristic K_α x-rays of the fluorescers. By recording the x-ray spectrum emitted by the two foils, we can estimate the energy-dependent range of the electrons and their numbers.

Teresa E. Tutt

Rensselaer Polytechnic Institute

Lawrence Livermore National Laboratory
Livermore, California 94550

December 14, 1994

I. INTRODUCTION

Short-Pulse Lasers and Inertial Confinement Fusion

To achieve ignition in an Inertially-confined fusion target, the driver energy (we will consider laser drivers here) must be effectively transported, or coupled, into the fuel during all stages of confinement and compression. As the fuel is compressed by the laser driver, it decreases in volume while it increases in density. Before reaching fusion densities, however, a coronal plasma surrounding the fuel is formed. This plasma is critical in coupling driver energy into the fuel because both the underdense region and the region in the vicinity of the critical density layer n_c:

$$n_c = \pi m_e c^2 / e^2 \lambda^2$$

(where energy from a laser driver of wavelength λ is classically reflected) absorb and transport energy. The plasma easily absorbs the driver energy at densities less than n_c. At the critical density n_c, the plasma becomes reflective, allowing no further coupling of the driver energy[1].

The problem is: how do we efficiently couple energy into the high-density fuel where the density of the coronal plasma exceeds the critical density of the driver laser.

Energetic electrons can be used to couple driver energy into the plasma where laser light is deflected. This is the scope of current *Fast-Ignitor*[2] experiments, so called because they employ an extremely short "fast" burst of laser energy, typically in the sub-picosecond (10^{-12}-10^{-15}s) range. Short pulse lasers can produce extremely high intensities on target. Given equal energies, the shorter pulse delivers a much greater intensity. As the pulse is compressed, its intensity increases proportional to 1/ t.

At sufficient intensity, plasma electron energies become relativistic. Langmuir waves (electron plasma waves) are produced, along with K_α x-rays[2]. These "hot" electrons can easily penetrate solids to produce characteristic K_α x-

ray emissions in layered targets. By studying the emitted K_α x-ray spectra, we hope to better understand energetic electron behavior and develop optimal methods of energy transport.

This report deals primarily with the measurement of x-ray spectra by means of charge-coupled device (CCD') cameras.

Experimental setup

Our solid target experiments employ a ten-terawatt, chirped-pulse amplification laser system. A Titanium-Sapphire master oscillator generates a 420mW 130 femtosecond (fsec) pulse. It is then stretched in time ("chirped") through a series of gratings and is then amplified several times. The pulse also passes through a series of spatial filters which further aids in preserving the modal structure of the laser pulse[3]. Finally, the pulse is compressed by a series of gratings, in vacuum, to produce a 630 fsec 5 J pulse in the infrared, which is focused on the target. This produces the 10^{15}-10^{18} w/cm^2 intensities needed for our experiments[4].

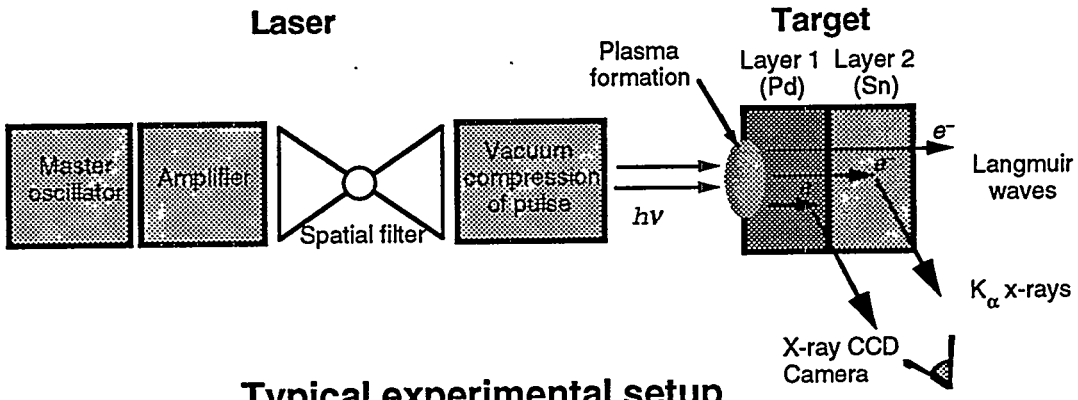

Typical experimental setup

Figure 1

We use targets made of several different materials, both single and layered films . A target of particular interest is shown in figure 1. It consists of a thin foil of metallic palladium (Pd) bonded to a thin foil of metallic tin (Sn). Since the two metals have different K_α energies (21 keV for Pd, and 25 keV for Sn), it

is easy to determine the penetrating power of the energetic electrons by the relative amounts of K_α emissions produced by the foils, since the electrons must first pass through the Pd to fluoresce the Sn.

II. DIAGNOSTIC TECHNIQUE

To observe these K_α emissions, we use a Princeton Instruments x-ray CCD camera equipped with a Reticon 1024 x 1024 pixel chip. This records individual photon strikes (events). In the simplest case the brightness of an event (i.e. the energy deposited in the pixel by the photon) is equal to the energy of the photon that produced the strike. The analog value of the intensity is converted to digital data and is recorded in the imaging software as an arbitrary integer value, in Analog-to-Digital conversion Units (ADU's). This is converted to the energy value by the following relationship:

$$\left(3.6\ \frac{\text{eV}}{\text{hole pair}}\right)\left(2.3\ \frac{\text{hole pair}}{\text{ADU}}\right)$$

Or about 8.28 eV per ADU for the camera used in this work.

We obtain a distribution of the photon energies by constructing a *histogram* plot. First, we calculate the range of the data from minimum to maximum. Then, we divide the range into a number of equal incremental values (bins). Finally we count the number of events with energies within the range of each bin value. By plotting the energy distribution (X-axis) and number of the energetic electrons (Y-axis) it is possible to obtain a spectrum of the emitted x-rays[5] (Figure 2).

CCD image

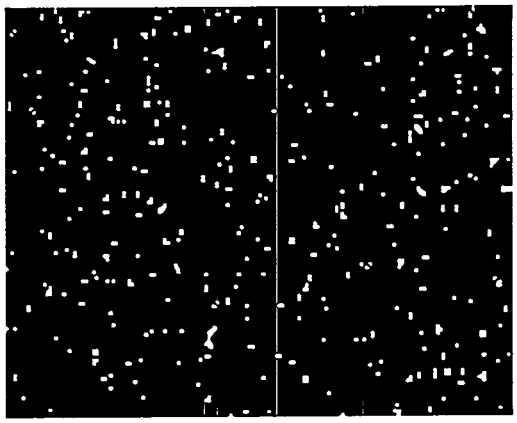

(single photon events)

Histogram plot

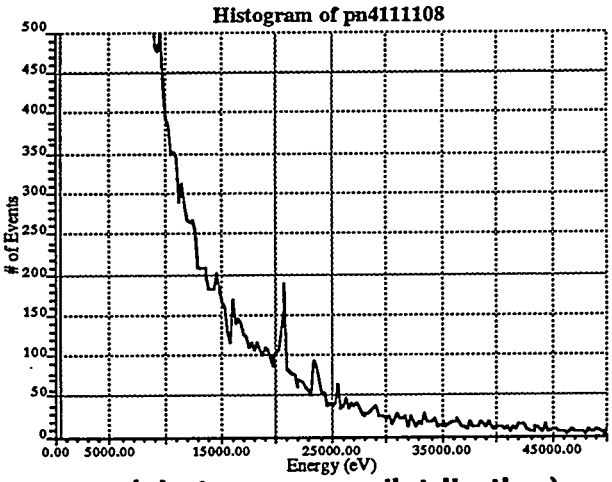

(photon energy distribution)

Figure 2

Detector Calibration

A radioactive isotope of cadmium (Cd 109) was used to establish the 8.28 eV per ADU conversion factor. Cd 109 naturally decays to silver (Ag) and in the process emits x-ray photons identical to Ag K_α (22keV) and Ag K_β (25 keV). An exposure of 180 seconds was taken (Figure 3a). A blank image taken by the CCD with no input at -40° C (Figure 3b).revealed a thermal background intensity peak of approximately 340 ADU with a half-maximum width of about 40 ADU. This introduces an error of ±10 x 8.28 or ~83eV to the final energy value. By subtracting the thermal background and multiplying the result by the conversion factor, we obtain peak values very close to characteristic[6] (Figure 3c).

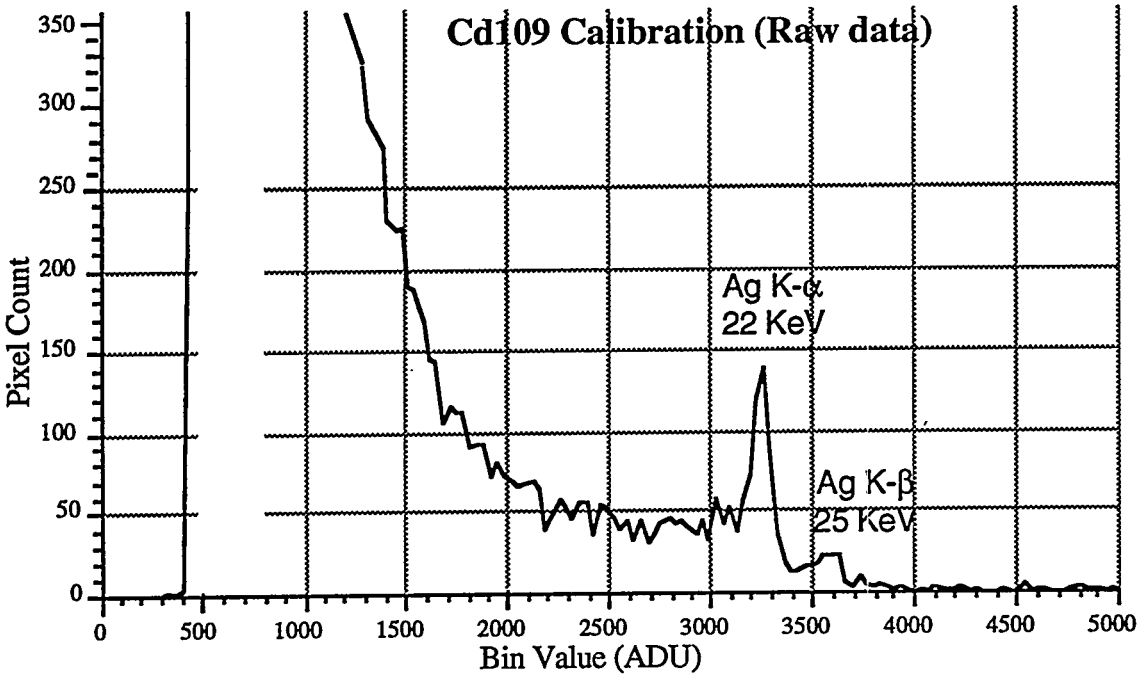

Figure 3a

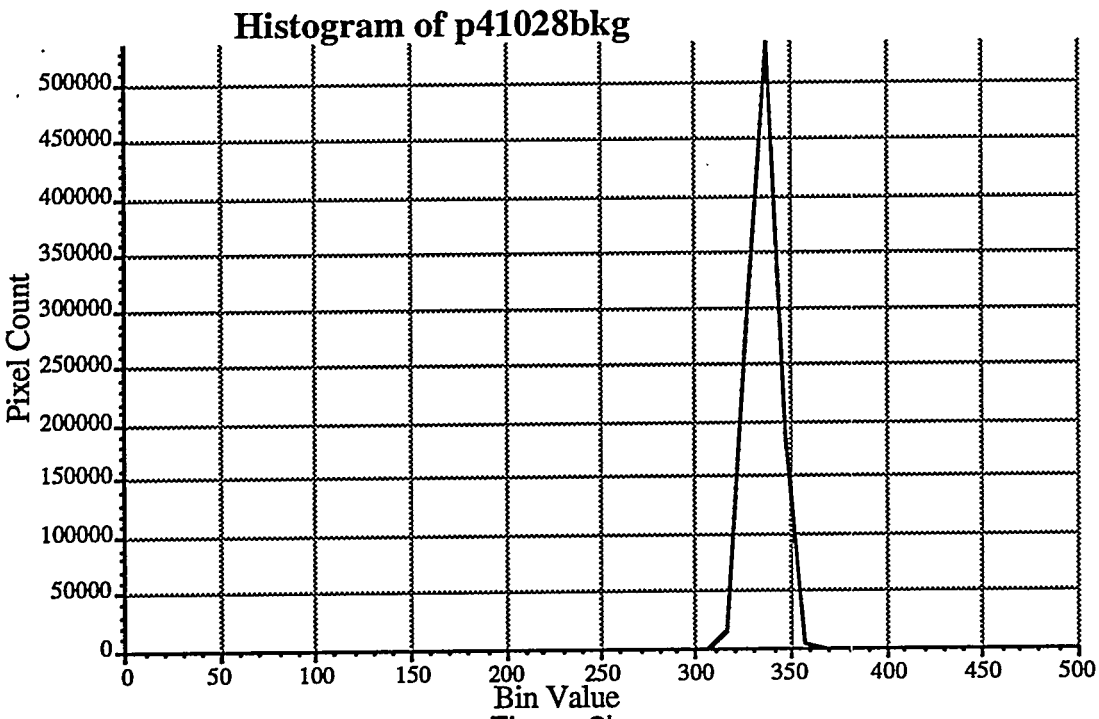

Figure 3b

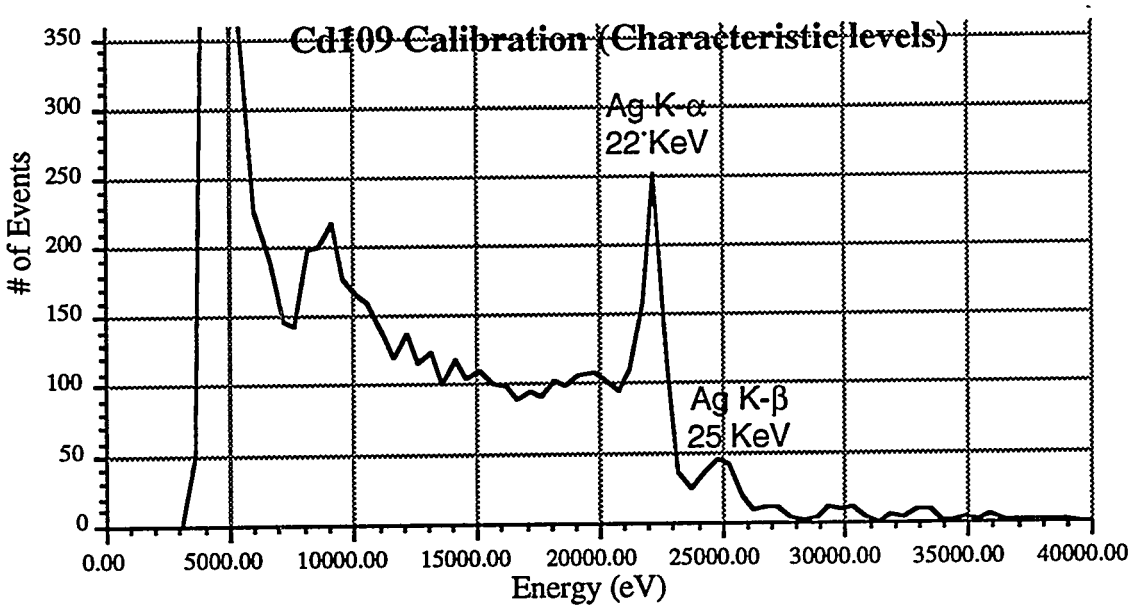

Figure 3c

To obtain an accurate x-ray spectrum, it is first necessary to accurately record the energy of the photon strike. Ideally each photon should strike a pixel directly, imparting its full energy to it. This is not always the case, however. Many photons pass completely through the CCD chip without interaction (resulting in no event) or are deposited deep in the CCD substrate, causing the energy to be distributed among neighboring pixels. Thus, a single event may be spread over a segment of several pixels (Figure 4a). Since the individual pixels by themselves do not contain the full energy of the event, this can give the appearance of several events of lower energy. This can cause a blurring of the energy peaks in the lower-energy direction (a "tail" attached to the peak on the "red" side), or, if the energy is scattered evenly enough across a segment, produce false peaks altogether (Figure 4b).

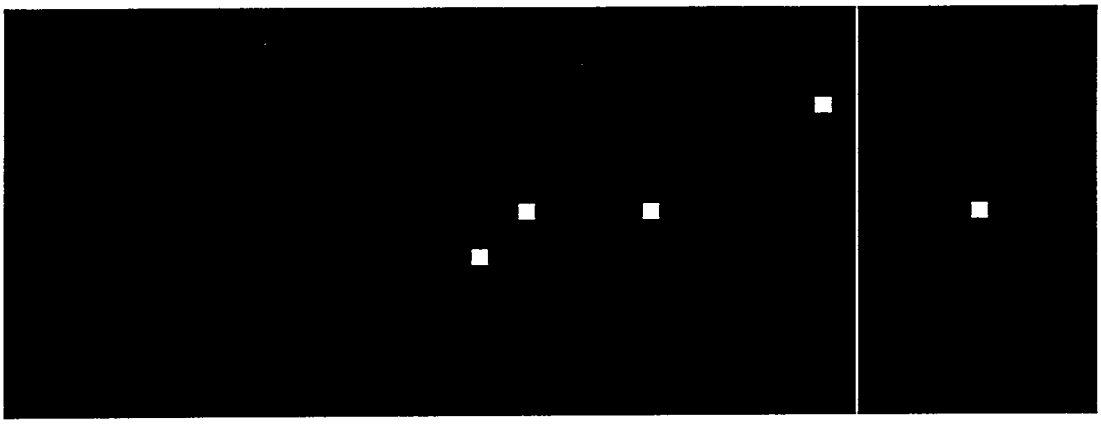

Figure 4a

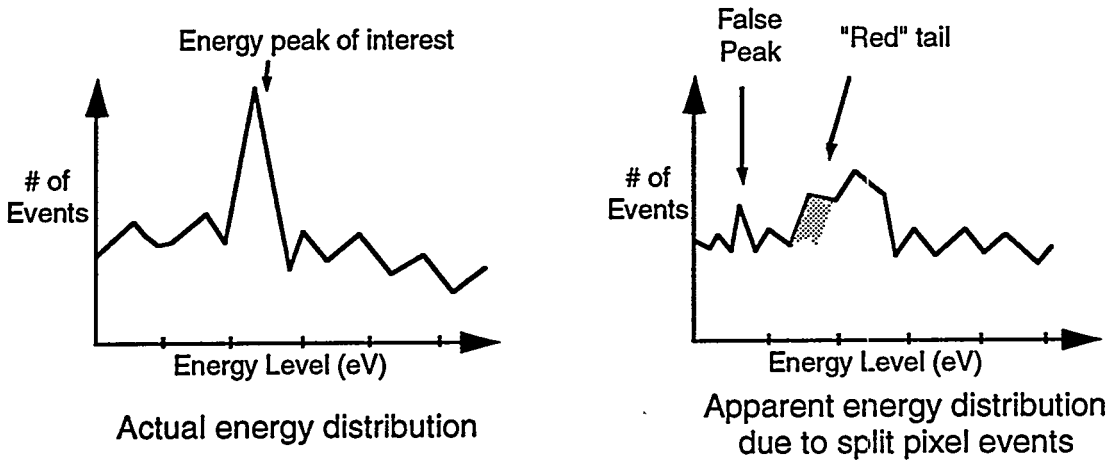

Actual energy distribution

Apparent energy distribution due to split pixel events

Figure 4b

The use of a CCD with a special "back thinned" chip can greatly reduce this problem. However such a chip is very fragile and is, in many cases, cost-prohibitive. When we are limited to conventional instruments, we need an alternate method to recover lost or distorted data.

It is therefore necessary in this case to sum the energies deposited in each group of pixels comprising an event before plotting a histogram We accomplish this by means of a method known as *smart binning.* An algorithm in the imaging software allows measurements to be made of segments as opposed to individual pixels.

"Smart" Binning

First we need to determine the most probable area (in pixels) of an event and to establish an upper limit of size. From analysis of a distribution of segment areas we find that less than 2.5 % of the segments have an area greater than five.

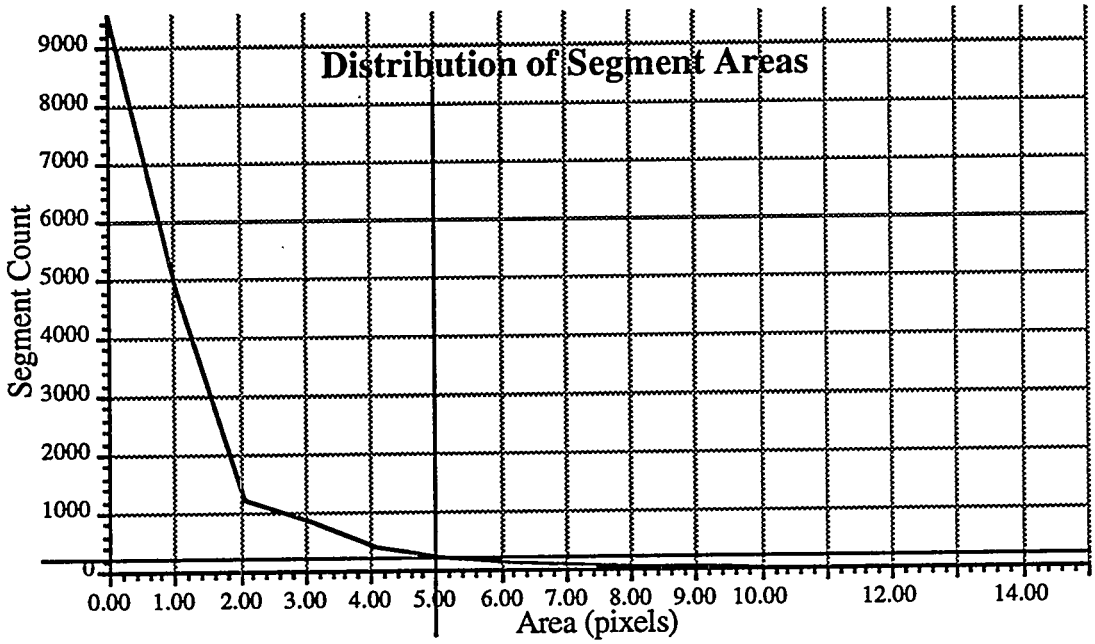

Figure 5

Next, we need to filter out segments caused by multiple hits. This can be done with simple geometric constructions if we assume that the energy dispersion is fairly circular or elliptical, depending upon the angle of incidence. Figure 6 illustrates the difference between segments of equal area caused by single & multiple events.

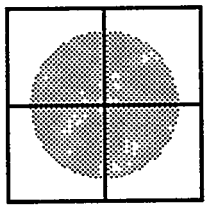

segment produced by single event

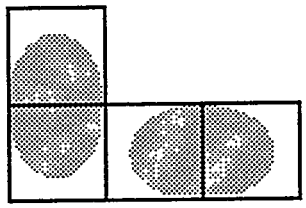

segment produced by two events

Figure 6

While the two segments are of equal area, they are not of equal perimeter. If we count the exposed sides of the squares for each segment we find that the single event segment on the left has a perimeter of eight, while the one on the right has a perimeter of ten. Table A shows the optimum perimeter constraints when measuring segments of areas between one and five.

Area	Perimeter
1	4
2	6
3	8
4	8
5	12

Table A

Further, we can filter out certain multiple-event segments by defining an upper limit to the major axis of the segment in question. The major axis is the longest chord passing through the center of an imaginary ellipse superimposed on the segment (Figure 7). By construction we find the maximum allowable major axis value for a single-event segment to be 2.7.

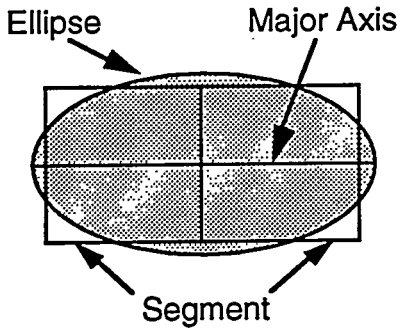

Figure 7

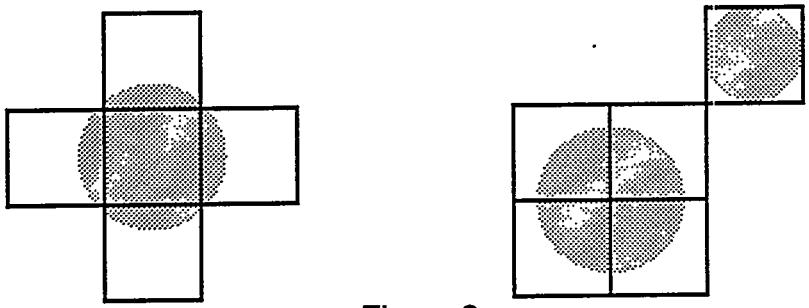

Figure 8

A special problem arises with segments of areas of five pixels or greater. Figure 8 shows two segments of five pixels each. We also see that each segment has a perimeter of twelve. For this case we need to further differentiate the segments by comparing the second-order intensity moments as calculated by the following formulas:

$$M_x = [\sum (x-a_x)^2 I_{xy}] / \text{area}$$
$$M_y = [\sum (y-a_y)^2 I_{xy}] / \text{area}$$
$$M_{xy} = [\sum (x-a_x)(y-a_y) I_{xy}] / \text{area}$$

where:

$$a_x = [\sum x I_{xy}] / \text{area}$$
$$a_y = [\sum y I_{xy}] / \text{area}$$

and I_{xy} is the pixel intensity value at the location (x, y). A plot of the distribution of intensity moments taken from the calibration shot shows a population reaching a minimum with a relative maximum following shortly thereafter. Figure 9 shows how we can use this minimum to approximate a dividing line between single and multiple hits. From figure 10, we see these values to be approximately 0.31 for M_x and M_y, and 0.80 for M_{xy}

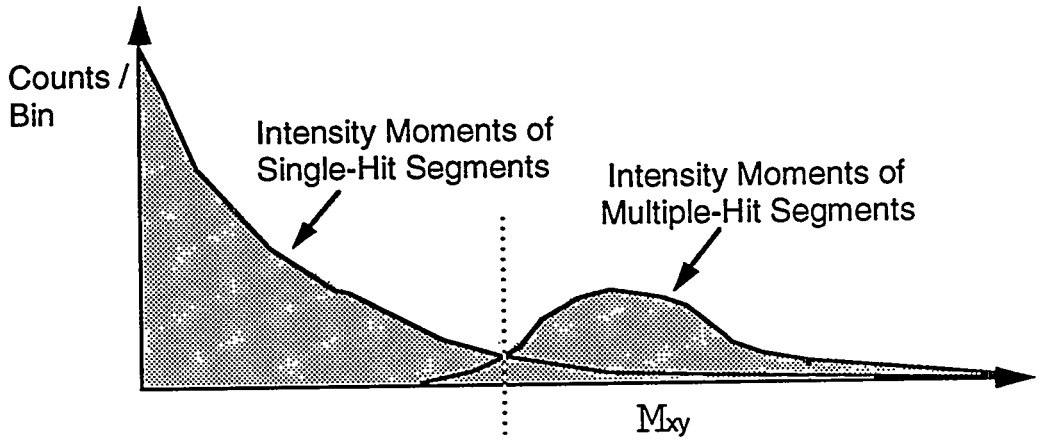

Figure 9

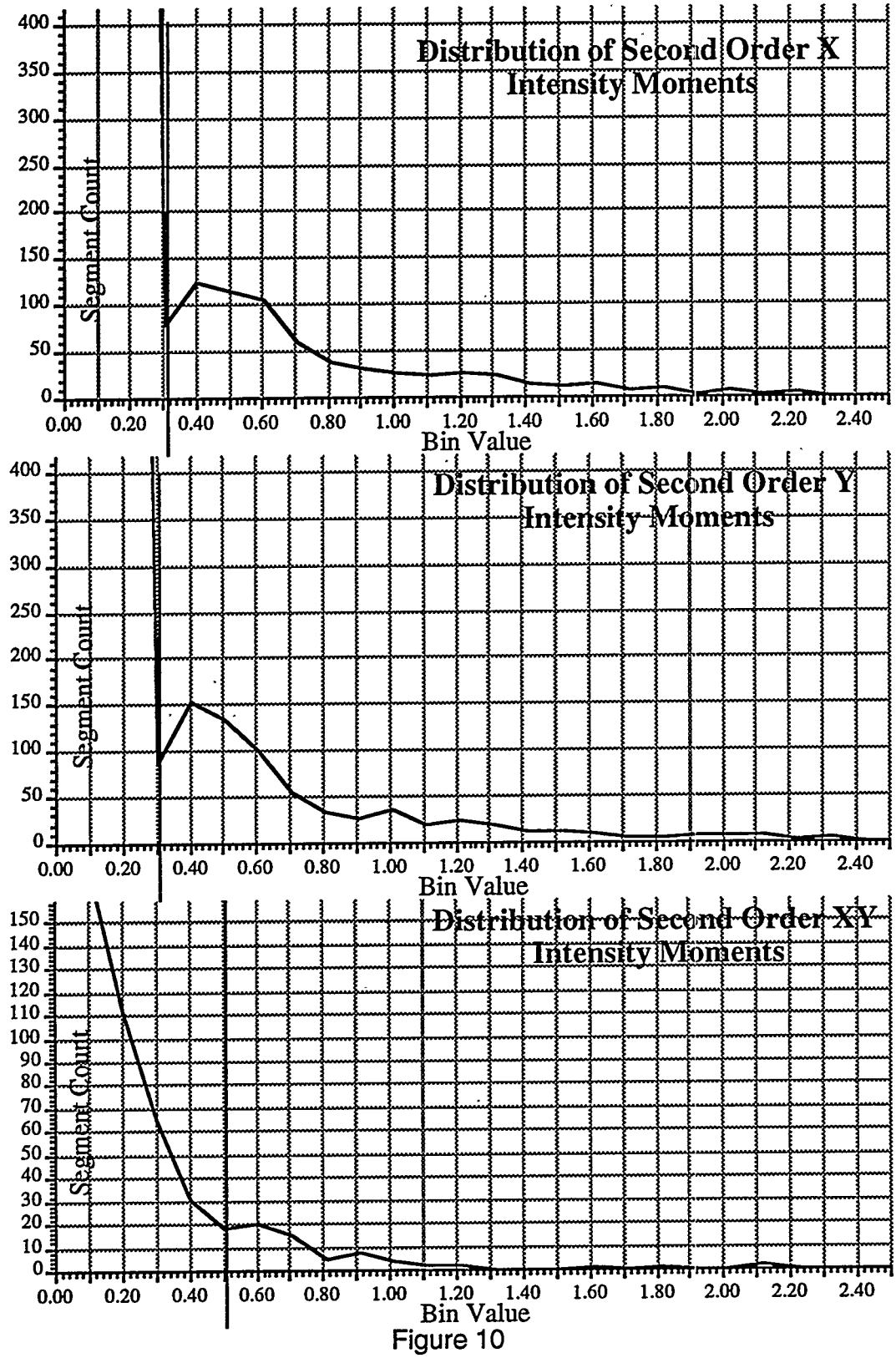
Distribution of Second Order X Intensity Moments
Segment Count
Bin Value
Distribution of Second Order Y Intensity Moments
Segment Count
Bin Value
Distribution of Second Order XY Intensity Moments
Segment Count
Bin Value

Figure 10

The Smart-bin routine was written using IPLab v.2.5 software. A scripting routine similar to a macro was employed to perform all the functions listed above. First, two point functions are performed on all the pixels in the region of interest. The first converts intensity to eV by the formula:

$$E = [\text{(pixel intensity)} - \text{(thermal background)}] * \text{(CCD gain)}$$
$$= (I_{xy} - 340)\,\text{ADU} * 8.28\ \text{eV/ADU}$$

The second point function filters out all values outside of the range:

$$0 < I_{xy} < 10^8$$

Next, the segments are grouped and their energy is measured according to the previously defined constraints:

Parameter	Minimum	Maximum
Area	1	5
Perimeter	4	12
Major Axis	0	2.7
2nd int. mom.-x	0	0.31
2nd int. mom.-y	0	0.31
2nd int. mom.-xy	0	0.80

Table B

of area, perimeter, major axis and second order intensity moments. Finally, a histogram is plotted of the resulting segments by their energy value.

CCD Camera Arrangement

Frequently in our experiments we will employ two x-ray CCD cameras (Figure 11). Sometimes it is of interest to compare the K_α electron emission on the incident surface ("front" side) with that of the subsequent layers ("back" side). This allows us to make a comparison of the amount of energetic electrons produced vs. how many are penetrating through the target layers.

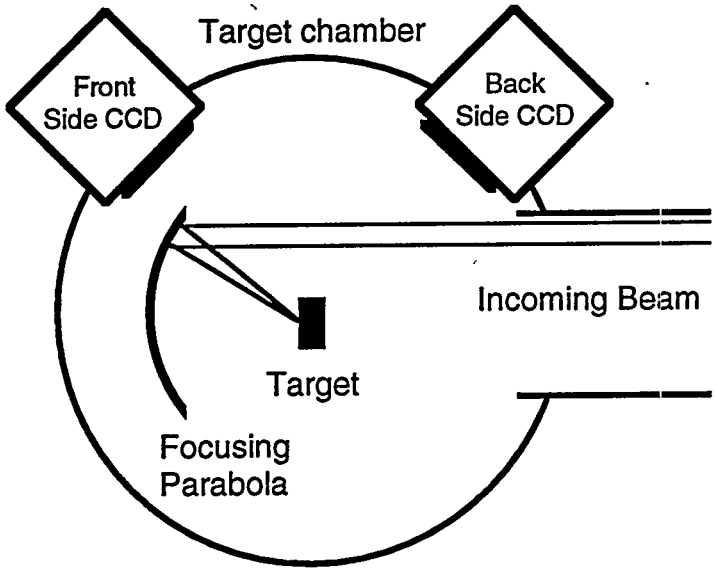

"Front" vs. "Back" side CCD

Figure 11

III. EXPERIMENTAL RESULTS

Signal-to-Noise Ratio

Figure 12 shows a recent calibration shot measured with and without smart binning. The first plot (no binning) shows a signal -to -noise ratio of about 3:1. There is also an extensive thermal background peak (off-scale between zero an 2.5 keV. The second plot (with smart binning) shows a vastly improved signal-to-noise ratio (> 7:1, an improvement of more than a factor of two). There is also a nearly complete filtering out of the thermal background altogether.

Use of Back-Thinned CCD

Recent calibration shots with "back thinned" CCD cameras have also shown smart-binning to be effective.

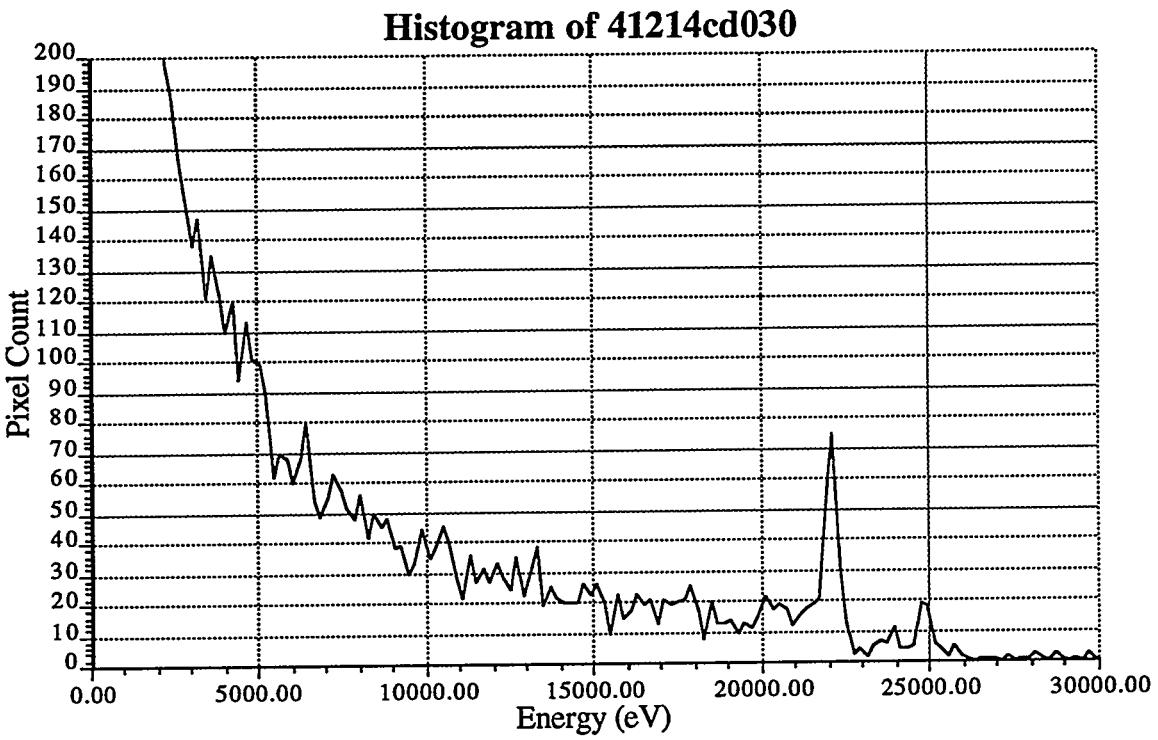
Histogram of 41214cd030
Pixel Count
Energy (eV)
0.00
5000.00
10000.00
15000.00
20000.00
25000.00
30000.00

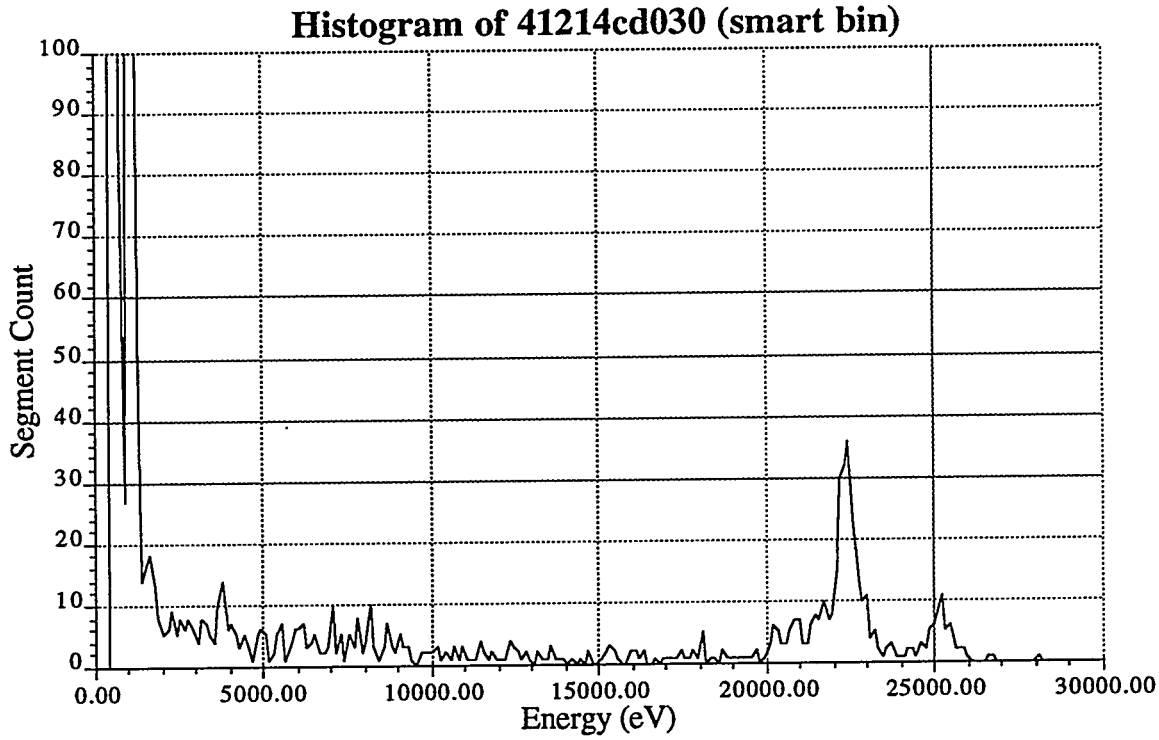
Histogram of 41214cd030 (smart bin)
Segment Count
Energy (eV)
0.00
5000.00
10000.00
15000.00
20000.00
25000.00
30000.00

Figure 12

Linearity of Detector Response

During calibration, six exposures were taken of the source in increasing intervals of 30s each. The minimum exposure was 30s and the maximum was 180s. This was done to test the linearity of the detector response to increasing amounts of radiation (measured in counts per bin value). A non-linear response of the detector could have detrimental effects on measurements of shots taken with varying amounts of energy on target. These shots are often necessary to study the response of materials to increasing laser intensities.

After histograms were taken of the images, the energy of each peak above the background was measured. This was done by subtracting the thermal background continuum and taking the integral of the remaining function within the base of the peak. This was accomplished using PDS SHRINK 83t Macintosh II code (figure 13).

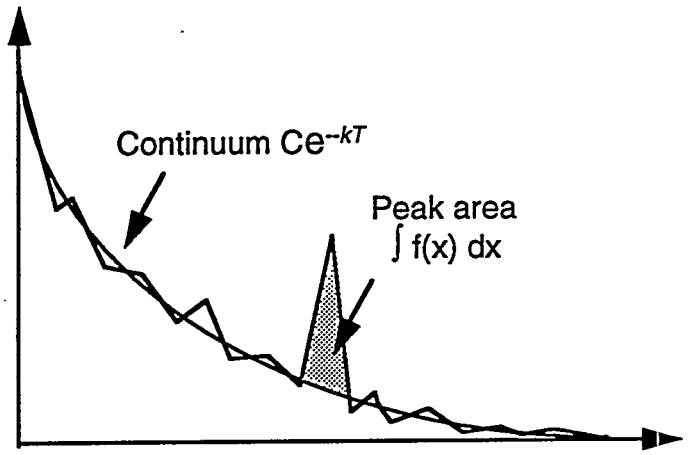

Figure 13

The peak areas were then plotted vs. the exposure time of the detector. Figure 14 shows plots made with and without smart binning. The raw pixel data shows a linear response up to about 90s. With smart binning the linear range is extended to approximately 180s - nearly double.

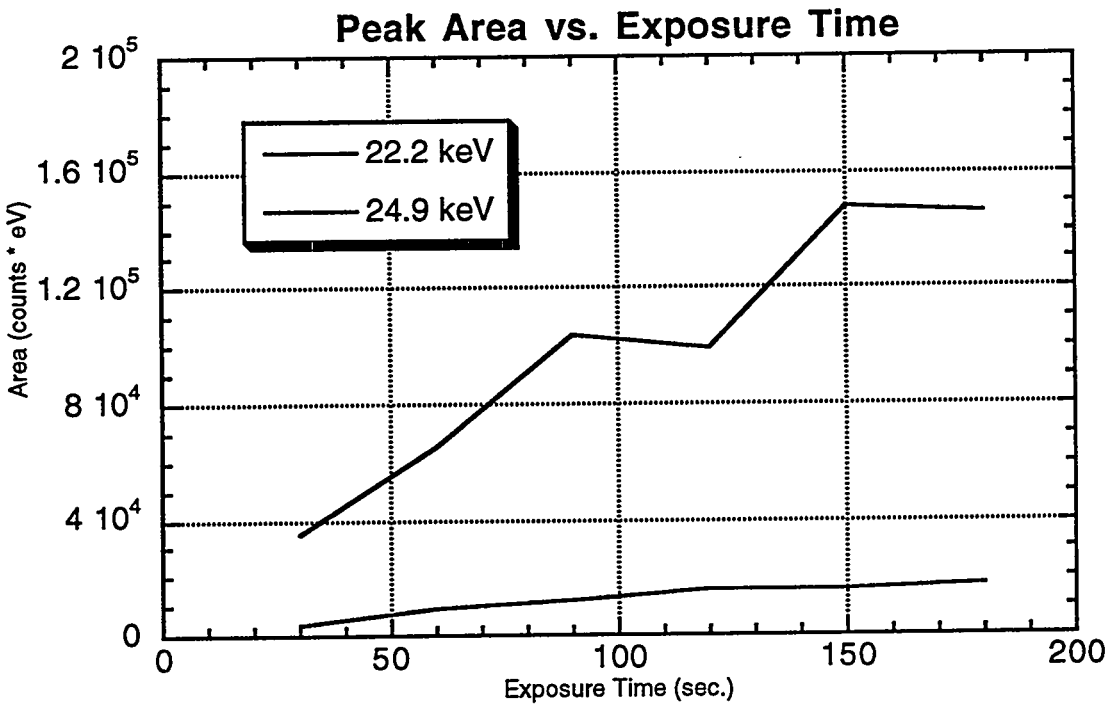
Peak Area vs. Exposure Time
2 10^5
1.6 10^5
1.2 10^5
8 10^4
4 10^4
0
Area (counts * eV)
22.2 keV
24.9 keV
0
50
100
150
200
Exposure Time (sec.)

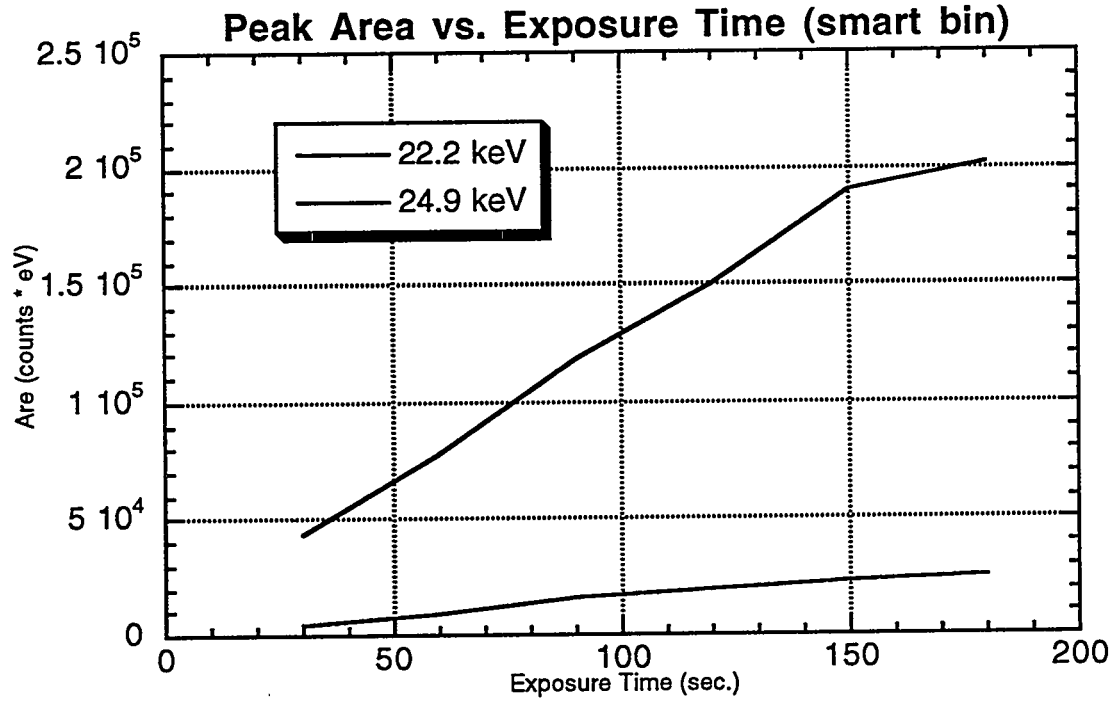
Peak Area vs. Exposure Time (smart bin)
2.5 10^5
2 10^5
1.5 10^5
1 10^5
5 10^4
0
Are (counts * eV)
22.2 keV
24.9 keV
0
50
100
150
200
Exposure Time (sec.)

Figure 14

IV. Summary

The CCD is a powerful tool for x-ray spectroscopy. When used in conjunction with today's generation of short-pulse high-intensity lasers, new regimes of plasma behavior are opened up for study. These regimes are still largely unexplored. Many exciting discoveries are yet to be made, some of which may ultimately lead to energy breakeven in inertial confinement fusion.

Acknowledgments

I would like to thank my mentor C. B Darrow for his invaluable support, without which this report would not be possible. I also thank G. Hay, Y. Zakharenkov, H. Nguyen, & C. Coverdale for their help with many technical questions. Finally, I thank our group leader B. Hammel.

This work was partially funded by the U. S. Dept. of Energy Science & Engineering Research Semester (SERS program), and the University of California Lawrence Livermore National Laboratory.

References

[1]N. G. Basov, Y. Zakharenkov, N. N. Zorev, G. V. Skilizkov, A.A.Rupasov, A. S. Shikanov - "Heating and Compression of Thermonuclear Targets by Laser Beam" p. 32

[2]Ibid. p.221

[3]F. G. Patterson, M. D. Perry and J. T. Hunt - "Design and Performance of a Multiterawatt Neodymium/Glass Laser" secs. 2, 4.

[4]G. Mourou and D. Umstadter -"Development and Applications of Compact High-Intensity Lasers" Phys. Fluids B 4 July 1992 p.2317

[5]B. Hammel, F. N. Beg, A. R. Bell, A. E. Dangor, C. B. Darrow, A. P. Fews, M. Glinsky, M. Holden P. Lee, P. A. Norreys, M. Tafarakis, and G. J. Tallents - "K-α spectroscopic measurements of MeV electrons from high intensity laser plasmas" p. 6

[6]Ibid. p.5